



**HAL**  
open science

# Controlling radiation pattern of patch antenna using Transformation Optics based dielectric superstrate

Chetan Joshi

► **To cite this version:**

Chetan Joshi. Controlling radiation pattern of patch antenna using Transformation Optics based dielectric superstrate. Electronics. Télécom ParisTech, 2016. English. NNT : 2016ENST0079 . tel-01844684

**HAL Id: tel-01844684**

**<https://pastel.hal.science/tel-01844684>**

Submitted on 19 Jul 2018

**HAL** is a multi-disciplinary open access archive for the deposit and dissemination of scientific research documents, whether they are published or not. The documents may come from teaching and research institutions in France or abroad, or from public or private research centers.

L'archive ouverte pluridisciplinaire **HAL**, est destinée au dépôt et à la diffusion de documents scientifiques de niveau recherche, publiés ou non, émanant des établissements d'enseignement et de recherche français ou étrangers, des laboratoires publics ou privés.



EDITE ED 130

## Doctorat ParisTech

# THÈSE

pour obtenir le grade de docteur délivré par

## Télécom ParisTech

Spécialité “ **Electronique et Communications** ”

*présentée et soutenue publiquement par*

**Chetan JOSHI**

le 8 Décembre 2016

## **Contrôle du diagramme de rayonnement d'une antenne en technologie imprimée à l'aide d'un superstrat diélectrique inspiré de la transformation d'espace**

Directeur de thèse : **Xavier BEGAUD**

Co-encadrement de la thèse : **Anne Claire LEPAGE**

### Jury

**M. Eric LHEURETTE**, Professeur, IEMN, Université Lille 1  
**M. Kourosh MAHDJOUBI**, Professeur, IETR, Université de Rennes 1  
**M. André DE LUSTRAC**, Professeur, C2N, Université Paris Sud  
**M. Giacomo OLIVERI**, Associate Professor, ELEDIA Research Center, University of Trento  
**Mme. Divitha SEETHARAMDOO**, Chargée de Recherche, LEOST, COSYS, IFSTTAR  
**M. Shah Nawaz BUROKUR**, Maître de conférences HDR, Université Paris Ouest  
**M. Gérard Pascal PIAU**, Senior Expert, Airbus Group Innovations

Rapporteur  
Rapporteur  
Examineur  
Examineur  
Examineur  
Invité  
Invité

**T  
H  
È  
S  
E**

Télécom ParisTech

école de l'Institut Mines Télécom – membre de ParisTech

46, rue Barrault – 75634 Paris Cedex 13 – Tél. + 33 (0)1 45 81 77 77 – [www.telecom-paristech.fr](http://www.telecom-paristech.fr)



*Dedicated to my parents: Indira and Lalit Mohan*



## Acknowledgments

First and foremost, I would like to express my sincerest thanks towards my supervisors, Prof. Xavier Begaud and Dr. Anne Claire Lepage. It has been my honor to study under their guidance. Both of them were highly supportive to me. I would like to express my gratitude towards them for providing me a great research topic, a great environment to carry out my research, for offering their constructive criticism and collaborating with me incessantly during the course of the thesis.

I thank Prof. André De Lustrac for presiding over my thesis committee. Also, I would like to express my great appreciation of Prof. Eric Lheurette and Prof. Kouroch Mahdjoubi, who reviewed and provided valuable feedback to improve the manuscript. I also thank Dr. Giacomo Oliveri and Dr. Divitha Seetharamdoo for serving on my defence committee.

The research results presented in this thesis have also been made possible due to gracious participation of Dr. Gérard Pascal Piau, Airbus Group Innovations. Gérard Pascal has been a great influence on me during my time at Telecom ParisTech. From mentoring me during an academic-industrial exchange program to his active partnership during the fabrication of the prototype, Gerard Pascal has always went a step ahead to help me. For this, I shall always remain indebted to him.

I would like to thank Dr. Shah Nawaz Burokur for his valuable guidance during the course of the thesis. Working on Project NanoDesign, I had the valuable opportunity to interact with him alongside Prof. De Lustrac and benefitted immensely with their collective expertise in the field of Transformation Optics.

I would like to thank Dr. Mark Clemente Arenas, whose thesis laid the groundwork for the discussion presented in this thesis. During the one year that I had the chance to interact with him, Mark was extremely generous with his time despite a very busy schedule in the last year of his thesis.

I would like reserve a special mention for Dr. Julien Sarrazin, who has been a great inspiration for me since my undergraduate courses in Pilani, India. I had the pleasant opportunity to collaborate with him on one of the projects pursued during the course of this thesis.

I thank the faculty and members in the Radio Frequency and Microwave Group in the COMELEC department. I would like to specially thank Dr. Christophe Roblin, Dr. Yunfei Wei and Mr. Antoine Khy for helping me during the measurements.

The fabrication of different prototypes would not have been possible without precious help and generous participation of Alain Croullebois and Karim Ben Kalaia.

The friends I made during the three years enriched my time at the institute. I would like to thank Stefan, Yenny, Ehsan, Wiem, Abdi, Abby, Marwa, Rafael, Alaa, Louise, Abdou, Mai, Reda, José, Rupesh, Jinxin, Longuang, Chaibi, Taghrid, Zahra, Hussein, Chaidi, Selma, Elie, Asma, Abir, Achraf, Chahinaz, Narsimha, for their friendships and support. I would also like to thank the ALOES choir group, with whom I spent my Thursday afternoons during the three years.

I would like to thank Smrati, Himanshu and Shashank for their unending friendship over almost ten years. They make sure that I enjoyed my life outside work as much as I do inside. I would like to specially acknowledge Smrati for her unwavering confidence in my abilities and for the immense support she provided me during the time of my thesis.

Finally, I would like to thank my family. I thank Naini, my sister, for being a bundle of joy over the years. She makes me more proud of her than any of my own achievements. I cannot thank enough my mother, Indira, for being my first teacher of every subject. I thank her for her words of wisdom and encouragement each day, which motivates me to pursue my goals. I thank my father, Lalit Mohan, who has been a role model and a guiding light for me all my life. In my pursuit to be more like him, I treasure the opportunity to be able to learn from him each day.

# Résumé

Cette thèse présente les travaux de recherche réalisés dans le cadre du projet NanoDesign financé par l'IDEX Paris-Saclay. Les participants académiques de ce projet sont Telecom ParisTech et l'Institut d'Electronique Fondamentale. Le travail présenté ici a été effectué au sein du groupe RFM (Radiofréquences et Micro-ondes) du département Communications et Electronique de Telecom ParisTech. Airbus Group Innovations est le partenaire industriel de cette thèse et a fourni un accès à son équipement d'impression 3D à Suresnes, France pour la fabrication des prototypes.

L'industrie aéronautique cherche sans cesse des solutions innovantes pour rendre les avions plus sûrs, plus rapides et plus économiques. Cela nécessite d'optimiser chaque aspect de l'appareil, y compris les systèmes de communication embarqués et par conséquent les antennes qui font partie intégrante de ceux-ci. Aujourd'hui, un avion est connecté avec des satellites et des stations au sol grâce à plusieurs antennes. Celles-ci servent souvent des applications différentes telles que la réception des signaux GPS, le système d'atterrissage aux instruments (ILS), le système d'alerte de trafic et d'évitement de collision (TCAS), le système de contrôle du trafic aérien (ATCRBS), etc.

De nombreuses applications nécessitent que l'antenne rayonne de façon omnidirectionnelle dans le plan azimutal. Ainsi, les systèmes TCAS et ATCRBS sont deux applications qui nécessitent une antenne fonctionnant en bande L. TCAS détecte les aéronefs environnants équipés de transpondeur et alerte le pilote. Ainsi, TCAS-II est composé de deux antennes placées sur le haut et le bas de l'aéronef. Typiquement, des antennes sabres sont utilisées pour une telle application. Elles sont fixées sur le fuselage de l'aéronef.

Même si les solutions classiques comme l'antenne sabre fonctionnent bien aujourd'hui, la nouvelle génération d'avions exige le remplacement de ces antennes par des solutions conformes. En effet, ces antennes fixées sur l'avion sont protubérantes, ce qui dégrade le profil aérodynamique de l'aéronef. Ainsi, une antenne conforme ou de profil réduit, tout en gardant le rayonnement dans le plan azimutal comme l'antenne sabre, améliore l'aérodynamisme et conduit à une réduction de la consommation de carburant et à une distance parcourue plus longue. Cette thèse porte sur la conception de telles antennes en utilisant l'optique de transformation (TO).

La TO est un outil de conception électromagnétique qui permet de concevoir des espaces transformés afin de contrôler le trajet des ondes électromagnétiques. La TO est devenue populaire grâce aux travaux précurseurs de Pendry sur l'invisibilité électromagnétique [1]. Par la suite, de nouveaux dispositifs électromagnétiques ont été

proposés et réalisés. On peut citer, par exemple, la cape d'invisibilité de type tapis, les super lentilles, etc. Une fois que les propriétés du matériau sont connues, le profil est réalisé en utilisant des métamatériaux ou des matériaux diélectriques standards. Pour une application industrielle, une réalisation à base des matériaux diélectriques standards est à privilégier car elle met en œuvre des procédés connus et maîtrisés. De plus, les matériaux diélectriques offrent l'avantage d'une large bande passante.

Le groupe RFM de Télécom ParisTech a déjà effectué des travaux sur la TO. Ainsi, la thèse de M.D. Clemente Arenas a présenté différentes applications de cette méthode [2]. Clemente Arenas a fait des contributions importantes dans la conception des dispositifs TO, qui ont permis la modification du diagramme de rayonnement d'antennes. Ses travaux servent de point de départ à cette thèse. Dans sa thèse, Clemente Arenas a étudié l'application de la TO dans la conception de réflecteurs diélectriques plats et de superstrats diélectriques pour élargir le diagramme de rayonnement d'une antenne patch. Une preuve de concept a été également fabriquée grâce à la technologie de l'impression 3D. Il a aussi étudié le fonctionnement d'un tel superstrat en présence d'un large plan de masse pour simuler son installation sur un aéronef. Dans le dernier chapitre de sa thèse, Clemente Arenas a proposé un superstrat TO pour réorienter le rayonnement directif d'une antenne patch dans son plan azimutal. Ce type de rayonnement correspond au rayonnement d'une antenne sabre. Néanmoins, la solution met en œuvre des paramètres constitutifs avec une variation simultanée de la permittivité ( $\epsilon_r$ ) et la perméabilité ( $\mu_r$ ). De plus, ces valeurs varient dans des plages importantes ( $1 < \epsilon_r < 15$ ,  $0.2 < \mu_r < 3$ .) ce qui rend la réalisation très difficile. Par conséquent, un des objectifs de cette thèse est d'obtenir la réorientation du rayonnement avec un superstrat de profil tout diélectrique. Nous reprendrons les équations représentant les espaces physique et virtuel utilisées par Clemente Arenas, et nous les modifierons pour ajouter de nouveaux degrés de liberté permettant un meilleur contrôle de la transformation. Pour cela, nous utiliserons des outils de simulation électromagnétique commerciaux. Au départ, le problème est formulé en deux dimensions pour diminuer la complexité et faciliter la conception. Nous présenterons une démarche systématique pour atteindre la solution finale, qui sera un dispositif tridimensionnel imprimé grâce à la technologie de l'impression 3D.

### **Introduction à la transformation d'espace**

Dans un premier temps, nous présentons les bases théoriques de la Transformation d'Espace ou Optique de Transformation (TO). Depuis plusieurs siècles, l'homme a étudié la lumière et ses propriétés afin de pouvoir mieux contrôler sa propagation dans le vide ou dans les milieux divers. La propagation de la lumière dans des milieux avec un indice de réfraction  $n$  variable a rendu possible la conception d'objets et de dispositifs qui nous servent

aujourd'hui dans la vie quotidienne aussi bien que dans la recherche, par exemple, les lentilles de corrections de vue, télescopes, microscopes, etc.

Selon le principe de Fermat, la lumière parcourt le chemin  $P$  entre deux points  $a$  et  $b$  dans un espace Cartésien  $(x, y, z)$  en un minimum de temps. Ceci est donné par l'expression (R.1)

$$P = \int_a^b n \cdot dl$$

where,

$$dl = \sqrt{(x_b - x_a)^2 + (y_b - y_a)^2 + (z_b - z_a)^2}$$

( R.1 )

Quand  $n$  est constant, la lumière propage dans le milieu en ligne droite. En revanche, ce n'est plus le cas lorsque le milieu est inhomogène. Effectivement,  $n$  est lié à la trajectoire de la lumière. Dans [1], il a été proposé de lier le changement dans la trajectoire de la lumière à l'indice de réfraction à travers la transformation des coordonnées, car la forme des équations de Maxwell ne change pas par transformation. En revanche, l'indice de réfraction, et par conséquent la permittivité et la perméabilité changent, ce qui permet de changer la trajectoire d'une onde électromagnétique. Ainsi est née la technique de Transformation d'Espace ou Optique de Transformation (TO). Comme nous pouvons le constater, la TO est un outil révolutionnaire, qui permet non seulement de changer la direction de propagation à volonté, mais aussi de réaliser une compression ou une expansion électromagnétique d'espace, de créer des illusions, etc. Dans cette thèse, la notion de compression est abordée au chapitre 3.

Nous proposons à présent une introduction détaillée sur la transformation d'espace. Considérons deux espaces; le premier est nommé l'espace physique, le deuxième est l'espace virtuel. Dans la plupart des cas nécessitant la transformation d'une onde plane, l'espace physique peut être traité comme un espace cartésien défini en  $(x, y, z)$ . L'espace virtuel est défini dans un système de coordonnées  $(x', y', z')$  selon la transformation souhaitée. La transformation est définie par une matrice jacobienne,  $J$  donnée par (R.2).

$$J = \begin{bmatrix} \frac{\delta x'}{\delta x} & \frac{\delta x'}{\delta y} & \frac{\delta x'}{\delta z} \\ \frac{\delta y'}{\delta x} & \frac{\delta y'}{\delta y} & \frac{\delta y'}{\delta z} \\ \frac{\delta z'}{\delta x} & \frac{\delta z'}{\delta y} & \frac{\delta z'}{\delta z} \end{bmatrix}$$

( R.2 )

Pendry *et al.* ont proposé d'utiliser l'opérateur  $J$  pour calculer les nouveaux paramètres constitutifs. Ceux-ci sont obtenus à partir des relations données en (R.3)

$$\varepsilon' = \frac{J\varepsilon J^T}{\det(J)}; \mu' = \frac{J\mu J^T}{\det(J)} \quad (\text{R.3})$$

Avec ces nouveaux paramètres  $\varepsilon'$  et  $\mu'$  obtenus, il est possible de retrouver la propagation désirée dans l'espace physique. Il est important de noter ici qu'une solution TO est caractérisée par son anisotropie, ce qui est lié à la présence de  $J$ , i.e. les paramètres  $\varepsilon'$  et  $\mu'$  sont des tenseurs. Cela aboutit à un profil avec des paramètres constitutifs qui dépendent de la direction de la propagation. Il faut alors se poser la question suivante : quelles conséquences y a-t-il du point de vue de la réalisation ? En effet, les matériaux naturels ne présentent pas l'anisotropie souhaitée, ce qui rend la réalisation d'une solution anisotrope impossible. Les méta matériaux sont souvent utilisés pour concevoir l'anisotropie du dispositif. Les matériaux artificiels comme les SRR (résonateurs du type *split ring*), les ELC (résonateurs *Electric LC*) permettent de modéliser les éléments diagonaux. Plusieurs exemples de réalisations à base de méta matériaux sont présentés dans le chapitre 2. On peut noter que les éléments non-diagonaux sont toujours négligés à cause de la complexité de la réalisation. Néanmoins, il existe des stratégies pour simplifier la conception.

Dans une première étape, la conception est effectuée en deux dimensions ( $x, y$ .) Cela facilite la modélisation des espaces physique et virtuel, et permet de déduire une solution préliminaire. Remarquons ici qu'un espace bidimensionnel peut avoir les composantes des champs électriques et magnétiques selon le troisième axe,  $z$ .

Dans l'étape suivante, nous simplifions la conception en choisissant une polarisation du champ. Comme discuté auparavant, il est impossible de réaliser une solution TO avec tous les éléments des tenseurs, 18 en total. Si le champ incident est polarisé selon une direction définie, cela permet de réduire le nombre d'éléments nécessaires. Par exemple, si l'étude favorise un champ électrique polarisé suivant  $z$  i.e.  $E_z$ , cela réduit le nombre d'éléments pour réaliser la transformation à cinq :  $\mu_{xx}$ ,  $\mu_{xy}$ ,  $\mu_{yx}$ ,  $\mu_{yy}$  et  $\varepsilon_{zz}$ .

Rappelons que ce nouveau profil permet de réaliser le gradient de l'indice de réfraction effectif,  $n_{eff}$ . Lorsque le champ  $E_z$  traverse l'espace transformé, l'indice de réfraction à un endroit donné est calculé avec la relation (R.4.) Ici, nous négligeons les éléments non diagonaux.

$$n_{eff} = \frac{\sqrt{\mu_{xx}\epsilon_{zz}}\sqrt{\mu_{yy}\epsilon_{zz}}}{\epsilon_0\mu_0}$$

( R.4 )

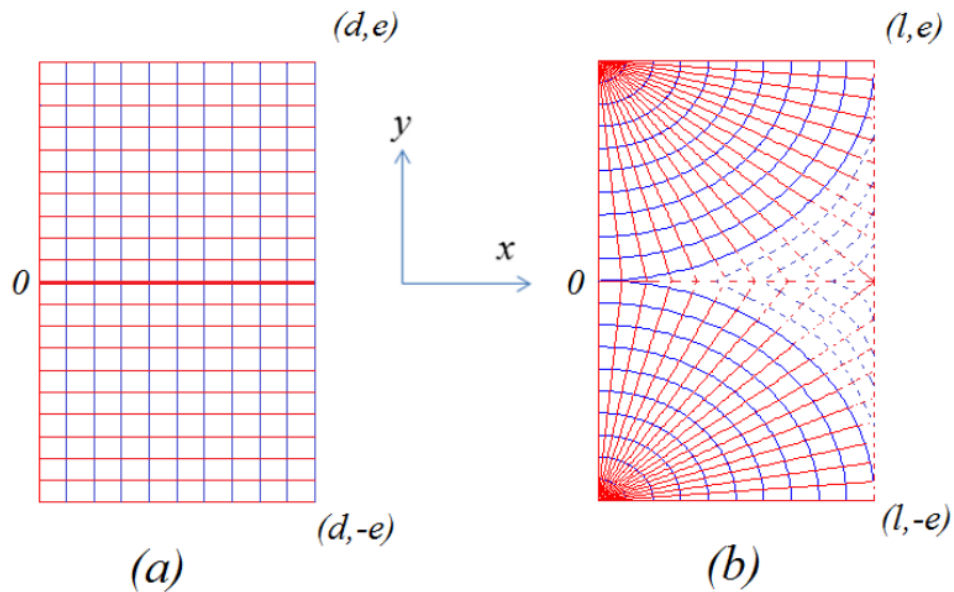
Comme nous pouvons le constater, il est important d'obtenir le bon profil de  $n$  pour une interprétation correcte de la transformation. Mais, cela n'exige pas de réaliser tous les éléments des tenseurs. Ainsi, la normalisation d'éléments de tenseurs permet de respecter le profil de  $n$ , tout en réduisant encore le nombre d'éléments. Plusieurs exemples d'une telle conception seront présentés dans le chapitre 2 (2.3.1.) Dans le 3<sup>ème</sup> chapitre de sa thèse, Clemente Arenas a proposé d'utiliser la normalisation pour concevoir un superstrat afin d'obtenir un rayonnement antipodal dans le plan azimutal. L'inconvénient majeur de sa conception était la variation simultanée de la permittivité et la perméabilité, ainsi que leurs valeurs extrêmes.

La deuxième approche est dite Quasi Conformal Transformation Optics (QCTO). Une transformation liant l'espace Cartésien (maillage orthogonal) avec un espace virtuel ayant un maillage quasi-orthogonal permet d'éliminer toute dépendance sur les éléments magnétiques  $\mu_{xx}$  et  $\mu_{yy}$  dans l'équation (R.4). Cette approche est utilisée dans différents travaux pour montrer plusieurs concepts tout-diélectriques. Les détails de la conception peuvent être consultés en 2.3.2. Dans cette thèse nous abordons une solution à base de QCTO afin de simplifier le problème et faciliter la construction. Dans la section suivante, nous allons aborder la conception d'un superstrat tout diélectrique d'une faible épaisseur qui fonctionne à 1.25 GHz (bande L.)

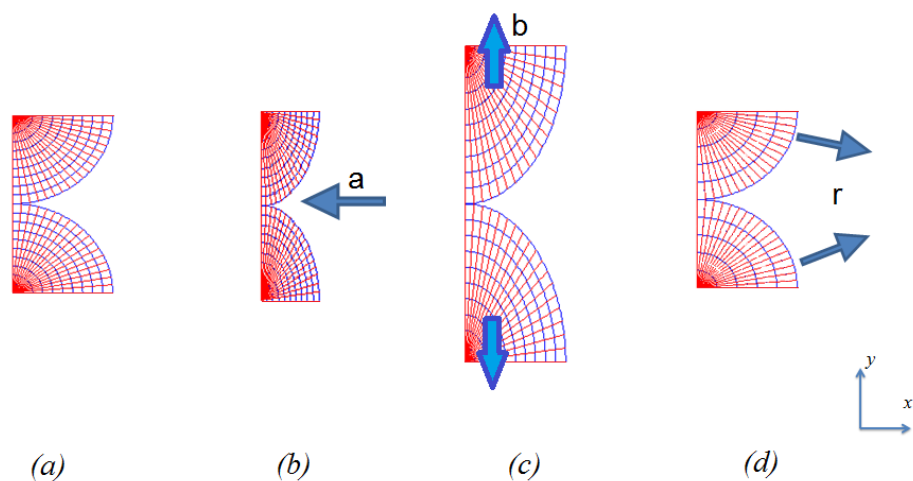
### **Le concept**

L'objectif principal de l'étude menée dans cette thèse est de réorienter le rayonnement d'une antenne patch dans son plan azimutal en utilisant la TO. Il est donc important d'identifier les espaces physique et virtuel. Une antenne patch a un rayonnement directif, avec un maximum du gain selon la normale au patch (*broadside*). Il est difficile de formuler mathématiquement un espace physique qui soit une représentation exacte du front d'onde émanant de l'antenne, car ce dernier dépend de la forme de l'antenne, du plan de masse, etc. Un tel rayonnement directif peut être modélisé par une onde plane, et par conséquent l'espace cartésien peut être utilisé. L'espace virtuel gouverne la transformation d'espace. Pour changer la direction vers l'azimut, nous proposons d'utiliser un espace virtuel composé des deux quadri-ellipses. Les deux espaces sont montrés sur la Figure R 1. Les

lignes bleues verticales sont transformées en cercles bleus, alors que les lignes rouges sont transformées en lignes radiales.



Il est aussi possible de compresser ou dilater l'espace virtuel. La Figure R 2 présente différents types de compressions appliquées sur un espace non compressé. Dans le contexte de cette thèse, une compression suivant  $x$  est appelée « compression axiale ». Elle joue sur l'épaisseur du dispositif, permettant ainsi un profil réduit. Le degré de compression est maîtrisé grâce à un facteur de compression axiale,  $a$ . Une compression suivant l'axe  $y$  est dite « compression latérale », et elle est maîtrisée grâce au facteur de compression latérale,  $b$ . Une compression radiale peut être aussi imaginée. Elle est gouvernée par le facteur,  $r$ . Plus de détails sur chaque type de compression sont fournis dans le chapitre 3.



(R.5) et (R.6) sont les équations de la transformation (avec les facteurs de compression). Il est important de souligner que les facteurs définis ci-dessus ont une valeur strictement positive. Quand ils sont égaux à 1, il n'y a pas de compression, ni d'expansion. Ils introduisent une compression lorsque leurs valeurs sont plus grandes que 1 ( $a, b, r > 1$ ), et une dilatation d'espace lorsque les valeurs sont comprises entre 0 et 1.

$$x' = r\sqrt{(ax)^2 + (b(y \mp e))^2} \quad (\text{R.5})$$

$$y' = \frac{e}{\pi} \tan^{-1} \left( \frac{b(y \mp e)}{ax} \right) \quad (\text{R.6})$$

En utilisant ces équations, nous pouvons calculer ensuite la matrice jacobienne,  $J$  qui correspond à la transformation de l'espace Cartésien en espace virtuel.

$$J = \begin{bmatrix} \frac{a^2rx}{\sqrt{(ax)^2 + (b(y \mp e))^2}} & \frac{b^2r(y \mp e)}{\sqrt{(ax)^2 + (b(y \mp e))^2}} & 0 \\ -\frac{abe}{\pi} \frac{(y \mp e)}{(ax)^2 + (b(y \mp e))^2} & \frac{abe}{\pi} \frac{x}{(ax)^2 + (b(y \mp e))^2} & 0 \\ 0 & 0 & 1 \end{bmatrix} \quad (\text{R.7})$$

Une fois  $J$  est connue, nous pouvons utiliser (R.3) pour calculer les nouveaux profils de permittivité et perméabilité. Lorsqu'on considère une transformation sans prendre en compte les compressions ( $a = b = r = 1$ ),  $J$  est donnée par (R.8).

$$\varepsilon = \mu = \begin{bmatrix} \frac{\pi x'}{e} & 0 & 0 \\ 0 & \frac{e}{\pi x'} & 0 \\ 0 & 0 & \frac{\pi x'}{e} \end{bmatrix} \quad (\text{R.8})$$

Comme discuté auparavant, la transformation ne dépend que de  $\mu_{xx}$ ,  $\mu_{yy}$  et  $\varepsilon_{zz}$  pour un champ électrique polarisé suivant l'axe  $z$ . Donc, les autres éléments dans le tenseur peuvent être négligés. De plus, nous pouvons remarquer que les éléments  $\mu_{xx}$  et  $\mu_{yy}$  sont inverses l'un de l'autre, et par conséquent, leur produit et  $\mu_0$  vont s'annuler dans (R.4). Ainsi, on peut constater que ce profil initial permet une conception du type QCTO, et le profil de l'indice de réfraction peut être réalisé uniquement à partir de la variation de permittivité.

Il est important de noter ici que pour un espace compressé ou dilaté non-uniformément ( $a \neq b$ ), les éléments diagonaux ( $\mu_{xx}$  et  $\mu_{yy}$ ) ne vont plus s'annuler. Aussi, les éléments non-diagonaux ( $\mu_{xy}$  et  $\mu_{yx}$ ) apparaîtront à cause d'une telle compression non-uniforme. Néanmoins, la transformation initiale étant réalisable en permittivité, nous ne prenons plus en compte les éléments du tenseur de perméabilité dans le contexte de cette thèse. (R.9) est l'expression de la permittivité comprenant des facteurs de compression.

$$\varepsilon_{zz} = \frac{m\pi x^1}{abre}$$

( R.9 )

Ici,  $m$  est une nouvelle variable, facteur de décalage de l'indice de réfraction,  $n$ . Elle permet de décaler la permittivité, et par conséquent les valeurs de  $n$  selon le besoin. C'est un choix important de négliger les éléments magnétiques, ce qui facilite le prototypage éventuel avec des matériaux standards. En revanche, il est tout à fait possible qu'un tel profil issu de la TO ne réoriente plus l'onde électromagnétique à cause du non-respect de la solution théorique. Mais, nous proposons d'adapter la solution en utilisant les nouveaux degrés de liberté, par exemple les facteurs de compression ( $a$ ,  $b$  et  $r$ ), ainsi que le facteur de décalage  $m$ .

Nous utilisons COMSOL Multiphysics™ pour valider le concept en 2D. Pour modéliser l'antenne, nous utilisons une source idéale composée d'une nappe de courant polarisée suivant  $z$ . Ce modèle ne prend pas en compte les désadaptations à cause des réflexions à l'interface entre l'antenne et le superstrat. On peut noter que COMSOL permet de définir le tenseur complet.

Les dimensions de l'espace Cartésien de départ sont  $\lambda$  par  $0.5 \lambda$ , où  $\lambda$  correspond à la fréquence de conception, 1.25 GHz. Le choix de la taille est canonique. Elle est aussi motivée par des contraintes liées à l'épaisseur et la dimension latérale du superstrat. Cet espace est transformé selon l'équation de transformation. Pour les facteurs de compression,  $a = 4.16$ ,  $b = 1.6$ ,  $r = 1$ , la taille du superstrat est  $0.625 \lambda$  par  $0.12 \lambda$ . Le facteur de décalage est choisi à  $m = 14$ , ce qui permet d'adapter le profil de permittivité pour une réorientation complète du champ dans le plan azimutal. La Figure R 3 montre le profil de permittivité,  $\varepsilon_{zz}$  et la distribution du champ électrique,  $E_z$ .

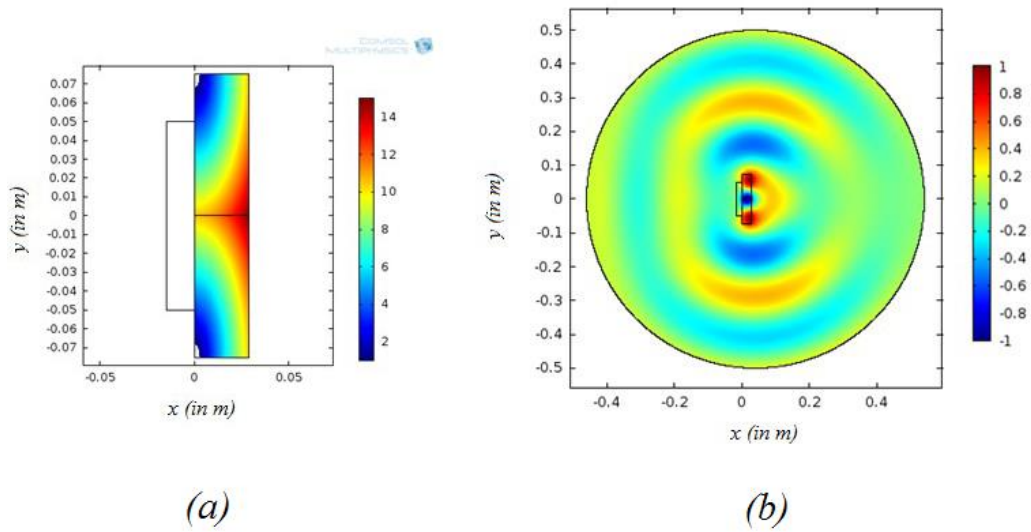


Figure R 3 (a) Profil de permittivité  $\epsilon_{zz}$ , (b) Carte du champ électrique normalisé,  $E_z$ .

Ce profil est tout diélectrique et ne contient pas d'élément magnétique. La variation dans le profil est  $0 < \epsilon_{zz} < 14.8$ . Dans la Figure R 3(a), la région où la permittivité est  $0 < \epsilon_{zz} < 1$  étant très petite, nous pouvons la négliger et remplacer par 1. Cela permettra éventuellement d'utiliser les matériaux standards pour la fabrication. Nous pouvons donc utiliser les valeurs diélectriques isotropes  $\epsilon_r$ .

Nous avons alors un profil 2D avec une variation continue de la permittivité. Mais il est impossible d'obtenir un gradient continu de la permittivité dans la pratique. Le gradient est souvent conçu par un milieu effectif comprenant 2 ou plusieurs matériaux. La proportion de ces matériaux diélectriques permet de contrôler la permittivité. Pour une telle conception, il est nécessaire de discrétiser le profil continu en pixels. La discrétisation est présentée en détails dans la section 3.3.2.2 de la thèse. Nous proposons de discrétiser le profil continu en 48 pixels (16 par 3). La Figure R 4 montre le profil discrétisé et la cartographie du champ électrique normalisé.

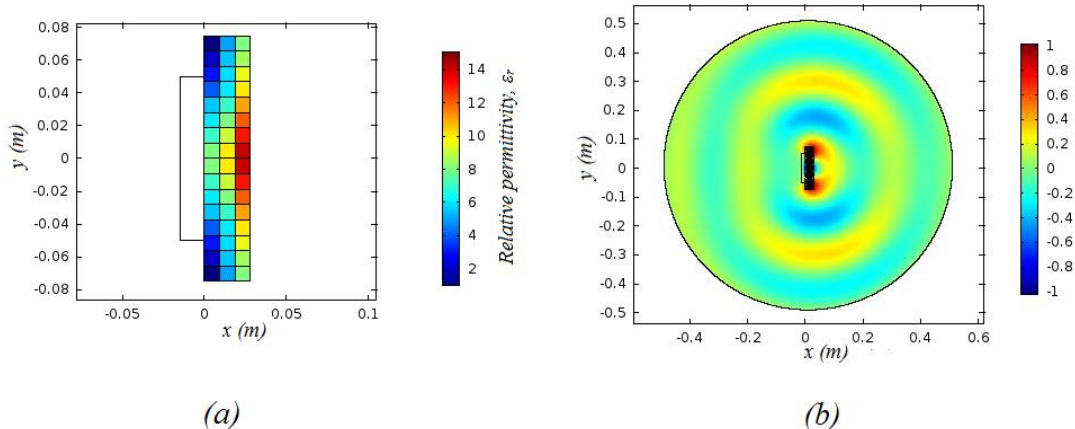


Figure R 4 (a) Profil discrétisé en 48 pixels (16 par 3), (b) Cartographie du champ électrique normalisé,  $E_z$

La discrétisation n'a pas d'effet sur les performances du profil issu de la TO. Cela confirme notre proposition d'un profil tout diélectrique capable à réorienter le champ électromagnétique dans le plan azimutal. L'étape suivante consiste à la conception de la solution 3D à partir du profil discrétisé, de telle sorte que la transformation soit préservée lors de passage de 2D à 3D. Cela est faisable soit en tournant le profil selon l'axe  $x$  dans le plan  $y-z$  pour un superstrat cylindrique ; ou en extrayant le profil selon  $z$  pour un superstrat cuboïde. Dans cette thèse, nous étudions davantage le superstrat cuboïde car il offre une facilité de fabrication. Néanmoins une application d'un superstrat cylindrique est présentée dans les annexes.

Nous étudions la solution 3D dans le logiciel CST Microwave Studio. Contrairement à COMSOL, ce logiciel permet la simulation du superstrat 3 D en présence d'une antenne (et non d'une nappe de courant). Pour nos simulations, nous utilisons le solveur temporel de CST. Ce choix est motivé a priori par la géométrie du superstrat. Nous pouvons contrôler la précision du calcul par le maillage.

Dans une première étape, nous concevons une antenne patch carrée. La longueur du patch est 68 mm et celle du plan du masse est 100 mm. Elle est alimentée par un connecteur coaxial, qui est simulé également. La fréquence d'opération est 1.25 GHz. La simulation de l'antenne seule montre qu'elle présente un rayonnement classique avec un lobe principal dans la direction normale à l'antenne (selon l'axe  $x$ ) et un gain réalisé de 6.7 dBi. Lorsque l'antenne est placée en dessous du superstrat, nous observons que l'antenne n'arrive pas à coupler l'énergie électromagnétique dans le superstrat. Par conséquent, le superstrat ne rayonne pas. Ce non-couplage peut être attribué aux réflexions à l'interface due à la forte variation dans la permittivité.

Pour éviter cela, nous proposons d'éloigner l'antenne du superstrat pour faciliter l'entrée de l'énergie électromagnétique dans le superstrat. Avec une couche d'air de 10 mm

entre le superstrat et l'antenne, nous observons qu'il existe un couplage à 1.33 GHz. A cette fréquence d'opération, le rayonnement est réorienté dans le plan azimutal de l'antenne grâce au superstrat. De plus, une couche diélectrique avec une permittivité  $\epsilon_r > 1$  permet d'abaisser la fréquence d'opération. Le superstrat continue de réorienter le champ dans le plan azimutal tant que la taille électrique du superstrat ne devient pas petite. La permittivité et l'épaisseur de la couche entre le superstrat et l'antenne permettent de fixer la fréquence d'opération et l'adaptation de l'antenne. Davantage d'explications sur le rôle de cette couche sont fournies dans la section 3.3.3.2. L'ensemble fonctionne à 1.25 GHz lorsqu'on utilise une couche diélectrique de permittivité  $\epsilon_r = 1.8$  et d'épaisseur 12 mm. Le gain réalisé est 3.5 dB. La Figure R 5 présente le diagramme du rayonnement de l'ensemble à 1.25 GHz. Nous observons une réorientation complète dans le plan azimutal, et un nul de rayonnement selon l'axe principal de l'antenne (axe  $x$ ).

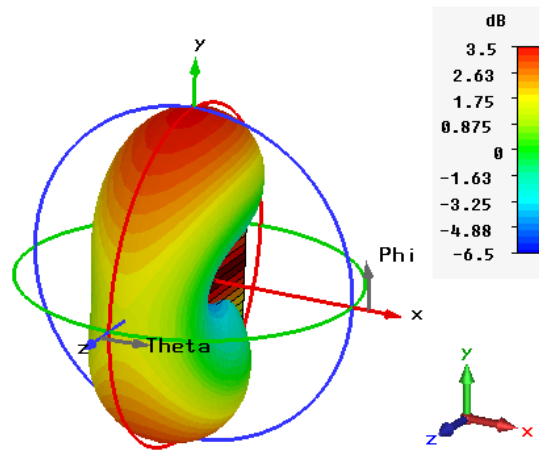


Figure R 5 Diagramme du rayonnement de l'ensemble à 1.25 GHz.

Donc, nous avons démontré un concept TO, qui permet d'introduire un fort changement dans le diagramme du rayonnement d'une antenne patch. Le superstrat a une faible épaisseur ( $0.12\lambda$  à 1.25 GHz.) Le dispositif peut être construit à partir de matériaux diélectriques standards, ce qui facilite sa fabrication par rapport aux autres solutions TO qui nécessitent l'utilisation des matériaux artificiels. Pourtant la réalisation d'un prototype est un défi à cause de la variation importante de permittivité ( $1 < \epsilon_r < 14.$ ) Nous abordons la question de la réalisation dans la section suivante.

### **Réalisation d'un prototype**

Les réalisations pratiques des concepts TO tout diélectriques sont généralement basés sur l'utilisation d'un milieu effectif. Une combinaison d'un premier matériau de permittivité élevée  $\epsilon_{\text{high}}$  et d'un second matériau de permittivité faible,  $\epsilon_{\text{low}}$  (souvent de l'air) permet d'atteindre une valeur de permittivité entre  $\epsilon_{\text{low}}$  et  $\epsilon_{\text{high}}$ . Il est possible, par exemple, de faire des trous dans un matériau de permittivité élevé. Le profil discrétisé de permittivité présenté

dans la section précédente contient de fortes valeurs de permittivité ( $\epsilon_r$  allant jusqu'à 14). Peu de matériaux offrent une permittivité élevée et des propriétés mécaniques permettant de faire facilement des trous. Plus la permittivité est élevée, plus il est difficile de travailler mécaniquement avec le matériau. Il est donc difficile de fabriquer une solution à partir de deux valeurs de permittivité.

Dans le chapitre 4 de la thèse, nous proposons une première solution à partir de 3 valeurs de permittivité:  $\epsilon_{\text{high}}$ ,  $\epsilon_{\text{low}}$  et de l'air. Selon l'approche proposée, la permittivité des pixels dans le profil est simplifiée de la façon suivante :

- $\epsilon_{\text{high}}$  remplace toutes les valeurs  $\epsilon_r > \epsilon_{\text{high}}$ . Cela se traduit par une région contenant trois plaques de  $\epsilon_{\text{high}}$ .
- Milieu de permittivité effective construit à partir de  $\epsilon_{\text{low}}$  et  $\epsilon_{\text{high}}$  pour réaliser les valeurs intermédiaires  $\epsilon_{\text{low}} < \epsilon_r < \epsilon_{\text{high}}$ . Des tiges de  $\epsilon_{\text{high}}$  sont intégrées dans le matériau hôte,  $\epsilon_{\text{low}}$ .
- Milieu de permittivité effective construit à partir de  $\epsilon_{\text{low}}$  et 1 pour réaliser  $1 < \epsilon_r < \epsilon_{\text{low}}$ .

Dans cette thèse, nous utilisons l'alumine pour le matériau  $\epsilon_{\text{high}}$ , dont la permittivité est 9.9. En remplaçant toutes les valeurs plus grandes que 9.9, nous obtenons une région constituée de trois plaques d'alumine.  $\epsilon_{\text{low}}$  correspond à une permittivité d'un matériau compatible avec une imprimante 3D. L'impression 3D est une technologie qui facilite le prototypage des formes complexes. Nous choisissons  $\epsilon_{\text{low}} = 4.4$ , ce qui est la plus grande permittivité d'un matériau déjà commercialisé compatible avec l'impression 3D. La Figure R 6 montre la réalisation du profil discrétisé. La couche diélectrique  $\epsilon_r = 2.5$  a été utilisée pour fixer la fréquence d'opération à 1.25 GHz.

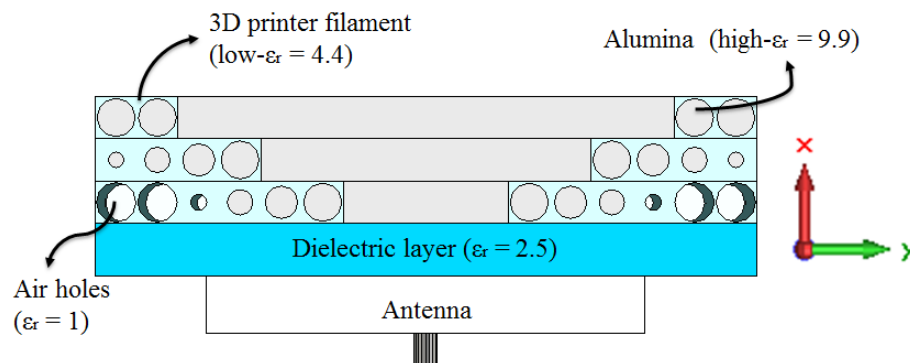


Figure R 6 Réalisation du profil discrétisé.

Comme discuté auparavant, le gradient dans la permittivité est atteint en changeant la proportion des matériaux diélectriques. Cela peut être réalisé en variant le diamètre des tiges de matériau  $\epsilon_{\text{high}}$  ou des trous d'air. Les performances de ce profil peuvent être consultées dans la section 4.2.1.

On s'aperçoit très vite qu'il est difficile de mettre en œuvre un tel concept. Malgré la facilité offerte par l'imprimante 3D, la précision dans la fabrication présente un obstacle important. Si l'objet est imprimé en utilisant des matériaux plastiques, il est sensible à la chaleur. Cela peut induire une expansion et une déformation de l'objet. Ces déformations se produisent souvent pour un objet massif. L'Alumine n'étant pas un matériau mécaniquement facile, les déformations compliquent l'insertion des tiges ou plaques d'alumine dans les trous de la partie imprimée. Nous cherchons donc un moyen de réduire encore la complexité. Pour cela, nous proposons de remplacer toutes les valeurs de permittivité entre 1 et  $\epsilon_{\text{high}}$  par  $\epsilon_{\text{low}}$ . Cela permet d'éliminer les trous d'air et tiges d'alumine, facilitant ainsi l'impression. Notons que l'absence de variation de permittivité dans la région imprimée, se traduit par une réduction du gain réalisé par rapport au profil précédent. Néanmoins l'impact sur la forme du diagramme du rayonnement est limité et nous retrouvons le rayonnement antipodal avec deux lobes opposés dans le plan azimutal. La Figure R 7 présente cette simplification du superstrat et le principe de l'assemblage antenne + superstrat. Ainsi un profil de 48 pixels de permittivité différente a été simplifié en une solution avec seulement deux valeurs de permittivité. Ici, la couche diélectrique de  $\epsilon_r = 2.2$  permet de fixer la fréquence d'opération à 1.25 GHz.

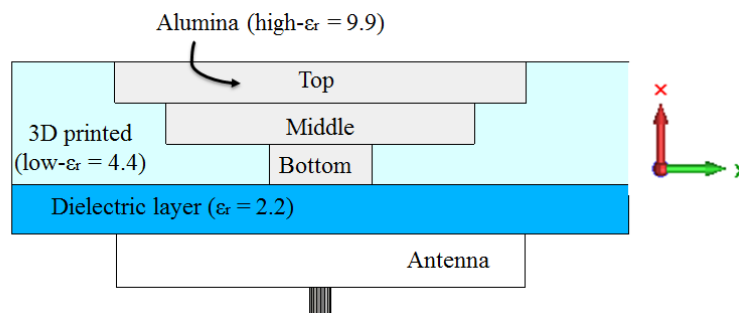


Figure R 7 Simplification du superstrat et le principe de l'assemblage antenne + superstrat

Pour faciliter la fabrication de la preuve du concept, nous nous permettons d'imprimer la couche diélectrique avec l'imprimante 3D. Avec cet objectif, nous relâchons la contrainte de fréquence d'opération. Cela permet d'imprimer une seule pièce avec l'imprimante qui joue à la fois le rôle d'une couche diélectrique, ainsi que la structure d'accueil pour les plaques d'alumine.

Au lieu de fabriquer une nouvelle antenne patch, nous réutilisons une antenne patch carrée disponible chez Airbus Group Innovations. La fréquence d'opération de l'antenne est 1.189 GHz en simulation et 1.206 GHz en mesures. Aussi, la fréquence d'opération de l'antenne avec le superstrat conçu ci dessus est 1 GHz dans les simulations. Rappelons que le superstrat a été conçu pour fonctionner à 1.25 GHz. Nous avons donc modifié les dimensions du superstrat pour compenser le décalage de fréquence. Toutes les dimensions sont

transposées à 1 GHz. La transposition est expliquée en détails dans la section 4.3.2. La Figure R 8 montre le dispositif. La plaque de PlexiGlas est fixée au-dessus du superstrat grâce aux vis de Nylon, elle permet de tenir les plaques d'alumine à l'intérieur du superstrat. Nous imprimons également un système de 3 accroches pour fixer l'antenne en dessous du superstrat.

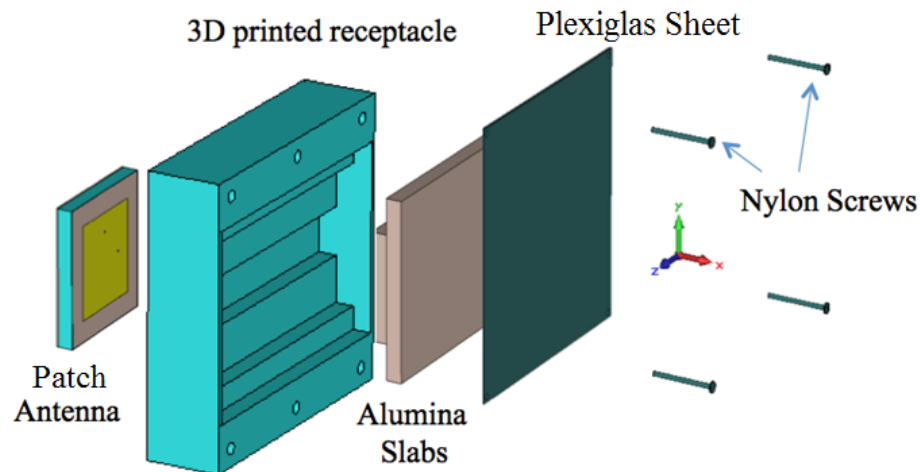


Figure R 8 Vue éclatée du prototype.

Nous avons acheté les plaques d'alumine chez GoodFellow, un fournisseur spécialiste des céramiques, métaux, etc. Grâce à la participation d'Airbus Group Innovations, nous avons accès à deux imprimantes 3D, fonctionnant avec deux technologies différentes. Le matériau diélectrique correspondant à la permittivité  $\epsilon_{low} = 4.4$  utilisé dans nos simulations précédentes n'est pas compatible avec les deux imprimantes. Donc, nous utilisons deux matériaux différents pour l'impression 3D:

- Résine FullCure photo-curable ( $\epsilon_r = 2.56$ )
- Filament de PLA (*Poly Lactic Acid*) ( $c = 2.8$ )

La résine FullCure est un matériau qui est sensible à la lumière ultra-violet. L'imprimante Objet Eden260 VS permet de traiter un jet de résine avec la lumière UV qui résulte dans la plastification instantanée. Cette imprimante permet d'imprimer un superstrat massif. La Figure R 9 montre le superstrat imprimé en FullCure. Notons que les trous pour les vis de nylon sont imprimés en cours de fabrication dans l'imprimante 3D. Lorsque nous étudions le comportement de l'ensemble (antenne + superstrat FullCure), la fréquence d'opération est 1.10 GHz en simulation et 1.14 GHz en mesure. Ce décalage est dû au décalage en fréquence de l'antenne elle-même. L'ensemble antenne + superstrat présente une bande passante de 65 MHz (soit 5.2% à 1.14 GHz). La Figure R 10 montre le gain réalisé simulé à 1.10 GHz. Dans les Figure R 11-13, nous comparons le diagramme de rayonnement dans les 3 plans aux fréquences d'opération en simulation et mesures.

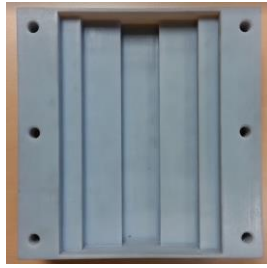


Figure R 9 Superstrat imprimé en FullCure

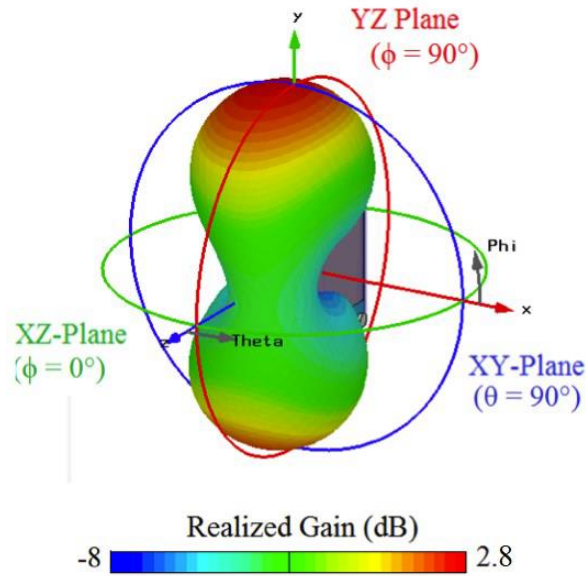


Figure R 10 Diagramme de rayonnement 3D : gain réalisé (dB) de l'antenne avec le superstrat.

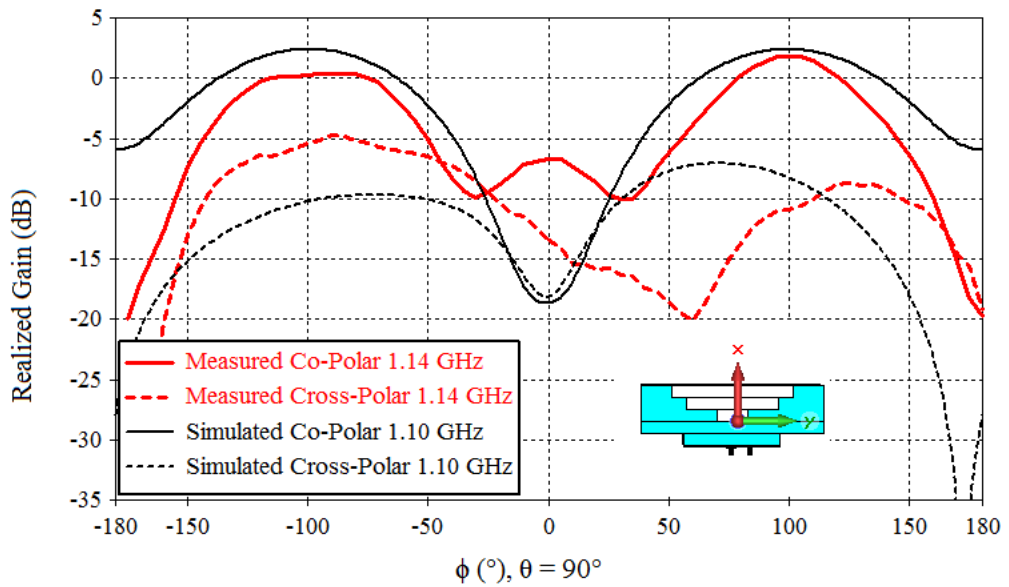


Figure R 11 Comparaison du gain réalisé dans le plan x y en simulation (à 1.10 GHz) et mesure (1.14 GHz) de l'antenne avec le superstrat.

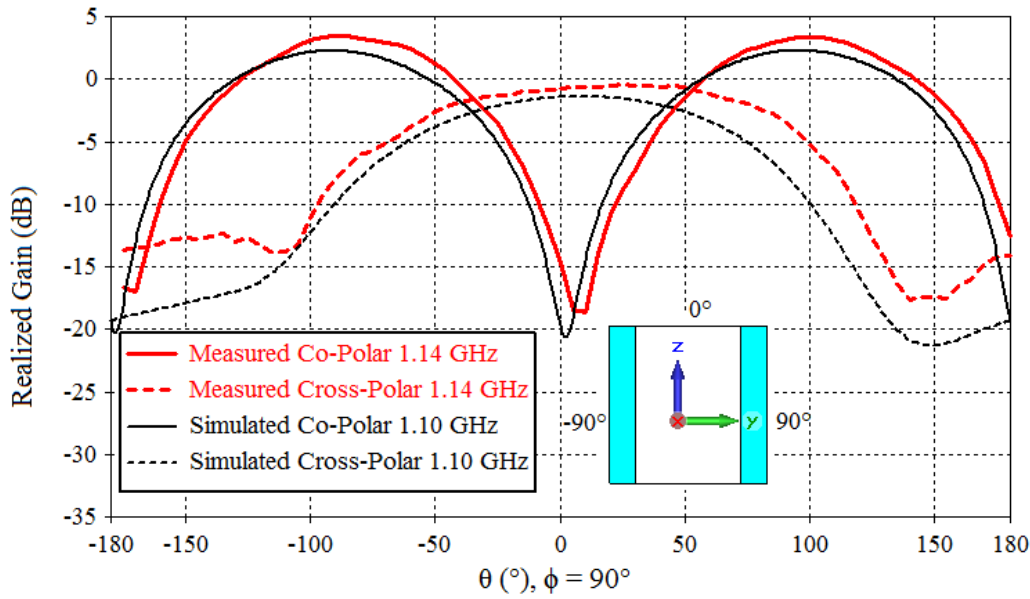


Figure R 12 Comparaison de gain réalisé dans le plan y z en simulation (à 1.10 GHz) et mesure (1.14 GHz) de l'antenne avec le superstrat.

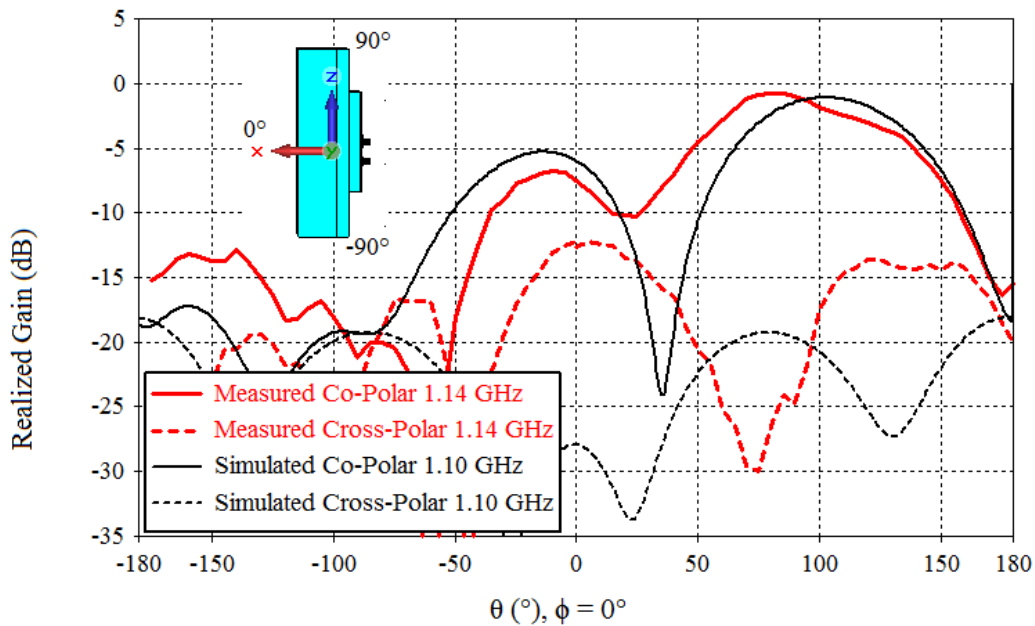


Figure R 13 Comparaison de gain réalisé dans le plan x z en simulation (à 1.10 GHz) et mesure (1.14 GHz) de l'antenne avec le superstrat.

Comme nous pouvons le noter sur la Figure R 11, les maxima de rayonnement sont selon l'axe y (soit  $\phi = \pm 100^\circ$ ). Ces résultats valident la proposition. Nous avons fait un deuxième prototype en utilisant le PLA. Le filament de PLA est passé par le bec de l'imprimante CraftBot 3D. Tout d'abord, le bec est chauffé jusqu'à  $160^\circ\text{C}$ . Le filament passant par le bec fond et est ensuite déplacé sur une plateforme pour imprimer le superstrat. La Figure R 14 montre le superstrat PLA. Notons que ce superstrat n'est pas massif à cause

des limitations technologiques de l'imprimante utilisée. La permittivité effective est donc proche de 1. L'ensemble fonctionne à 1.245 GHz. Nous retrouvons une bonne cohérence entre les simulations et mesures, nous observons la réorientation dans le plan azimutal à la fréquence d'opération. Le gain maximum réalisé dans ce cas est 4.1 dB. Notons que le processus de fabrication utilisant le filament de PLA n'est pas très précis. Les résultats sont présentés dans la section 4.3.4.2.

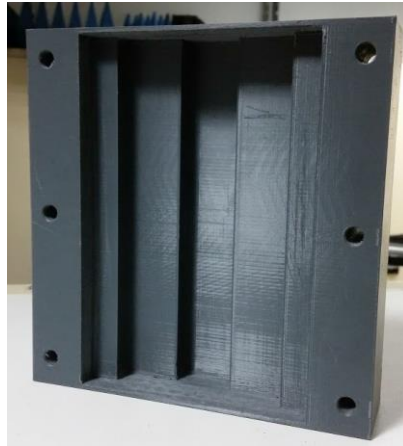


Figure R 14 Superstrat imprimé en PLA

Nous avons donc pu valider le concept TO avec deux technologies de fabrication différentes. Le superstrat permet de réorienter le rayonnement directif initial selon la normale vers le plan azimutal. Un profil très complexe contenant 48 pixels a été simplifié en un concept ne contenant que 3 plaques d'alumine et le superstrat imprimé. La facilité de fabrication du superstrat est un avantage. Ensuite, nous discutons les possibilités d'étendre le concept proposé vers d'autres applications innovantes.

### **Les extrapolations et nouvelles applications**

Suite à la validation du concept TO, nous proposons de mener de nouvelles études portant sur l'applicabilité de la transformation d'espace définie dans le chapitre 3. Puis nous présentons un guide de conception pour la fabrication de superstrats à partir de 2 matériaux diélectriques. Finalement, nous offrons une perspective sur l'installation de ces superstrats à proximité d'un grand plan de masse.

Tout d'abord, nous présentons un concept TO pour un rayonnement semi-circulaire. Dans une première étape, considérons l'espace virtuel choisi auparavant. Grâce aux degrés de libertés ( $a$ ,  $b$ ,  $r$  et  $m$ ) que nous avons intégrés dans l'équation de transformation d'espace, nous pouvons adapter la solution pour une nouvelle forme de rayonnement. Pour valider notre proposition, nous proposons de choisir les paramètres suivants :  $a = 3$ ,  $b = 1.5$ ,  $r = 1$  et  $m = 5.5$ . La taille du profil est  $0.67\lambda \times 0.16\lambda$  à 1.25 GHz. La Figure R 15 représente la permittivité

dans l'espace transformé. Elle varie entre  $1 < \epsilon_r < 8.14$ . La Figure R 16 montre un front d'onde semi-circulaire issu de l'espace transformé.

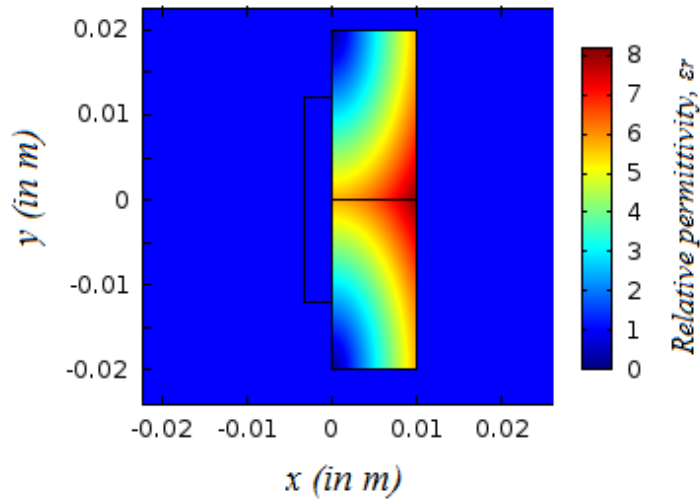


Figure R 15 Profil de permittivité pour un rayonnement semi-circulaire.

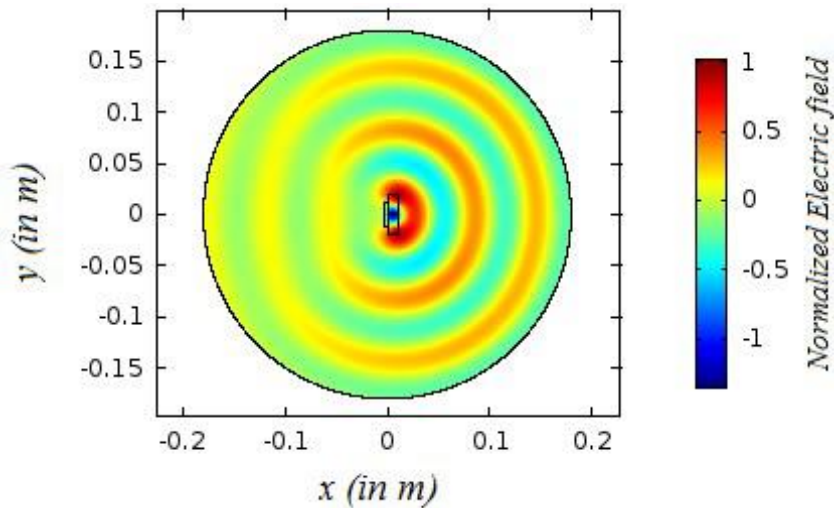


Figure R 16 Front d'onde semi-circulaire.

Comme auparavant, nous discrétisons le profil continu de permittivité en 48 pixels. La permittivité de ces pixels varie entre  $1 < \epsilon_r < 8$ . Nous utilisons une antenne patch fonctionnant à 1.25 GHz comme source. Une couche diélectrique de permittivité  $\epsilon_r = 1.5$  et d'épaisseur 12 mm a été utilisée pour faire une interface entre le superstrat et l'antenne. La fréquence d'opération de l'ensemble est 1.25 GHz. Dans la Figure R 17, nous présentons la directivité de l'antenne seule et de l'ensemble à 1.25 GHz. Nous observons que le faisceau est élargi dans le plan  $x y$ , alors qu'il n'est pas affecté dans le plan  $x z$ . À la fréquence d'opération, la largeur du faisceau est de  $297^\circ$ . Un tel élargissement du faisceau peut être très utile pour améliorer la performance d'une antenne patch dans les applications aéronautiques. Plus des détails sont fournis dans la section 5.1.1. Dans la section 5.1.2, nous proposons aussi

d'utiliser les degrés de liberté pour concevoir un superstrat avec un diagramme du rayonnement reconfigurable.

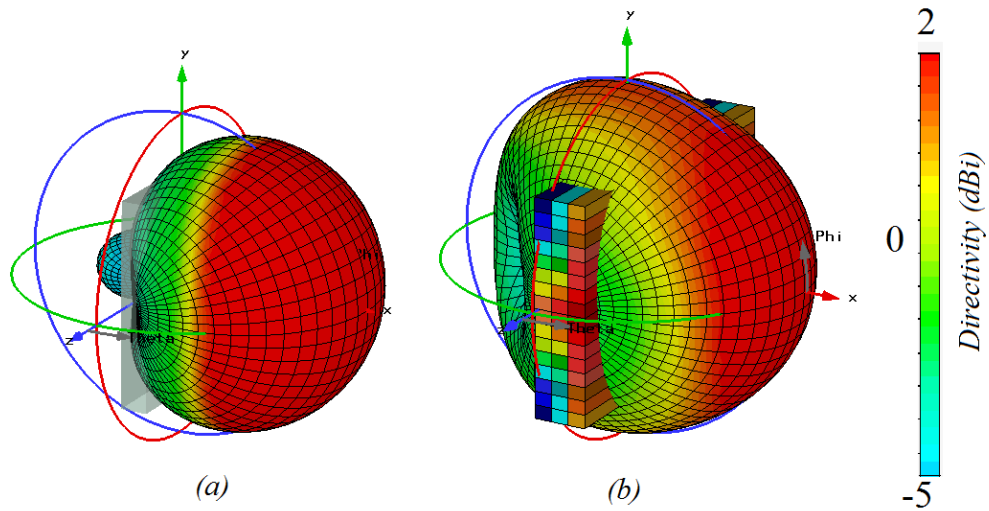


Figure R 17 Directivité (dBi) (a) Antenne seule; (b) Antenne avec superstrat. Maxima dans le plot limité à 2 dBi pour comparaison.

Dans la section 5.1.3, nous proposons un concept TO qui transforme l'espace physique Cartésien selon un espace virtuel compris d'une seule ellipse. La Figure R 18 montre les espaces physique et virtuel. Il permet de réorienter le rayonnement dans une seule direction dans le plan azimutal.

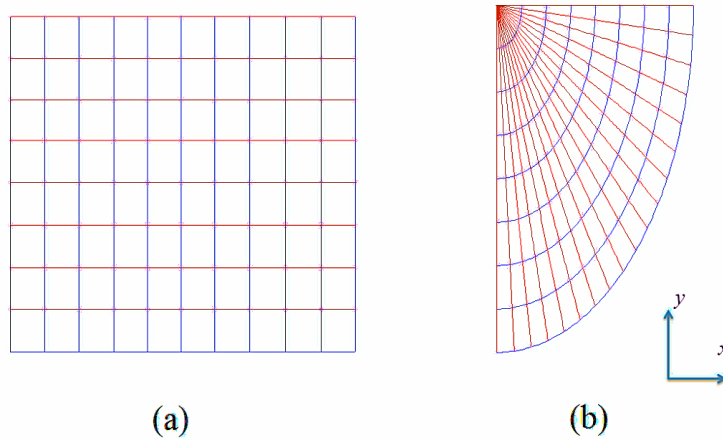


Figure R 18 (a) Espace physique (b) Espace virtuel

Les paramètres choisis pour obtenir la réorientation désirée sont  $a = 4.16$ ,  $b = 0.8$ ,  $r = 1$  and  $m = 14$ . Cela conduit à un superstrat de taille  $0.625\lambda \times 0.12\lambda$  à  $1.25\text{GHz}$ . La Figure R 19 montre la variation de la permittivité dans le profil. Elle varie entre  $0 < \epsilon_r < 14.9$ . Remarquons que l'antenne n'est pas positionnée symétriquement par rapport au superstrat. La Figure R 20 montre la réorientation du champ électrique suivant  $+y$ . Nous pouvons aussi remarquer la présence de champ selon  $-y$ , ce qui est probablement dû au positionnement de la source.

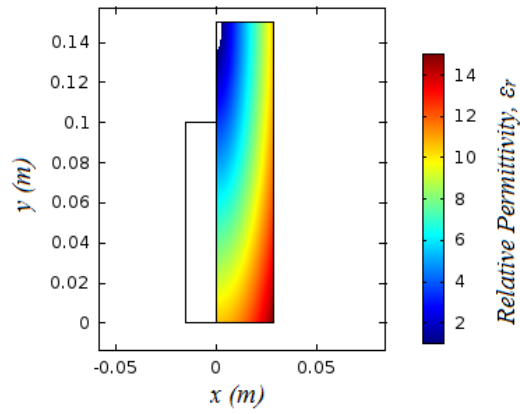


Figure R 19 Variation de la permittivité dans le profil

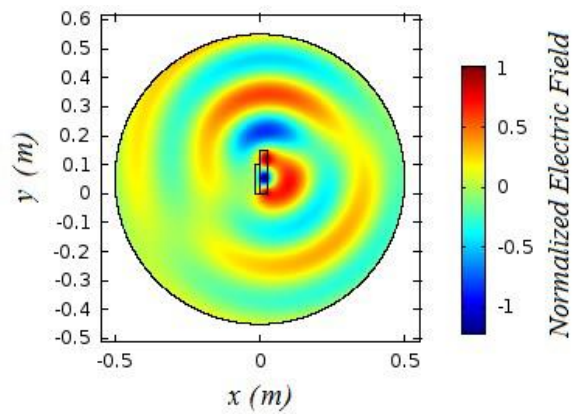


Figure R 20 Redistribution du champ électrique

Ensuite, nous discrétisons le profil continu en 24 pixels. Nous obtenons un superstrat tridimensionnel en extrayant le profil discrétisé selon l'axe  $z$ . La taille du superstrat est  $0.78\lambda \times 0.62\lambda \times 0.12\lambda$  à 1.25 GHz. Nous utilisons une couche diélectrique  $\epsilon_r = 2.2$ , et une épaisseur de 12 mm pour fixer la fréquence d'opération à 1.25 GHz. La Figure R 21 montre la directivité de l'ensemble à 1.25 GHz. La directivité maximum est de 5.6 dBi.

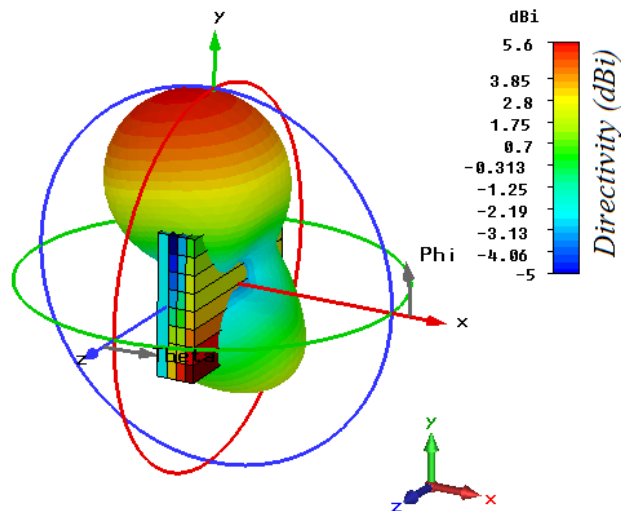


Figure R 21 Directivité (dBi) de l'antenne avec superstrat à 1.25 GHz.

Un tel concept peut être utilisé pour obtenir un rayonnement de type end-fire depuis une antenne patch. Nous pouvons donc conclure que le concept défini dans la première partie de la thèse peut être étendu et adapté pour des nouvelles applications.

La réalisation de la preuve du concept présentée dans le chapitre 4 est une approche très simple. Ici, nous proposons des consignes pour la réalisation pratique des superstrats présentés dans cette thèse en n'utilisant que deux matériaux. Nous concevons un superstrat et le simulons avec CST Microwave Studio avec 2 matériaux. La distribution de ces deux matériaux peut être contrôlée avec un paramètre  $q$ . La Figure R 22 montre différentes distributions des permittivités autour de l'axe  $x$  pour différentes valeurs de  $q$ . Ici, la zone blanche a une permittivité élevée ( $\epsilon_{\text{high}} = 9.9$ ) et la zone jaune a une permittivité faible ( $\epsilon_{\text{low}} = 4.4$ ). Dans la Figure R 23, le diagramme du rayonnement est tracé dans le plan  $x y$  pour différentes valeurs de  $q$ . Comme nous pouvons constater sur la courbe orange, le superstrat réoriente le rayonnement complètement dans le plan azimutal quand  $q = 1$ . En revanche, le superstrat a un maximum dans la direction normale (axe  $x$ ) quand  $q = 0.4$ . Plus des détails sont fournis dans la section 5.2.

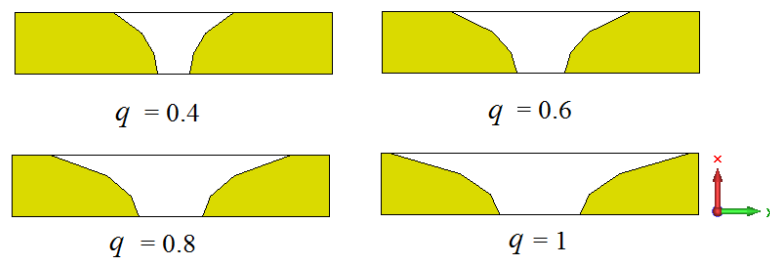


Figure R 22 Distribution des matériaux pour différentes valeurs de  $q$ .

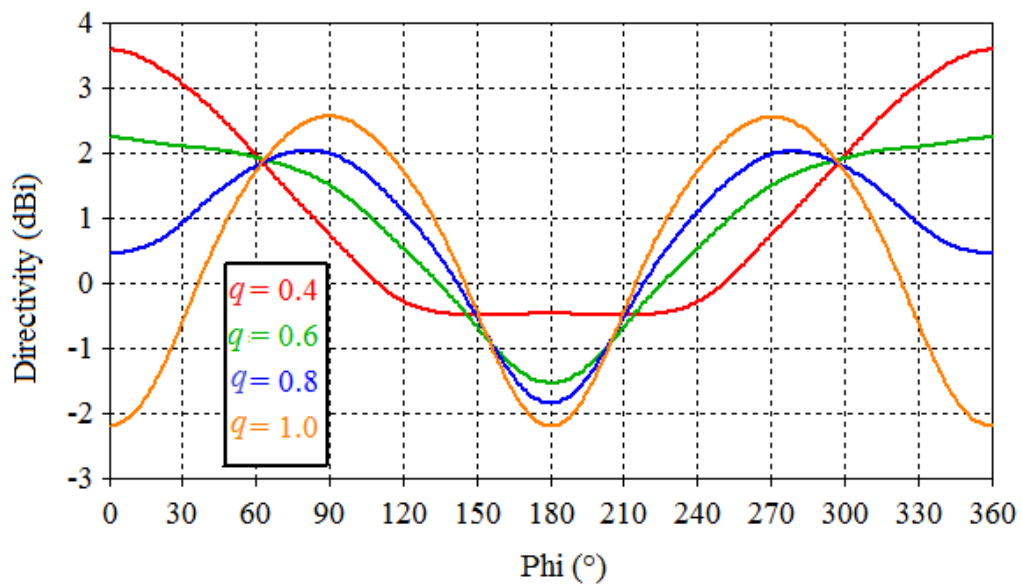


Figure R 23 Diagramme de rayonnement dans le plan  $x y$  pour différentes valeurs de  $q$ .

Lors de la conception initiale, nous ne prenons pas en compte l'effet de l'environnement du superstrat afin de simplifier l'étude. Ici, nous présentons les résultats préliminaires de l'étude menée sur les performances des superstrats en présence d'un grand plan de masse, ce qui représente l'environnement d'un superstrat installé, par exemple, sur un fuselage. La Figure R 24(a) représente la forme du rayonnement en l'absence d'une surface réfléchissante. Ensuite, nous vérifions la performance du superstrat à proximité d'un plan métallique. Quand le superstrat est entouré par une surface de conducteur électrique parfait (CEP), la forme du rayonnement dictée par la transformation d'espace est perdue. Ceci est dû aux réflexions du champ électrique suivant  $z$  depuis la surface CEP qui reconstituent un front d'onde dans la direction normale (selon  $x$ ).

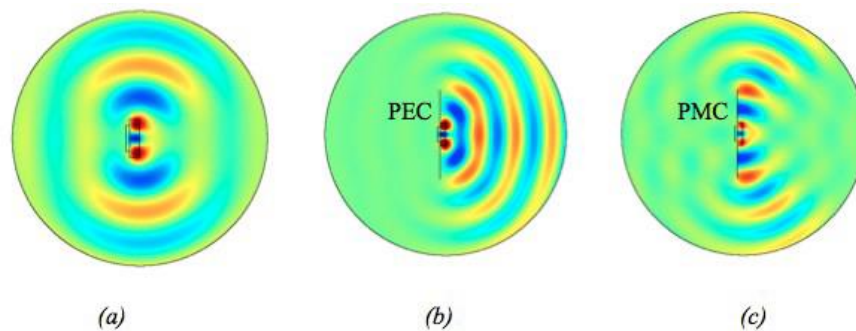


Figure R 24 Propagation d'onde électromagnétique (a) Sans plan autour du superstrat, (b) plan CEP, (c) plan CMP.

Une solution possible pour conserver la forme du rayonnement est d'utiliser une surface constituée d'un conducteur magnétique parfait (CMP). Contrairement au CEP, le champ électrique suivant  $z$  est non nul sur la surface CMP et il n'est pas réfléchi. Le champ électrique propage sur la surface CMP et nous n'observons pas de champ dans l'axe principal, comme montré sur la Figure R 24. Notons que le CMP est une surface théorique qui n'existe pas dans la nature. Néanmoins, le comportement d'un CMP peut être approché avec une surface artificielle: Conducteur Magnétique Artificiel (CMA.) Dans la section 5.3.3, nous menons une étude de faisabilité où nous proposons d'utiliser les CMA pour faciliter la propagation d'une onde en incidence rasante.

### Conclusion

Les résultats de recherche dans cette thèse ont présenté de nouveaux superstrats tout diélectriques de faible épaisseur. Nous abordons à la fois la conception théorique et la réalisation pratique. Grâce au superstrat développé, une antenne patch ayant un gain réalisé de 7 dB devient une antenne présentant deux lobes dans le plan azimutal de gain réalisé 3.5 dB. Le superstrat, d'épaisseur  $0.12\lambda$ , est conçu à l'aide de deux matériaux uniquement : Alumine ( $\epsilon_r = 9.9$ ) et Fullcure ( $\epsilon_r = 2.8$ ). Le concept est validé à l'aide d'une maquette réalisée avec une

imprimante 3D et avec le soutien d'Airbus Group Innovations. Une telle solution peut trouver une application notamment dans le domaine de l'aérospatiale, où les solutions antennaires protubérantes (e.g. antenne sabre) dégradent l'aérodynamisme du porteur. Divers degrés de libertés dans la conception permettent d'adapter notre solution pour concevoir d'autres superstrats avec des fonctionnalités différentes: diagramme ayant une ouverture de plus de 180° dans un plan, diagramme end-fire, etc.. Nous présentons aussi les résultats préliminaires sur l'influence de l'installation du superstrat sur les structures métalliques.



# Table of Contents

<b>Acknowledgments .....</b>	<b>i</b>
<b>Résumé.....</b>	<b>iii</b>
<b>List of Tables.....</b>	<b>xxxi</b>
<b>List of Figures .....</b>	<b>xxxiii</b>
<b>Abbreviations.....</b>	<b>xli</b>
<b>1. Introduction .....</b>	<b>1</b>
<b>2. Transformation Optics: origins and advances.....</b>	<b>5</b>
<b>2.1 Metamaterials: a prelude to TO.....</b>	<b>5</b>
<b>2.2 TO method: design possibilities .....</b>	<b>8</b>
2.2.1 TO method for guiding electromagnetic waves.....	8
2.2.2 TO for compression of space.....	11
2.2.3 TO for optical illusions.....	12
2.2.4 Challenges of TO-solutions .....	13
<b>2.3 Simplifying the anisotropy in material profile.....</b>	<b>14</b>
2.3.1 Normalization of elements in material tensor.....	14
2.3.2 Quasi Conformal Transformation Optics .....	16
<b>2.4 A review of important TO results .....</b>	<b>18</b>
2.4.1 Metamaterial based TO-solutions.....	18
2.4.1.1 Metamaterial TO concepts.....	18
2.4.1.2 Metamaterial based TO-solutions for antenna applications .....	22
2.4.1.3 Discussion on metamaterial based TO solutions.....	26
2.4.2 TO-solutions with standard materials.....	27
2.4.2.1 Dielectric material based TO Concepts.....	27
2.4.2.2 Dielectric TO-solutions for antenna applications.....	31
2.4.2.3 Discussion on metamaterial based TO solutions.....	36
<b>2.5 Parallel research tracks .....</b>	<b>36</b>
2.5.1 Methods .....	37
2.5.2 Materials .....	38
<b>2.6 Context of present work.....</b>	<b>38</b>
<b>3. Concept Definition .....</b>	<b>41</b>

<b>3.1</b>	<b>Physical and Virtual Spaces .....</b>	<b>42</b>
3.1.1.	Physical & Virtual Spaces– without compression.....	42
3.1.2.	Physical & Virtual Spaces– size change.....	44
3.1.2.1	Axial change .....	44
3.1.2.2	Lateral change.....	45
3.1.2.3	Radial change.....	47
3.1.2.4	Generalized spatial transformation .....	48
<b>3.2.</b>	<b>Wave propagation in the transformed 2D medium.....</b>	<b>48</b>
3.2.1.	Design rules and COMSOL design definition.....	49
3.2.1.1	Design rules .....	49
3.2.1.2	COMSOL simulation setup.....	49
3.2.1.3	Patch antenna model .....	50
3.2.2.	Wave propagation in uncompressed transformed space.....	51
3.2.3.	$n$ -based interpretation and Shift factor ‘ $m$ ’ .....	53
3.2.4.	A dielectric profile.....	55
3.2.5.	Wave propagation in compressed/expanded spaces .....	55
3.2.5.1	Wave propagation in compressed profile.....	56
3.2.5.2	Wave propagation in expanded profile .....	57
3.2.5.3	Remarks on designing compressed/expanded TO-designs .....	58
<b>3.3</b>	<b>Full wave solutions with discretized profile .....</b>	<b>59</b>
3.3.1	Square patch antenna.....	60
3.3.2	Designing isotropic profile with finite permittivity values.....	61
3.3.2.1	From anisotropic to isotropic solution .....	62
3.3.2.2	Discretizing a continuous profile in sub-wavelength sized pixels .....	62
3.3.2.3	Designing a three-dimensional superstrate .....	65
3.3.3	Antenna with the T.O. superstrate .....	66
3.3.3.1	Antenna with superstrate.....	66
3.3.3.2	Dielectric layer to match antenna superstrate assembly at design frequency.....	68
<b>3.4</b>	<b>Discussion .....</b>	<b>75</b>
<b>4.</b>	<b>Proof of concept of dielectric superstrate for antipodal radiation.....</b>	<b>77</b>
<b>4.1.</b>	<b>Materials and design strategy.....</b>	<b>77</b>
<b>4.2.</b>	<b>Towards a practical design .....</b>	<b>80</b>
4.2.1	Strict interpretation of discretized profile.....	81
4.2.2	Relaxed interpretation of discretized profile .....	85
<b>4.3</b>	<b>Experimental verification .....</b>	<b>88</b>
4.3.1	New Antenna .....	88
4.3.2	Adjustment of superstrate to new dielectric matching layer and new antenna	90

4.3.3	Fabrication of the superstrate .....	92
4.3.4	Performance of the new antenna with 3D printed superstrates .....	96
4.3.4.1	Performance of new antenna with FullCure superstrate .....	96
4.3.4.2	Performance of new antenna with PLA Superstrate .....	103
<b>4.4</b>	<b>Discussion .....</b>	<b>110</b>
<b>5.</b>	<b>Extrapolations and New Designs.....</b>	<b>113</b>
<b>5.1</b>	<b>Extrapolations using degrees of freedom in design .....</b>	<b>113</b>
5.1.1	Case 1: Superstrate for semi-circular radiation pattern .....	114
5.1.1.1	Interplay of a, b and m .....	115
5.1.1.2	Dielectric superstrate for semi circular radiation pattern .....	116
5.1.2	Reconfigurable Materials .....	121
5.1.3	Case 2: Dielectric superstrate for single beam in azimuth .....	122
5.1.3.1	Spatial transformation from Cartesian to quarter circle .....	123
5.1.3.2	Superstrate for reorienting electromagnetic waves in one direction .....	125
<b>5.2</b>	<b>Guideline for practical implementation using two materials .....</b>	<b>129</b>
<b>5.3</b>	<b>Integration of antenna and superstrate into a structure, limitations .....</b>	<b>133</b>
5.3.1	Antenna superstrate assembly in presence of PEC plane .....	133
5.3.2	PMC based ground plane.....	134
5.3.3	Possibility of using AMC as a support structure .....	136
5.3.3.1	Design of AMC.....	136
5.3.3.2	Comparison of PEC and AMC reflectors.....	137
<b>5.4</b>	<b>Discussion .....</b>	<b>139</b>
<b>6.</b>	<b>Conclusions and Perspectives .....</b>	<b>141</b>
<b>6.1</b>	<b>Conclusions .....</b>	<b>141</b>
<b>6.2</b>	<b>Perspectives.....</b>	<b>143</b>
	<b>List of Publications .....</b>	<b>145</b>
	<b>References.....</b>	<b>147</b>
	<b>Appendices.....</b>	<b>157</b>
	<b>Appendix A. Software.....</b>	<b>157</b>
a)	COMSOL Multiphysics.....	157
b)	CST Microwave Studio .....	158
	<b>Appendix B. Cylindrical Superstrate.....</b>	<b>160</b>
	<b>Appendix C. Materials.....</b>	<b>163</b>
a)	Alumina .....	163
b)	Additive Manufacturing: Printers & compatible materials .....	164

i.	FullCure Superstrate .....	164
ii.	PLA Superstrate.....	166
iii.	Premix TP20280 .....	167

## List of Tables

Table 2.1 Metamaterial based TO solutions.....	26
Table 2.2 Dielectric TO Solutions.....	36
Table 4.1 Dielectric constants and losses of typical 3D printer compatible filaments.....	78
Table 4.2 Materials with large dielectric constant.....	79
Table 4.3 Spatial distribution of permittivity in discretized profile .....	81
Table 4.4 Spatial distribution of permittivity in discretized profile with upper bound fixed at high- $\epsilon_r$ .....	82
Table 4.5 Characteristics of the effective medium.....	83
Table 4.6 Spatial distribution of relative permittivity in effective medium.....	84
Table 4.7 Two value interpretation of effective medium.....	86
Table 4.8 Readapting dimensions of alumina layer .....	86
Table 4.9 Dimensions of patch antenna .....	89
Table 4.10 Alumina sheet dimensions.....	94
Table 5.1 Directivity and HPBW comparison of patch antenna with and without superstrate.....	119



## List of Figures

Fig. 2.1 Lycurgus Cup .....	6
Fig. 2.2 Left-handed material for achieving a negative index of refraction [9]. .....	7
Fig. 2.3 Schematic of a perfect lens with simultaneously negative $\epsilon$ , $\mu$ [4]. .....	7
Fig. 2.4 A representative image of a cloaking concept [1]. .....	8
Fig. 2.5 (a) Physical Space; (b) Virtual Space [1]. .....	9
Fig. 2.6 Untransformed space (on left); Transformed space (on right)[26]. .....	11
Fig. 2.7 Squeezer of a Gaussian beam [29]. .....	12
Fig. 2.8 Illusion Optics: (a) Scattering pattern for a dielectric spoon, (b) Scattering pattern from an illusion device, (c) Scattering pattern for a dielectric cup [30]. .....	12
Fig. 2.9 An electromagnetic source place in vacuum can be delocalized using an illusion medium [32]. .....	13
Fig. 2.10 A non-magnetic cloak concept with inner cylindrical region ( $r < a$ ) cloaked by a cylindrical shell ( $a < r < b$ ) [36]. .....	15
Fig. 2.11 A composite medium containing alternating layers of electric & magnetic metamaterials [37]. .....	16
Fig. 2.12 Virtual space with a curved PEC reflector (top); corresponding physical space with new material parameters (bottom) [39]. .....	17
Fig. 2.13 (a) cylindrical metamaterial cloak, (b) SRR unit cell [43]. .....	18
Fig. 2.14 Square cloak with of anisotropic material profile: (a) Cloak parallel to the incident wavefront (b) Cloak rotated by $22.5^\circ$ [45]. .....	19
Fig. 2.15 Instantaneous electric field (V/m) in sharp waveguide bend, (a) conventional solution, (b) TO-based solution [48]. .....	20
Fig. 2.16 Taper to connect waveguide of different cross sections [51]. .....	20
Fig. 2.17 TO-based Maxwell fish-eye lens concept (a) TE polarized line source in untransformed space, (b) Line source in transformed space [54]. .....	21
Fig. 2.18 Focusing behavior of (a) TO-based flat reflector (b) Traditional parabolic reflector [55]. .....	22
Fig. 2.19 Composite medium with ELC and SRR [37]. .....	23
Fig. 2.20 (a) Ray trajectories from a directive source (b) Field of view of directive source, (c) Isotropic radiation due to optically transformed medium (d) Field of view of TO based solution [58]. .....	24
Fig. 2.21 Multi beam antennas (a)&(d) Three beam lens, (b)&(e) Four beams, (c)&(f) Six beams [59]. .....	25

Fig. 2.22 (a) Beam tilting device designed using QCTO; (b)&(c) ELC resonator based design [61].	26
Fig. 2.23 (a) Representative image of a carpet cloak;(b) SEM image of the fabricated device [73].	28
Fig. 2.24 Fabricated prototype of Luneburg lens [78].	29
Fig. 2.25 3D printed waveguide bend [85].	31
Fig. 2.26 (a) Permittivity variation in the flat hyperbolic lens, (b) Manufactured prototype using processed titanate powders, (c)&(d) Different sized particles (e) Permittivity vs. frequency plots for materials [89].	32
Fig. 2.27 Dielectric focusing lens in Ku-band realized using extrusion 3D printing [90].	33
Fig. 2.28 Cut-offs of dielectric Luneburg lenses (LL): A flat LL inspired from TO (left), Uncompressed spherical LL (right) [91].	33
Fig. 2.29 3D printed Luneburg lens with extended flat focal surface [92].	34
Fig. 2.30 3D printed dielectric superstrate for restoring in phase emission from non-planar microstrip array [95].	35
Fig. 2.31 Perforated Teflon layers of a dielectric superstrate to increase HPBW realized at Telecom ParisTech with help of Airbus Group Innovations [2].	36
Fig. 2.32 Discretized profile of relative permittivity and permeability [2].	39
Fig. 3.1 (a) Physical space (Cartesian), (b) Virtual space.	43
Fig. 3.2 (a) Uncompressed space (b) Axially compressed space.	44
Fig. 3.3 (a) Uncompressed space (b) Laterally expanded space.	46
Fig. 3.4 (a) Uncompressed Space, (b) Radially expanded space.	47
Fig. 3.5 Representative diagram showing solution setup in COMSOL.	50
Fig. 3.6 A representative image of the patch antenna model and region of spatial transformation.	51
Fig. 3.7 Wave propagation in untransformed space, $E_z$ (normalized to maximum value.)	51
Fig. 3.8 Constitutive parameter profile in a transformed uncompressed space (a) $\epsilon_{zz}$ , $\mu_{xx}$ ; (b) $\mu_{yy}$ .	52
Fig. 3.9 Wave propagation in uncompressed space, $E_z$ (normalized to maximum value.)	53
Fig. 3.10 Wave propagation in uncompressed space, refractive index changed by a factor $m = 0.5$ , $E_z$ (normalized to maximum value.)	54
Fig. 3.11 Constitutive Parameter Profile plotted in $1 < \epsilon_{zz} < 14.8$ ; $\epsilon_{zz} < 1$ values in the corners outside the plotting range.	56
Fig. 3.12 Wave propagation in compressed space: $a = 4.16$ , $b = 1.6$ ; shift factor $m = 14$ , $E_z$ (normalized to maximum value).	57
Fig. 3.13 Time averaged power flow (in dB) in $x y$ plane at the scattering boundary.	57

Fig. 3.14 Constitutive Parameter Profile; $1 < \epsilon_{zz} < 8.8$ , $\epsilon_{zz} < 1$ values in the corners not in plotting range.....	58
Fig. 3.15 Wave propagation in axially compressed and laterally expanded space: $a = 4.16$ , $b = 0.745$ , $r = 1$ ; shift factor $m = 7$ , $E_z$ (normalized to maximum value).....	58
Fig. 3.16 Square patch antenna resonating at $f$ ; used as source for conceptual demonstrations .....	60
Fig. 3.17 Far field radiation pattern of antenna at $f$ ; Realized Gain (in dB); $G_{\max} = 6.7$ dB ....	61
Fig. 3.18 Profile discretized in 192 pixels (6 layer with 32 pixels each.) .....	63
Fig. 3.19 Normalized electric field in a discretized profile with 192 pixels. ....	63
Fig. 3.20 Profile discretized in 48 pixels (3 layer with 16 pixels each.) .....	64
Fig. 3.21 Normalized electric field in discretized profile with 48 pixels. ....	64
Fig. 3.22 Passage from a continuous anisotropic dielectric profile to a discretized isotropic dielectric profile with finite pixels (16x3).....	65
Fig. 3.23 3D superstrate obtained by extruding the discretized profile along z-axis .....	66
Fig. 3.24 Antenna superstrate assembly with an air gap. ....	67
Fig. 3.25 Magnitude of reflection coefficient for antenna only, antenna-superstrate without gap, antenna+superstrate with an additional air gap of 10mm. ....	67
Fig. 3.26 Realized Gain of antenna-superstrate at $f' = 1.33$ GHz (in dB); 10 mm air layer between antenna and superstrate. ....	68
Fig. 3.27 Comparison of magnitudes of reflection coefficients for different values of relative permittivity of the intermediate 10 mm thick dielectric layer. ....	69
Fig. 3.28 Directivity (dBi) comparison at operating frequencies for antenna-dielectric layer-superstrate assembly with variation of relative permittivity of dielectric layer. ....	70
Fig. 3.29 Comparison of magnitudes of reflection coefficients for different thicknesses of intermediate dielectric layer of relative permittivity value of 2. ....	71
Fig. 3.30 Directivity (dBi) comparison of antenna-dielectric layer-superstrate assembly with varied thickness of dielectric layer. ....	71
Fig. 3.31 Comparison of $ S_{11} $ : Antenna only vs. Antenna-Superstrate with a dielectric layer ( $\epsilon_r = 1.8$ ); Antenna-superstrate assembly is matched at $f = 1.25$ GHz. ....	72
Fig. 3.32 3D far field plot showing realized gain (in dB) of antenna superstrate assembly with a dielectric matching layer at $f$ ; Max. Realized gain = 3.5 dB .....	73
Fig. 3.33 Comparing realized gain (dB) in $x y$ plane for antenna only and antenna with superstrate at 1.25 GHz. ....	73
Fig. 3.34 Comparing realized gain (dB) in $y z$ plane for antenna only and antenna with superstrate at 1.25 GHz. ....	74

Fig. 3.35 Comparing realized gain (dB) in $xz$ plane for antenna only and antenna with superstrate at 1.25 GHz. ....	74
Fig. 4.1 Pixel in an effective medium comprised of two materials. ....	82
Fig. 4.2 Pixel-by-pixel interpretation of TO concept in an effective medium. ....	84
Fig. 4.3 Realized gain (dB) (a) Pixilated Profile, (b) Effective medium. ....	85
Fig. 4.4 Staircase arrangement of alumina sheets in the 3D printed superstrate structure. ....	87
Fig. 4.5 Realized Gain (dB) of superstrate, (a) dimensions of alumina sheets corresponding to shaded region in Table 4.7 (peak realized gain 2.8 dB), (b) Off-the-shelf alumina sheets (peak realized gain 2.7 dB). ....	87
Fig. 4.6 Patch antenna prototype .....	89
Fig. 4.7 Simulated and measured magnitudes of reflection coefficient of two port antenna ..	89
Fig. 4.8 Simulated realized gain (dB) of the new antenna at 1.189 GHz. ....	90
Fig. 4.9 Comparison of realized gains of dielectric superstrate with new antenna and 3D printed dielectric layer (a) at 1 GHz prior modification; (b) at 1.06 GHz after modification .	91
Fig. 4.10 Schematic of the proposed design. ....	92
Fig. 4.11 Three layers of alumina sheets: (a) Bottom, (b) Middle, (c) Top. ....	94
Fig. 4.12 Receptacle made from photo cured FullCure resin. ....	94
Fig. 4.13 Receptacle made from PLA filament. ....	95
Fig. 4.14 Cross-section of PLA based superstrate showing mesh structure. ....	95
Fig. 4.15 Comparison of simulated and measured magnitudes of reflection coefficients for new antenna with FullCure superstrate. ....	97
Fig. 4.16 Simulated realized gain (dB) of new antenna with FullCure superstrate at 1.10 GHz. ....	97
Fig. 4.17 Measured realized gain of FullCure superstrate at 1.11 GHz in $xy$ plane ( $\theta = 90^\circ$ ).98	
Fig. 4.18 Measured realized gain of FullCure superstrate at 1.11 GHz in $yz$ plane ( $\phi = 90^\circ$ ).99	
Fig. 4.19 Measured realized gain of FullCure superstrate at 1.11 GHz in $xz$ plane ( $\phi = 0^\circ$ ).99	
Fig. 4.20 Comparison of simulated (1.10 GHz) and measured (1.14 GHz) realized gains of FullCure superstrate in $xy$ plane ( $\theta = 90^\circ$ ). ....	100
Fig. 4.21 Comparison of simulated (1.10 GHz) and measured (1.14 GHz) realized gains of FullCure superstrate in $yz$ plane ( $\phi = 90^\circ$ ). ....	101
Fig. 4.22 Comparison of simulated (1.10 GHz) and measured (1.14 GHz) realized gains of FullCure superstrate in $xz$ plane ( $\phi = 0^\circ$ ). ....	101
Fig. 4.23 Measured realized gain of FullCure superstrate at 1.17 GHz in $xy$ plane ( $\theta = 90^\circ$ ). ....	102
Fig. 4.24 Measured realized gain of FullCure superstrate at 1.17 GHz in $yz$ plane ( $\phi = 90^\circ$ ). ....	102

Fig. 4.25 Measured realized gain of FullCure superstrate at 1.17 GHz in $xz$ plane ( $\phi = 0^\circ$ ).	103
Fig. 4.26 Simulated and measured magnitudes of reflection coefficient for PLA superstrate. .....	104
Fig. 4.27 Simulated realized gain (dB) of new antenna with PLA superstrate at 1.245 GHz. .....	104
Fig. 4.28 Comparison of simulated and measured realized gain (dB) of PLA superstrate at 1.21 GHz in $xy$ plane ( $\theta = 90^\circ$ ).	105
Fig. 4.29 Comparison of simulated and measured realized gain (dB) of PLA superstrate at 1.21 GHz in $yz$ plane ( $\phi = 90^\circ$ ).	106
Fig. 4.30 Comparison of simulated and measured realized gain (dB) of PLA superstrate at 1.21 GHz in $xz$ plane ( $\phi = 0^\circ$ ).	106
Fig. 4.31 Comparison of simulated and measured realized gain (dB) of PLA superstrate at 1.245 GHz in $xy$ plane ( $\theta = 90^\circ$ ).	107
Fig. 4.32 Comparison of simulated and measured realized gain (dB) of PLA superstrate at 1.245 GHz in $yz$ plane ( $\phi = 90^\circ$ ).	107
Fig. 4.33 Comparison of simulated and measured realized gain (dB) of PLA superstrate at 1.245 GHz in $xz$ plane ( $\phi = 0^\circ$ ).	108
Fig. 4.34 Comparison of simulated and measured realized gain (dB) of PLA superstrate at 1.27 GHz in $xy$ plane ( $\theta = 90^\circ$ ).	109
Fig. 4.35 Comparison of simulated and measured realized gain (dB) of PLA superstrate at 1.27 GHz in $yz$ plane ( $\phi = 90^\circ$ ).	109
Fig. 4.36 Comparison of simulated and measured realized gain (dB) of PLA superstrate at 1.27 GHz in $xz$ plane ( $\phi = 0^\circ$ ).	110
Fig. 5.1 Radiation patterns: (a) antenna alone, (b) antenna with dielectric superstrate to increase HPBW. ....	114
Fig. 5.2 Relative permittivity profile ( $\epsilon_r$ ) in the transformed profile for a semi-cylindrical wavefront.....	115
Fig. 5.3 Normalized electric field, $E_z$ (V/m) at 1.25 GHz.....	115
Fig. 5.4 3D superstrate designed from a discretized profile; variation in permittivity restricted between 1 and 8.....	116
Fig. 5.5 Comparison of magnitudes of reflection coefficients of antenna alone and antenna with superstrate.....	117
Fig. 5.6 Directivity (dBi): (a) Antenna alone (b) Antenna with superstrate. Maximum value in plots limited to 2 dBi for highlighting reorientation along $y$ -axis.....	117
Fig. 5.7 Directivity (dBi) in $xy$ plane at 1.25 GHz. ....	118
Fig. 5.8 Directivity (dBi) in $xz$ plane at 1.25 GHz.....	118

Fig. 5.9 Directivity (dBi) in $y z$ plane at 1.25 GHz.....	119
Fig. 5.10 Directivity values in operational bandwidth at $x$ and $y$ -axes for an antenna without and with superstrate (dBi). .....	120
Fig. 5.11 Voltage controlled permittivity values in profile. Changing $V$ represents a change in $p$ . .....	121
Fig. 5.12 Directivity plot of superstrate with controllable permittivity values.....	121
Fig. 5.13 Radiation patterns: (a) antenna alone, (b) antenna with dielectric superstrate for reorientation in single direction in azimuth.....	122
Fig. 5.14 (a) Physical square Cartesian space, (b) Virtual space for reorientation in azimuthal plane along $y$ -axis .....	123
Fig. 5.15 Relative permittivity profile ( $\epsilon_r$ ) in the transformed profile for reorienting electromagnetic waves along positive $y$ -axis. ....	124
Fig. 5.16 Normalized electric field, $E_z$ (V/m) at 1.25 GHz. ....	124
Fig. 5.17 3D superstrate designed from a discretized profile; variation in permittivity restricted between 1 and 14. ....	125
Fig. 5.18 Comparison of magnitudes of reflection coefficient of antenna alone and antenna with superstrate.....	126
Fig. 5.19 Directivity (dBi) of the antenna superstrate assembly at 1.25 GHz.....	126
Fig. 5.20 Directivity (dBi) in $x$ - $y$ plane at 1.25 GHz. ....	127
Fig. 5.21 Directivity (dBi) in $y$ - $z$ plane at 1.25 GHz. ....	127
Fig. 5.22 Directivity (dBi) in $x$ - $z$ plane at 1.25 GHz. ....	128
Fig. 5.23 Directivity plot (dBi) at 1.25 GHz (a) Antenna alone; (b) Antenna with superstrate. ....	129
Fig. 5.24 Distribution of two materials along quasi-elliptical locus controlled by parameter ' $q$ '. .....	130
Fig. 5.25 Material distribution corresponding to different values of $q$ .....	130
Fig. 5.26 Magnitude of reflection coefficient of the superstrates for different values of $q$ ..	131
Fig. 5.27 Comparison of directivity in $x y$ plane ( $\theta = 90^\circ$ ) for different values of $q$ .....	131
Fig. 5.28 Directivity in $x y$ plane ( $\theta = 90^\circ$ ). for different values of $eps_h$ .....	132
Fig. 5.29 Dielectric superstrate in presence of large ground plane. ....	133
Fig. 5.30 3D polar plot of realized gain of dielectric superstrate in presence of a circular PEC plane at 1.25 GHz.....	134
Fig. 5.31 Wave propagation with a surrounding ground plane (a) Without ground plane (b) With a PEC ground plane (c) With a PMC ground plane. ....	135
Fig. 5.32 Rectangular waveguide for parallel incidence of electric field on: (a) PEC, (b) AMC.....	136

Fig. 5.33 AMC unit cell.....	137
Fig. 5.34 Phase of reflection coefficient of the unit cell for a plane wave incident at $80^\circ$ ....	137
Fig. 5.35 Directivity (dBi) comparison for PEC and AMC reflectors.....	138
Fig. 5.36 Comparison of directivities (dBi) of PEC and AMC reflectors in $x y$ plane. ....	138
Fig. B.1 A three-dimensional cylindrical superstrate designed from the two dimensional pixilated profile. ....	160
Fig. B.2 Magnitude of reflection coefficient of different of input excitations of antenna-cylindrical superstrate assembly.....	161
Fig. B.3 3D polar plots of realized Gain of antenna-cylindrical superstrate as seen in $y z$ plane (top-view): (a) Port-1ON, Port 2-OFF, (b) Port-1ON ( $0^\circ$ ), Port 2-ON ( $0^\circ$ ), (c) Port-1OFF, Port 2-ON, (d) Port-1ON ( $0^\circ$ ), Port 2-ON ( $180^\circ$ .) ....	162
Fig. C.1 Objet Eden260 VS by Stratasys™.....	164
Fig. C.2 CraftBot 3D printer by CraftUnique™.....	166
Fig. C.3 3D printer compatible PLA filaments of different colors (Arianplast™.) ....	167



## Abbreviations

<u>Abbreviation</u>	<u>Meaning</u>
ABS	Acrylonitrile Butadiene Styrene
AMC	Artificial Magnetic Conductor
ELC	Electric field driven LC resonators
GRIN	Gradient Index
HPBW	Half Power Beam Width
PEC	Perfect Electric Conductor
PLA	Poly Lactic Acid
PMC	Perfect Magnetic Conductor
QC	Quasi Conformal
SRR	Split Ring Resonators
TO	Transformation Optics



# 1. Introduction

This thesis presented research results carried out under NanoDesign project funded by IDEX Paris-Saclay ANR-11-IDEX-0003-02. Academic participants in the project include Telecom ParisTech and Institut d'Electronique Fondamentale from the Université Paris-Saclay. The research work is carried out in RF and Microwave (RFM) group of Communications and Electronics Department at Telecom ParisTech. We benefited of the expertise from Airbus Group Innovations, especially to access to their 3D printing facility at Suresnes, France for fabrication purposes.

The modern aviation industry is constantly looking for innovative solutions to make the next generation of aircrafts safer, faster and economical to operate. This requires optimizing each aspect of the aircraft, including on-board communication systems. Antenna is a key component of on-board communication systems. Today, an aircraft ensures connectivity with satellites and ground stations by at least a dozen antennas. The antennas often serve different applications like communicating with GPS satellites, Instrument Landing System (ILS), Traffic Collision Avoidance Systems (TCAS), Air Traffic Control Radar Beacon System (ATCRBS), etc.

Many such applications require the antenna to radiate in the azimuthal plane. TCAS and ATCRBS are two main applications that require an antenna operating in L-band. TCAS is responsible for alerting the pilot for incoming traffic. For this, a TCAS-II system employs a system comprised of two antennas mounted on top and bottom of the aircraft. The bottom antenna searches the airspace in an omnidirectional radiation pattern in the azimuthal plane for incoming traffic. Typically, blade antennas fixed on the fuselage of the aircraft are used for this application.

While legacy designs like blade antenna work well today, new generation of aircrafts will require replacing these antennas with low-profile solutions. The blade antennas fixed on the aircraft protrude from the surface; hence they degrade the aerodynamic profile of the aircraft. An improved aerodynamic profile can lead to reduction in fuel consumption and longer mileage. A conformal or low profile antenna is required which radiates in azimuthal plane like blade antenna. This thesis addresses this problem using Transformation Optics (TO).

TO method, sometimes also referred to as Transformation Electromagnetics, is a powerful tool to design transformed spaces that allow controlling the propagation path of electromagnetic waves. It gained popularity through the seminal work of Pendry and others on design of electromagnetic invisibility by the means of metamaterial cloaking structure [1]. Subsequently, exciting research and new concept electromagnetic devices have also been

proposed e.g. carpet cloak, super lenses, etc. The method is used for analytical derivation of the required material properties for modeling the spatial transformations between physical and virtual spaces. Once the material properties are known, the profile is realized using either metamaterials or standard dielectric materials.

Metamaterial is a term used to define an artificial, engineered material that exhibits exotic properties not found in naturally occurring materials. These properties arise, not due to chemical composition, but due to the arrangement of individual elements of the metamaterials. Metamaterials are relevant to TO method because the material profiles after spatial transformations are anisotropic i.e. the material properties depend upon the direction of propagation of an electromagnetic wave. Due to absence of naturally occurring anisotropic media, metamaterials are used to design the analytically derived anisotropic profiles. However, metamaterials are not an ideal answer because of various design considerations (e.g. bandwidth, losses, etc.) TO solutions using standard dielectric materials are highly desirable owing to various design advantages (e.g. ease of fabrication, wide bandwidth, etc).

The potential of TO-method for low-profile antenna design in aerospace industry is of keen interest in our group and studied previously. M.D. Clemente Arenas has presented different applications of TO method in his Ph.D. dissertation [2]. His contributions in the design of TO devices allow modifying radiation pattern of antennas and serve as a starting point for the research work presented in this thesis. In his thesis, TO inspired design of dielectric flat reflectors and half power beam width increasing superstrates have been presented. A proof-of-concept has also been fabricated using 3D printing techniques. The antenna superstrate assembly has been studied in presence of a large ground plane to simulate its behavior while installed on large structures like aircraft fuselage. In the final chapter of his thesis, a TO concept is proposed that completely reorients the broadside radiation pattern of a patch antenna in the azimuthal plane. This radiation pattern of this superstrate closely resembles to that of blade antenna with radiation maxima in the azimuthal plane. However, the material properties required to achieve this behavior comprise of some extreme values, which are only accessible by use of metamaterials. As said previously, metamaterial increases the complexity in fabrication. It is highly desirable to achieve this behavior using standard dielectric materials.

In this thesis, TO based superstrates will be presented to reorient radiation pattern in azimuthal plane of a patch antenna. The objective of this research is to accentuate the design flexibility of TO method in order to derive the combined advantages of a thin profile and use of standard dielectric materials in the design. This shall make the presented solutions appealing for diverse industrial applications, especially for aeronautical applications described above. The solutions presented in this thesis shall harness the potential of the disruptive technology of 3D

printing to fabricate the superstrates. The bulk of this thesis is divided in four chapters. A chapter-by-chapter breakdown of the thesis is provided below.

In the chapter 2, a review of existing literature of TO optics will be presented. The advent of TO method will be understood in context of metamaterials. The TO method, anisotropy in TO solutions and the design strategies used for simplification of this anisotropy will also be discussed. Important theoretical concepts and practical results in open literature will be discussed to highlight the most prominent as well as recent advances in use of TO towards applications in field of optics and electromagnetics. A special emphasis will be provided on metamaterial and dielectric material based TO solutions for antenna related applications, including a discussion on 3D printed solutions.

In essence, chapter 3 will provide an insight to the physics behind the functioning of the various TO concepts proposed in this thesis. Design of TO dielectric superstrate concept for achieving antipodal radiation pattern will be described in detail. Essentially, this chapter will allow the reader to comprehend the design methodology and different degrees of freedoms available in the design. It will provide the basic analytical design, upon which practical implementations and extrapolations presented in later chapters will be based. The simple design methodology will be used to arrive at a two-dimensional analytical solution problem in reduced complexity. Finally, full wave simulation results will be presented to highlight the feasibility of an all-dielectric TO solution for enacting the spatial transformation.

In chapter 4, a practical fabrication of the TO superstrate for antipodal superstrate will be discussed. The objective of this chapter will be to propose a prototype using 3D printing. Standard dielectric material will be used to enact the spatial transformation achieved described in chapter 3. Strict and lenient interpretations of the TO concept will be presented using only two materials. Two prototypes realized using two different 3D printing processes will be presented along with their measured performances. Their fabrication has been made possible due to generous participation of Airbus Group Innovations.

Extrapolations of the previously developed analytical concept and new complementary research work will be presented in Chapter 5. In the first measure, this chapter will allow the reader to appreciate the different degrees of freedom in the analytical solution of chapter 3 by adapting it to different applications. Two distinct applications of the low profile dielectric superstrates will be presented: to increase half power beam width; and to achieve end-fire operation from a patch antenna. Next, a general design guideline will be presented for fabrication of these low profile dielectric superstrates. Finally, a preliminary insight will be provided using simulation results on the complementary structures required around the dielectric superstrates for their integration in relatively large metallic surfaces like the fuselage of the aircraft.

Chapter 6 will be used to present the concluding notes and offer perspectives on the

## *Introduction*

possible research axes coming out from this research work. Complementary information pertaining to software, materials and fabrication processes used in this thesis has been provided at the end in the form of Appendices, and has been referenced in the thesis for aiding the reader.

## 2. Transformation Optics: origins and advances

In Chapter 1, a general outline of the thesis was presented. As explained, transformation optics (TO) method is used in this thesis to provide innovative solutions to a problem of significant complexity. Indeed, TO method is a very powerful analytical tool that can vastly increase the capabilities of present day antenna solutions. However, there are inherent problems in interpretation of TO-based solutions from an engineering point of view, which require using different simplification strategies for designing practically feasible solutions. It is necessary to understand the existing literature before introducing solutions presented in later chapters. This chapter is an essay on transformation optics as a design tool. Also, advances in TO-based solutions are presented.

First, a historical backdrop is provided to understand the advent of TO method. Next, theoretical results on the design procedure are presented. The tall challenges of material anisotropy are discussed. Furthermore, various strategies for designing dielectric-only TO-solutions are presented. Then, results that shaped the research on this topic: theoretical and experimental realizations are shown. Also, a note on the interesting parallel tracks is presented towards the end.

### 2.1 Metamaterials: a prelude to TO

Controlling the trajectories of light has captivated our attention since ancient times. Classical lenses are in use since 12<sup>th</sup> and 13<sup>th</sup> centuries, but the history of optics far outdates the lenses themselves. The first rudimentary attempts to control the nature of light can be attributed to Romans who used glass alloys doped with gold and silver to achieve exotic effects. One famous example is that of ‘Lycurgus Cup’, as shown in Fig. 2.1. The artifact appears to be red when illuminated from behind and green when illuminated from the front. The roman craftsmen of the day did not have a physical explanation of the effect, yet they were able to consistently reproduce these effects by mastering the compositions of *sub-wavelength* alloy nano-particles. Unknowingly, they had laid the foundation of an exciting branch of physics that would generate huge interest in optical physics and engineering communities centuries later.



Fig. 2.1 Lycurgus Cup.

According to Fermat's principle, the path taken by a ray of light between two points  $a$  and  $b$  defined in Cartesian space  $(x, y, z)$  is the path that can be traversed in the least time. Let this path be denoted by  $P$ . The mathematical description of this path is given in ( 2.1 ).

$$P = \int_a^b n \cdot dl$$

where,

$$dl = \sqrt{(x_b - x_a)^2 + (y_b - y_a)^2 + (z_b - z_a)^2}$$

( 2.1 )

Here,  $n$  represents the refractive index. When  $n$  is homogenous,  $P$  is a straight line. However, when the medium is composed of non-homogenous refractive index profile, the trajectories are not linear. Thus, the trajectories can be designed by reassigning the refractive indices of the propagation medium by linking  $n$  to a new coordinate system. Pendry *et al.* first propose such a concept and its application in design of invisibility cloak in a seminal paper published in 2006 [1]. But the inspiration behind this work can be directly found in earlier works, as explained in the following paragraphs.

In 1968, Veselago wrote a paper describing the physical behavior expected from substances with simultaneously negative values of permittivity and permeability [3]. He theorized that such a medium exhibit exotic properties like divergent rays from a convex lens and focusing effect from a concave lens. This is discussed further in [4], where Pendry argues that negative permittivity medium is capable of producing images of sources of magnetic fields with sub-wavelength resolution, which otherwise is not possible using conventional optical solution. At that time, Veselago's theory did not find popularity in the physics community due to the lack of naturally occurring materials with negative permittivity or permeability.

An advance was reported in [5], [6] and [7], which allowed artificially synthesizing media with negative values of permittivity and permeability. These media were made of sub-wavelength wire and Split Ring Resonator (SRR) structures. A composite medium with simultaneously negative permittivity and permeability was studied in [8] and [9] that allowed achieving a negative index of refraction, as shown in Fig. 2.2. Moreover, a Electric field driven LC resonator (ELC) was proposed in [10] to synthesize negative permittivity values. The general principle behind negative index materials is that the phase velocity is opposite of the group velocity close to a particular resonant frequency of the medium with strong dispersion. It must be noted here that the first experimental validations of negative permittivity and permeability materials happened initially in RF frequency ranges because of the convenience of standard Printed Circuit Board (PCB) fabrication techniques.

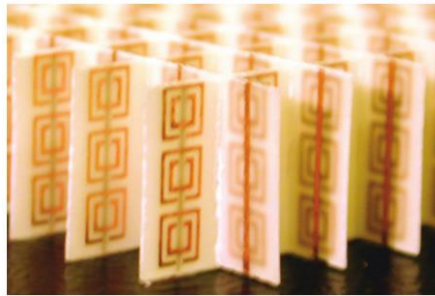


Fig. 2.2 Left-handed material for achieving a negative index of refraction [9].

The above reported solutions allow designing a material with simultaneously negative permittivity and permeability. Such a composite medium is used in design of a perfect lens capable of resolving the sub-wavelength features as shown in Fig. 2.3. Capasso's group has recently proposed high aperture flat metalenses at optical wavelengths using standard fabrication techniques to resolve nano-scale features separated by sub-wavelength distances [11]. Foundry based processes are proposed to create a nanoscale array of smooth and high-aspect ratio nanostructures using Titanium dioxide ( $\text{TiO}_2$ ).

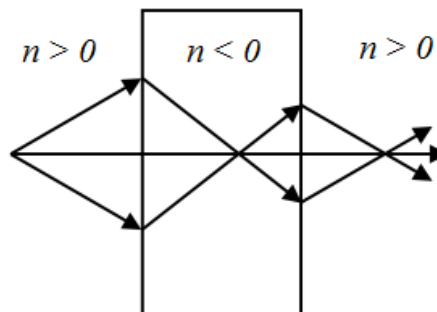


Fig. 2.3 Schematic of a perfect lens with simultaneously negative  $\epsilon$ ,  $\mu$  [4].

The capability to tailor the material properties by artificially arranging materials is a scientific breakthrough for the physics community in general and has generated a lot of

interest because of the potential applications with engineered media. Herein are also the beginnings of TO method.

## 2.2 TO method: design possibilities

The metamaterials described in the previous section allow generating media with arbitrarily chosen material parameters from optical frequencies down to DC. Many other non-cited papers report that it is possible to design independently varying permittivity and permeability values that should allow an unprecedented arbitrary control on the light propagation. The natural progression in research is therefore to devise a technique for engineering controlled trajectories. In this section, we present TO method, and three examples about how control over light is exerted in literature.

### 2.2.1 TO method for guiding electromagnetic waves

The first and most popular application of TO method is to distort space to control the direction of wave propagation in space. The metamaterials can be used to continuously vary the refractive indices. This allows modeling non-linear trajectories for electromagnetic waves in the medium.

In [12], it is shown that moving from a Cartesian coordinate system to a second general coordinate system is equivalent to renormalizing the permittivity ( $\epsilon$ ) and permeability ( $\mu$ ) in the Cartesian space according to the second space. In [13], Pendry discussed use of this coordinate transformation technique to design cylindrical lenses. In 2006, two papers in Science magazine attempted to propose how tailored trajectories could be used to propose a theoretical construction of invisibility cloaks [1], [14]. A representative image of a cloaking concept inspired from transformation optics is shown in Fig. 2.4. This immediately brought a lot of attention to the topic and it was soon realized that many interesting concepts can be proposed by exerting control over ray trajectories [15].

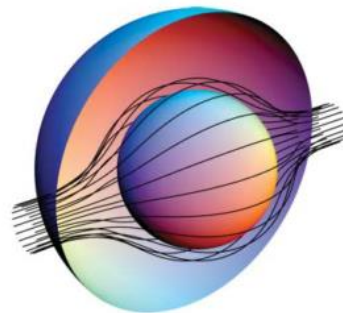


Fig. 2.4 A representative image of a cloaking concept [1].

The technique proposed in [1] is based on coordinate transformation. The underlying principle behind this approach is that the form of Maxwell's equations is invariant under

coordinate transformation. The electromagnetic quantities of electric displacement field, magnetic field intensity and the Poynting vector can be completely controlled using  $\epsilon$  and  $\mu$  calculated using the coordinate transformation, which can be synthesized using metamaterials. Two coordinate systems were considered: a Cartesian system  $(x, y, z)$ , (here called physical space) that governs the wave propagation in untransformed space; and a second coordinate system  $(x', y', z')$  based on the desired trajectory (called virtual space). This is shown in Fig. 2.5. Pendry *et. al* have envisioned the physical space embedded in an elastic medium, which was distorted until it resembled the virtual space. The distortions themselves are recorded in form of a coordinate transformation using a Jacobian matrix. Therefore, this matrix is essentially a representation of spatial variation of one space with respect to other. The matrix is given in ( 2.2 ).

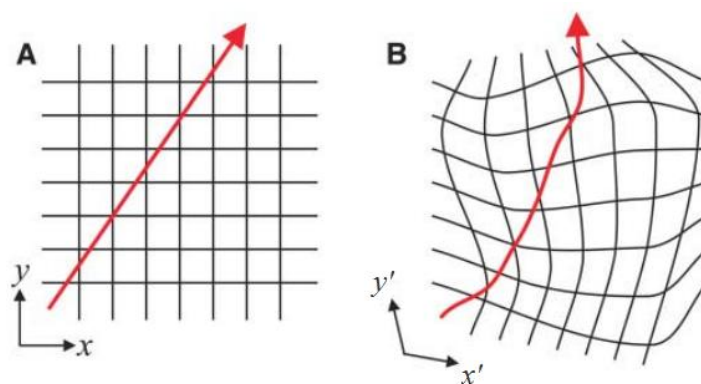


Fig. 2.5 (a) Physical Space; (b) Virtual Space [1].

$$J = \begin{bmatrix} \frac{\delta x'}{\delta x} & \frac{\delta x'}{\delta y} & \frac{\delta x'}{\delta z} \\ \frac{\delta y'}{\delta x} & \frac{\delta y'}{\delta y} & \frac{\delta y'}{\delta z} \\ \frac{\delta z'}{\delta x} & \frac{\delta z'}{\delta y} & \frac{\delta z'}{\delta z} \end{bmatrix}$$

( 2.2 )

Once the relation between the two coordinate systems is identified, it can be used to calculate the new set of material parameters and consequently the new refractive index profile required to design the coordinate transformation. They can be found out using ( 2.3 ). Thus change in trajectory is compensated by renormalized permittivity and permeability values.

$$\epsilon' = \frac{J\epsilon J^T}{\det(J)}; \mu' = \frac{J\mu J^T}{\det(J)}$$

( 2.3 )

It may be noted in ( 2.3 ) that the new material profile is not scalar, but a matrix. It implies that the transformed medium is inherently anisotropic. While a few natural materials are known to show optical anisotropy, also known as birefringence (e.g. Calcite crystals), the gradient issued from the TO-solution may only be achieved using metamaterials. A discussion on challenges of interpretation of anisotropic material profiles using metamaterials is presented in last sub-section. Simplification strategies of anisotropic profiles are discussed in the next section.

The technique described above is especially useful for volumetric transformation. However, limitations due to constitutive properties of surface prevent from achieving full tensor solution required to achieve the spatial transformation. This is discussed in detail in Patel [16]–[21]. It is explained in [16] that the transformed fields can be related to the initial fields using ( 2.4 ) and ( 2.5 ), where the non-primed and primed notations represent untransformed and transformed media according to the previously established convention.

$$E = J^T E'$$

( 2.4 )

$$H = J^T H'$$

( 2.5 )

But for a two dimensional space, this assumes a transformation of the space above the surface, leading to an inaccurate interpretation of the 2D-problem. Surface impedances can be used to control trajectories of surface waves. Tensor Impedance Boundary Conditions (TIBC) is proposed as an alternative. TIBC is given in ( 2.6 ).

$$E_t = \eta_{surf} \times H_t$$

( 2.6 )

Here,  $E_t$  and  $H_t$  represent the components of field tangential to the surface and  $\eta_{surf}$  is a matrix with spatially variant surface impedance values as shown in ( 2.7 ).

$$\eta_{surf} = \begin{bmatrix} \eta_{xx} & \eta_{xy} \\ \eta_{yx} & \eta_{yy} \end{bmatrix}$$

( 2.7 )

Quarfoth also presents a discussion on using transformation electromagnetics for design of two dimensional devices to manipulate surface waves [22]. Use of anisotropic

artificial impedance surfaces is proposed to interpret the spatial transformation required to design wave shifter and splitting devices. Maci's group has presented the theoretical development of isotropic and anisotropic metasurfaces [23]–[25]. Circular and elliptical patches are proposed to design transformed surfaces with anisotropically varying surface impedance [24]. This is a developing field with many interesting results. However, the presented discussion is limited to volumetric transformations only in the interest of brevity.

### 2.2.2 TO for compression of space

The second application of TO method is shortening or elongating the medium. This is of great practical interest in a variety of applications, and specifically for compression of optical lenses. Compression of space is demonstrated in [26] as a viable way to reduce lens thickness. The authors show compression of a Cartesian space along  $x$ -axis governed by a compression factor, ' $a$ '. While the diagonal element in material tensor along  $x$ -axis sees a multiplication of ' $a$ ', the other two dimensions are multiplied by ' $1/a$ ', as shown in ( 2.8 ).

$$\varepsilon' = \begin{bmatrix} a & 0 & 0 \\ 0 & \frac{1}{a} & 0 \\ 0 & 0 & \frac{1}{a} \end{bmatrix} \cdot \varepsilon$$

( 2.8 )

The permeability tensor is also similar, as governed by relations previously defined in ( 2.3 ). A representative image of linear compression is shown in Fig. 2.6, where the transformed space is compressed using a compression factor of 2. This result is important for this thesis because compression of the profile is used as a means to compress the proposed superstrate for reducing thickness and lateral dimension of the device. This is discussed in detail in Chapter 3.

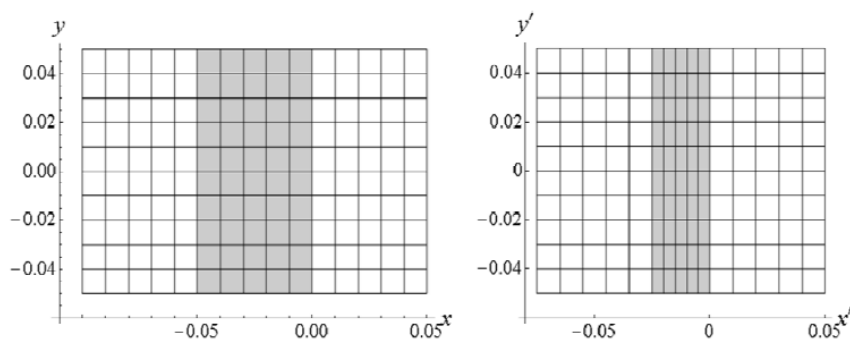


Fig. 2.6 Untransformed space (on left); Transformed space (on right)[26].

Pendry makes an observation on compression in [1]. When compression isn't applied uniformly in all directions, the resulting transformed profile exhibits off-diagonal elements in the material tensor. This requires metamaterials for designing the anisotropy. On the other hand, a uniform compression can be interpreted using isotropic materials.

In [27], [28], Tichit provides an interesting discussion on reducing the physical appearance of electromagnetic sources using compression factors. It is shown that a linear space compression followed by a space expansion makes the radiation pattern of a small aperture antenna appear like that of a large one. Also, a very interesting application of compression is demonstrated in [29], where a Gaussian beam is squeezed in to a waveguide via a TO interface. A representative image is shown in Fig. 2.7.

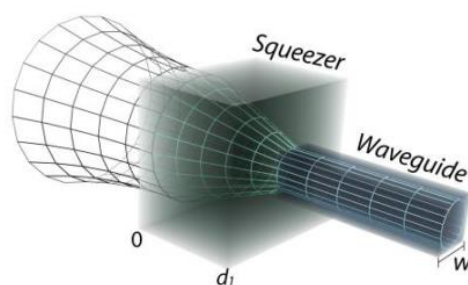


Fig. 2.7 Squeezer of a Gaussian beam [29].

### 2.2.3 TO for optical illusions

TO method can also be used to change the appearance of the object [30], [31]. The invisibility cloak can be considered as an illusion of free space, and that a generalized solution can be envisaged to link a pair of physical and virtual objects via an illusion device. An illusion device consists of two distinct metamaterial-based media: a complementary space to cancel the space including the physical object; and a restoring medium to compensate for the cancelled space and recreating the scattering pattern of the virtual object. An example is shown in Fig. 2.8. When the dielectric spoon is embedded in the illusion media, its scattering pattern becomes equivalent to that of the cup.

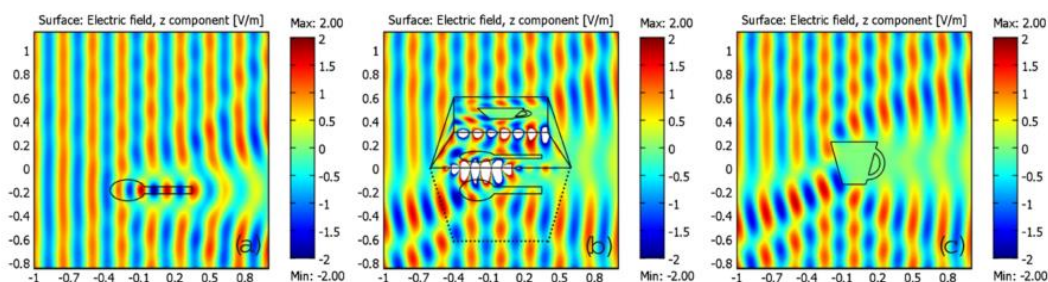


Fig. 2.8 Illusion Optics: (a) Scattering pattern for a dielectric spoon, (b) Scattering pattern from an illusion device, (c) Scattering pattern for a dielectric cup [30].

The idea is further extended to more practical problems like changing the nature, position or radiation pattern of antenna in [32], [33]. It is proposed to embed the antenna in an illusion medium. The illusion medium allows delocalizing the source using a radial transformation, such that the observer sees the incoming radiation from a different direction. A representative image is shown in Fig. 2.9. Such techniques allow antenna designers to hide the antennas line of sight, yet achieve radiation in desired direction. However, the complex nature of wave manipulation requires anisotropic material parameters, which is extremely challenging in practice. A detailed discussion on problems associated with anisotropy in TO-solutions is presented in the next subsection.

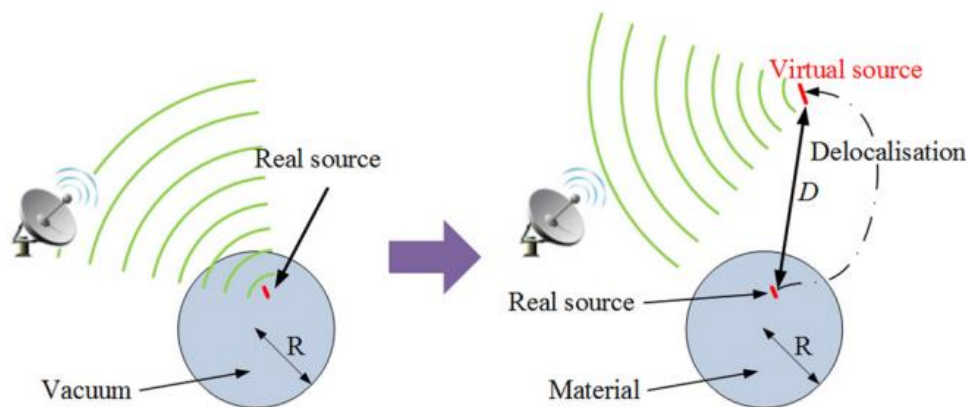


Fig. 2.9 An electromagnetic source place in vacuum can be delocalized using an illusion medium [32].

#### 2.2.4 Challenges of TO-solutions

As explained in all the previous sub-sections, TO offers new possibilities in modeling light trajectories. However, there are challenges in interpreting the transformed profiles. Essentially, the discussion boils down to the availability or design of materials capable of responding to the material parameters derived from TO method. The challenges are discussed in this paragraph.

##### Anisotropy

As seen in each of the previous sub-sections, anisotropy is the main challenge associated with TO-solutions. Anisotropy is inherent to TO method. A composite medium may be composed of uniquely diagonal elements or both on and off-diagonal elements in material tensor. The off-diagonal values vary along two different axes (biaxial) at any given instant and are extremely difficult to achieve in practice. Plasma techniques allow achieving bi-axial anisotropy. Gyration of electrically charged particles in steady ambient magnetic fields show these off-diagonal elements in the tensor [34]. Such a medium is called a magnetoplasma. However, it is impractical to implement a system of such complexity to design anisotropic TO solutions. Alternatively, a material with anisotropic material profile with asymmetrical

elements in material profile is presented in [35], which functions in absence of external magnetic fields. However, it uses active elements like amplifiers to achieve the off-diagonal elements. This again highlights the heightened levels of complexity in implementation. On the other hand, diagonal elements of material tensor can be implemented using metamaterials described in the first section.

A second drawback of anisotropy is that TO-solutions are often polarization specific. It is impractical to design all elements of material tensor in a composite medium. Thus, the TO-solutions often work only in a single polarization. This is shown in examples cited later in this section.

### Performance of metamaterials

It is much easier to interpret the uniaxial anisotropy using standard metamaterial designs discussed earlier in the chapter [5]-[10]. But using these metamaterials has inherent disadvantages. The SRR and ELC structures show extremely high or low permittivity values near the resonant frequency of the resonator, making their behavior highly frequency dependent. Therefore, the resonator based composite media is narrowband in nature. Additionally, the resonant nature of the structure leads to losses, which makes a metamaterial-based solution a non-ideal choice for antenna applications. It may be noted here that using SRR and ELC resonators outside the bandwidth of resonance may improve the bandwidth of the solution. A broadband solution is possible using isotropic dielectric materials; however this requires considerable simplification of anisotropy in the profile. This is discussed in the next subsection.

## 2.3 Simplifying the anisotropy in material profile

Various studies are carried out to adapt TO method for dielectric-only solutions. An ideal TO-solution should be an isotropic, dielectric only solution. Reduction in anisotropic exigency inside the transformed profile has also been proposed. In this section, we present commonly used simplification strategies:

- Normalization of elements in material tensor
- Quasi Conformal Transformation Optics

### 2.3.1 Normalization of elements in material tensor

Renormalizing permittivity and permeability is the most common approach adopted in early literature. In an effort to arrive at a dielectric only solution, permeability is forced as  $\mu' = 1$  while the refractive index of the transformed profile is conserved. In [36], an invisibility cloak concept is proposed using coordinate transformation technique introduced in the

previous section. The initial material tensors derived for the cloak defined in a cylindrical coordinate system  $(r, \theta, z)$  are given in (2.9). The cloaking concept is shown in Fig. 2.10.

$$\varepsilon_r = \mu_r = \frac{r-a}{r}, \varepsilon_\theta = \mu_\theta = \frac{r}{r-a}, \varepsilon_z = \mu_z = \left(\frac{b}{b-a}\right)^2 \frac{r-a}{r} \quad (2.9)$$

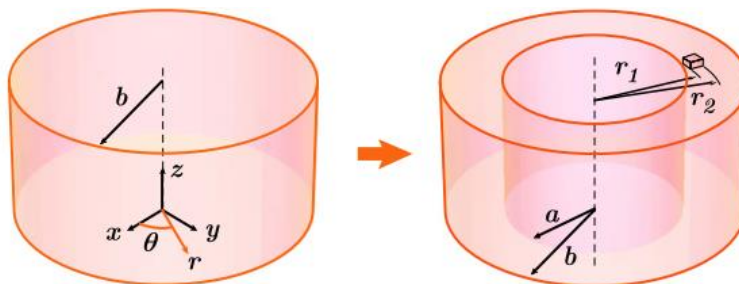


Fig. 2.10 A non-magnetic cloak concept with inner cylindrical region ( $r < a$ ) cloaked by a cylindrical shell ( $a < r < b$ ) [36].

Next, a simplification strategy based on renormalization is applied to remove all dependence on magnetic parameters. Conserving dispersion relations by normalization is an extremely interesting approach for achieving dielectric only solutions. A Transverse Magnetic (TM) incident field directed along  $z$ -axis was used, which limits the required parameters in the tensor to three elements:  $\mu_z$ ,  $\varepsilon_r$  and  $\varepsilon_\theta$ . The dispersion relation is respected as long as products of  $\mu_z \varepsilon_r$  and  $\mu_z \varepsilon_\theta$  maintain their values. This allowed imposing  $\mu_z = 1$  and the new values of permittivity components were achieved by multiplying  $\mu_z$  to original permittivity components. New material profile is given in (2.10).

$$\mu_z = 1, \varepsilon_\theta = \left(\frac{b}{b-a}\right)^2, \varepsilon_z = \left(\frac{b}{b-a}\right)^2 \left(\frac{r-a}{r}\right)^2 \quad (2.10)$$

By favoring the incidence of a Transverse Electric (TE) field with electric field along  $z$ -axis, the dependence can be reduced to two orthogonal permeability ( $\mu_\perp$ ) components and a parallel permittivity ( $\varepsilon_{||}$ ) element. In such a scenario, normalization technique can also be used for limiting magnetic dependence along a single axis in the transformed space. This is important because it is difficult to experimentally achieve magnetic permeability values along two different axes simultaneously in a composite medium. In [37], Tichit achieved an ultra directive emission concept. The problem was defined in Cartesian coordinate system  $(x, y, z)$ . The choice of TE polarization along  $z$ -axis allows limiting the dependence on three elements in material tensor:  $\mu_{xx}$ ,  $\mu_{yy}$  and  $\varepsilon_{zz}$ . The material profile is then renormalized to eliminate

dependence on  $\mu_{xx}$ , such that only  $\mu_{yy}$  and  $\epsilon_{zz}$  are required for transformation. This is also achievable in practice using alternating layers of magnetic and dielectric metamaterial layers, as shown in Fig. 2.11.

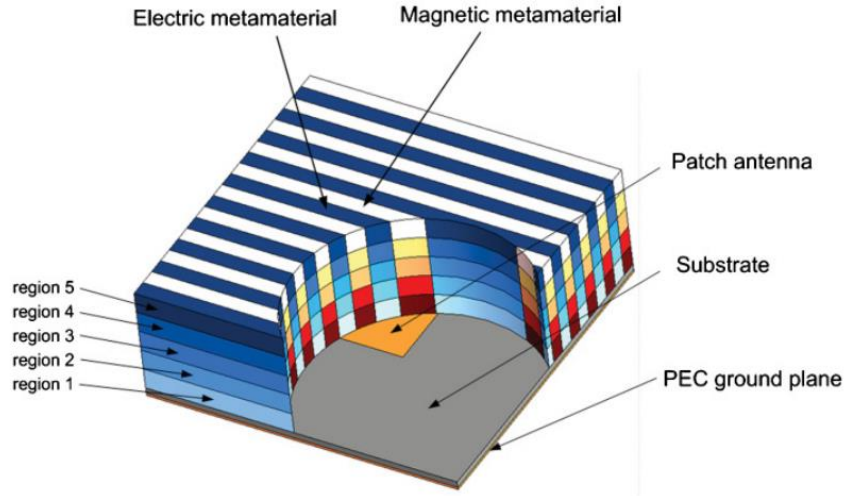


Fig. 2.11 A composite medium containing alternating layers of electric & magnetic metamaterials [37].

The normalization strategy allows non-magnetic solutions while conserving the dispersion relations. But it introduces impedance mismatch at the interface of two different regions with different transformation kernels, resulting in scattering and reflections. An area preserving affine coordinate transformation strategy is presented in [38] to overcome this problem, where a unity matrix is imposed for all permeability values, thus eliminating the need of renormalization. As an example, a TO based wave bend is designed by deconstructing the bend into area-preserving triangles. Such geometries may introduce limitations in shape of virtual spaces, which may be required in many cases. Nevertheless, it shows that alternative strategies can overcome the disadvantages of normalization technique. One widely used technique is discussed next.

### 2.3.2 Quasi Conformal Transformation Optics

It is possible to generate Quasi-Conformal (QC) mappings, which are a special subset of coordinate transformations. QC-mappings are capable of generating TO-solutions requiring only positive permittivity. A discrete coordinate transformation based method is proposed in [39] which could be applied to design conventional devices which do not have sharp boundaries. Assuming a TE polarization along  $z$ -axis, the anisotropy is limited to following elements in material tensor:  $\mu_{xx}$ ,  $\mu_{yy}$ ,  $\mu_{xy}$ ,  $\mu_{yx}$  and  $\epsilon_{zz}$ . The effective refractive index of anisotropic profiles may be defined according to ( 2.11 ).

$$n_{eff} = \frac{\sqrt{\mu_{xx}\epsilon_{zz}}\sqrt{\mu_{yy}\epsilon_{zz}}}{\epsilon_0\mu_0} \quad (2.11)$$

In [39], the authors explain that the transformation can be achieved using permittivity profile only if the Jacobian of ( 2.2 ) satisfies the condition provided in ( 2.12 ).

$$\begin{aligned} \mu_{xx}\mu_{yy} &= \mu_0^2 \\ \text{if} \\ \frac{\delta x'}{\delta y} &\approx 0, \frac{\delta y'}{\delta x} \approx 0 \end{aligned} \quad (2.12)$$

A grid representing the virtual space with quasi-orthogonal cells can be used to physically interpret ( 2.12 ). As a result,  $n_{eff}$  can be simply approximated using  $\epsilon_{zz}$  in ( 2.11 ). The authors have verified this strategy by designing a flat dielectric superstrate that achieves the focusing behavior of a concave reflector from a flat Perfect Electric Conductor (PEC). The physical and transformed spaces are shown in Fig. 2.12.

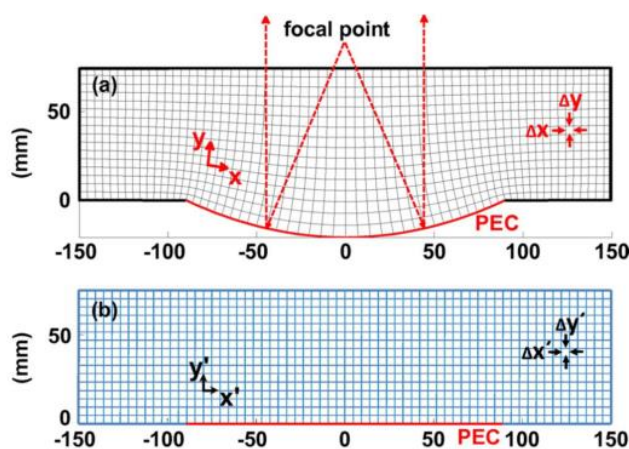


Fig. 2.12 Virtual space with a curved PEC reflector (top); corresponding physical space with new material parameters (bottom) [39].

In the context of present work, we draw inspiration from Quasi Conformal Transformation Optics (QCTO) technique; more on this is discussed in next chapter. For a comprehensive QCTO technique, one may refer to first chapter of [40]. Apart from the above presented techniques, an interesting comparison of approaches to reduce anisotropy in TO-solutions can be found in [41]. Also, review of TO-solutions based on conformal mapping is presented in [42].

## 2.4 A review of important TO results

TO method, its uses and disadvantages were all presented in the previous sections. Strategies to address the anisotropy in material profile were also discussed. In this section, a review of TO-based designs is presented. Results in TO literature are presented in decreasing order of complexity. An emphasis is given on TO-solutions for improving and modifying radiation patterns of antennas. First metamaterial-based solutions are discussed. Challenges of anisotropic material profiles are highlighted. Next, solutions comprised of standard dielectric materials are presented. Attention is drawn to the perforated dielectric and 3D printed superstrates for antenna applications.

### 2.4.1 Metamaterial based TO-solutions

#### 2.4.1.1 Metamaterial TO concepts

Invisibility cloak is certainly the most discussed application of TO method. A metamaterial based cylindrical cloak is presented in [43] to hide a metallic cylinder placed at the center of the cylinder. The cloak functions at 8.5 GHz and contains both permittivity and permeability elements. Normalization techniques discussed in the previous section are used to limit the variation to two elements:  $\mu_r$  and  $\epsilon_z$ . Furthermore, renormalization also assures that  $\epsilon_z$  is constant, hence the only variable in the design is  $\mu_r$ . The reduced set of material parameters respects the dispersion relation, but this simplification results in reflectance at the boundary of the transformed domain. The manufactured cloak and a SRR unit cell are shown in Fig. 2.13. The radial size of cloaked domain is  $1.6\lambda$  at 8.5 GHz. The cloak carries out the desired function in a narrow frequency band which can be explained by the fact that composite media is composed of naturally resonant materials. More details on measuring phase fronts of such cloak and negative index composite medium is discussed in [44].

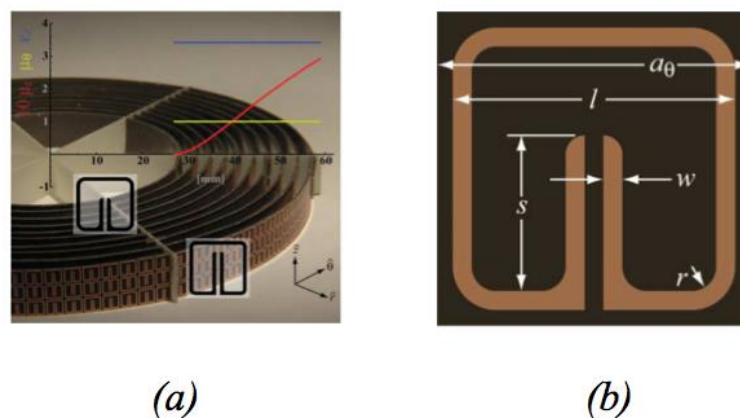


Fig. 2.13 (a) cylindrical metamaterial cloak, (b) SRR unit cell [43].

A square cloak device is also introduced in [45]. A TE polarized wave at 8.5 GHz is incident on the transformed space consisting of diagonal elements in material tensor ( $\mu_{xx}$ ,  $\mu_{yy}$  and  $\varepsilon_{zz}$ .) The impinging plane wave front conserves the phase irrespective of the angle of rotation of the cloak. This is shown in Fig. 2.14. The cloak guides the wavefronts impinging in parallel to the cloak, as well as when the cloak is turned at an angle of  $22.5^\circ$ .

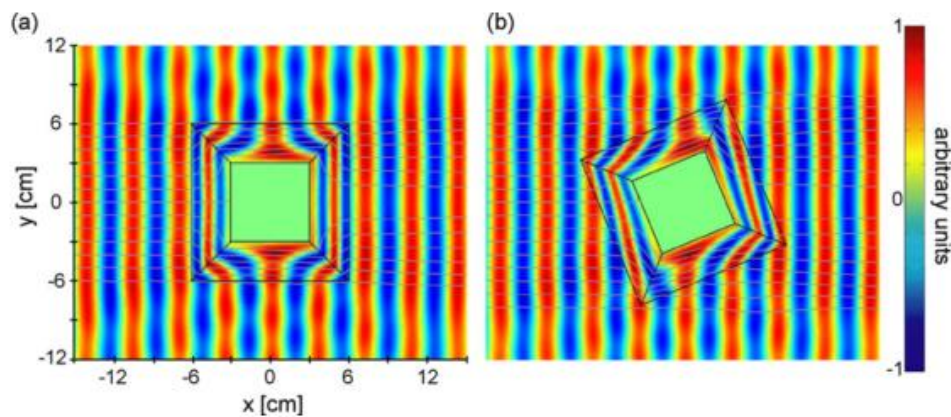


Fig. 2.14 Square cloak with of anisotropic material profile: (a) Cloak parallel to the incident wavefront (b) Cloak rotated by  $22.5^\circ$  [45].

Similarly, a carpet cloak can also be envisaged to conceal an object under a bump by a transformed medium. A metamaterial based implementation of such a cloak is experimentally shown in [46]. The gradient in refractive index required for hiding an object under the cloak is realized using a large number of PCB based metamaterial unit cells designed using conventional FR-4 substrate. The cloak operates in bandwidth (13-16 GHz). This is explained by the fact that the unit cells are used in non-resonant frequency range. Nevertheless, the solution is complex, as each unit cell needs to be optimized for achieving desired refractive index values. While not exactly based on coordinate transformation techniques, an alternate approach to achieve transparency is presented in [47] and is based on reduced scattering using metamaterial and plasmonic coatings.

Apart from cloaking other interesting applications of TO can be found in the literature. Bends in waveguides are classic components in microwave engineering required for changing the wave propagation direction. Traditionally, this is done using gentle bends to avoid reflections. The curved bends consume space and are therefore inconvenient in certain areas of application. An alternative is to use sharp bends, but increased reflections and mode distortions inherently reduce the transmitted power through the bend.

An anisotropic TO-solution for achieving sharp bends is presented in [48], where a  $90^\circ$  waveguide bend with cut-off frequency at 4.3 GHz is discussed. Next, the transformed media is designed using coordinate transformation and by considering appropriate boundary conditions. The transformed medium fits the sharp  $90^\circ$  bend. In Fig. 2.15, performances of

conventional and TO-based 90° waveguide bends are compared at 8.6 GHz by plotting the instantaneous electric field inside the waveguide. It is clear that TO-solution improved the transmission from one port to other. The results are especially more interesting and have consequence in the present context because of the strong change in propagation direction. Furthermore, the expressions for elements in material tensor of transformed medium are identical to those derived later in Chapter 3.

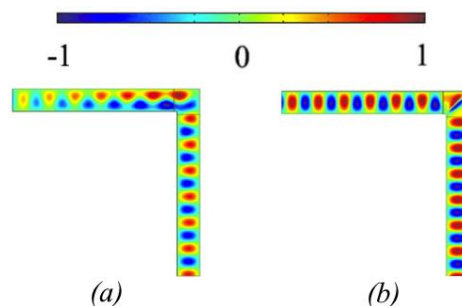


Fig. 2.15 Instantaneous electric field (V/m) in sharp waveguide bend, (a) conventional solution, (b) TO-based solution [48].

This discussion is extended to general waveguide bends in [49]. It is proposed to design arbitrary waveguide bends (60°, 90°, U-bend, etc.) using non-magnetic Anisotropic Epsilon Near Zero (AENZ) materials. Simulations show low reflection and high transmittance of propagating modes inside the waveguide. The authors suggest designing the required AENZ material using standard metamaterial techniques presented earlier in this chapter. An experimental realization of metamaterial based waveguide bends is presented in [50]. A TE polarized wave is introduced in a waveguide bend comprised of metamaterial-based Anisotropic Zero Index Material (AZIM). This AZIM is based on SRR circuits with Epsilon Near Zero (ENZ) elements in material tensor at the resonant frequency (10 GHz).

In [51], TO-based tapers to connect waveguides with different cross sections is presented. The transmission through the taper is simulated at 30 GHz. A representative image of the required transformation is shown in green lines in Fig. 2.16. Using TO method, a composite medium with anisotropic permittivity and permeability values is designed. Furthermore, a comparison of three different transformations: linear, parabolic and exponential, is presented. The permittivity and permeability values in the exponentially transformed profile can be achieved using metamaterials. An experimental realization based on metamaterials is not reported.

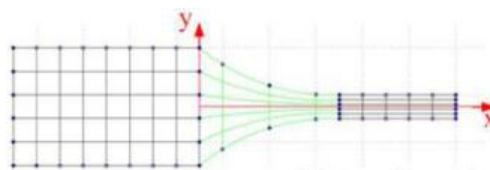


Fig. 2.16 Taper to connect waveguide of different cross sections [51].

Recently, a concept of TO-based two or three dimensional power dividers has also been proposed [52]. A 3-port power divider is simulated at a design frequency of 2.3 GHz. The profile is highly anisotropic with off-diagonal elements in the material tensor. Experimental realization is not reported.

One of the major applications of TO method is the design of flat lenses. Flat focusing lenses with minimized reflection are discussed in [53]. Using these TO-based lenses, it is proposed to convert cylindrical phase fronts to plane wave fronts. Simulation results from two-dimensional problem are presented. At 3 GHz ( $\lambda = 0.1$  m), the size of the lens is  $6\lambda$  (lateral size)  $\times \lambda$  (thickness). In the context of the present thesis, the lens thickness is not appropriate. For L-band applications (1-2 GHz), the wavelength is significantly larger and such lenses cannot be considered conformal or low profile. Hence compression of such optical lenses is necessary. In addition, the reported variation in material profile is highly anisotropic for the rigorous solution and requires negative permeability values. Experimental realization is not reported.

In [54], a flattened Maxwell fish eye lens based on TO method is proposed. The article presents 2D simulations of a TE polarized line source at 10 GHz. The line source is surrounded with a flat, optically transformed medium for achieving collimated beam, as shown in Fig. 2.17. The medium contains both on and off diagonal elements in material tensor. Such a lens may be considered for applications in imaging systems. However, a concrete approach to practically achieve this material profile with off-diagonal elements has not been provided.

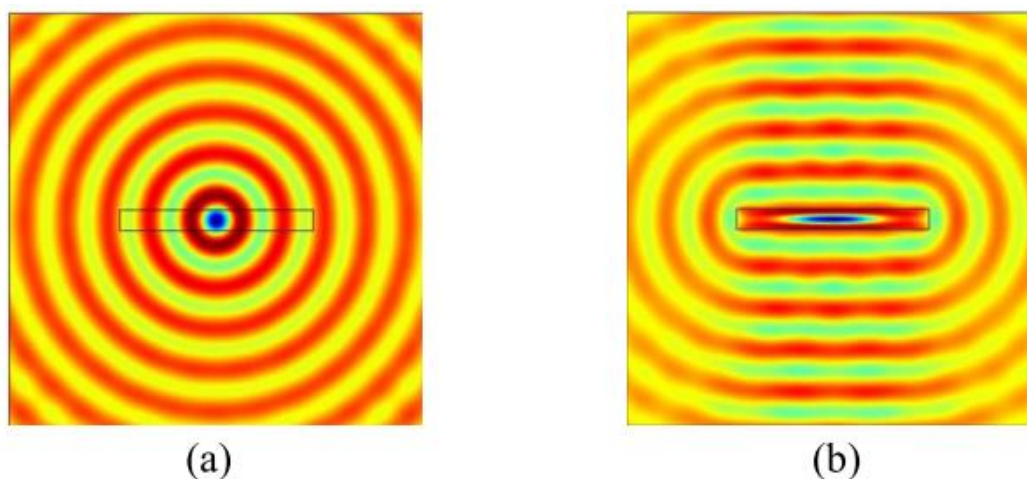


Fig. 2.17 TO-based Maxwell fish-eye lens concept (a) TE polarized line source in untransformed space, (b) Line source in transformed space [54].

In the next section, a discussion is presented on metamaterial based TO solution for improving or modifying radiation patterns of antennas.

### 2.4.1.2 Metamaterial based TO-solutions for antenna applications

Many recent publications show that TO allows envisioning antenna engineering in a fundamentally different way. A great level of control can be exercised on the radiation patterns of antennas using TO. In this section, a few examples of TO-solutions with anisotropic material profiles for antenna applications are discussed. Examples of solutions using SRR and ELC type metamaterials are also presented.

- Flattening a parabolic reflector

In [55], a flattened parabolic reflector concept working at 6 GHz is presented. The material profile is derived using TO method for a rectangular slab corresponding to that of a parabolic dish. The number of elements required in material tensor of the profile is limited by favoring TE polarization. The derived material profile contains extremely large values of permeability (as high as 40). This is only achievable in SRR based composite medium. Thus a practical implementation of such a device may be narrowband in nature due to inherent properties of metamaterial-based medium. Nevertheless, the focusing behavior for an incident plane wave is achieved using the transformed profile, as shown in Fig. 2.18.

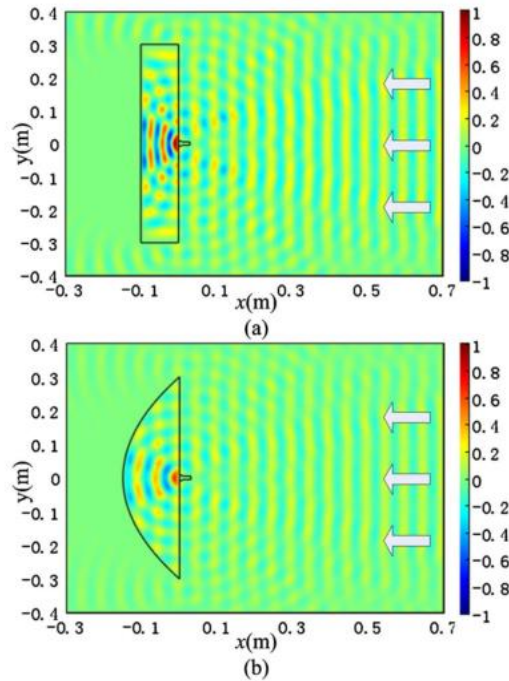


Fig. 2.18 Focusing behavior of (a) TO-based flat reflector (b) Traditional parabolic reflector [55].

In [56], a TO-based dielectric-only flat reflector is presented, wherein the permittivity profile is designed using an array of printed dipoles. A short monopole antenna placed at the focal point of the reflector acts as TM-polarized source. The chosen coordinate transformation leads to an isotropic but inhomogeneous permittivity distribution in the transformed region. Dipoles of varying lengths are used because they increase the average

polarizability of the material in its vicinity leading to increased local permittivity. An optimized version of the reflector is realized using 520 such dipoles. The design presents 67% bandwidth in measurements. However, the major drawback is that the thickness of the device is  $1.3\lambda$  at the design frequency.

- Ultra directive radiation

In [37], [57], Tichit presents a superstrate concept and an experimental verification of a highly-directive emission using metamaterials. The design is optimized to give a peak-radiated power at 10.6 GHz. As seen in the section 2.3, normalization strategies have allowed simplifying material profile to limit variation to  $\mu_{yy}$  and  $\epsilon_{zz}$  for a TE polarized source. The material profile is interpreted using alternate layers of ELC and SRR materials as seen in Fig. 2.19. The axial permittivity  $\epsilon_{zz}$  and permeability  $\mu_{yy}$  show respectively values ranging from 0.12 to 4.15 and from 1.58 to 15.3. It can be remarked that despite the renormalization of permittivity along  $x$ -axis, the construction of the device remains very complex. The superstrate allows focusing the radiation in a narrower beam than a conventional parabolic reflector of the same size.

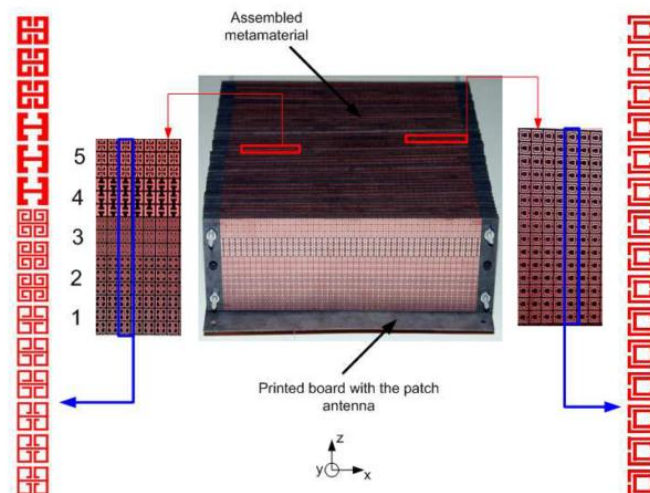


Fig. 2.19 Composite medium with ELC and SRR [37].

- Isotropic radiation

In [58], Tichit proposes to use TO method to achieve isotropic radiation from a finite sized source by appropriately transforming the surrounding space around the source. The physics laws dictate that isotropic radiation may only be achieved using infinitesimal point sources. In [58], a radial transformation allows reducing the size of the finite sized source such that the directive source is perceived as a point source. Furthermore, it is shown that the transformation can be designed by non-magnetic profile with anisotropic permittivity. A prototype based on ELC resonators is realized at 10 GHz. The variation in angular and radial permittivity inside the transformed profile is in the range 0.05 to 4.71. As explained earlier,

ENZ values are achieved near the resonant frequencies, hence the proposed isotropic radiator has a narrowband operation. The fabricated prototype consists of 30 PCB's containing angular and radial permittivity elements of material tensor, with a 3.3 mm ( $\sim 0.1\lambda$ ) air layer of separation between adjacent boards. Therefore, the height of the final device is about  $3\lambda$ . A representative image of the transformation is shown in Fig. 2.20.

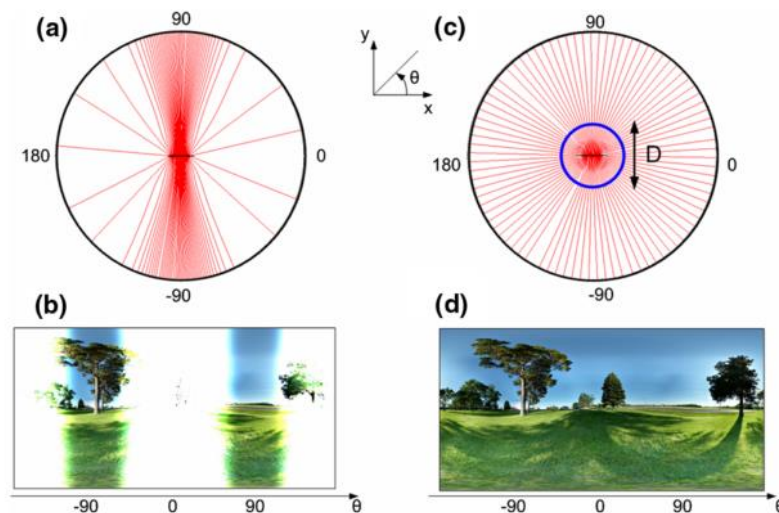


Fig. 2.20 (a) Ray trajectories from a directive source (b) Field of view of directive source, (c) Isotropic radiation due to optically transformed medium (d) Field of view of TO based solution [58].

- Beam collimators

In [59], a multi-beam antenna TO concept is presented. An optically transformed media surrounds a monopole antenna and depending on the chosen spatial transformations, the device can provide multiple highly collimated beams as shown in Fig. 2.21. The anisotropic lenses are designed using ELCR and SRR type metamaterials. A monopole antenna is considered as a source for the first case. A QCTO-based all-dielectric version designed using Gradient Index (GRIN) material is also presented; an open sleeve monopole (for wider bandwidth) is considered as the source in the second case.

The reported lenses increase the directivity of the antenna in a broad range of frequencies. The reported bandwidths are 27% centered at 4.8 GHz for anisotropic lens and 53% around 5.7 GHz for the GRIN lens. The anisotropic lens provides a gain enhancement of up to 6.5 dB in the bandwidth, whereas the GRIN lens enhanced the gain by 6 dB.

These types of devices are very interesting in the present context because they enhance the gain of the antenna in the horizon, which is the central objective of this thesis. However, one major inconvenience is that the thickness of the lens is linked to the height of the source. Considering 5 GHz as the operating frequency, the lenses have a thickness of  $0.5\lambda$  (30 mm). A similar solution at lower frequencies (1 GHz) for L-band applications will result in a 150 mm thick solution, which is not conformal or low profile as desired.

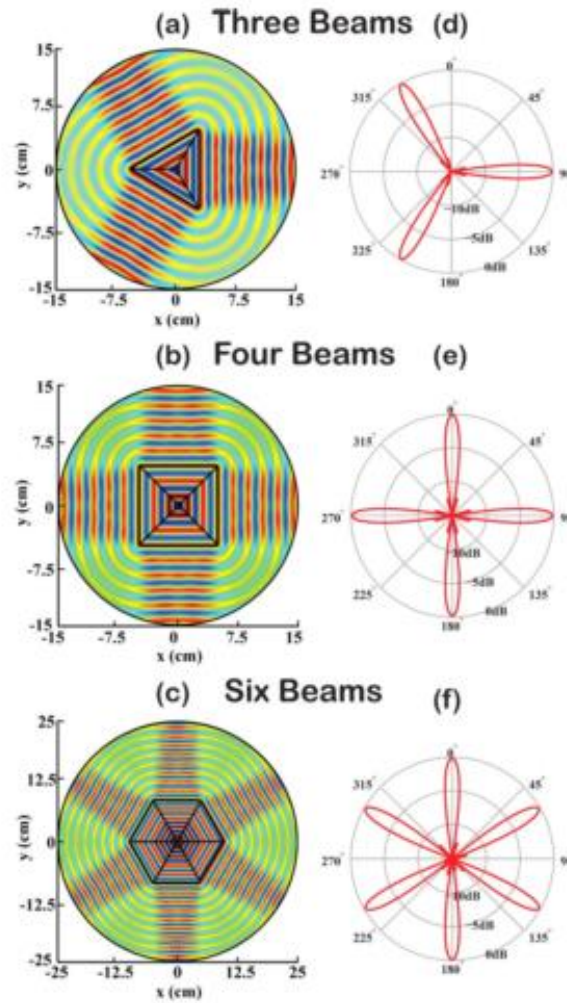


Fig. 2.21 Multi beam antennas (a)&(d) Three beam lens, (b)&(e) Four beams, (c)&(f) Six beams [59].

- *Beam tilting*

Essentially, the objective pursued in this thesis is to tilt the beam in the azimuthal plane. Dielectric metamaterial-based superstrates are discussed in [60], [61], that introduce a tilt in the main beam of an antenna using QCTO techniques. The superstrate type lens is placed over a TE polarized planar 4-element microstrip antenna array. Laplace equation is used to construct mapping between physical and virtual spaces. Appropriate simplifications allow an isotropic design with achievable permittivity variation. The concept is demonstrated using 10 printed boards, each containing 20 rows of 5 ELC resonators, as shown in Fig. 2.22. The effective values of these metamaterial unit cells are extracted at 10 GHz. The boards are separated by 5 mm each, which leads to effective thickness of  $1.6\lambda$  at the design frequency. A  $13^\circ$  tilt in the main beam of the antenna is introduced. The superstrate is said to be capable of operating in a non-narrow frequency range. However, the patch antenna array used as source for the superstrate operates in narrowband.

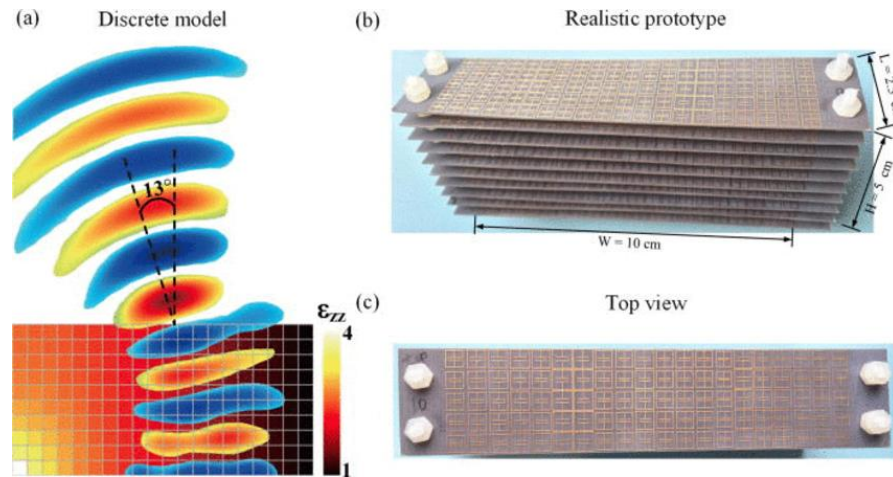


Fig. 2.22 (a) Beam tilting device designed using QCTO; (b)&(c) ELC resonator based design [61].

Apart from the above-discussed solutions, many other interesting concepts have been proposed to use metamaterials to design complex anisotropic profiles e.g. Super-lenses [62]–[65], Illusion optics [20], [21], [45]–[47], control on polarization of light [69], [70], etc.

#### 2.4.1.3 Discussion on metamaterial based TO solutions

Table 2.1 is a recapitulation of a few theoretical and experimentally verified TO concepts presented above.

Table 2.1 Metamaterial based TO solutions

Reference	Application	Frequency of operation (GHz)	Thickness ( $\lambda$ )	Anisotropy	Metamaterial	Bandwidth
[43]	Cylindrical cloak	8.5	1.6	Diagonal elements	SRR	Narrowband
[46]	Carpet cloak	13-16	4.6	Isotropic	Non-resonant	Wideband
[50]	Waveguide bend	10	-	Diagonal	SRR	Narrowband
[54]	Fish-eye lens	10	2	Off-diagonal	COMSOL Simulation	-
[56]	Flat reflector	5-10	1.3	Isotropic	Electric dipoles	Wideband
[59]	Beam collimating lens	4.8	0.5	Diagonal	SRR	Not narrow
[61]	Beam tilting	10	1.6	Isotropic	ELC	Not narrow

It may be remarked here that most of the experimental work using metamaterials is in X and Ku-band with a few exceptions. This may be due to ease of manufacturing and measurements. The size of devices is also therefore manageable. However, as one starts designing similar solutions in lower frequency ranges (S, L or UHF), the size of the device becomes a considerable issue. In the table above, the thickness of transformed region has

been presented in terms of wavelength at the frequency of operation. The thinnest profile achieved in [59] is half-wavelength thick, which is also too much for designing a low-profile application in L-band frequencies. Hence, the required transformation behavior needs to be achieved in a much thinner profile ( $\sim 0.1\lambda - 0.2\lambda$ ). Thinner profiles may be achieved, but at the expense of extreme material parameters, which would require using resonant metamaterials.

It is evident from the table above that anisotropic resonant metamaterial-based TO-solutions provide a narrowband performance. Indeed, the bandwidth performance improves by using non-resonant metamaterials to describe quasi-isotropic dielectric material profiles. But non-resonant metamaterials cannot provide exotic (very high or low) permittivity and/or permeability values. Thus, using metamaterials for designing TO-solution may be considered a compromise between achieving extreme material parameters in the profile and wide bandwidth.

In the next section, progress in TO-based solutions using standard dielectric materials is reviewed.

## 2.4.2 TO-solutions with standard materials

TO-solutions have a great potential to address practical problems in industry, but their adoption for commercial application may be marred by the inertia in industrialization of metamaterials. While decent performances are achieved using metamaterials in variety of experiments, there is reluctance in using resonant SRR and ELC metamaterials in TO solutions for industrial applications owing to various considerations. This is an impediment for wide scale adoption of TO method. Fortunately, many TO concepts do not require extreme material parameters i.e. negative or near zero values of permittivity and permeability. In addition, anisotropic profiles can be simplified using strategies like normalization and QCTO as seen in section 2.3. Therefore, such profiles can be interpreted using standard isotropic dielectric materials fabricated using standard industrial techniques. Perforated dielectrics are often employed. Also the advent of additive manufacturing techniques (3D printing, extrusion printing, etc.) has greatly facilitated the design of dielectric solutions. In this section, a variety of TO-solutions using standard dielectric materials are presented. Firstly, a review of diverse TO concepts is presented and thereafter antenna solutions are presented.

### 2.4.2.1 Dielectric material based TO Concepts

- Dielectric solutions using through-hole techniques

Invisibility cloak is the most popular application of TO method. A dielectric cylindrical invisibility cloak is presented in [71]. It is reported that reduction in appearance (i.e.

imperfect invisibility) can be achieved using isotropic dielectric cloaks, albeit with a narrowband performance. This concept can be traced back to [72], where it is shown that cloaking behavior could be achieved using material profile with no singular parameters and a devices made of standard dielectric materials can show cloaking behavior over a wide range of frequencies.

In [73], an experimental demonstration of cloaking at optical frequencies is discussed. The cloak works for wavelengths in range 1400-1800 nm. This cloak hides any object placed behind a reflecting metallic bump, as shown in Fig. 2.23. Quasi-conformal mapping technique is used to derive the required material profile. The cloak is composed of two distinct regions: C1 and C2. C2 is a constant refractive index region and its effective permittivity is 2.5 designed by milling holes with a diameter of 110 nm in silicon wafer ( $\sim 0.06\lambda$ ). C1 is the region with variable index. The variation of refractive index in this region is achieved by varying the density of holes. The 250 nm ( $\sim 0.14\lambda$ ) thick silicon wafer serves as an optical waveguide to confine the incident light and the cloaking behavior is achieved in the remaining two dimensions. The dimension of C1 region in Fig. 2.23(a) in terms of wavelength is approximately  $3\lambda \times 2\lambda$ . In theory, Gaussian light beam reflects off the bump without scattering. The measurements carried out on the fabricated prototype show nearly 58% transmittance at 1540 nm; the reduced performance is attributed to errors in drilling sub-wavelength nanometer sized holes. The takeaway from this study is that standard industrial fabrication processes can work well for TO-solutions in optical frequencies. Other cloak configurations for hiding bumps at optical and RF frequencies have also been experimentally fabricated as laser written photonic crystal (PC) [74], or by drilling inhomogeneous holes in multi-layered dielectric plates [75].

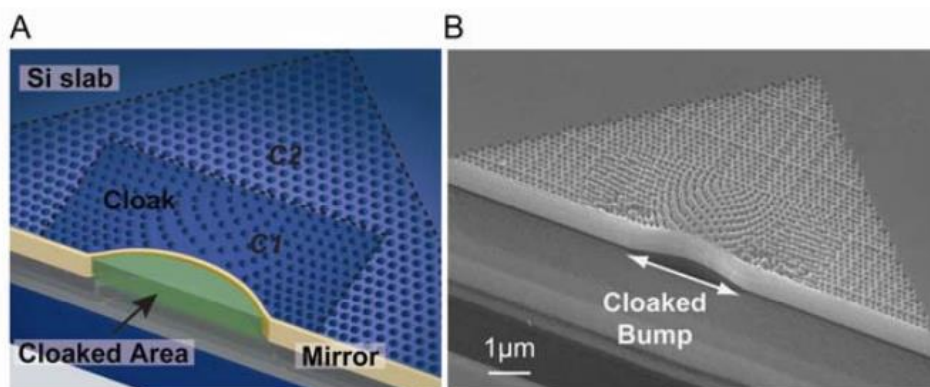


Fig. 2.23 (a) Representative image of a carpet cloak;(b) SEM image of the fabricated device [73].

The through hole technique seen above is very useful for achieving gradient in refractive index. The underlying principle is that drilling air holes in a dielectric material can change the

effective permittivity value. The effective dielectric constant,  $\epsilon_{eff}$  of a block of drilled dielectric can be estimated using ( 2.13 ):

$$\epsilon_{eff} = \epsilon_d - (\epsilon_d - \epsilon_a) f_a \quad (2.13)$$

Here,  $\epsilon_d$  and  $\epsilon_a$  are the relative permittivity of dielectric material and air and  $f_a$  is the volume ratio of air inside the dielectric material. The technique can be applied across different frequency ranges i.e. optical (seen above) and THz [76] , down to microwaves. In [77], a magnifying lens made of perforated isotropic dielectric material is shown for use in broadband sub-wavelength imaging applications. The lens shows super-resolution properties in wide frequency range of 7-10 GHz. It is shown that the perforations in standard dielectric materials with different permittivity values: TP-2 (9.6), FR-4 (4.4) and F4B (2.65) allow designing the spatial transformation.

A Luneburg lens is a spherical lens that concentrates incoming plane wave on diametrically opposite end. It is widely used in conjunction with antennas for scanning applications. In [78], a dielectric implementation of a Luneburg lens is proposed. A device is fabricated using polymer-ceramic material, in which 0.125in wide holes are drilled using milling machine. Variation in relative permittivity (between 1 and 5.5) is achieved using the spatial distribution of holes in a polymer-ceramic material, as shown in Fig. 2.24. The designed lens measures  $10\lambda$  at the design frequency of 10 GHz. The device is intended for use in 8-12 GHz range.

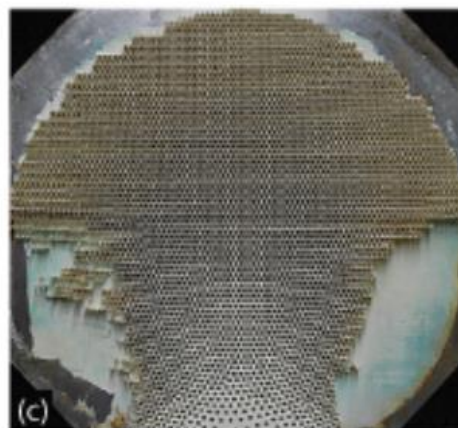


Fig. 2.24 Fabricated prototype of Luneburg lens [78].

In [79], perforated dielectrics are proposed to design a broadband zone plate lens operating in K-Ka bands. The dielectric lens essentially acts as a Fresnel lens. It is proposed to realize such a device using 2200 individual permittivity blocks. The required variation in the permittivity to interpret the transformation lies in the range of 2.6 to 15. The zone plate is

9mm thick, which is  $0.9\lambda$  at the design frequency. It is proposed that filling the air holes with high- $\epsilon$  powders to approximate high values of permittivity values. The lens provides broadband performance in 20-40 GHz range.

The recent work published by Cui's group presents a semispherical dielectric lens working in X-band (8-12 GHz) [80]. The lens behaves as a magnifying device to resolve the sources in sub-wavelength scale. The variation in permittivity is between 1 and 16 and the authors have used Teflon with air-holes in conjunction with  $\text{TiO}_2$  and polyphenylene oxide to achieve the gradient in practice. The all-dielectric construction allows achieving broadband behavior.

- *Dielectric solutions using 3D printing techniques*

New fabrication strategies like 3D printing can achieve complex shapes with relative ease. Therefore, they are of particular interest in designing TO solutions. In [81], 3D arbitrarily shaped devices designed using QCTO techniques with isotropic material properties are proposed. This isotropic nature of material profile allows designing polarization independent devices compatible with 3D printing techniques. As an example, a 3D wave-bending device is demonstrated in simulations.

In [82], a 3D printed broadband dielectric Eaton lens working in Ku band (12-18 GHz) is presented. The permittivity variation in the transformed profile is very high,  $1 < \epsilon_r < 40$ . Lower permittivity values ( $1 < \epsilon_r < 3$ ) are realized using 3D printed woodpile PC. Higher permittivity values are realized by the compound liquid medium approach using a mixture of benzene and acetonitrile. Additive manufacturing techniques are used to fabricate the PC structure [83].

For waveguide type applications, a broadband 3D printed tapered waveguide concept is demonstrated in [84]. The design consists of 300 isotropic dielectric unit cells. The gradient in effective permittivity is approximated by printing air holes in a dielectric host medium of a relative permittivity of 2.8. The taper connects two waveguides with different cross-sections and provides a wideband performance in 7-13 GHz.

In [85],[86] fusion deposition type 3D printing technique is used to fabricate spatially variant electromagnetic structures. The waveguide bend is printed using polycarbonate ABS (Acrylonitrile Butadiene Styrene) blend with relative permittivity of 2.45 at 15 GHz, as shown in Fig. 2.25. The device may have wideband characteristics, however authors define the effective bandwidth as the frequency range in which the collimation at output is higher than a predetermined criterion. The reported effective bandwidth is measured as 6.5% at the design frequency. Highly collimated beam shows that the lattice structure adequately interprets the transformation and radically changes the propagation direction. However, this

transformation is achieved in a dimension of  $1.75\lambda \times 1.75\lambda \times 0.87\lambda$  at 15 GHz. The effective thickness in the direction of propagation is  $1.75\lambda$  in the direction of propagation, which is not suitable for applications in lower frequencies.

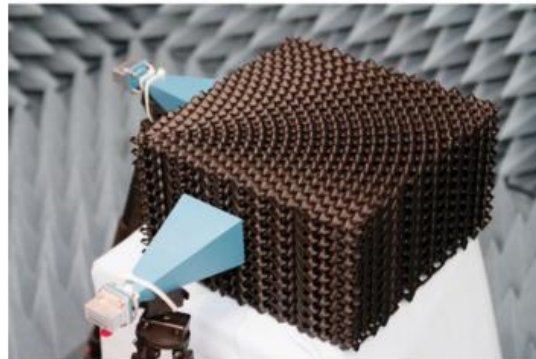


Fig. 2.25 3D printed waveguide bend [85].

#### 2.4.2.2 Dielectric TO-solutions for antenna applications

Dielectric TO-solutions are indeed interesting for antenna applications. There is a huge potential to reengineer legacy antennas for novel applications. In this section, few notable examples are described. A special emphasis is made on 3D printed solutions.

- Dielectric flat reflectors

The concept of dielectric flat reflectors is introduced in [39]. In [87], optically transformed flat reflectors for beam steering applications has been designed in Ku band (15 GHz). The transformation between the physical and virtual space is mapped on a grid comprised of quasi-orthogonal grids. The flat reflector offers a wideband operation in 13-17 GHz range. Furthermore, a steering operation is proposed by integrating p-i-n diodes in the dielectric to tune the exiting wave front. The superstrate is 52mm thick, which is equivalent to  $2.6\lambda$  at 15 GHz.

In [88], [2], a standard dielectric flat reflector is designed at Telecom ParisTech by Clemente *et al.*, the device works at 5 GHz. From calculation, the variation in the permittivity in profile device is between 0.2 and 1.45. The dispersive permittivity values are reassigned to unity, such that the variation in permittivity profile is limited between 1 and 1.45 and can be realized using standard dielectric materials. The profile is implemented by drilling airholes in Teflon. The diameter of air holes is 4 mm, which is equivalent to  $0.067\lambda$  at 5 GHz. In terms of thickness, the dielectric layer is 10 cm thick, which is equivalent to  $1.67\lambda$  at 5 GHz.

- Dielectric focusing lenses for antenna applications

Lenses made with standard dielectric materials are demonstrated to modify the antennas radiation patterns. In [89], a transformed planar dielectric hyperbolic lens is proposed which

retains the focusing properties of an original curved lens. This is shown in Fig. 2.26. Due to an all-dielectric construction, the lens presents broadband radiation characteristics. The relative permittivity varies between 3 and 14.

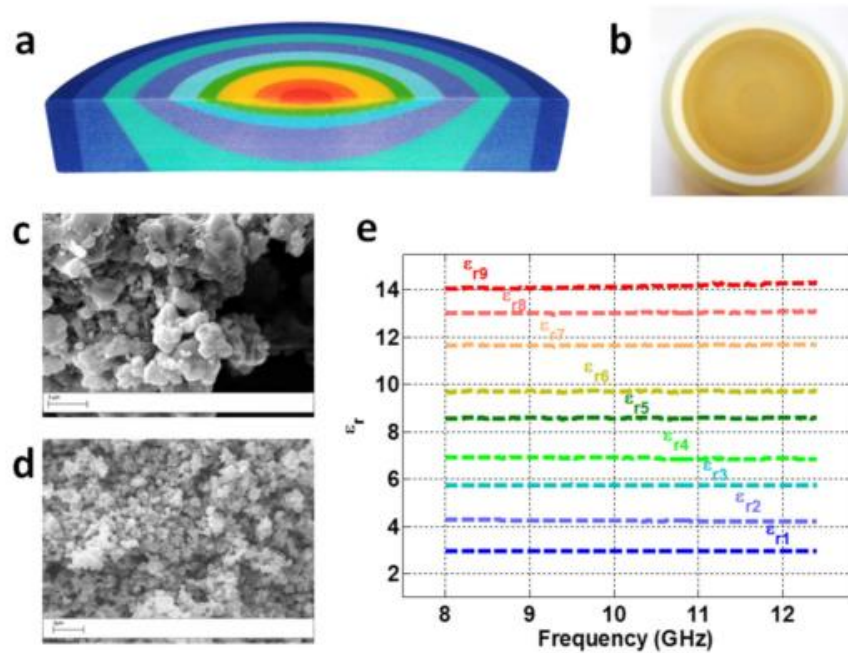


Fig. 2.26 (a) Permittivity variation in the flat hyperbolic lens, (b) Manufactured prototype using processed titanate powders, (c)&(d) Different sized particles (e) Permittivity vs. frequency plots for materials [89].

Indeed, high value of permittivity is a challenge for prototyping the devices. Here, processed titanate powders are presented as a solution, which are a great choice due to the frequency independence of the permittivity values. Depending upon the size ratios of the titanate powders, micro and nano-sized powders are used to approximate the permittivity gradient. The relative permittivity in the final profile varies between 3 and 12.6. The lens offers in an extremely large bandwidth; the measurements are reported from 2-14 GHz. The lens stops to operate below 2 GHz because its dimensions are small compared to the wavelength.

A 3D printed planar focusing lens is presented in [90] to convert spherical waves to planar waves. A Ku-band waveguide was used as the source to generate spherical wave fronts. The variation in relative permittivity is limited to a small range from 1 to 3. A 3D printer compatible Poly-Lactic Acid (PLA) thermoplastic material is used as the host dielectric material. Micron scale air holes created using 3D printing techniques are used to achieve the permittivity gradient. The superstrate type lens acts as a broadband device with high gain (8-10 dB) over a wide range of frequencies (12-18 GHz). The fabricated prototype

is shown in Fig. 2.27. In terms of size, the lens is 18.5 mm thick, which is equivalent to  $\sim 0.3\lambda$  at 15 GHz.



Fig. 2.27 Dielectric focusing lens in Ku-band realized using extrusion 3D printing [90].

- Dielectric lenses and superstrates for beam control

Dielectric lenses and superstrate devices have also been used as a way to control the main antenna beam direction. Luneburg lens has already been introduced in previous section; it is also used for antenna applications, as demonstrated in various works.

The spherically shaped Luneburg lens can be compressed to achieve a flat profile. The material profile required for this compression can be achieved using TO method, as discussed in [91]. In this paper, a flat Luneburg lens is designed using titanate powders; a representative image is shown in Fig. 2.28. Due to the nature of the materials, the lens presents a broadband behavior, with no significant difference in performance across different frequency ranges. Maximum directivity at 10 GHz is reported as 18.2 dBi with low side lobe levels. Also, a beam steering of  $34^\circ$  was achieved. In terms of size, the lens is remarkably low profile with a thickness of  $0.16\lambda$ . Thinner profiles can also be designed, but this requires higher permittivity values.

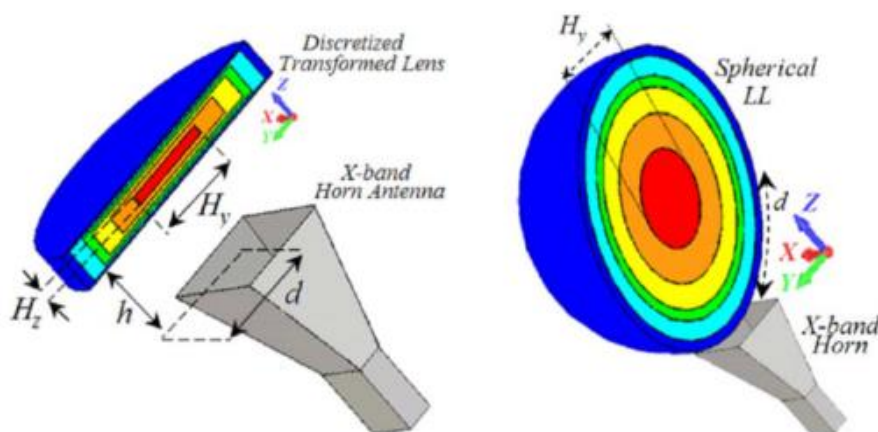


Fig. 2.28 Cut-offs of dielectric Luneburg lenses (LL): A flat LL inspired from TO (left), Uncompressed spherical LL (right) [91].

In [92], a Luneburg lens with an extended flattened focal plane is designed using QCTO techniques for use in conjunction with a microstrip antenna array. The extension beneath the spherical Luneburg lens allows attaching microstrip antenna array in the focal plane of the lens. The lens functions in Ku-band (12-18 GHz). A relative permittivity in the profile varies between 1 and 2.26. This variation is achieved in a 3D printed effective permittivity medium with VisiJet M3 Crystal polymer material acting as base material. The fabricated device is shown in Fig. 2.29. The microstrip antenna array also allows implementing electronic beam scanning.

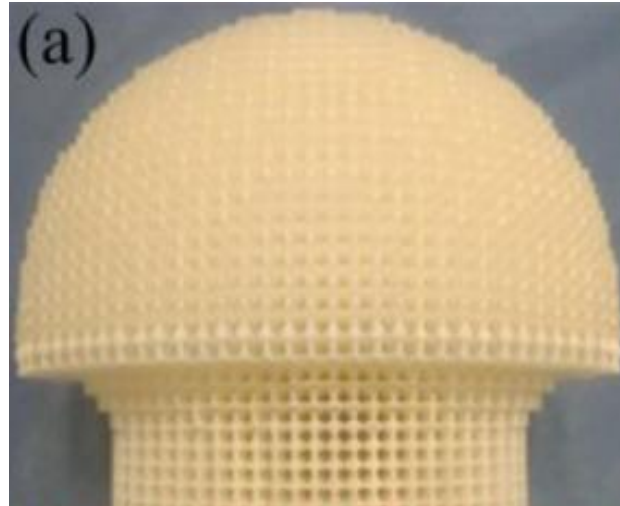


Fig. 2.29 3D printed Luneburg lens with extended flat focal surface [92].

In [93], [94], Yi presents a dielectric 3D printed superstrate to introduce a tilt in the main beam of a microstrip patch antenna array radiating in X-band (8-12 GHz). A broadband behavior is reported in simulations due to use of all-dielectric non-resonant materials. The variation in relative permittivity inside the transformed profile is reported between 1 and 2.8. In practice, an effective permittivity medium is designed using a polymer medium with 2.8 as a based medium. Air holes of variable radii allow approximating the gradient in permittivity. Peak directivities as high as 31.4 dB are shown and tilt of up to  $24^\circ$  is achieved in the main beam.

In [95], a conformal 3D printed dielectric superstrate is presented to restore in-phase emissions from non-planar radiating elements. QCTO techniques used to transform the space also allowing achieving a broadband behavior. The superstrates provides nearly identical radiation performance in 8-12 GHz frequency range. Such a solution allows avoiding the use of expensive and complex phase-shift systems to compensate for the different phase shifts caused by the varying path lengths of the electromagnetic waves. The variation in relative permittivity is between 1.5 and 2.6 and is fabricated using polyjet-printing technique. A photo

of fabricated prototype is shown in Fig. 2.30. In terms of the size, the height of the superstrate is  $0.67\lambda$  at 10 GHz.



Fig. 2.30 3D printed dielectric superstrate for restoring in phase emission from non-planar microstrip array [95].

This research theme has also been developed at Telecom ParisTech. In [2], a dielectric superstrate is presented for aeronautical applications, which improve the HPBW of aircraft mounted patch antennas for GPS applications. The design is optimized for performance in L-band at 1.21 GHz. The required permittivity distribution is achieved by vertically inverting the permittivity distribution of [39]. Since the superstrate is specifically destined for a GPS related application, its performance in the vicinity of a large PEC ground plane to simulate installation considerations is also presented. The bandwidth of the source antenna is not significantly affected due to the presence of the superstrate. A slight shift in bandwidth is reported, which is deemed correctable by changing the position of source vis-à-vis the superstrate, or by changing the size of the ground plane.

The prototype is fabricated using a 3D printer using Fullcure (relative permittivity of 2.9) as the base material. The distribution of relative permittivity in the profile is achieved by varying the density of holes. The superstrate has a thickness of 40 mm which is  $\sim 0.16\lambda$  at 1.2 GHz. The low profile is a major advantage for this solution. The fabricated prototype is shown in Fig. 2.31. The measurements have demonstrated the proof of concept. These good results are also one of the motivations to go further through this thesis.



Fig. 2.31 Perforated Teflon layers of a dielectric superstrate to increase HPBW realized at Telecom ParisTech with help of Airbus Group Innovations [2].

### 2.4.2.3 Discussion on metamaterial based TO solutions

Table 2.2 is presented as a recapitulation of TO results realized using standard dielectric materials. All these results present broadband behavior.

Table 2.2 Dielectric TO Solutions

Reference	Application	Frequency of operation (GHz)	Thickness ( $\lambda$ )	Design technique	Highest $\epsilon_r$
[73]	Ground plane cloak	214 (THz)	2	Silicon slab with milled holes	2.5
[78]	Planar Luneburg lens	8-12	10	Perforated dielectric medium	5.5
[86]	Waveguide bend	15	1.75	3D printed	2.45
[88]	Flat reflector	5	1.67	Perforated Teflon	1.45
[91]	Flattened Luneburg Lens	10	0.16	Titanate Powder	12
[95]	Restoring in-phase emissions	8-12	0.67	3D printed	2.6
[2]	Increasing HPBW	1.2	0.16	3D printed	2.9

It may be remarked here that the lenses and superstrates that introduce strong modification in the propagation behavior (e.g. Dielectric Fresnel lens [79], Luneburg lens [91], etc.) in a *thin* profile require high permittivity values. Thus, a trade-off exists between the size and the higher bound of relative permittivity values in the TO device.

## 2.5 Parallel research tracks

The previous sections presented the basics of TO method so that the reader can comprehend the solutions proposed in this thesis. A comprehensive review of research from

origin to latest advances in the domain was presented. For more information, one may refer to [96]–[98]. It is clear that research on volumetric Transformation Optics is gearing towards an arbitrary control over the wave propagation. Today, a lot of research in the domain is being pursued. Parallel tracks in research have emerged which can be broadly classified under following headings:

- New methods to design optimum transformations optics, and
- New materials to design the spatial transformations

Some of the research in parallel tracks is briefly reviewed here to appreciate the excitement for TO method in the larger physics and engineering community. While the discussed works are not directly related to the present thesis, they shine a light on the possible future of the field.

### 2.5.1 Methods

The coordinate transformation based TO method as proposed by Pendry et al. rotates and scales the fields inhomogeneously as dictated by the chosen spatial mappings. In [99], an alternative approach towards TO has been proposed which uses conformal mappings to generate a nontensorial (NT) field transformation. The underlying principle of the original TO method requires the transformed fields to be the solutions of the Maxwell's equation for the given medium. In this alternative method, the authors propose that the condition above can also be satisfied in a NT medium using unphysical transformations. Such unphysical transformation allows transforming each field component independently as if it is a scalar. Unlike in standard TO approach where fields are scaled and rotated, fields in the NT medium are simply transported. However, the drawback of this approach is that the material profile of the transformed medium is essentially anisotropic and contains non-reciprocal off-diagonal elements, which complicates its implementation. The authors propose simulations of nontensorial optical squeezers and isolators to validate the design approach. Microscopy, particle acceleration, optical communications, etc. may be potential areas of application for NT TO solutions.

There are also other interesting discussions based on TO method. A parallel research track is optimization algorithms. In [100], QCTO technique combined with global optimization algorithm are used to design GRIN lenses. In [101], a beam forming application has been presented. The approach uses a FEM solver constrained to non-linear minimization algorithm to find a material space with achievable values. In [102], it is proposed to use TO method in conjunction with FEM and Genetic Algorithm (GA) to address the problem of shape optimization. A shape optimization problem is an inverse scattering problem, where the measured scattered field data is used to reconstruct the shape of the scattering object.

Traditionally, it is required to remesh the object geometry post each iteration. In this work, authors propose to interpret the boundary as a TO media and upon each iteration, only the material parameters of TO media are changed.

## 2.5.2 Materials

A complete control over the effective refractive index is necessary for faithfully interpret the spatial transformation. Even with standard dielectric solutions, achieving extreme material parameters is indeed a challenge. Greater collaboration with material scientists is often necessary to understand the true limits in fabricating TO-solutions. A far more interesting opportunity, however, is to look at the aspect of reconfigurable transformation optics with tunable materials.

The most notable example of achieving re-configurable TO-solutions is by using Graphene [103]–[105]. Vakil discusses in [103] that by designing and manipulating spatially inhomogeneous, non-uniform conductivity patterns across a flake of Graphene, one can have this material as a one-atom-thick platform for infrared metamaterials and transformation optical devices. Indeed, Graphene’s properties can be tuned by modulating electric field, which changes Graphene’s chemical potential. An implementation of Luneburg lens for mid-IR surface plasmons has also been numerically demonstrated; wherein different chemical potentials applied on Graphene flakes allows achieving the refractive index gradient.

Active metamaterials are also frontier of research in the domain. Their use enables designing reconfigurable TO-solutions [106]–[108]. For example in [106], manipulation of electromagnetic waves is shown using digital metamaterial unit cells, whose individual states can be controlled using FPGA hardware. As an example, the authors show over a control of scattering pattern off a metasurface by simply changing the sequence of bits input through FPGA array. Indeed, such a concept can also be envisaged for volumetric metamaterials.

An interesting approach to re-configurability is discussed in [109], where use of fluids is proposed to vary the refractive index profiles and achieve spatial transformations. As an example, waveguide with laminar liquid flow is shown to present novel focusing and interference patterns. The control over the continuous GRIN profile inside the channel is achieved by tuning flow rates of liquids in the channel i.e. ethylene glycol and de-ionized water. While a promising approach for simple structures like waveguides, the implementation of such a profile may be significantly complex for volumetric transformations.

## 2.6 Context of present work

A thorough review of the existing solutions allows us to position our approach to solve the problem stated in Chapter 1. A part of this thesis is to demonstrate that it is possible to

design and realize a low profile dielectric solution is required that reorients the broadside radiation pattern of a patch antenna in the azimuthal plane. At Telecom ParisTech, Clemente Arenas first proposed the concept in [2], [110]. A rectangular physical space is optically transformed into a virtual space composed of two opposite quarter-ellipses. Normalization of material parameters is used to limit the variation to two values in material tensor:  $\epsilon_{zz}$  and  $\mu_{yy}$ . A concept device functioning in L-band is also reported using CST simulation results, which achieves the reorientation of electromagnetic waves in azimuthal plane. The profile is  $0.15\lambda$  thick at 1.2 GHz, which is an admissible thickness when compared to other solutions in literature. However, the profile contains extreme values of anisotropic material parameters ( $1 < \epsilon_{zz} < 15$  and  $0.3 < \mu_{yy} < 3$ ). The variation of permittivity and permeability inside a profile with discrete number of pixels is shown in Fig. 2.32.

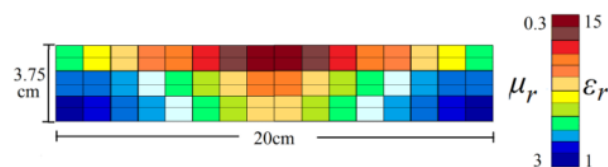


Fig. 2.32 Discretized profile of relative permittivity and permeability [2].

While simultaneous variation of permittivity values is achievable using alternating layers of electric and magnetic metamaterials, the high values of permittivity and permeability require the metamaterials to operate in the resonant frequency range of unit cells. Such fabrication would be feasible but very difficult, because it requires careful tuning of individual unit cells for achieving correct values of  $\epsilon_{zz}$  and  $\mu_{yy}$ . Also, a solution with resonant metamaterials is inherently lossy and not suitable for many applications.

In this thesis, the procedure proposed by Clemente Arenas will be reused and new degrees of freedoms will be investigated to simplify the realization of the superstrate. Various simplification techniques presented in this chapter are used to arrive at a simplified dielectric only profile, which paves the path for an easy fabrication using standard dielectric materials.

In the next chapter, the theoretical design of TO concept is presented, which introduces a radical reorientation of main beam of patch antenna in its azimuthal plane.



## 3. Concept Definition

After considering the possibilities offered by T.O. method to address the problem described in Chapter 1 and a thorough literature review in chapter 2, the theoretical development of a T.O. superstrate capable of reorienting electromagnetic waves in the azimuthal plane of the source is presented in this chapter. The main objective of this chapter is to come up with a procedure required to arrive at a quasi-final superstrate design presented at the end of this chapter, which reorients broadside directive radiation pattern of a classic patch antenna in the azimuthal plane. This design will be then reused in the next chapter for designing a proof of concept. Moreover, in Chapter 5, we will demonstrate that the design procedure described here can be easily extended to the entire family of superstrate type devices based on the used transformation relations.

For an easier comprehension, the problem will be initially studied in sections 3.1 and 3.2 as a simplified problem under ideal conditions and in a two-dimensional space. Then the analytical deductions from these two sections will be extended to a 3D problem in 3.3 where full-wave solution results will be presented to validate the proposition.

Thus, mathematical construction of the virtual space and the spatial transformation linking it to the physical Cartesian space will be discussed in section 3.1.1. In the same context, the concept of spatial compression will also be described in the next subsection. Various examples of compression are presented. Once the spatial transformations will have been described, the propagation of electromagnetic waves in the transformed space will be discussed. The strategy for simplification of anisotropy in material parameters is presented while highlighting the design steps. The wave propagation is studied in the uncompressed and compressed spaces. Once the primary anisotropic solution with varying permittivity and permeability profiles is validated, the feasibility of a dielectric only solution is studied in the next step. A low thickness dielectric profile will be presented as the primary analytical solution. A second profile is also discussed to highlight the great flexibility in design due to the established procedure. In section 3.3, a full wave solution of the problem based on the analytical solution of previous section will be presented. First, a square patch antenna used to excite the T.O. superstrate in the study is presented. Then, we discuss the pixelated versions of the continuous profile proposed in section 3.2. Finally, a cuboidal superstrate is presented using the pixelated profile in section 3.3.3. Use of a dielectric layer to match the patch

antenna to superstrate is also described in detail and the radiation performance of the superstrate is discussed.

### 3.1 Physical and Virtual Spaces

It is expected that the superstrate device in this chapter will change the directive radiation of a patch antenna to provide visibility in the azimuthal plane. An ideal outcome will be an antipodal radiation pattern with a radiation minimum in the broadside. Therefore, an appropriate spatial transformation needs to be defined to achieve such a behavior. Spatial compression also needs to be accounted in the transformation because the proposed solution needs to achieve the aforementioned reorientation in a low profile.

In this section, the physical and virtual spaces have been defined and discussed in detail. Spatial transformation of uncompressed space is first discussed. Later, spaces with various compression factors will be presented.

#### 3.1.1. Physical & Virtual Spaces– without compression

In the present problem, the radiation from a classic patch antenna is assumed to be directive in broadside with maximum along  $x$ -axis. In order to simplify the theoretical development, the directive radiation may be assumed as a plane wave travelling in Cartesian space. Here, the physical space is defined in the Cartesian coordinate system given by  $x$ - $y$  plane. A rectangular profile comprising of two identical square blocks is considered. The rectangle's dimensions are linked to the wavelength,  $\lambda$  at which the device will work. The initial size of the uncompressed, untransformed rectangular space is fixed to canonical dimensions in terms of wavelength i.e.  $\lambda$  by  $0.5\lambda$ . This choice is dictated by the objective of this i.e. to design low profile compact superstrates. It may also be noted that these dimensions are good representation of other superstrates studied in literature, as discussed in the last chapter: [59] ( $0.5\lambda$ ), [61] ( $1.6\lambda$ ), [95] ( $0.67\lambda$ ), [88] ( $1.67\lambda$ ), etc. Representative images of physical and virtual space are shown in Fig. 3.1. The physical space is a 2-D Cartesian space i.e.  $x$ - $y$  plane. The virtual space is comprised of two opposing quarter circles. As shown in Fig. 3.1(a), the space is considered made of vertical constant  $x$  lines shown in blue color and horizontal constant  $y$  lines shown in red color. In (a),  $d$  and  $e$  represent the dimensions of the rectangular region, where  $d = e = 0.5\lambda$ .

The virtual space is defined in a second, primed coordinate system in the  $x'$ - $y'$  plane. The space comprises of two opposed quarter circles joined together at the origin, as explained in [110]. This choice of virtual space geometry is guided by the required  $90^\circ$  change in the direction of propagation. The size of the virtual space is also linked to the wavelength; the radius of the circles is  $0.5\lambda$ . In Fig. 3.1(b) color-coding indicates how the red horizontal lines

in  $x$ - $y$  plane are transformed into red radial lines in  $x'$ - $y'$  plane. Similarly, the vertical blue lines in  $x$ - $y$  plane have been transformed into blue circular curves in  $x'$ - $y'$  plane. Here, it may be noted that the dimensions of the virtual space are given by the variables  $l$  and  $e$ , such that  $l = e = 0.5\lambda$ . It is also important to note the presence of dotted blue red curves along the  $x'$ -axis in (b). This shows that while the solid curves represent the desired reorientation after transformation, the grid formed with dotted curves is also transformed.

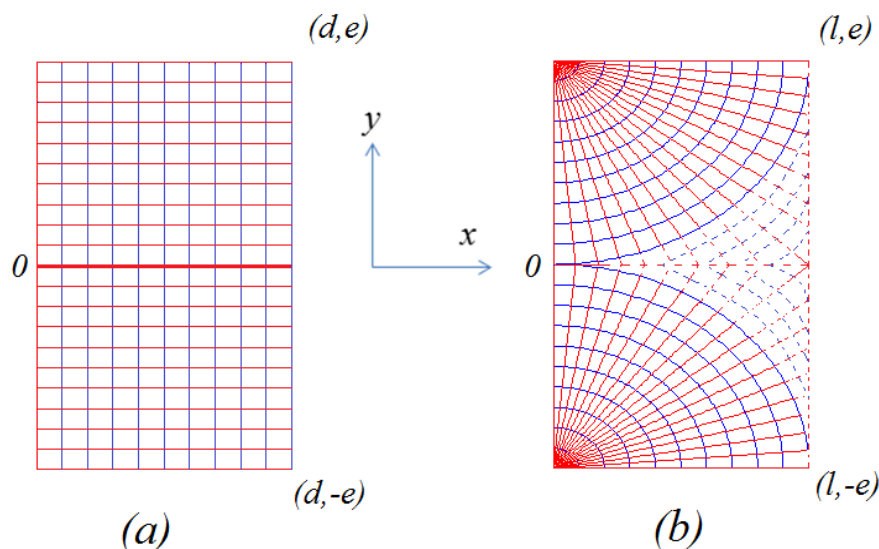


Fig. 3.1 (a) Physical space (Cartesian), (b) Virtual space.

Mathematically, the transformation of blue and red lines can be expressed using following equations:

$$x' = \sqrt{(x)^2 + (y \mp e)^2} \quad (3.1)$$

$$y' = \frac{e}{\pi} \tan^{-1} \left( \frac{y \mp e}{x} \right) \quad (3.2)$$

The  $\pm$  sign represents the symmetrical shift of center of quarter circles along  $y$ -axis. As previously seen in chapter 2, the Jacobian matrix,  $J$  links the virtual space to physical space. Using ( 2.2 ), ( 3.1) and ( 3.2 ),  $J$  is found out to be:

$$J = \begin{bmatrix} \frac{x}{\sqrt{(x)^2 + (y \mp e)^2}} & \frac{y \mp e}{\sqrt{(x)^2 + (y \mp e)^2}} & 0 \\ \frac{e}{\pi (x)^2 + (y \mp e)^2} & \frac{x}{\pi (x)^2 + (y \mp e)^2} & 0 \\ 0 & 0 & 1 \end{bmatrix} \quad (3.3)$$

In the next subsection we discuss the various types of compressions that may be used while transforming the space.

### 3.1.2. Physical & Virtual Spaces– size change

As previously discussed in chapter 2, T.O. allows achieving spatial compression. The current application requires the T.O. device to present a low profile to minimize the thickness of the transformed space. The spaces defined in the previous section may be changed further in at least 3 different ways:

1. Axial change
2. Lateral change
3. Radial change

In the following subsection, the spatial transformations resulting due to these three different types of compression are discussed.

#### 3.1.2.1 Axial change

The axial change in size of transformed space can be presented in form of compression along x-axis. This particular operation is governed by ‘a’, the compression factor along x-axis. ‘a’ is the most relevant compression factor in context of this thesis as it allows achieving the low profile. As an example, the compressed space with a compression factor  $a = 2$  is shown in Fig. 3.2.

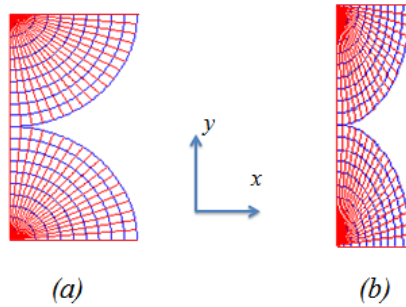


Fig. 3.2 (a) Uncompressed space (b) Axially compressed space.

Essentially, the x-axis has been compressed by 'a' while no compression is applied along y-axis. The dimensions of the physical space are changed such that the new space measures  $d/a$  by  $e$ . The spatial transformation between the physical and virtual spaces can be expressed by following equations:

$$x' = \sqrt{(ax)^2 + (y \mp e)^2} \quad (3.4)$$

$$y' = \frac{e}{\pi} \tan^{-1} \left( \frac{y \mp e}{ax} \right) \quad (3.5)$$

The Jacobian relating the physical and compressed virtual space is given by

$$J = \begin{bmatrix} \frac{a^2 x}{\sqrt{(ax)^2 + (y \mp e)^2}} & \frac{y \mp e}{\sqrt{(ax)^2 + (y \mp e)^2}} & 0 \\ -\frac{ae}{\pi} \frac{(y \mp e)}{(ax)^2 + (y \mp e)^2} & \frac{ae}{\pi} \frac{x}{(ax)^2 + (y \mp e)^2} & 0 \\ 0 & 0 & 1 \end{bmatrix} \quad (3.6)$$

The compression factor 'a' can be used to interpret compression as well as expansion of spaces. When  $a > 1$ , the space is compressed. When  $a < 1$ , the space is considered expanded. An example of expansion is discussed in the next sub section.

### 3.1.2.2 Lateral change

The size of the space may also be changed laterally to control the footprint of the superstrate on the installation surface. Towards this objective, a second factor 'b' accounting for lateral compression factor has been introduced. The new space measures  $d$  by  $e/b$ . As discussed in previous sub-section,  $b < 1$  represents a lateral expansion of space along y-axis.

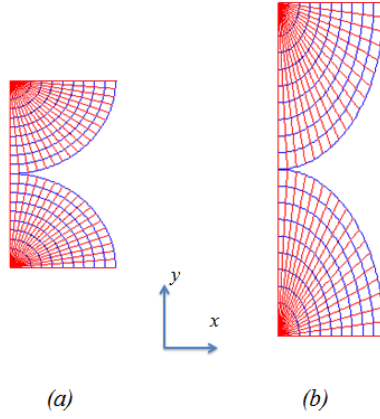


Fig. 3.3 (a) Uncompressed space (b) Laterally expanded space.

As an example, an uncompressed space shown in Fig. 3.3 (a) has been compared to a laterally expanded space along y-axis. The amount of compression applied in the space is governed by ‘ $b$ ’, here  $b = 0.5$ . The laterally expanded space is shown in Fig. 3.3 (b). It is visible that the y-axis has been expanded while dimensions of space along x-axis remains unchanged. The spatial transformation between the physical and virtual spaces can be expressed by following equations:

$$x' = \sqrt{(x)^2 + (b.(y \mp e))^2} \quad (3.7)$$

$$y' = \frac{e}{\pi} \tan^{-1} \left( \frac{b.(y \mp e)}{x} \right) \quad (3.8)$$

The Jacobian relating the physical and compressed virtual space is given by

$$J = \begin{bmatrix} \frac{x}{\sqrt{(x)^2 + (b(y \mp e))^2}} & \frac{b^2(y \mp e)}{\sqrt{(x)^2 + (b(y \mp e))^2}} & 0 \\ -\frac{be}{\pi} \frac{(y \mp e)}{(x)^2 + (b(y \mp e))^2} & \frac{be}{\pi} \frac{x}{(x)^2 + (b(y \mp e))^2} & 0 \\ 0 & 0 & 1 \end{bmatrix} \quad (3.9)$$

When  $b > 1$ , the space is compressed. When  $b < 1$ , the space is considered expanded.

### 3.1.2.3 Radial change

The previous two compression factors acted on the Cartesian space. However, a change in size as viewed from the virtual space may be envisaged also. For example, when a radial expansion factor, ‘ $r$ ’ is applied with  $r = 0.5$ , lesser circles (shown in blue) can be accommodated in a given physical space as shown in Fig. 3.4. For a physical space with fixed dimensions, this factor allows controlling the radial space (number of blue circles) included in the transformation. This factor is an additional degree of freedom for adjusting the transformation.

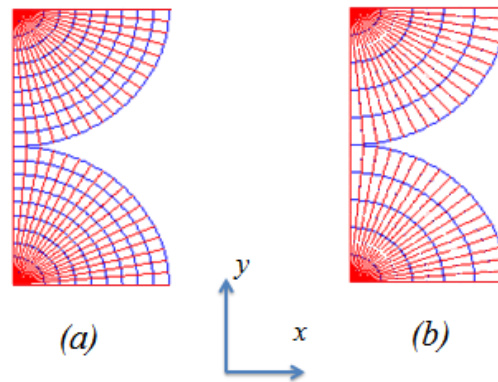


Fig. 3.4 (a) Uncompressed Space, (b) Radially expanded space.

The mathematical expression considering radial compression in spatial transformation is given by following equation. Only the expression for  $x'$  has been modified, as only points lying along by constant radius have been modified.

$$x' = r\sqrt{(x)^2 + (y \mp e)^2} \quad (3.10)$$

The Jacobian for this case is given by:

$$J = \begin{bmatrix} \frac{rx}{\sqrt{(x)^2 + (y \mp e)^2}} & \frac{r(y \mp e)}{\sqrt{(x)^2 + (y \mp e)^2}} & 0 \\ -\frac{e}{\pi (x)^2 + (y \mp e)^2} & \frac{e}{\pi (x)^2 + (y \mp e)^2} & 0 \\ 0 & 0 & 1 \end{bmatrix}$$

(3.11)

### 3.1.2.4 Generalized spatial transformation

A generalized version of the spatial transformation is formulated, where all the size change factors discussed above are accommodated in a single equation system. This allows controlling the transformed space dynamically controlling the space by simply changing  $a$ ,  $b$  and  $r$ . These relations are given in ( 3.12 ) and ( 3.13 ).

$$x' = r\sqrt{(ax)^2 + (b(y \mp e))^2} \quad (3.12)$$

$$y' = \frac{e}{\pi} \tan^{-1} \left( \frac{b(y \mp e)}{ax} \right) \quad (3.13)$$

Jacobian matrix corresponding to above set of spatial transformation is given by ( 3.14 ).

$$J = \begin{bmatrix} \frac{a^2rx}{\sqrt{(ax)^2 + (b(y \mp e))^2}} & \frac{b^2r(y \mp e)}{\sqrt{(ax)^2 + (b(y \mp e))^2}} & 0 \\ -\frac{abe}{\pi} \frac{(y \mp e)}{(ax)^2 + (b(y \mp e))^2} & \frac{abe}{\pi} \frac{x}{(ax)^2 + (b(y \mp e))^2} & 0 \\ 0 & 0 & 1 \end{bmatrix} \quad (3.14)$$

In the next section, the wave propagation in the transformed space is discussed. The Jacobian matrices derived in this section will be used to find the constitutive material parameters corresponding to the spatial transformations.

## 3.2. Wave propagation in the transformed 2D medium

In the previous section, the mathematical transformation to transform Cartesian space into the chosen virtual space for antipodal radiation pattern was discussed. A description of the spatial transformation was provided and then interpretation of the same transformation with various kinds of compressions was given. For each of the above-discussed cases, the Jacobian was also calculated.

As discussed in chapter 2, the material parameters to interpret the spatial transformation can be found by following ( 2.3 ). In this section, the wave propagation will be studied in the

material profiles resulting from the previously described spatial transformations. These studies have been carried out using the COMSOL Multiphysics simulation suite that allows defining tensor material properties, thus allowing complete theoretical analysis of the factors affecting the propagation.

In this section, the wave propagation will be first studied in an uncompressed space. The refractive index based interpretation and feasibility of a dielectric only solution will be studied. A shift factor ‘ $m$ ’ to shift the effective refractive index of the profile will also be introduced. Next, the wave propagation will be discussed in compressed and expanded spaces. A combination of compression and shift factors has been used to arrive at a preliminary solution for an antipodal superstrate. Finally, a study of the discretized profile containing finite number of permittivity values is presented.

### 3.2.1. Design rules and COMSOL design definition

#### 3.2.1.1 Design rules

We start by explicitly stating two design rules that have been followed in the following sub-sections. As seen in many cited references in chapter 2, the standard practice in designing T.O. solutions is to reduce material tensor dependence by:

- *Restricting the design in two dimensions:* This has already been done in section 3.1 by defining the transformation relations in 2D  $x$ - $y$  plane. As the design is considered invariant along  $z$ -axis, elements in tensor varying with respect to  $z$  except in diagonal are 0, as seen in ( 3.3 ). This allows eliminating dependence on  $\epsilon_{xz}$ ,  $\epsilon_{yz}$ ,  $\epsilon_{zx}$ ,  $\epsilon_{zy}$ ,  $\mu_{xz}$ ,  $\mu_{yz}$ ,  $\mu_{zx}$  and  $\mu_{zy}$ .
- *Using polarization along particular axis of coordinate system:* This allows the design to be dependent only on a reduced set of tensor elements. For example, if the electric field of an electromagnetic wave propagating inside a transformed  $x$ - $y$  plane is polarized along  $z$ -axis, then wave propagation will only be dependent on  $\mu_{xx}$ ,  $\mu_{xy}$ ,  $\mu_{yx}$ ,  $\mu_{yy}$  and  $\epsilon_{zz}$ .

Indeed, in the following sub-sections, an ideal current sheet representing a patch antenna is considered with a polarization along  $z$ -axis.

#### 3.2.1.2 COMSOL simulation setup

It is desired to simulate the wave propagation behavior inside an electromagnetically transformed region. The electromagnetic transformation of this region is governed by the coordinate transformation presented in the previous section. As also stated in the previous sub-section, the problem is formulated in reduced complexity by obeying the design rules set in the previous sub-section. COMSOL Multiphysics™ is a simulate software package that

among other features, allows the user to define the anisotropy of a material and selecting polarization of the source. The software suits well the simulation requirement of the present study. More details on the software are provided in Appendix A. Material properties obtained from T.O. have been assigned to the regions representing the transformed physical space. The antenna and transformed space are defined in vacuum as the background medium. Scattering boundary conditions are placed on the boundary of the calculation, which is defined by a circle. The radius of this circle is fixed at a value greater than Fraunhofer distance ( $2D^2/\lambda$ , where  $D$  is the largest dimension in the design). This allows the boundary condition lies to lie in the far field region of the superstrate device. This arrangement has been shown in a representative image in Fig. 3.5. The simulations are carried out at the design frequency,  $f = 1.25$  GHz in lower L-band, where the target applications also operate.

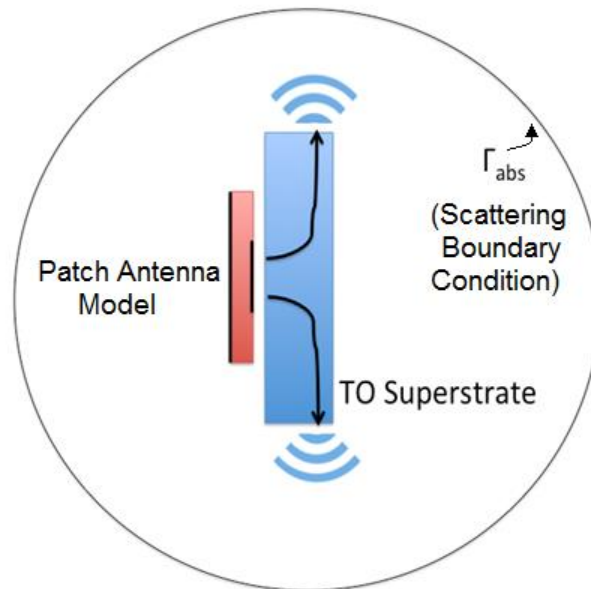


Fig. 3.5 Representative diagram showing solution setup in COMSOL.

### 3.2.1.3 Patch antenna model

A directive radiation along  $x$ -axis is usually simulated using a plane wave excitation along  $x$ -axis. But it is not an accurate representation of the radiation from patch antenna, as required in the current problem. The broadside directive radiation pattern like that of a patch antenna is best approximated using a current sheet backed with a PEC sheet, which acts as the ground plane. This is shown in Fig. 3.6, where the current sheet has been highlighted in blue. Also, the transformed space is represented by the two squares whose dimensions have been chosen earlier in Section 3.1.1

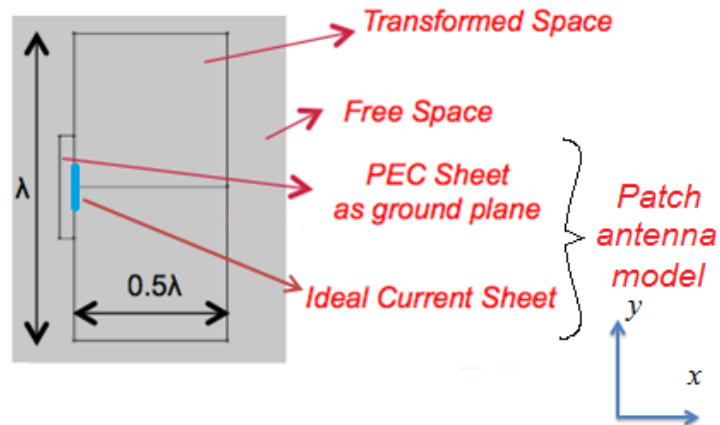


Fig. 3.6 A representative image of the patch antenna model and region of spatial transformation.

In Fig. 3.7, instantaneous electric field  $E_z$  (normalized to maximum values in the plot) has been plotted in the circular domain in absence of superstrate. It is representative of the broadside radiation pattern as shown by a classic patch antenna. Next, wave propagation in uncompressed space has been studied.

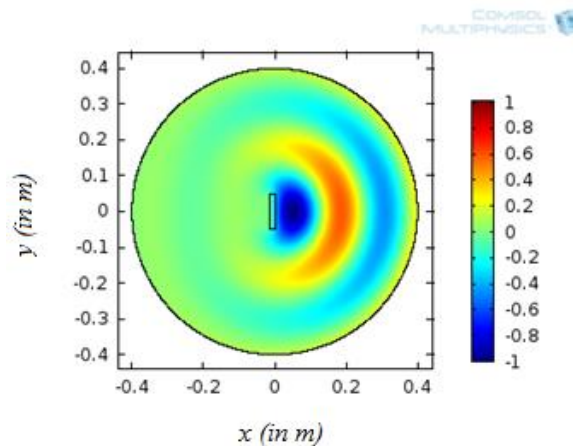


Fig. 3.7 Wave propagation in untransformed space,  $E_z$  (normalized to maximum value.)

### 3.2.2. Wave propagation in uncompressed transformed space

In this section, the wave propagation has been studied in a transformed space so as to obtain radiation in azimuthal plane from an untransformed space. The physical and virtual spaces earlier defined in 3.1.1 have been considered i.e.  $a = b = 1$ . The physical space has dimensions of  $2d$  by  $e$ , where  $d = e = 0.5\lambda$ ,  $\lambda$  corresponding wavelength at  $f$ . Using ( 3.3 ) and ( 2.3 ), the material parameter anisotropy can be defined by following tensor, as given in ( 3.15 ). It should be noted here that the expression of elements in permittivity and permeability tensors issued from TO method are independent of  $y'$  defined in ( 3.2 ).

$$\boldsymbol{\varepsilon} = \boldsymbol{\mu} = \begin{bmatrix} \frac{\pi x'}{e} & 0 & 0 \\ 0 & \frac{e}{\pi x'} & 0 \\ 0 & 0 & \frac{\pi x'}{e} \end{bmatrix}$$

(3.15)

Respecting the design conditions previously stated in 3.1.2.1, the dependence could be reduced to 3 elements in the tensor given in (3.16).

$$\mu_{xx} = \frac{\pi x'}{e}; \mu_{yy} = \frac{e}{\pi x'}; \varepsilon_{zz} = \frac{\pi x'}{e}$$

(3.16)

In Fig. 3.8 the spatial variation in permittivity and permeability tensors have been plotted in the transformed region.

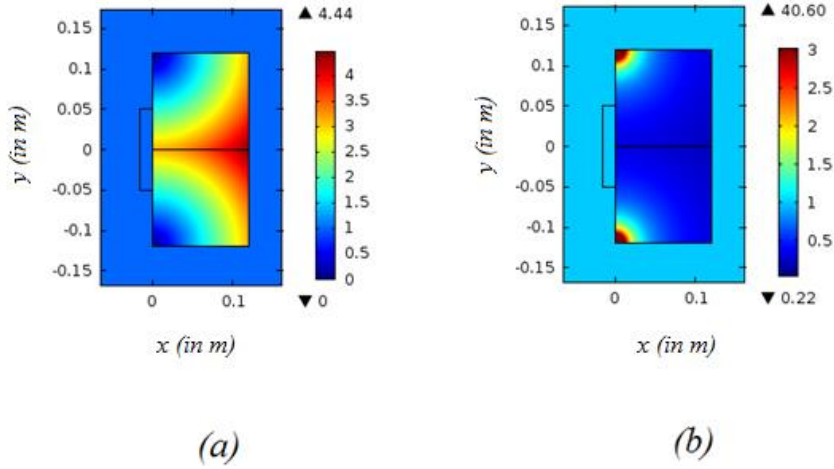


Fig. 3.8 Constitutive parameter profile in a transformed uncompressed space (a)  $\varepsilon_{zz}$ ,  $\mu_{xx}$ ; (b)  $\mu_{yy}$ .

It is clearly seen in the figure above that material parameters vary along the circular locus with centers at the top and bottom corners. The material parameters vary in following range:  $0 < \varepsilon_{zz}, \mu_{xx} < 4.4$ ;  $0.22 < \mu_{yy} < 40$ . Indeed, the spatial transformations result in some extreme material parameters inside the profile ( $\varepsilon_{zz}, \mu_{xx}, \mu_{yy} < 1$ ,  $10 < \mu_{yy}$ ). Interpreting such a profile would require resonant metamaterials. It may also be observed here that the expression in material tensor are independent of  $y'$ . The normalized  $E_z$  plot is shown in Fig. 3.9.

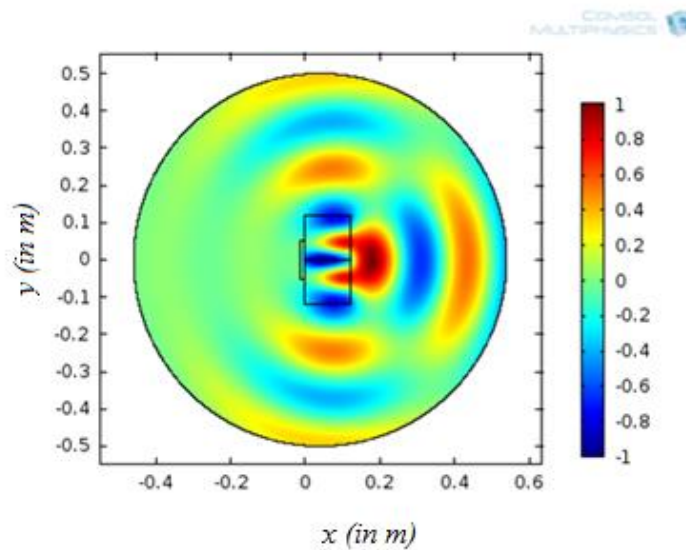


Fig. 3.9 Wave propagation in uncompressed space,  $E_z$  (normalized to maximum value.)

When the problem is simulated with this material distribution, the electric field is found to be reoriented in the azimuthal plane of the device (along  $y$  axis). However, there is also a strong field presence along  $x$ -axis. This leads to the question why the transformation isn't completely carrying out its mathematically defined function. It is possible to speculate the cause of this anomalous behavior. Firstly, the use of Cartesian space as the physical medium in the coordinate transformation implies that a plane wave is incident on the transformed space. However, the source used to illuminate the device is not perfectly directive. This deviation from the coordinate transformation recorded in the Jacobian used to transform this space may result in the anomalous propagation behavior. Secondly, it may also be due to inadequate size of the transformed space. Optically transforming a thicker profile may lead to perfect reorientation with a minimum in the axis. However, this has not been investigated further in this thesis, as the primary objective of this thesis is to design low profile superstrates. It may be noted here that the optically transformed profile does not generate  $E_x$ ,  $E_y$  or  $H_z$  components of electric and magnetic fields.

The shape of wave fronts exiting from transformed space may be controlled by different techniques. One such technique is discussed in the next section.

### 3.2.3. $n$ -based interpretation and Shift factor ' $m$ '

In the previous subsection, ( 3.16 ) governs the variation in the permittivity and permeability values in the transformed profile. These values can be used to define the variation of effective refractive index,  $n_{eff}$  in the modified space. In ( 3.17 ),  $n_{eff}$  has been interpreted using the permittivity and permeability elements found earlier in ( 3.16 ) and a new factor ' $m$ ' has also been introduced that will be used to shift the refractive index profile.

$$n_{eff}^2 = m \frac{\sqrt{\epsilon_{zz}\mu_{xx}}\sqrt{\epsilon_{zz}\mu_{yy}}}{\epsilon_0\mu_0} \quad (3.17)$$

On multiplication by  $m$ , only the value of refractive indices in the profile is changed but the new  $n_{eff}$  continues to vary along the previously defined loci. This factor can be used to eliminate extremely high or low values of material parameters. Consider a hypothetical: an arbitrary optical transformation results the profile with certain values of  $\epsilon_{zz}$  between 0.5 and 1; which would require using in fabrication. However, by implementing a scalar multiplication of  $m = 2$ , the  $\epsilon_{zz} < 1$  can be removed without changing the distribution, which is governed by the coordinate transformation relations. Indeed, the scalar multiplication by  $m$  has an effect on the wave propagation behavior, but this can be used to our advantage, as will be in shown later section. In the simulation, this can be achieved by including  $m$  in the expression of  $\epsilon_{zz}$ , as seen in ( 3.18).

$$\mu_{xx} = \frac{\pi x'}{e}; \mu_{yy} = \frac{e}{\pi x'}; \epsilon_{zz} = \frac{m\pi x'}{e} \quad (3.18)$$

For  $m = 0.5$ , reoriented electric field is shown in Fig. 3.10. The new profile generates a quasi-hemispherical wave front. Thus, the shift factor  $m$  provides an extra degree of freedom over the transformation.

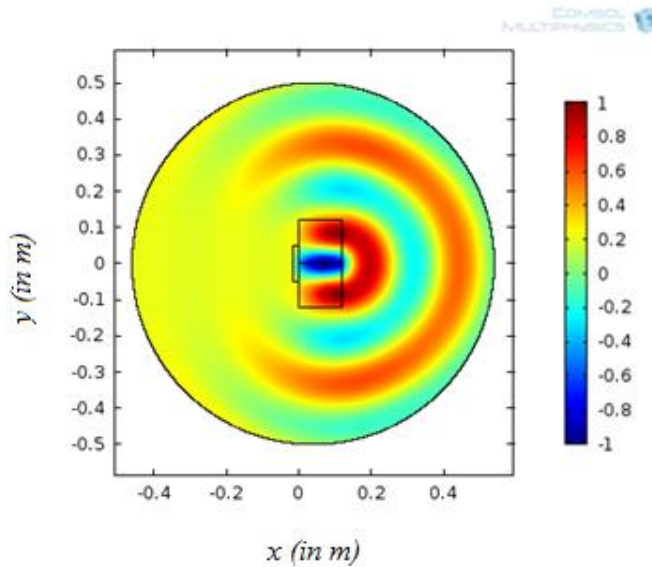


Fig. 3.10 Wave propagation in uncompressed space, refractive index changed by a factor  $m = 0.5$ ,  $E_z$  (normalized to maximum value.)

### 3.2.4. A dielectric profile

Taking further the case presented in the previous sub-section, here we discuss the possibility of a dielectric only solution. As presented in [72], if the permeability components are reciprocal expressions, then they effectively cancel each other in ( 3.17 ). Indeed,  $\mu_{xx}$  and  $\mu_{yy}$  are reciprocal values, as in ( 3.16 ). This implies that the calculations may also be done by assuming  $\mu_{xx} = \mu_{yy} = 1$ . This allows reducing the dependence only on one element in the tensor,  $\epsilon_{zz}$ . Therefore, the expression for the effective refractive index can be rewritten as follows.

$$n_{eff}^2 = m \cdot \frac{\epsilon_{zz}}{\epsilon_0} \quad (3.19)$$

This simplification step in the design process allows us to effectively forego all the permeability values in the design, thereby leading us one step closer to an isotropic dielectric solution. The value of  $\epsilon_{zz}$  for the generalized transformation relation can be calculated using Jacobian matrix defined in ( 3.14 ). The new expression for  $\epsilon_{zz}$  is presented in ( 3.20 ), where  $x'$  is given by ( 3.12 ).

$$\epsilon_{zz} = \frac{m\pi x'}{abre} \quad (3.20)$$

It should be noted here that the compression along x-axis, y-axis or radius leads to a rarefaction of the material tensor along the z-axis. This is evidenced by the presence of the product ' $abr$ ' in the denominator of ( 3.20 ). However, ' $r$ ' does not play any role as it gets cancelled in the expression of  $x'$  in ( 3.12 ). The previously defined shift factor  $m$  comes in handy to implement the radial change on the material profile as it acts on all constant  $x'$ . In the next subsections, only dielectric profiles with  $\epsilon_{zz}$  of ( 3.20 ) will be discussed. Examples of compressed and expanded profiles will be presented.

### 3.2.5. Wave propagation in compressed/expanded spaces

As seen in the previous sections, the uncompressed space is capable of at least partially reorienting the electric field in the azimuthal plane, and that the exiting wave front can be modified by using a shift factor on the effective refractive index of the material profile. In this section, we shall discuss the use of compression/expansion to exert a further degree of control. Both compression and expansion are discussed in two different examples.

### 3.2.5.1 Wave propagation in compressed profile

In this study, we discuss a compressed version of the optically transformed profile of previous sections. As said previously in sub-section 3.1.2.1, compression is important operation in the desired application for designing a low thickness superstrate. But it can also be used to reduce the lateral footprint of the profile. In this section, an axially and laterally compressed space has been presented as an example.

Following compression factors are chosen to design the profile: axial compression,  $a = 4.16$  and lateral compression,  $b = 1.6$ . These correspond to a  $0.625\lambda$  by  $0.12\lambda$  profile. Thus, the thickness of the superstrate at  $f$  is 28.8 mm. Effectively, the profile can be controlled using the interplay of the compression and shift factors:  $a$ ,  $b$  and  $m$ .

In the present scenario, the shift factor  $m$  has been optimized by running parametric simulation in COMSOL for a field maximum along y-axis, such that  $m = 14$ . This leads to the following variation of the relative permittivity inside the transformed space:  $0 < \epsilon_{zz} < 14.8$ . It also helps reducing the spatial presence of  $\epsilon_{zz} < 1$  to very small regions in the upper and lower corners of the material profile, and these values can be effectively ignored in eventual discretization discussed later in this chapter. This is shown in Fig. 3.11.

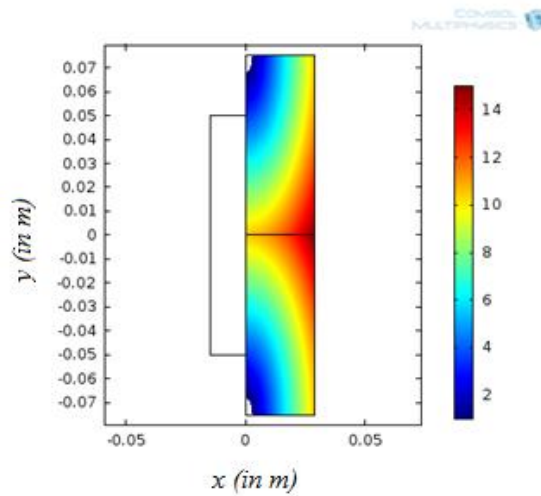


Fig. 3.11 Constitutive Parameter Profile plotted in  $1 < \epsilon_{zz} < 14.8$ ;  $\epsilon_{zz} < 1$  values in the corners outside the plotting range.

The reoriented electric field is shown in Fig. 3.12. Compared to Fig. 3.9, it is clear that the electric field  $E_z$  has been completely reoriented along the y-axis. This is also shown in Fig. 3.13, where the time averaged power flow through the scattering boundary has been plotted.

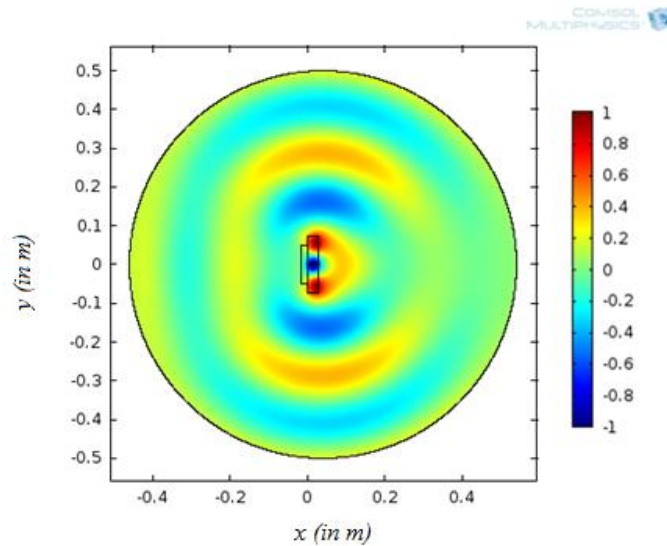


Fig. 3.12 Wave propagation in compressed space:  $a = 4.16$ ,  $b = 1.6$ ; shift factor  $m = 14$ ,  $E_z$  (normalized to maximum value).

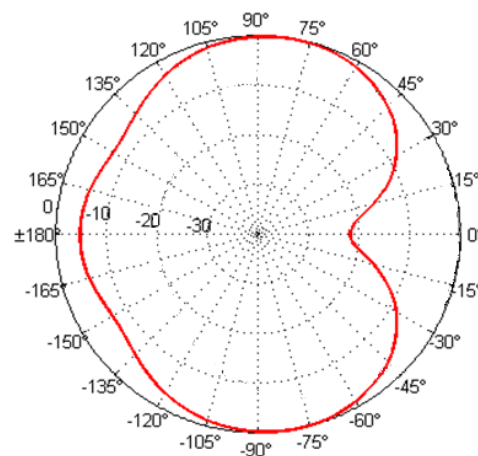


Fig. 3.13 Time averaged power flow (in dB) in  $x y$  plane at the scattering boundary.

### 3.2.5.2 Wave propagation in expanded profile

An expansion of the profile may also be envisaged to cater a different application. The profile presented in the previous subsection has been laterally expanded. When compression factors employed in ( 3.12 ) are assigned a value between 0 and 1, it leads to an expansion of the profile. The procedure defined in the previous sections is robust enough to adapt to change in the compressions. This has been demonstrated by the study case presented in this section.

In this study, compression factors have been chosen to result in a profile  $1.34\lambda$  by  $0.12\lambda$ . This corresponds to an axial compression,  $a = 4.16$  and a lateral expansion,  $b = 0.745$ . Again, no radial compression has been used i.e.  $r = 1$ . The shift factor has been optimized for a field

maximum along y-axis such that  $m = 14$ . The resulting profile is shown in Fig. 3.14. The variation in relative permittivity inside the transformed space is  $0 < \epsilon_{zz} < 8.88$ . However,  $\epsilon_{zz} < 1$  in the top and bottom left corner of the transformed profile are not plotted.

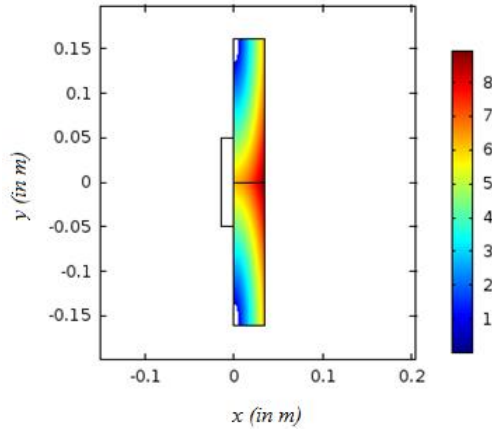


Fig. 3.14 Constitutive Parameter Profile;  $1 < \epsilon_{zz} < 8.8$ ,  $\epsilon_{zz} < 1$  values in the corners not in plotting range.

The reoriented electric field is shown in Fig. 3.15. The electric field  $E_z$  has been reoriented along the y-axis, however propagation along x-axis is observed. The reasons for this were speculated prior in 3.2.2.

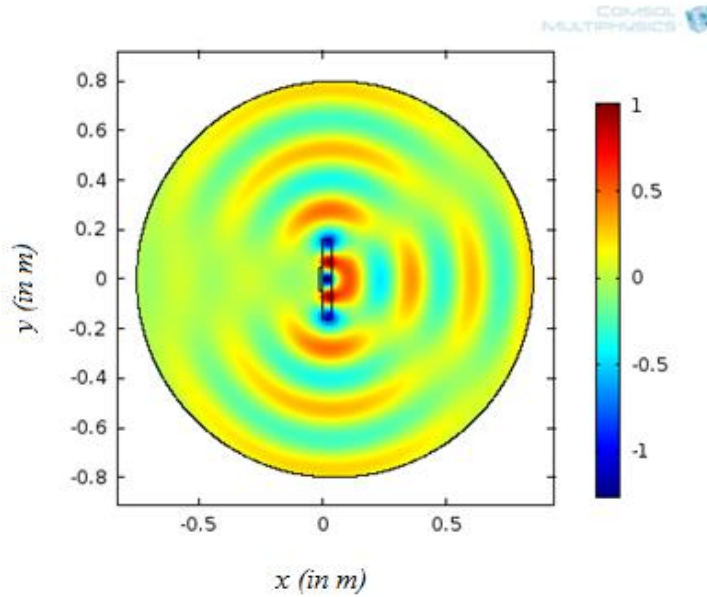


Fig. 3.15 Wave propagation in axially compressed and laterally expanded space:  $a = 4.16$ ,  $b = 0.745$ ,  $r = 1$ ; shift factor  $m = 7$ ,  $E_z$  (normalized to maximum value)

### 3.2.5.3 Remarks on designing compressed/expanded TO-designs

All the above case studies bring us to conclusion that the defined relations allow us to exert control over the exiting wave front from the superstrate using different degrees of

freedom like compression and shift factors. The main contribution has been the identification of underlying design rules. By following these design rules, arbitrary compression factors can be used while retaining a control over the transformation. Also, in 3.2.5.1 a laterally compact and thin profile was identified for complete reorientation of electric field in the azimuthal plane of an electromagnetic source. The performance of this profile corresponds to the specifications of the desired superstrate. This profile will be used in the coming sections to study the feasibility of such a device in practical conditions. In the next section, we shall define the procedure to study the full wave solutions with a real antenna and a superstrate with finite size along z-axis.

### 3.3 Full wave solutions with discretized profile

In the previous section, an approach was identified to conceptually define superstrates capable of reorienting the propagating electromagnetic waves in the azimuthal plane. While some steps were introduced in order to simplify the underlying physics, these solutions in themselves are still based on coordinate transformation. The transformation allows achieving the smooth gradient in permittivity profiles identified at the end of section 3.2. However an implementation of a real life superstrate cannot be based on a continuously varying permittivity profile, as achieving the gradient is impractical. Thus, a new study needs to be initiated to separately study the 3D implementation of the profile deduced above. The problem is significantly different when studied in three dimensions, as a variety of factors need to be accounted for, e.g. matching T.O. device to antenna, pixilation of profile, etc.

In this section, a 3D superstrate device based on the profile of sub-section 3.2.5.1 is presented. Moreover, this section introduces the step-by-step procedure adopted to correctly simulate the performance of 3D superstrates obeying the same spatial transformation relations. First the design of a square patch antenna used to excite the superstrate is described in 3.3.1. Then the discretization of the profile is discussed in 3.3.2. The discretized profile is then used to design a cuboidal superstrate. The superstrate-antenna combination is studied in 3.3.3. The use of impedance matching layer is also described in this sub-section. The procedure prescribed in these sections can be employed to study other superstrate devices presented in Chapter 5.

CST Microwave Studio Suite has been used to carry out full wave solutions. More details on use of CST Microwave Studio are provided in Appendix A. In this thesis, the transient solver is used for simulations. The transient solver is fast and takes less memory compared to frequency domain solver. The superstrate and the antenna do not have curved geometries (apart from coaxial feed) and a rectangular mesh with appropriate step size can provide accurate results. Special attention has been given to meshing; at least three mesh cells have

been applied in all layers. In the next sub-section the antenna used in this sub-section is described.

### 3.3.1 Square patch antenna

It may be recalled here that in section 3.2, the patch antenna was modeled using an ideal current sheet with electric field polarized along  $z$ -axis. In practice, a linearly polarized square patch antenna is considered. Unlike the current sheet used in COMSOL, a non-ideal source like the patch antenna requires taking couple of factors into consideration: The antenna needs to operate at the design frequency and the feeding system of the antenna should not affect the performance of the superstrate.

The square patch antenna used in shown in Fig. 3.16. The first step is to design an antenna operating at design frequency chosen in the previous section,  $f = 1.25$  GHz. The side of the square patch is 68 mm. A 0.035 mm thick copper layer is used to simulate copper thickness. The antenna substrate is 13 mm thick and has a relative dielectric constant of  $\epsilon_r = 2.5$ . The patch antenna is backed by a square ground plane of side 100 mm.

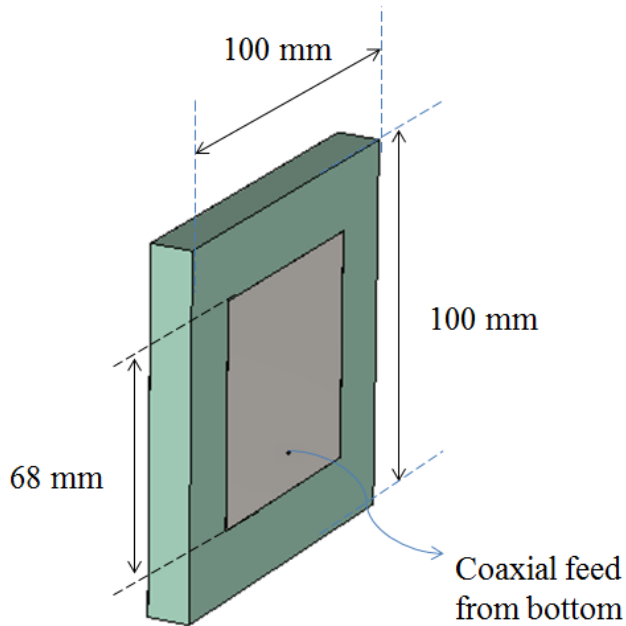


Fig. 3.16 Square patch antenna resonating at  $f$ ; used as source for conceptual demonstrations

The antenna has been fed using a coaxial feed. The choice of a coaxial feed is a precautionary and is motivated by the fact that a microstrip feed system may interact with the superstrate and eventually produce anomalous behavior due to undesired parasitic couplings. Simulations are carried out using transient solver in CST Microwave Studio. A waveguide port has been used to introduce input excitation signal in the design. The antenna presents a

broadside far-field radiation pattern typical of a patch antenna device, as shown in Fig. 3.17. The peak realized gain is 6.7 dB. This antenna shall be considered throughout this study.

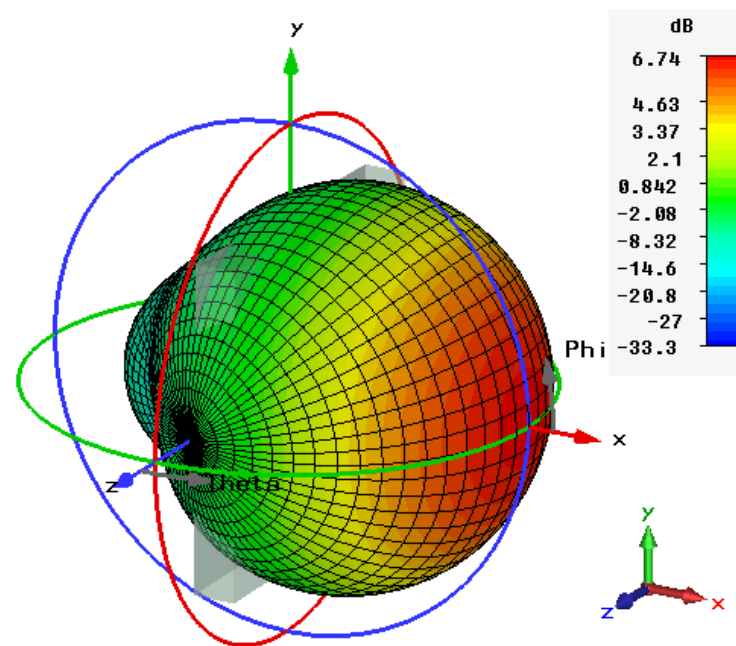


Fig. 3.17 Far field radiation pattern of antenna at  $f$ ; Realized Gain (in dB);  $G_{\max} = 6.7$  dB

### 3.3.2 Designing isotropic profile with finite permittivity values

The antenna acting as a source of electromagnetic waves has been defined in the previous section. In this sub-section, discretization of the continuous profile presented in 3.2.5.1 is addressed. The material parameters of transformed space described in 3.2 vary continuously according to a mathematical relation describing the spatial transformation. A continuous gradient cannot be achieved in practice. Therefore, the continuous 2D profile needs to be replaced by a discretized profile into finite dielectric pixels and finite size along the third dimension ( $z$ -axis). From a design standpoint, the discretization is also necessary because the continuous gradient in permittivity cannot be designed in CST Microwave Studio 2013, which has been used for calculating the full-wave solutions. Moreover this is essential from a practical standpoint as well, because it is extremely difficult to achieve the continuous variation in permittivity in fabrication. The discretization of the continuous profile allows approaching the practically achievable solution. In this section, the behavior of the transformed profile comprised of finite isotropic dielectric pixels is simulated in a two dimensional configuration.

### 3.3.2.1 From anisotropic to isotropic solution

The continuously varying permittivity in the material profile obtained from ( 3.20 ) can be discretized in to finite number of pixels. However before discretizing in to finite pixels, following simplifications are applied on the continuous profile:

- Dispersive values of permittivity in the profile, ( $\epsilon_{zz} < 1$ ) values are ignored due to low spatial presence in the profile and have been replaced by  $\epsilon_{zz} = 1$ .
- The values corresponding to  $\epsilon_{zz}$  calculated in ( 3.20 ) is a considered isotropic in a new  $\epsilon_r$  profile, such that permittivity variation in transformed profile is  $1 < \epsilon_r < 14$ .

This new profile obtained as a result of above-stated simplifications performs exactly as the profile presented in 3.2.5.1, because the TE polarized wave at input still only interacts with  $\epsilon_{zz}$  in the material tensor. Therefore, fabrication using standard dielectrics can be easily envisaged. The variation in relative permittivity inside the transformed space is  $1 < \epsilon_r < 14.8$ .

### 3.3.2.2 Discretizing a continuous profile in sub-wavelength sized pixels

As discussed in chapter 2, gradient in permittivity in TO-solutions is typically interpreted by designing effective permittivity media. The effective permittivity is extracted using the fill factor i.e. volume fraction of air in the dielectric host medium. Effective permittivity can be controlled by changing density of holes in the dielectric host medium, or radius of holes. The former approach has been implemented in a previous work presented by our group [2], wherein a dielectric superstrate to increase HPBW of patch antenna has been fabricated using 3D printing. The permittivity gradient has been achieved by varying the density of constant diameter holes in the host dielectric material; the diameter of holes is 3.34 mm ( $0.013\lambda$  at 1.2 GHz).

Alternatively, the gradient in effective medium can also be achieved by designing medium containing holes with variable diameters. In such a scenario, the continuous profile can be discretized into pixels of identical sizes. Thus, effective permittivity of complete medium can be simply controlled by adjusting volume fraction of individual pixel. This strategy is considered in this thesis and is explained in the next chapter. But first, a pixelated profile representing the permittivity gradient in effective medium needs to be calculated.

The continuous profile is discretized in 192 pixels, arranged in 6 layers of 32 pixels each. All the pixels have same sizes i.e. 4.8 mm x 4.68 mm ( $\sim 0.02\lambda$  at 1.25 GHz). The permittivity of pixels is spatially sampled from the continuous profile. The resulting discretized profile is

shown in Fig. 3.18. The variation in permittivity inside the profile is limited between 1 and 14.8. The normalized electric field is shown in Fig. 3.19.

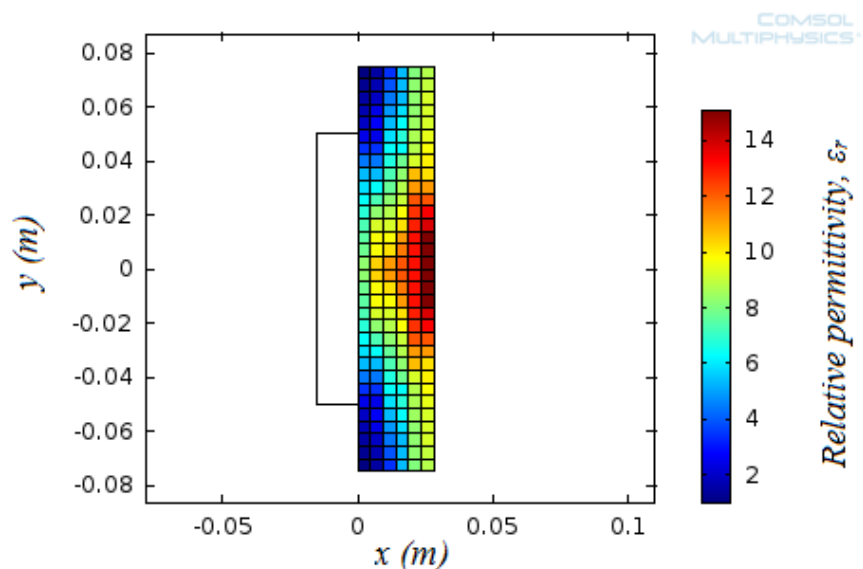


Fig. 3.18 Profile discretized in 192 pixels (6 layer with 32 pixels each.)

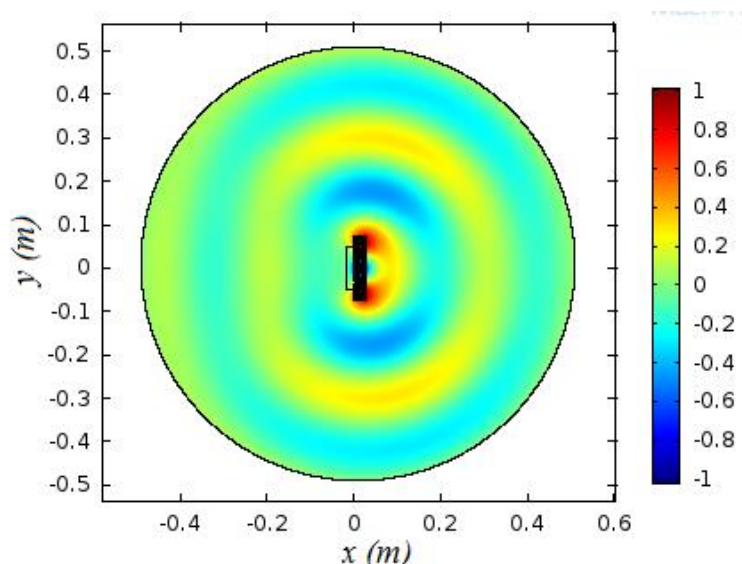


Fig. 3.19 Normalized electric field in a discretized profile with 192 pixels.

The electric field is found to be completely reoriented along  $y$ -axis in this discretized profile. This shows that the transformation can be effectively interpreted using finite number of pixels. This profile can be used to design the effective medium. However, the size of pixel may be an issue. In [2], the permittivity variation in the dielectric superstrate was between 1 and 2.9, thus the gradient in the profile can be achieved with subtle variation in hole density. However, the permittivity varies across a wide range in the current solution, i.e. between 1 and 15. An air-hole based dielectric medium to interpret such a wide variation would require larger pixel sizes. This is explained in detail in next chapter during the discussion on the two material fabrication. Therefore, a profile with larger pixels (coarser discretization) is

considered. In the new profile, the area of each pixel is quadrupled, which will allow designing holes with larger diameters. As a result of increased pixel size, number of pixels is reduced. The new discretized profile contains 48 pixels (3 layers of 16 pixels each.) Dimension of each pixel is 9.6 mm x 9.37 mm. In terms of wavelength, the size of pixels is  $0.04\lambda$  by  $0.04\lambda$ . This profile is shown in Fig. 3.20. The normalized electric field is shown in Fig. 3.21.

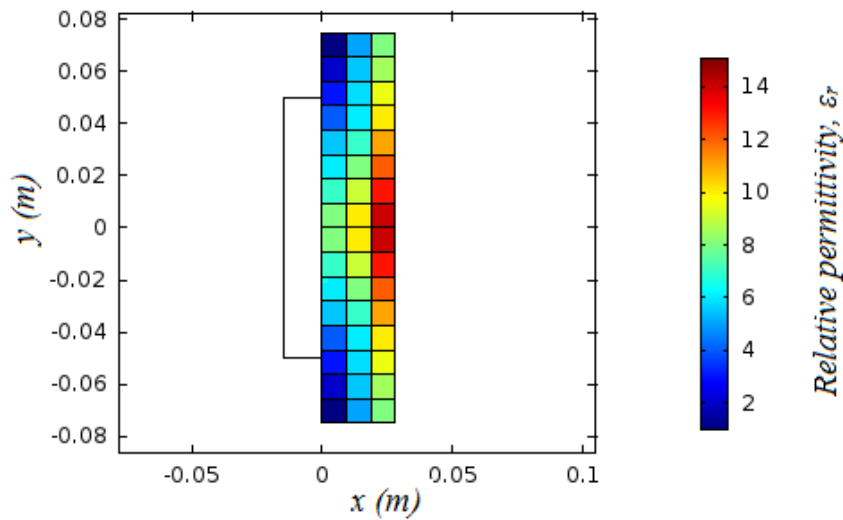


Fig. 3.20 Profile discretized in 48 pixels (3 layer with 16 pixels each.)

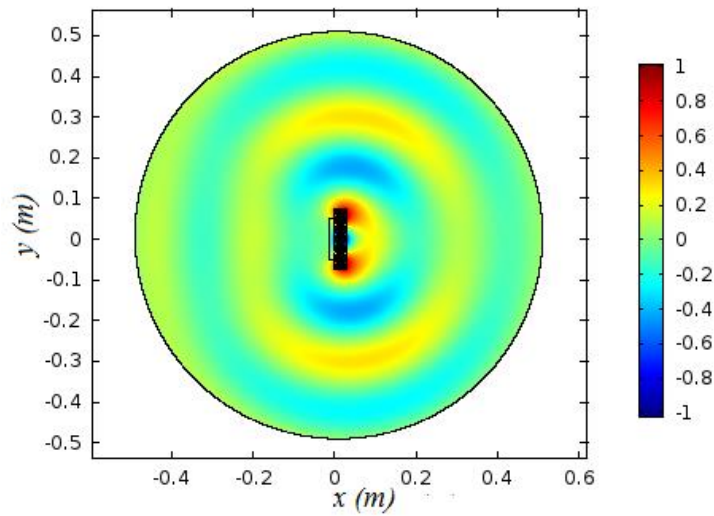


Fig. 3.21 Normalized electric field in discretized profile with 48 pixels.

It is observed that this new profile also completely reorients the electric field along y-axis. Complete reorientation has now been achieved in continuous profile, discretized profile with 192 pixels, and discretized profile with 48 pixels. Without grossly generalizing, it may be concluded from observations above that that the transformation is not very sensitive to the number of pixels of profile. Further studies may be carried out to determine the coarsest discretization, beyond which the transformation cannot be faithfully interpreted. This idea is

developed further in the next chapter. It may be noted here that the values of permittivity in the discretized profile have been spatially sampled from the continuous profile and are representative of the average value in that pixel. Indeed, these values may be tuned in an optimization problem for specific design goals. But this is out of the ambit of present discussion.

### 3.3.2.3 Designing a three-dimensional superstrate

The discretized profile with 48 pixels is chosen to design a three dimensional superstrate. The final profile is shown in Fig. 3.22. Next, full-wave solutions are calculated in CST Microwave Studio. There are two different methods to design a 3D device from the discretized profile:

- Revolved along  $x$ -axis for a cylindrical superstrate, or
- Extrude along  $z$ -axis for a cuboidal superstrate.

Both operations allow conserving isotropic nature of the optical transformation. The first approach was used previously in [110], where a cylindrical superstrate was simulated in conjunction with a dual polarized patch antenna. The behavior of the device was presented in both linear and circular polarizations. This can also be done in the present study. However, due to practical reasons (explained in the next chapter), the profile is extruded along  $z$ -axis. The resulting superstrate is shown in Fig. 3.23. The size of the superstrate in terms of wavelength is  $0.625\lambda$  by  $0.625\lambda$  by  $0.12\lambda$ . A cylindrical profile is also discussed in the Appendix B.

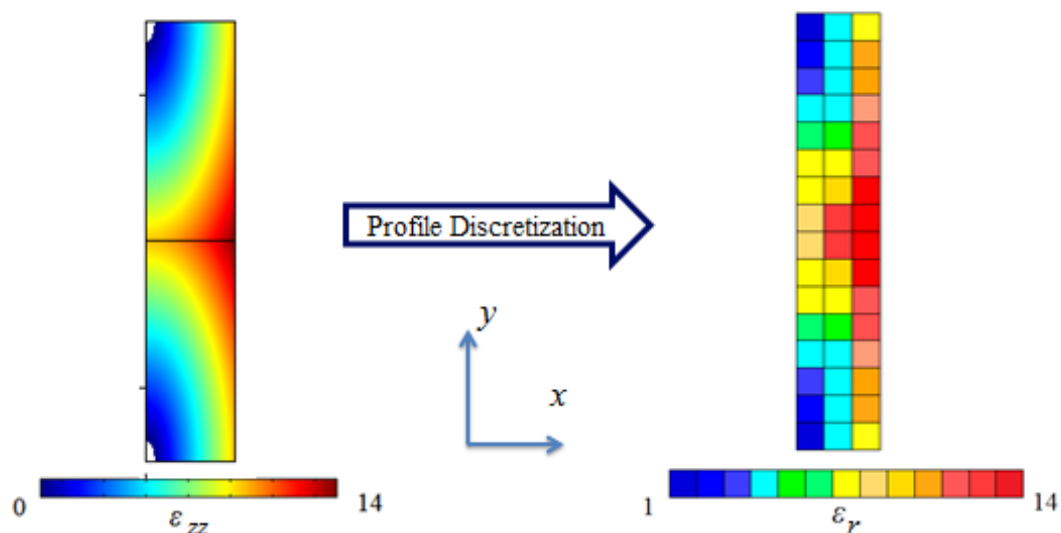


Fig. 3.22 Passage from a continuous anisotropic dielectric profile to a discretized isotropic dielectric profile with finite pixels (16x3)

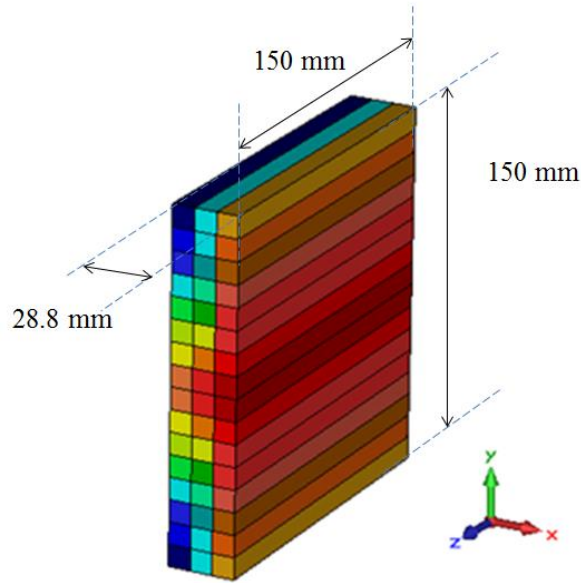


Fig. 3.23 3D superstrate obtained by extruding the discretized profile along z-axis

### 3.3.3 Antenna with the T.O. superstrate

In the previous two sub-sections, the design of antenna and superstrate has been described. In this section, the combination of the two is presented. The objective is to achieve an antipodal radiation pattern from a typical patch antenna by using the T.O. inspired superstrate by the end of this sub-section. However, this is a complex problem.

In this section, a thorough study is presented that investigates the practical issues arising during the fabrication of the superstrate. In the first step, we shall present the antenna coupled with the superstrate. Then, use of a dielectric layer is discussed to shift the resonant frequency of the final antenna superstrate assembly at the design frequency,  $f$ .

#### 3.3.3.1 Antenna with superstrate

In the previous sections, antenna and superstrate used in the design were designed separately. Based on inferences drawn from section 3.2, it is expected that on placing the superstrate over the patch antenna, the electric field emanating from the patch would be guided to the azimuthal plane and it will result in an antipodal radiation pattern in the far field at the design frequency. This configuration is simulated with CST Microwave Studio. In this first simulation, the antenna superstrate assembly does not function. Upon investigation, it is found that the antenna does not succeed in coupling enough power into the superstrate. Consequently, almost all the power at the input is reflected back in the port. It can be said that the rapidly changing impedance at the antenna-superstrate interface due to sharply changing values of  $\epsilon_r$  may be underlying cause of this problem. To overcome this problem, an air layer is introduced between the antenna and the superstrate, as shown in Fig. 3.24

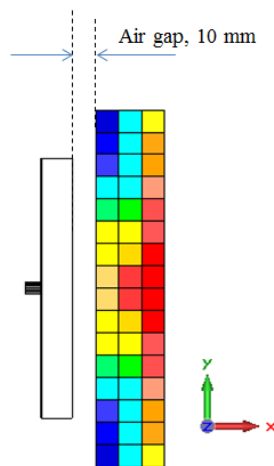


Fig. 3.24 Antenna superstrate assembly with an air gap.

The thickness of this air layer is 10 mm, which translates to  $0.04\lambda$  in terms of wavelength at 1.25 GHz. In Fig. 3.25, the magnitude of reflection coefficient is plotted for antenna alone, antenna-superstrate assembly with no gap and antenna superstrate with an additional gap of 10 mm thickness. The reference impedance in the simulation is  $50 \Omega$ .

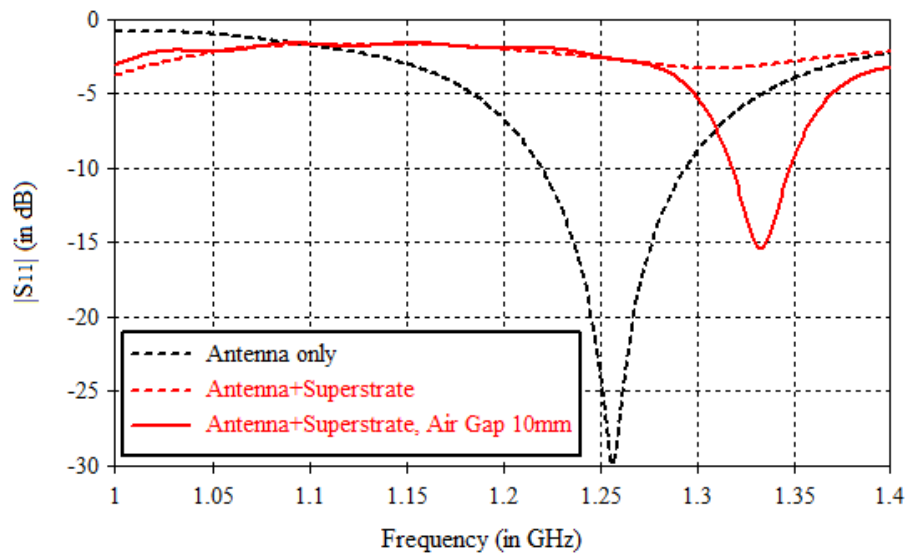


Fig. 3.25 Magnitude of reflection coefficient for antenna only, antenna-superstrate without gap, antenna+superstrate with an additional air gap of 10mm.

The antenna without superstrate resonates at the design frequency,  $f = 1.25$  GHz, as seen in black dashed line. The impedance bandwidth ( $|S_{11}| < -10$  dB) is 6.4% at  $f$ . The inability of antenna to couple power in the superstrate without the air layer is also seen in the red dashed line in the plot. The assembly does not have resonant frequency and magnitude of reflection coefficient is approximately -3 dB in the 1.1-1.4 GHz band. By introducing the air

layer between antenna and superstrate, the new design is matched at  $f' = 1.33$  GHz, as shown in red solid line in Fig. 3.25. The impedance bandwidth ( $|S_{11}| < -10$  dB) is 2.2% at  $f'$ . Thus, it is necessary to introduce a slight gap between the antenna and superstrate for matching the antenna to the superstrate. Next, the realized gain of the antenna has been plotted in Fig. 3.26.

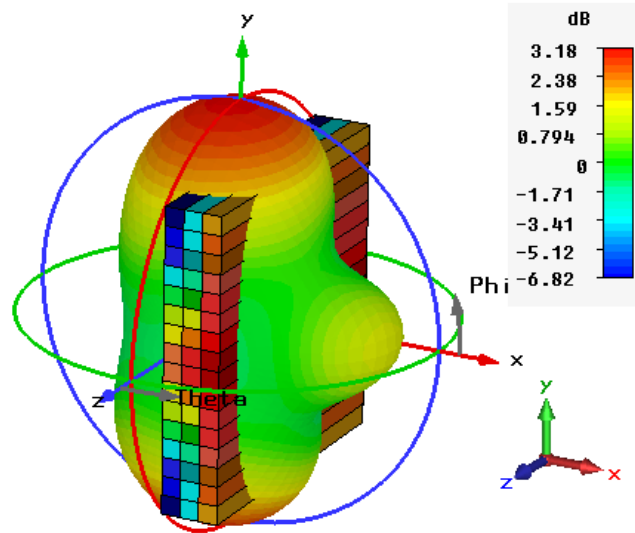


Fig. 3.26 Realized Gain of antenna-superstrate at  $f' = 1.33$  GHz (in dB); 10 mm air layer between antenna and superstrate.

The peak realized gain is approximately 3.2 dB in the azimuthal plane (y-axis). These results confirm that the underlying transformation is actually valid and can be achieved with the discretized profile. However, one of the main problems is the frequency shift from  $f$  to  $f'$ . In order to shift back the resonance to the design frequency, a dielectric layer has been used. This is discussed in the next section.

### 3.3.3.2 Dielectric layer to match antenna superstrate assembly at design frequency

It is well known that placing a dielectric layer over patch antenna allows changing the operating frequency of the antenna. Here, it is proposed to use a dielectric layer between patch antenna and dielectric superstrate to replace the air layer to shift the operating frequency of the antenna. Two different design parameters of the dielectric layer are investigated: relative permittivity and thickness.

First, results from parametric simulation study on relative permittivity ‘eps’ of dielectric layer are presented. A 10 mm thick dielectric layer is simulated in place of the air gap of same thickness of the previous section. ‘eps’ is iterated between from 1 to 4. The magnitude of reflection coefficient for the simulated values is shown in Fig. 3.27. The reference impedance in the simulation is 50  $\Omega$ .

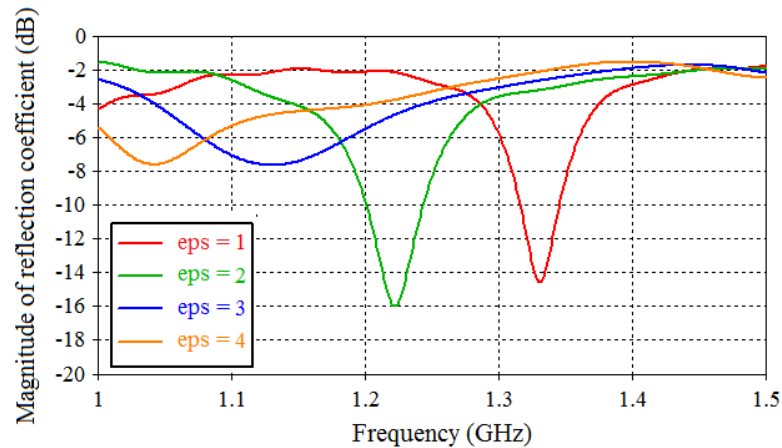


Fig. 3.27 Comparison of magnitudes of reflection coefficients for different values of relative permittivity of the intermediate 10 mm thick dielectric layer.

The red curve in the plot above corresponds to the 10 mm thick air layer, and the operating frequency is identical to red solid line in the plot of Fig. 3.25. As the value of relative permittivity value increases from 1 to 4, the operating frequency of the assembly decreases from 1.33 GHz to 1.04 GHz. It may also be remarked that the antenna is not matched to the superstrate in all the cases. The magnitude of reflection coefficient shows that the antenna is matched to the superstrate for relative permittivity values of 1 and 2 ( $|S_{11}| < -10$  dB), with better matching achieved for  $\text{eps} = 2$ . For  $\text{eps} = 3$  and 4, the antenna superstrate assembly is not matched at the respective operating frequencies. Nevertheless, it confirms that the dielectric layer can be used to shift the operating frequency.

However, shifting the operating frequency is not enough in the present context. The reorientation due to the dielectric superstrate also needs to be conserved. In Fig. 3.28, the 3D polar plots of directivity have been compared for the four different relative permittivity values at corresponding operating frequencies. Directivity is used to compare the radiation patterns instead of gain so as to discount the effects of mismatch at input. For facilitating a visual comparison, the values in the four plots are limited in the (-7, 3.5 dBi) range. It can be seen that the directivity pattern changes significantly upon changing the relative permittivity of the dielectric layer. For  $\text{eps} = 2$ , a reorientation with a maximum directivity of 3.5 dBi in azimuthal plane and a broadside null is achieved. For  $\text{eps} = 4$ , the antenna superstrate assembly nearly ceases to provide the desired spatial transformation. This is due to change in the electrical size of the superstrate. As seen in Fig. 3.27, the operating frequency for a dielectric layer of relative permittivity value,  $\text{eps} = 4$  is 1.05 GHz. At this frequency the physical dimensions correspond to an electrical size of  $0.52\lambda$  by  $0.52\lambda$  by  $0.10\lambda$ , whereas at the design frequency of 1.25 GHz, the electrical size of the superstrate is  $0.625\lambda$  by  $0.625\lambda$  by  $0.12\lambda$ , as discussed in 3.3.2.3. The reorientation behavior is observed for relative permittivity variation from 1 to 3. This discussion highlights the role played by relative permittivity value

of dielectric layer in shifting the operating frequency while still conserving the desired radiation pattern. Also, it provides an indication on the bandwidth of operation of the superstrate of given physical dimensions. Next, thickness of the dielectric layer is studied.

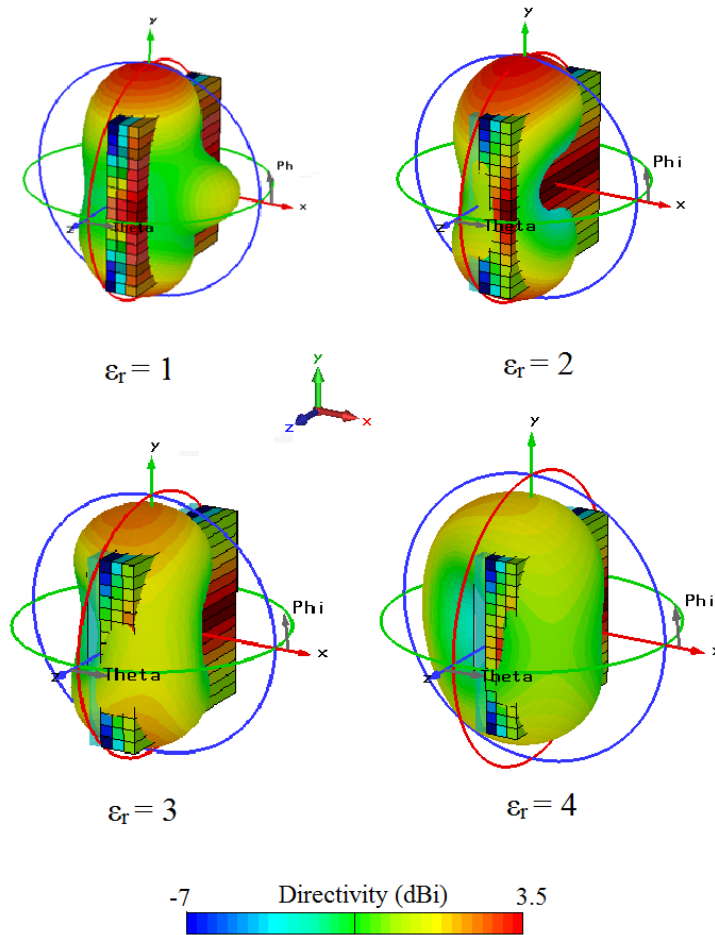


Fig. 3.28 Directivity (dBi) comparison at operating frequencies for antenna-dielectric layer-superstrate assembly with variation of relative permittivity of dielectric layer.

In the previous study, the thickness of the dielectric layer is kept constant to highlight the role of relative permittivity. However, the thickness of the dielectric layer is another variable that needs to be considered in the design. Here, results from parametric simulation on the thickness of the dielectric layer are presented. The relative permittivity of the dielectric layer is kept constant at 2. The thickness is varied from 6 to 12 mm with a step of 2 mm in each iteration or  $0.025\lambda$  to  $0.05\lambda$  in terms of wavelength at 1.25 GHz. It may be recalled that the thickness of individual pixel in the discrete version of the profile developed in 3.3.2.2 is  $\sim 0.04\lambda$ . The magnitudes of reflection coefficient for corresponding iterations are plotted in Fig. 3.29. The reference impedance in the simulation is  $50 \Omega$ . The red line in this plot is identical to the red line in the plot of previous parametric simulation (see Fig. 3.27.) It is seen here that the operating frequency does not shift upon increasing the thickness of the dielectric

layer. However, as the thickness of the dielectric layer increases, it improves the impedance matching of the antenna superstrate assembly. As previously, the information on impedance matching alone is not sufficient to assess the impact of thickness of the dielectric layer. Its impact on transformation also needs to be identified. 3D polar plots of directivities for different thickness of dielectric layer are plotted in Fig. 3.30. As done previously, values in the plot are limited in the (-7, 3.5 dBi) range.

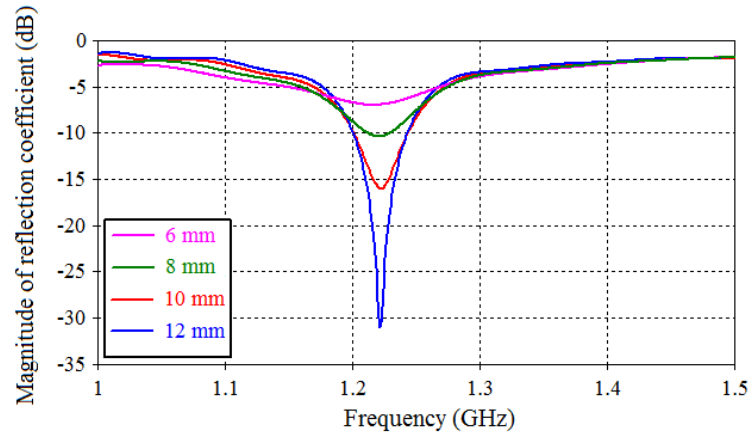


Fig. 3.29 Comparison of magnitudes of reflection coefficients for different thicknesses of intermediate dielectric layer of relative permittivity value of 2.

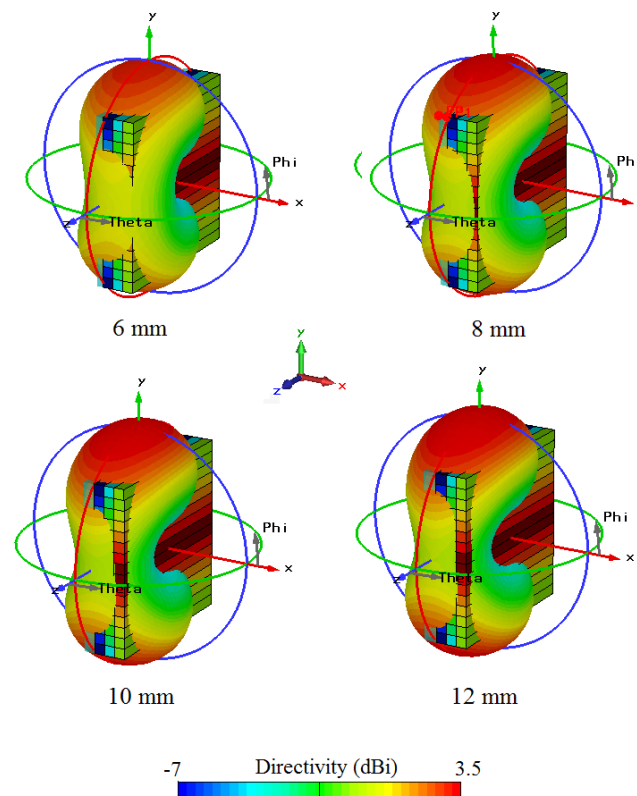


Fig. 3.30 Directivity (dBi) comparison of antenna-dielectric layer-superstrate assembly with varied thickness of dielectric layer.

The directivity increases from 3.4 dBi for 6 mm dielectric layer to 4 dBi for 12 mm dielectric layer. However, the form of directivity does not change significantly, maxima in azimuthal plane and a broadside null is retained in all the radiation patterns. Still thicker dielectric layers may improve the impedance matching, but will also increase the overall thickness. In this study, 12 mm thickness is conserved.

Thus, this above presented discussion on the use of dielectric layer to match the antenna to the superstrate. It shows that the operating frequency of the antenna superstrate assembly can indeed be shifted using dielectric layer. However, the radiation pattern achieved using TO superstrate is sensitive to this change; especially changing the permittivity of the dielectric layer can modify the radiation pattern. An appropriate value of relative permittivity may allow both shifting the operating frequency, and conserving the radiation pattern. Furthermore, the thickness of the dielectric sheet can be used in a trade off against the impedance matching without significantly changing the radiation pattern.

Using this information, the operating frequency is shifted to previously designated design frequency of 1.25 GHz. For this, a 12 mm thick dielectric layer with relative permittivity value  $\epsilon_r = 1.8$  is used to match the antenna to superstrate. In Fig. 3.31, the magnitude of reflection coefficient for this new antenna superstrate assembly has been compared with the antenna alone.

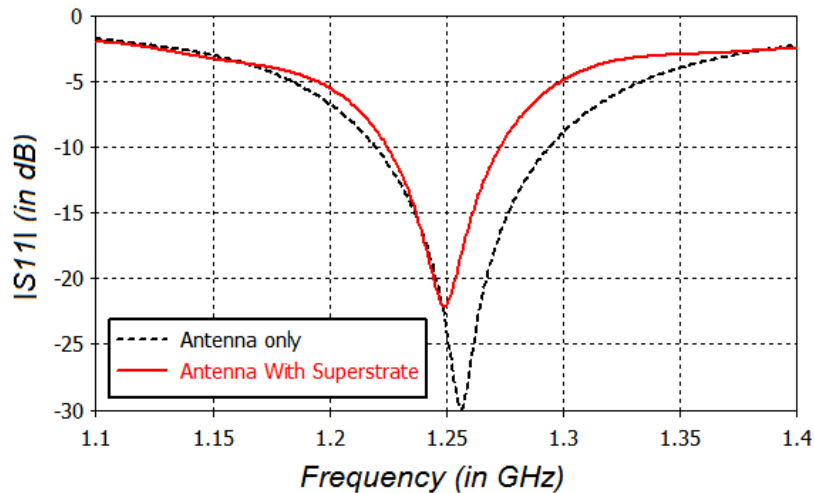


Fig. 3.31 Comparison of  $|S_{11}|$ : Antenna only vs. Antenna-Superstrate with a dielectric layer ( $\epsilon_r = 1.8$ ); Antenna-superstrate assembly is matched at  $f = 1.25$  GHz.

The red line in the plot shows that the antenna superstrate assembly is matched at the operating frequency of 1.25 GHz. The antenna with the superstrate presents a bandwidth of ~4% (1.22-1.27 GHz). In Fig. 3.32, 3D plot showing the far field pattern at the resonant frequency (1.25 GHz) has been plotted. The radiation pattern calculated from the far field data shows that the superstrate reorients the electromagnetic waves emanating from the

antenna in its azimuthal plane. The maximum realized gain in azimuthal plane is 3.5 dB. A plot minimum is observed along  $x$ -axis and the realized gain in the broadside is -11.7 dB.

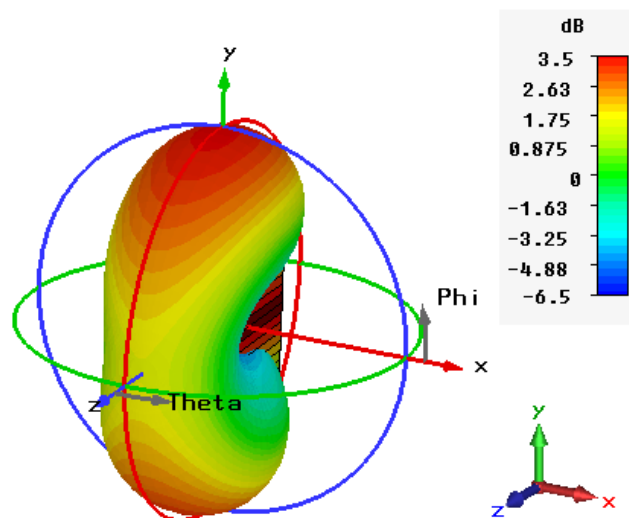


Fig. 3.32 3D far field plot showing realized gain (in dB) of antenna superstrate assembly with a dielectric matching layer at  $f$ ; Max. Realized gain = 3.5 dB

The radiation performance in individual planes is presented next. In the plots presented below, black colored lines correspond to the radiation pattern of antenna alone and red color represent the radiation pattern of antenna superstrate assembly. The co-polar radiation is plotted in solid lines; and cross-polar radiation by dashed lines. The realized gain is plotted in (-20, 10 dB) range. In Fig. 3.33, realized gain of antenna alone and antenna with superstrate is compared in  $x y$  plane at 1.25 GHz.

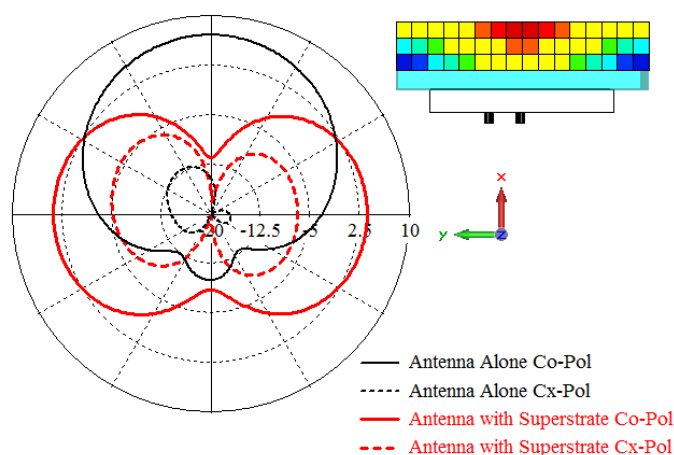


Fig. 3.33 Comparing realized gain (dB) in  $x y$  plane for antenna only and antenna with superstrate at 1.25 GHz.

The desired reorientation is clearly visible in the plot. The broadside radiation pattern of the antenna without superstrate (solid black line) is strongly modified in presence of the superstrate (solid red line) with radiation maxima of 3 dB at  $90^\circ$ ,  $270^\circ$  and minimum at  $0^\circ$  in

the plot. The level cross-polar component along  $y$ -axis is at least 8 dB smaller than co polar component. In Fig. 3.34, realized gain of antenna alone and antenna with superstrate is compared in  $x y$  plane at 1.25 GHz.

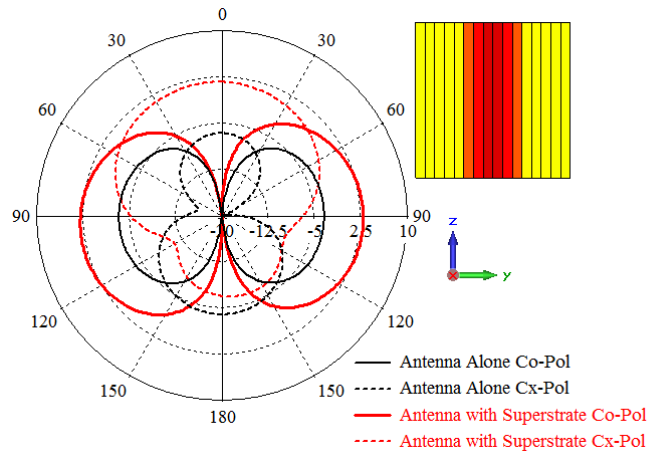


Fig. 3.34 Comparing realized gain (dB) in  $y z$  plane for antenna only and antenna with superstrate at 1.25 GHz.

The superstrate increases the realized gain in the  $y z$  plane. Co polar pattern of the antenna without superstrate (solid black line) has a peak value of -3.4 dB. This is expected as the patch antenna is designed to radiate in the broadside (along  $x$ -axis, out of page normal), and as a result gain in  $y z$  plane is justifiably low. Use of superstrate (solid red line) allows increasing the level of co-polar component along  $y$ -axis, such that the peak values are 2.9 dB i.e. an increase of 6.3 dB. The level cross-polar component along  $z$ -axis is 1.5 dB and is more than co-polar level. However, along the two principle lobes along  $y$ -axis, the cross polar level is at least 8 dB smaller than co polar component. In Fig. 3.35, realized gain of antenna alone and antenna with superstrate is compared in  $x z$  plane at 1.25 GHz.

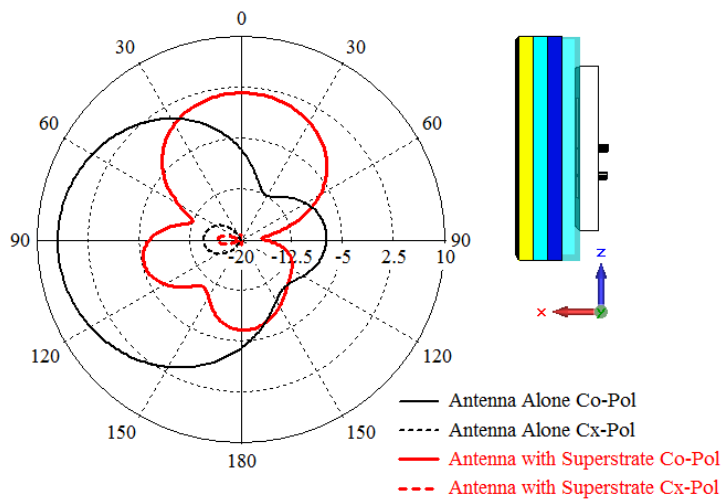


Fig. 3.35 Comparing realized gain (dB) in  $x z$  plane for antenna only and antenna with superstrate at 1.25 GHz.

The superstrate is designed to function in  $x y$  plane, such wave propagating along  $x$  axis are reoriented towards  $y$ -axis. Consequently, this results in reduced value of realized gain in the  $x z$  plane. The co-polar pattern of the antenna alone has a peak realized gain 6.8 dB along  $x$ -axis, as seen in the solid black line. The use of superstrate results in reduction of realized gain in this plane, with a peak realized gain of 1.6 dB. As a result the realized gain in the  $y z$  plane. The cross polar component in the radiation pattern is at least 17 dB smaller than the co polar component. In the discussion presented above, the cross polar component in the radiation pattern is high and may be seen as problematic. However the dielectric superstrate is shown to achieve the reorientation dictated by the coordinate transformations.

### 3.4 Discussion

This chapter provides a strong theoretical basis for the design of the superstrate. Essentially, the prescribed procedure allows designing solutions based on the transformed space. A clear design path has been laid out that starts from theoretical description of the problem and ends at a complete 3D superstrate solution. It has also been shown that propagation in the transformed space and consequently the shape of the exiting wave-front can be controlled using compression and shift factors.

In the proposed theoretical development, the material profile originating from the spatial transformation has been highly simplified to its present form. This has been achieved done by excluding permeability and replacing anisotropic by isotropic dielectric values. These simplifications in the design are necessary to achieve a practically feasible design. Of course, the simplifications in the profile come at a certain cost. The concept uniquely works with linear TE polarized sources. For sources with other polarizations, permeability elements will be required. The only practical way to achieve permeability gradient in profile would be to use metamaterial SRR resonators, which complicates the implementation.

Barring the above stated issues; a solution comprised of standard dielectric materials is far more favorable than an anisotropic, lossy, metamaterial-based design. Standard industrial facilities available for handling dielectric materials facilitate the implementation of the design towards a variety of applications e.g. aerospace, consumer electronics, etc. It may also be noted here that the design methodology does not respond to one single device/concept such as the one discussed in this chapter. The prescribed procedure can be used to design a new family of devices based on the used spatial transformations. Using the interplay of the defined factors  $a$ ,  $b$  and  $m$  other exiting wave-front and consequently different radiation patterns can be designed. Some of these conceptual designs are also discussed later in Chapter 5. But first, a proof-of-concept device based on the superstrate discussed in Section 3.3 has been investigated further. More details are presented in the next chapter.



## 4. Proof of concept of dielectric superstrate for antipodal radiation

In this chapter, the validation of the dielectric superstrate concept is presented. The discretized profile designed in the previous chapter (3.3.3) will be used as the starting point towards designing an experimental prototype. A systematic approach will be described, which allows going from discrete profile of last chapter with multiple permittivity values to a simple solution containing only 2 permittivity values. The radiation performance will be discussed in detail for the fabricated solutions.

A discussion on the available dielectric materials required to interpret the large gradient in permittivity will be presented first. Based on the available materials, a fabrication strategy to design the ‘effective medium’ is proposed. In the context of this chapter, the effective medium is defined as the medium designed using a combination of dielectric materials to interpret the spatial transformation identified in chapter 3. A superstrate based on strict implementation of the pixelated profile will be presented as the first solution. Next, a relaxed version with a simple staircase shaped profile comprising of only two materials will be presented. Measured performances of two prototypes will be discussed in detail at the end of the chapter.

First, a discussion on the available materials to design this profile is presented below.

### 4.1. Materials and design strategy

The dielectric superstrate presented at the end of 3.3.3.2 is a volumetric device with 48 pixels used to achieve the gradient in relative permittivity arranged in three layers of 16 pixels. The permittivity values in the pixelated profile vary from 1 to 14. Finding materials with permittivity corresponding to each pixel is difficult and cumbersome. Furthermore, increasing the number of materials used in fabrication would make the design more susceptible to fabrication errors. Such complexity is not suited for most industrial applications, and certainly not in the aerospace domain. Here, it is proposed to use 3D printing and standard dielectric materials to facilitate the fabrication of the superstrate. 3D printing techniques overcome limitations of conventional fabrication processes in the design of complex structures. This is advantageous for TO-related applications as effective media

can be designed easily, as already evidenced by the various 3D-printed TO concepts previously discussed in 2.4.2.

The theoretical pixelated profile is often realized by designing an effective medium. As explained in chapter 2, permittivity approximation allows synthesizing permittivity values by changing the volume fraction of medium comprised of two different relative permittivity values (see ( 2.13 )). The synthesized permittivity value lies between those of two dielectric materials. In practice, this is often achieved by drilling air holes in a dielectric host material. In such case, value of synthesized permittivity is lesser than that of the dielectric host. However, the air holes can also be filled with high permittivity dielectric materials for synthesizing larger values of permittivity. Subsequently, the gradient in relative permittivity inside the transformed medium can either be designed by changing the radius of holes or the intermediate distance. In [2], the dielectric superstrate to increase the HPBW, designed by Clemente Arenas *et. al* at Telecom ParisTech and fabricated at Airbus Group Innovations 3D printing facility at Suresnes, France, uses the change in distance between air holes in to achieve the gradient in relative permittivity. In this chapter, the alternate approach of changing the radius of holes in a pixel is chosen and will be discussed in the next section. But first, a discussion on the materials available for fabrication is presented.

In solutions using a single dielectric host material, the upper bound in the profile is defined by the permittivity of dielectric host material and lower bound corresponds to the permittivity of air i.e. 1. A comparison of 3D printer filaments typically used to design TO superstrates is provided in Table 4.1. Dielectric losses of these materials are also mentioned. However, they are not considered initially in calculations.

Table 4.1 Dielectric constants and losses of typical 3D printer compatible filaments.

Reference	Material for 3D printer	Relative permittivity ( $\epsilon_r$ )	Dissipation factor ( $\tan\delta$ )
[82]	Photo curable resin	3.0	N.A.
[84]	Photo curable liquid	2.8	N.A.
[86]	Polycarbonate-ABS Blend	2.5	0.04
[90]	Poly Lactic Acid (PLA) Thermoplastic	2.72	0.008
[2]	Fullcure Photo curable resin <sup>TM</sup>	2.9	0.0862

Appendix C.b)iii	Preperm™ TP20280	4.4	0.004
------------------	------------------	-----	-------

It may also be noted in the table above that the highest relative permittivity of commercially available 3D printing filaments does not go beyond 4.4, and most typically used blends have  $\epsilon_r$  in the range of 2.6-3. However, the highest permittivity value in the TO concept presented in the previous chapter is 14 (see Fig. 3.22). Hence, this solution cannot be entirely printed due to the non-availability of 3D printer compatible filaments with high relative permittivity. However, 3D printing may still be used to design the gradient in lower values in the range. It may be noted here that the various materials listed in the table above are used with different types of 3D printers. In this research, the prototypes are fabricated using photo curable resin and PLA filaments have been used, and will be described later in the section. The details about the materials and the printing processes have been provided in Appendix C.b).

Alternatively, implementation using multiple materials can be considered. Using two or more dielectric materials with different dielectric constants allow accessing a larger range of permittivity. For example: in [79], a dielectric Fresnel lens is presented. It is suggested to increase the relative permittivity of a perforated dielectric material by filling holes with high- $\epsilon_r$  powders. The fabricated Eaton lens discussed in [82] has a low and a high permittivity region interpreted using two different materials. In [77], three dielectric materials have been used to interpret a broadband magnifying lens. Other multiple material solutions have already been discussed in chapter 2.

In this thesis, a two-material design strategy is considered. The low permittivity 3D printer compatible material, as discussed above, can be considered as the first material to access lower permittivity values in the profile. Next, a high permittivity material is chosen to access the high permittivity values. Various materials may be used to achieve the upper bound of relative permittivity 14 inside the effective medium. Some of these are presented in Table 4.2.

Table 4.2 Materials with large dielectric constant

Reference	Material	Relative permittivity ( $\epsilon_r$ )
[82]	Pure Acetonitrile	40
[77]	F4B	9.6
[80]	TiO <sub>2</sub> and polyphenylene oxide	16
[89]	Titanate powders	12.6

Appendix C.a)	Alumina	9.3-9.9
---------------	---------	---------

In [82], all extremely high values of permittivity in the profile are implemented using a single region of pure acetonitrile. As seen in the table above, pure acetonitrile offers very high permittivity values that are much larger than the requirement in the current study. But other materials in the table are good candidates.

The above discussion is a representation of the limits within which dielectric superstrate can be practically implemented. In context of 3D printing, low-permittivity printer compatible material can be used to design a host structure, which accommodates higher permittivity materials to achieve the desired value of relative permittivity. The two materials are designated as low and high- $\epsilon_r$ . The high- $\epsilon_r$  corresponds to the highest permittivity value in the experimentally realized device. All values in discretized profile greater than high- $\epsilon_r$ , are replaced with high- $\epsilon_r$ . Low- $\epsilon_r$  corresponds to permittivity of the 3D printer filament. It is proposed to use these two values in the design to interpret the different ranges of permittivity:

- high- $\epsilon_r$  : for interpreting all  $\epsilon_r > \text{high-}\epsilon_r$ .
- low- $\epsilon_r$ : for interpreting  $1 < \epsilon_r < \text{low-}\epsilon_r$ .
- combination of both :  $\text{low-}\epsilon_r < \epsilon_r < \text{high-}\epsilon_r$ .

In this thesis, Alumina is considered as the high- $\epsilon_r$  material. Alumina is fairly common dielectric material. It is available in form of off-the-shelf components. Alternatively, it can be ordered from manufacturer according to design specifications. It offers a high relative permittivity ( $\epsilon_r = 9.9$  for 99.7% purity) and extremely low losses.

As for low- $\epsilon_r$ , a relative permittivity value of  $\epsilon_r = 4.4$  is considered that corresponds to the permittivity of Premix's PREPERM-20280 (see Table 4.1). Premix's product is compound based ABS blend that, according to our best knowledge, offers the highest dielectric constant for commercially available 3D printer compatible filaments. Higher values of low- $\epsilon_r$  facilitate the implementation of the gradient in the profile. Low and high- $\epsilon_r$  materials along with air holes are used to design effective medium for values in the range  $1 < \epsilon_r < \text{high-}\epsilon_r$ .

Now that the materials and the design strategy have been identified, design and performance of superstrate using effective medium are discussed in the next section.

## 4.2. Towards a practical design

Let us reconsider the antenna superstrate solution presented at the end of chapter 3. The device is comprised of a pixilated superstrate with 48 pixels to interpret the spatial transformation and a dielectric layer to match the superstrate and source antenna at the design frequency. The size of individual pixel in terms of wavelength at 1.25 GHz is approximately

$0.04\lambda$  by  $0.04\lambda$ . In this section, this profile is used to design an effective medium. In Fig. 3.22, the relative permittivity in a pixel in the profile is representation of local average relative permittivity in that pixel in a continuous profile. In this chapter, the permittivity values are rounded off to the nearest integer for easy calculation of radii of holes required to design effective medium, as shown in Table 4.3. The 24 values shown in the table correspond to permittivity values required to design coordinate transformation from rectangular to quarter ellipse in one half of the dielectric superstrate.

Table 4.3 Spatial distribution of permittivity in discretized profile

8	8	9	10	11	12	13	14	Plane of symmetry
5	6	7	8	9	10	11	12	
1	2	4	6	7	8	9	10	

It is also verified that this small local change in the permittivity values of the pixel does not affect the spatial transformation. The operating frequency of the new antenna superstrate is fixed to 1.25 GHz thanks to the intermediate 12 mm thick dielectric layer of a relative permittivity of 1.8. Use of the dielectric layer has been previously discussed in 3.3.3.2. At 1.25 GHz, the superstrate with a pixilated profile corresponding to permittivity values of Table 4.3 radiates with an antipodal radiation pattern. A maximum realized gain of 3.6 dB is achieved in the azimuthal plane. This version of the superstrate is now interpreted in two different ways. They are described in the following sub-sections.

### 4.2.1 Strict interpretation of discretized profile

First, an effective medium is designed for a pixel-by-pixel representation of the discretized profile. Since a pixel-by-pixel interpretation of permittivity values in Table 4.3 is desired, this approach is called as strict interpretation of discretized profile.

The medium can be designed to represent the above permittivity distribution using the low and high- $\epsilon_r$  materials identified in the previous section. First, all permittivity values greater than high- $\epsilon_r$  are replaced by high- $\epsilon_r$ , as shown by the shaded region in Table 4.4. This region represents the constant permittivity region in the profile. The variation in permittivity values inside the effective medium is then limited between 1 and 9.9. A 12mm thick dielectric layer with relative permittivity value of 2 is used to fix the operating frequency of the antenna at  $f = 1.25$  GHz. This new antenna superstrate assembly with upper permittivity value restricted at 9.9 provides an antipodal radiation pattern at the operating frequency with maximum realized gain of 3.2 dB.

Table 4.4 Spatial distribution of permittivity in discretized profile with upper bound fixed at high- $\epsilon_r$

8	8	9	9.9	9.9	9.9	9.9	9.9	Plane of symmetry
5	6	7	8	9	9.9	9.9	9.9	
1	2	4	6	7	8	9	9.9	

In practice, grey pixels are interpreted using alumina, whereas remaining pixels in the clear region can be approximated by an effective medium comprising of high and low- $\epsilon_r$  materials. As stated earlier, the permittivity values as presented in the above table can be synthesized by changing the volume fraction inside an effective medium. In Fig. 4.1, a representative image of a single pixel inside an effective medium is shown. In this pixel, rod is embedded inside the dielectric host. The volume fraction of such a pixel can be controlled by any of the following parameters:

- Dimensions of the pixel in host medium,  $a$  and  $b$  (not to be confused with compression factors  $a$  and  $b$ ).
- Diameter,  $d$  of the cylindrical rod embedded in the host pixel.
- Relative permittivity of the host ( $\epsilon_{\text{host}}$ ) or rod ( $\epsilon_{\text{rod}}$ ).

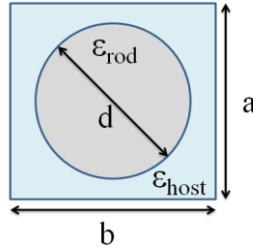


Fig. 4.1 Pixel in an effective medium comprised of two materials.

As stated in the first section, previous work at Telecom ParisTech by Clemente Arenas on design the dielectric superstrate for increasing HPBW used the variation in density of holes of constant diameter. The distance between holes of constant radius was changed to control volume fraction and hence achieve the desired variation of permittivity in the effective medium [2]. In this work, it is proposed to keep the distance between the centers of the holes constant and change the diameters instead in order to change the volume fraction. Thus, the permittivity value is synthesized by changing  $d$ , while  $a$ ,  $b$  and  $\epsilon_{\text{host}}$  are kept constant ( $a = 9.6$  mm,  $b = 9.375$  mm,  $\epsilon_{\text{host}} = \text{low-}\epsilon_r = 4.4$ ). Relative permittivity of the cylindrical rod,  $\epsilon_{\text{rod}}$  depends upon the value of relative permittivity required.

- If the relative permittivity value lies between 1 and low- $\epsilon_r$ , then  $\epsilon_{\text{rod}}$  corresponds to the permittivity of air i.e.  $\epsilon_{\text{rod}} = 1$ .

- If the relative permittivity value lies between low- $\epsilon_r$  and high- $\epsilon_r$ , then  $\epsilon_{rod}$  corresponds to high- $\epsilon_r$  i.e.  $\epsilon_{rod} = \text{high-}\epsilon_r$ .

Using this information, the volume fractions and diameters of holes in the effective medium required to synthesize the permittivity values in the un-shaded region of Table 4.4 are calculated. A simple Matlab code is used for this. In Table 4.5, required relative permittivity values, corresponding rod medium, volume fractions and diameters are provided.

Table 4.5 Characteristics of the effective medium

Relative permittivity in effective medium ( $\epsilon_{eff}$ )	Host medium ( $\epsilon_{host}$ )	Rod medium ( $\epsilon_{rod}$ )	Volume fraction (f)	Diameter (mm) (d)
1	4.4	1	1	10.70
2	4.4	1	0.70	8.99
3	4.4	1	0.41	6.86
4	4.4	1	0.11	3.67
5	4.4	9.9	0.10	3.53
6	4.4	9.9	0.29	5.77
7	4.4	9.9	0.47	7.36
8	4.4	9.9	0.65	8.66
9	4.4	9.9	0.83	9.78

It is seen in the table above that:

- For  $1 < \epsilon_r < \text{low-}\epsilon_r$ : volume fraction tends to 0 as we approach the upper bound of variation in permittivity range; diameter of air holes decreases.
- For  $\text{low-}\epsilon_r < \epsilon_r < \text{high-}\epsilon_r$ : volume fraction tends to 1 as we approach the upper bound of variation in permittivity range i.e. diameter of holes increases.

Furthermore, for  $\epsilon_r = 1$  and 9, the diameter  $d$  is greater than the size of the pixel. Such solution does not have a physical meaning and it is not possible to achieve these values of relative permittivity in the pixel of given size with given materials. Even for  $\epsilon_r = 2$  and 8, the diameters of the holes are barely smaller than the size of the pixel itself. This also highlights the importance of low- $\epsilon_r$  value. Larger values of low- $\epsilon_r$  would allow interpreting all permittivity values within the imposed pixel size.

Consequently, the pixels corresponding to  $\epsilon_r = 1$  are reassigned a relative permittivity of 2. Values between 1 and 2 are not chosen because they will still violate the imposed size limit on the pixel. Similarly, pixels with  $\epsilon_r = 9$  are reassigned as high- $\epsilon_r$ . Permittivity variation in the new effective medium is represented in Table 4.6. In simulation, a superstrate with this

permittivity profile provides the desired antipodal radiation pattern with a peak realized gain of 3.4 dB at 1.25 GHz.

Table 4.6 Spatial distribution of relative permittivity in effective medium.

8	8	9.9	9.9	9.9	9.9	9.9	9.9	Plane of symmetry
5	6	7	8	9.9	9.9	9.9	9.9	
2	2	4	6	7	8	9.9	9.9	

This is a significant simplification of the profile because the required antipodal radiation pattern can be very well achieved with standard commercially available dielectric materials. Such a superstrate is now designed in CST Microwave Studio. The design parameters required to achieve the relative permittivity values in the medium are available in Table 4.5 and Table 4.6 (i.e.  $\epsilon_{\text{host}}$ ,  $\epsilon_{\text{rod}}$ ,  $\epsilon_{\text{eff}}$  and  $d$ ). A 12 mm thick dielectric layer with relative permittivity  $\epsilon_r = 2.5$  is used to fix the operating frequency and achieve the impedance matching at the chosen design frequency of  $f = 1.25$  GHz. This new configuration is shown in Fig. 4.2.

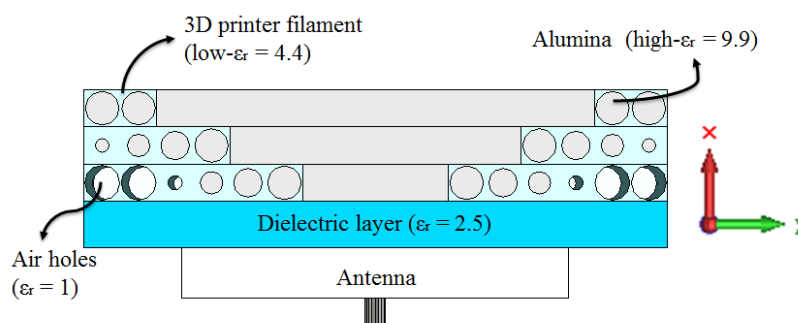


Fig. 4.2 Pixel-by-pixel interpretation of TO concept in an effective medium.

As seen in the figure, the holes/dielectric rods are orientated along  $z$ -axis. The length of the holes/alumina rods is equal to the length of the superstrate (150 mm or  $0.625\lambda$  at 1.25 GHz.) This choice of orientation of holes/alumina rods in the design is aimed towards simplifying implementation. While alternative solutions may be designed with holes oriented along  $x$  or  $y$ -axis, this would highly increase the number of holes and dielectric rods needed to interpret the permittivity gradient. While holes can still be printed easily using 3D printing techniques, increasing the number of alumina rods would definitely increase the cost and complexity of fabrication. In contrast, only 24 holes and 18 alumina rods are required in the proposed design. In this chapter, results from this version of the profile are presented; others hole orientations have not been investigated in this thesis.

It can be seen in Fig. 4.2 that the three pixels in left and right corners of the bottom layer are realized using air holes. The remaining pixels in the effective medium are realized

using cylindrical alumina rods. In Fig. 4.3, a comparison of the realized gain obtained from superstrates with discrete profile presented in the end of chapter 3 and effective medium designed in this section is provided at the design frequency,  $f = 1.25$  GHz. The values are plotted in a range of -7 to 3.5 dB in both plots.

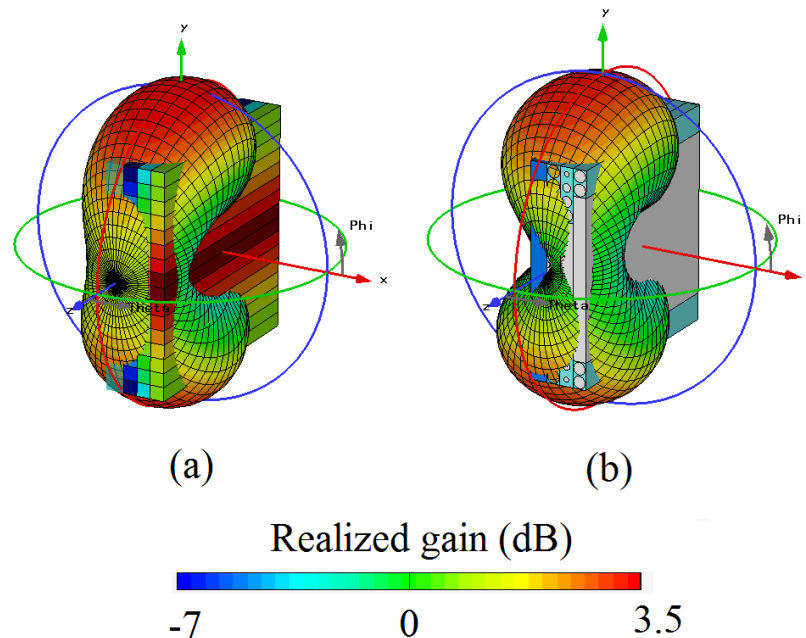


Fig. 4.3 Realized gain (dB) (a) Pixilated Profile, (b) Effective medium.

It is clear that the effective medium provides an antipodal radiation pattern with maxima along  $y$ -axis. The peak realized gain at  $f$  for pixilated superstrate is 3.5 dB; for effective medium superstrate, realized gain is 3.4 dB.

The results presented in this sub-section show that the spatial transformation achieved inside the theoretical dielectric superstrate solution presented at the end of chapter 3 can be interpreted in a relatively simple construction comprised of 3D printed structure and alumina. The effective medium contains a wide range of permittivity values (from 2 to 9.9.) The desired antipodal radiation pattern is also achieved, with peak realized gain in azimuthal gain nearly same as in chapter 3. The solution designed in this section is based on adherence to individual pixel permittivity values in the discrete profile. In the next section, a relaxed interpretation using only two permittivity values in the profile is presented.

## 4.2.2 Relaxed interpretation of discretized profile

The effective medium designed in the previous sub-section is a strict interpretation of the relative permittivity values calculated in Table 4.6. As explained above, holes and alumina rods allow achieving the gradient inside the effective medium. Indeed, this design can be 3D printed. Typically, designing holes in 3D printing requires additional step of filling holes with a gel-like material, which is washed away later [94]. Then, high permittivity

material needs to be machined in shape of cylindrical rods of diameters equal to the corresponding holes. Machining alumina needs special care, as it is brittle. It is clear that holes and rods in the profile increase the complexity in fabrication. It is highly desirable to achieve the reorientation without the complexity associated with the holes/rods. In this section, the holes and alumina rods are removed to further simplify the design. Thus, the superstrate is realized using only two values: low and high- $\epsilon_r$ . Furthermore, it is shown that a slight reduction in dimensions of high- $\epsilon_r$  does not impact the spatial transformation, but consequently allows reducing the weight of the overall design and moreover using off-the-shelf components.

As said above, it is planned to not use holes and alumina rods to facilitate fabrication. Only two values: low and high- $\epsilon_r$ , are used in this case. This is shown in Table 4.7. While this simplification may eventually greatly facilitate the fabrication, it also results in a significant deviation from the pixelated version of the permittivity profile calculated in chapter 3. This new profile broadly respects the distribution of high and low permittivity values in the profile, but the information regarding permittivity of individual pixels is lost. As the pixel-by-pixel permittivity synthesis of the pixelated profile is called a strict interpretation, this new profile with significant simplification is called a relaxed interpretation of the spatial transformation.

Table 4.7 Two value interpretation of effective medium.

4.4	4.4	9.9	9.9	9.9	9.9	9.9	9.9	Plane of symmetry
4.4	4.4	4.4	4.4	9.9	9.9	9.9	9.9	
4.4	4.4	4.4	4.4	4.4	4.4	9.9	9.9	

The shaded region corresponds to the permittivity of alumina and is interpreted using three sheets of alumina. Alumina sheets can be manufactured to these dimensions. Alternatively, alumina sheets with nearest dimensions may be bought off the shelf. The dimensions calculated from the pixels and off-the shelf alumina sheets are given in Table 4.8. The clear white cells represent the 3D printed region, which can be additively manufactured in a single block. Its dimensions may be adjusted with respect to dimensions of the alumina layer.

Table 4.8 Readapting dimensions of alumina layer

Layer	Dimensions from pixels (mm)	Off-the shelf (mm)
Top	150 by 112.5 by 9.6	150 by 100 by 10
Middle	150 by 75 by 9.6	150 by 75 by 10
Bottom	150 by 37.5 by 9.6	150 by 25 by 10

A corresponding superstrate is designed without the holes/rods, as shown in Fig. 4.4. The relative permittivity of the 12 mm thick dielectric layer is fixed at  $\epsilon_r = 2.2$  so as to match the antenna superstrate assembly at operating frequency of  $f = 1.25$  GHz.

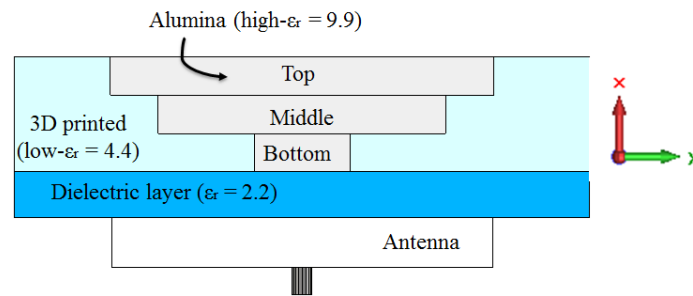


Fig. 4.4 Staircase arrangement of alumina sheets in the 3D printed superstrate structure.

A profile may be observed wherein the alumina sheets are placed on the 3D-printed staircase structure. In Fig. 4.5, realized gains of two configurations have been plotted at the design frequency,  $f = 1.25$  GHz. Fig. 4.5 (a) corresponds to superstrate with alumina sheet dimensions corresponding to Table 4.7, whereas Fig. 4.5 (b) presents the realized gain in a superstrate with off-the-shelf alumina. The values are plotted in the range (-7, 3.5 dB). Both patterns are identical, which shows that the small change in alumina dimensions does not induce any significant change. This facilitates using off the shelf components for the design.

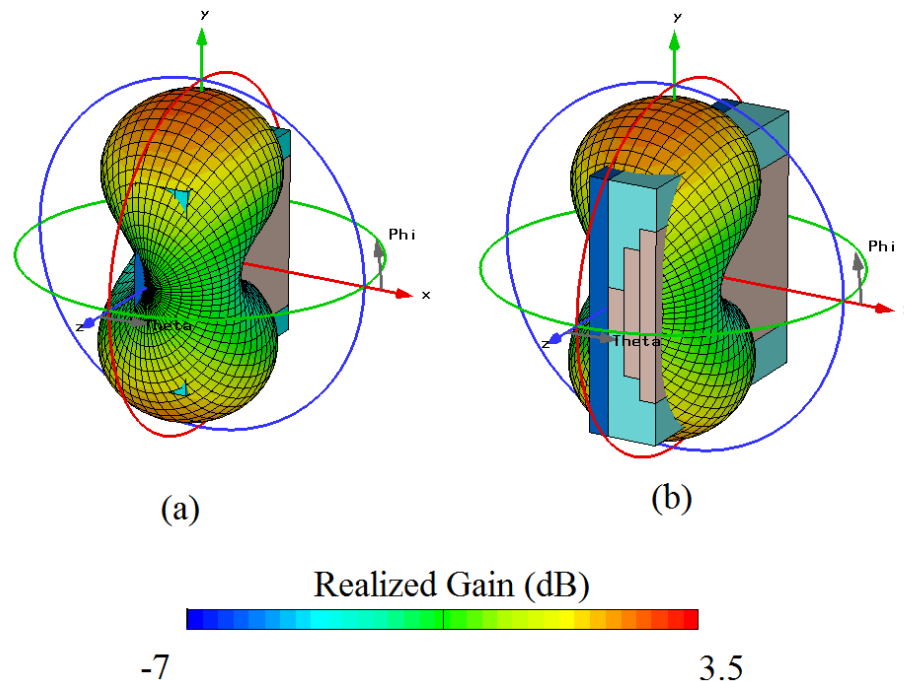


Fig. 4.5 Realized Gain (dB) of superstrate, (a) dimensions of alumina sheets corresponding to shaded region in Table 4.7 (peak realized gain 2.8 dB), (b) Off-the-shelf alumina sheets (peak realized gain 2.7 dB).

The passage from strict to relaxed interpretation has an impact on the realized gain of the superstrate. It may be recalled that realized gain obtained during strict interpretation is 3.4

dB. In Fig. 4.5, the peak realized gain is 2.7 dB (for superstrate with off-the-shelf alumina sheets) i.e. a 0.6 dB reduction. Nevertheless, the radiation pattern is reoriented in the azimuthal plane. Also, changing the dimensions of alumina as explained in Table 4.8 has no particular effect, and the realized gains for both the cases are nearly equal. The superstrate with off-the shelf alumina sheets is considered for realization.

Thus, results presented in this section have allowed highlighting a very significant trait of the spatial transformation i.e. the antipodal radiation pattern, which was earlier achieved using a large number of permittivity blocks, can also be achieved in a very simple arrangement of two dielectric materials arranged in a staircase structure. A discussion to provide further insight on the two material interpretations is provided in chapter 5. In the next section, practical implementation of the superstrate is presented.

### 4.3 Experimental verification

In this section, the superstrate of the previous section is adapted to work with an existing antenna. This antenna has been already used in the framework of the PhD thesis of Clemente Arenas [2]. It is fabricated in an industrial process and is destined for use in airborne applications. In the discussion presented below, this second antenna is referred to as new antenna. In this section, low- $\epsilon_r$  3D-printing filament material is considered for the dielectric layer. This allows printing the entire superstrate structure together. Any shift in resonant frequency resulting from this choice can be eventually explained from the arguments stated earlier in chapter 3. Here, the antenna and its characteristics are presented first. Next, the superstrate is adapted to function with the new antenna. Finally, the radiation performance of the antenna superstrate assembly is presented.

#### 4.3.1 New Antenna

Up until now, a square patch antenna functioning at 1.25 GHz (as described in chapter 3) has been considered as the source for various dielectric superstrates in this thesis. For the experimental validation, an existing antenna is used. This antenna has been provided by Airbus Group Innovations and is a dual-orthogonal polarized antenna (that can be used to perform circular polarization with the help of hybrid coupler). A photo of the antenna is shown in Fig. 4.6.

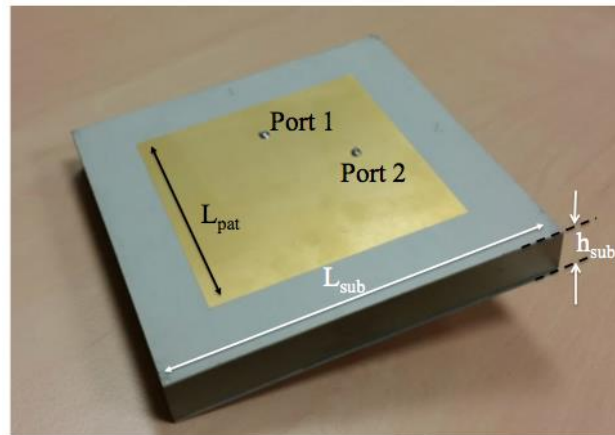


Fig. 4.6 Patch antenna prototype

Corresponding dimensions are provided in Table 4.9.

Table 4.9 Dimensions of patch antenna

Parameter	Value (mm)
$L_{pat}$	68.5
$L_{sub}$	100
$h_{sub}$	14.032

This antenna is almost identical in shape and size to the antenna described in chapter 3, but the composition of the antenna substrate is different. It comprises of 12mm thick Perspex sheet ( $\epsilon_r = 2.67$ ,  $\tan(\delta) = 0.021$ ) sandwiched between two layers (0.508 mm, 1.524 mm) of Rogers RT6002 substrates ( $\epsilon_r = 2.94$ ,  $\tan(\delta) = 0.0012$ ). The magnitude of simulated and measured reflection coefficients are plotted in Fig. 4.7.

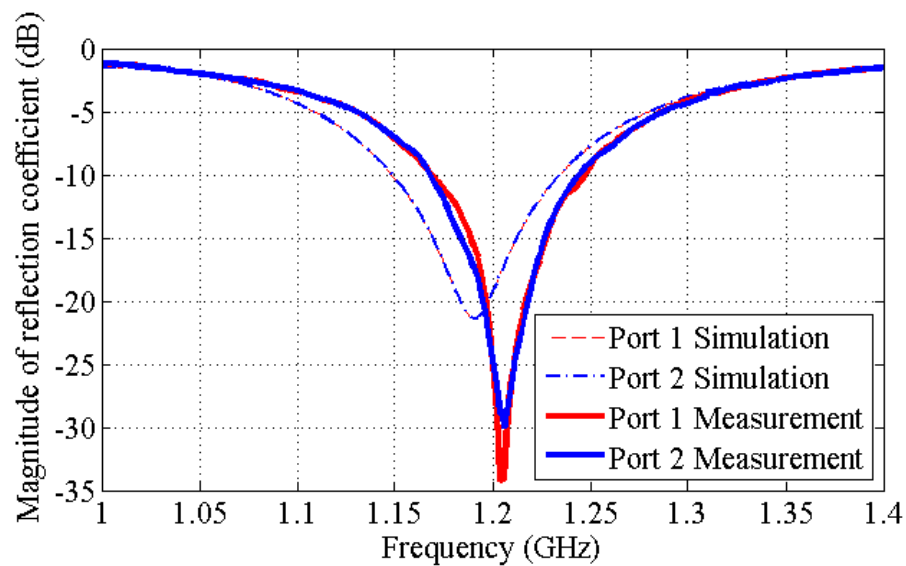


Fig. 4.7 Simulated and measured magnitudes of reflection coefficient of two port antenna

In simulation, the antenna operates at 1.189 GHz with an impedance bandwidth ( $|S_{11}| < -10$  dB) of 85 MHz or 7.1% at 1.19 GHz. In measurement, the antenna operates at 1.206 GHz with an impedance bandwidth of 76 MHz or 6.3% at 1.206 GHz. Since both ports are identical, either of them may be used in the current application. In the present study, Port-1 is considered, while Port-2 is terminated with 50  $\Omega$ . The antenna has the broadside radiation pattern like typical patch antenna, with a peak-realized gain of 5.7dB at 1.189 GHz in simulation, as shown in Fig. 4.8. The cross-polarization level of the antenna is at least 15 dB smaller than co-polar level at the operating bandwidth.

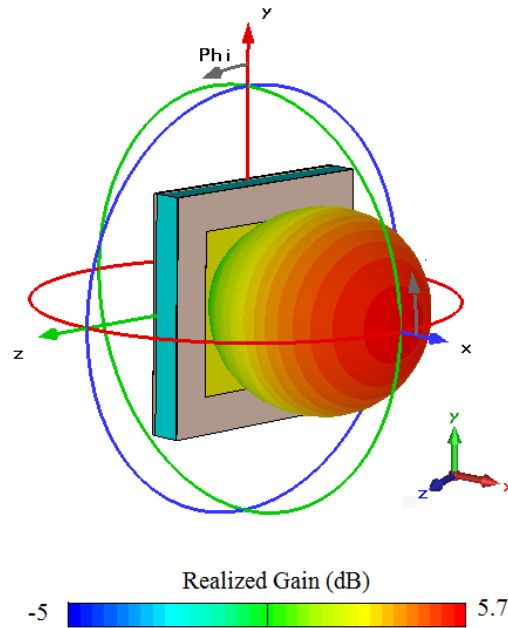


Fig. 4.8 Simulated realized gain (dB) of the new antenna at 1.189 GHz.

As this antenna behaves similarly to the previous one, it is concluded that this antenna can be used with the two material superstrate designed in 4.2.2. Nevertheless, it is necessary to slightly modify the superstrate as the operating frequency of this new antenna is different.

### **4.3.2 Adjustment of superstrate to new dielectric matching layer and new antenna**

In this section, some modifications in the design of superstrate are described. These modifications are necessary due to two reasons: firstly, the new antenna (described in the previous sub-section) operates at a different frequency. Secondly, relative permittivity of the dielectric matching layer is equal to low- $\epsilon_r$  (3D printer material) to facilitate the fabrication. Both these changes result in a shift of the operating frequency of the superstrate. As a result, adjustment in the dimensions of the superstrate is required. This is explained below.

The new antenna described in the previous sub-section is slightly different from the one used in chapter 3; its operating frequency is 1.189 GHz (in simulation.) As a result, the operating frequency of the antenna superstrate assembly has changed. Furthermore, the relative permittivity of dielectric matching layer is changed to low- $\epsilon_r$  (4.4) in order to facilitate fabrication. It may be recalled from 3.3.3.2 that changing the permittivity results in shift of operating frequency. Upon simulating the two-material superstrate designed in 4.2.2 with the new antenna and a dielectric matching layer of relative permittivity equivalent to low- $\epsilon_r$ , the new operating frequency is observed to be 1 GHz. Realized gain at 1 GHz is plotted in Fig. 4.9 (a). It is seen that the superstrate ceases to reorient the electromagnetic waves in the azimuthal plane as per spatial transformation. This deviation in performance of the superstrate is expected due to the change in electrical size of the superstrate, as explained in the following paragraph.

Originally, the superstrate is designed to function at  $f = 1.25$  GHz. At 1.25 GHz, physical dimensions (150 mm by 150 mm by 28.8 mm) correspond to  $0.625\lambda$  by  $0.625\lambda$  by  $0.12\lambda$  in terms of wavelength. But at the new operating frequency of  $f' = 1$  GHz, the same dimensions become  $0.50\lambda'$  by  $0.50\lambda'$  by  $0.09\lambda'$ . This implies that the superstrate is electrically smaller at the new operating frequency. To counter this change in electrical size, all dimensions in the design are transposed from 1.25 GHz to 1 GHz i.e. each dimension is multiplied by a factor of 1.25.

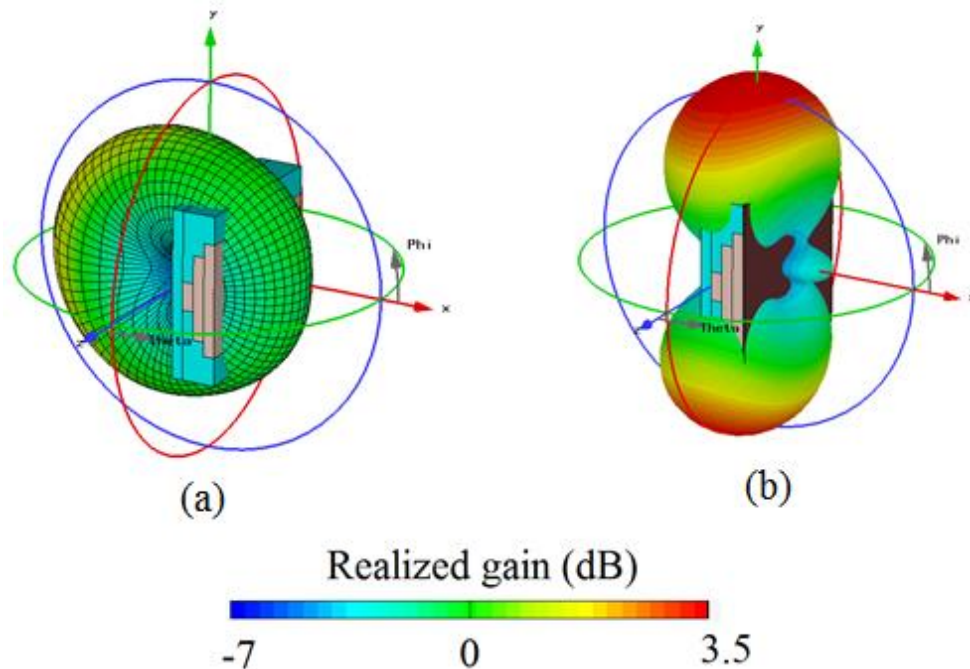


Fig. 4.9 Comparison of realized gains of dielectric superstrate with new antenna and 3D printed dielectric layer (a) at 1 GHz prior modification; (b) at 1.06 GHz after modification

On simulating this new superstrate with the new antenna and a dielectric layer with relative permittivity of 4.4, the operating frequency is found out to be  $f^* = 1.06$

GHz. The dimensions of the superstrate are  $0.66\lambda^*$  by  $0.66\lambda^*$  by  $0.13\lambda^*$  at  $f^*$ , which are similar to the dimensions in chapter 3. At 1.06 GHz, the new antenna-superstrate assembly radiates with an antipodal radiation pattern, as seen in Fig. 4.9 (b). This also allows concluding that performance of the superstrate is dependent upon the operating frequency.

This is the final superstrate design upon which the practically fabricated version is based. While the operating frequency of this design is different from 1.25 GHz (previously defined as design frequency in chapter 3), it may be recalled that the primary objective pursued in this chapter is to present a proof-of-concept and not respect a particular design specification. In the next section, some details on fabrication are provided.

### 4.3.3 Fabrication of the superstrate

Proof-of-concept devices are fabricated according to the readapted superstrate described in the previous section. However, certain modifications are made to prepare the superstrate for measurements. A schematic of the fabricated device in Fig. 4.10 shows these modifications. A system is devised to secure the alumina sheets inside the receptacle. A 3 mm thick Plexiglas cover sheet is used to cover the alumina sheets from the top to prevent them from falling out during measurement. Nylon screws are used to secure Plexiglas cover sheet to superstrate holes. Holes for the screws are 3D printed. 3 mm thick sheets are also 3D printed on either side of the superstrate's staircase structure along  $z$ -axis that alumina sheets don't slide out of the receptacle during the measurement. L-shaped bends are added on the backside of the superstrate to slide in and fix the antenna in position with respect to the superstrate. The addition of these cover sheets and screws to secure the position of alumina sheets does not affect the spatial transformation and antipodal radiation pattern is conserved. The radiation performances are discussed in context of the prototypes in the next sub-section.

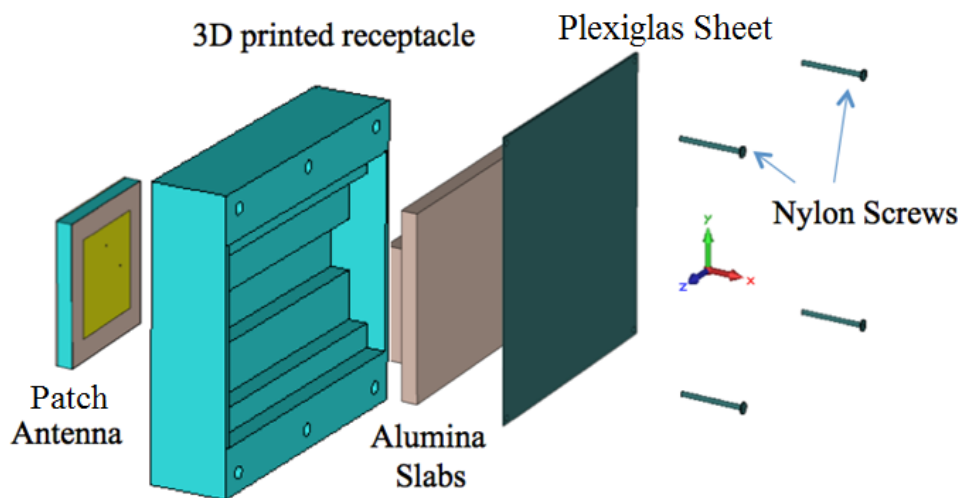


Fig. 4.10 Schematic of the proposed design.

The receptacle is fabricated at the 3D printing facility of Airbus Group Innovations. In the previous sections, the low- $\epsilon_r$  material was modeled on PREPERM TP 20280 with a relative permittivity of 4.4. The comparatively high relative permittivity of 4.4 of this material would allow strict implementation of the discretized profile by accessing a larger range of permittivity values, as seen in 4.2.1. But as the relaxed profile interpretation described in 4.2.2 also allows interpreting the spatial transformation without adherence to individual pixel permittivity values, the constraint of high permittivity 3D printing material can be eased. For practical implementation, two materials are considered:

1. **Objet-FullCure photo curable resin:** A photo curable resin by Objet's Fullcure photocurable resins is used to design a solid receptacle at Airbus Group Innovations. The resin has a relative permittivity of 2.8. Change in permittivity from 4.4 to 2.8 (with losses) results in a decrease of the realized gain from 4.1 dB to 2.7 dB. However, antipodal radiation pattern is conserved.
2. **PLA Thermoplastic:** Measured characteristics of sample material are reported as  $\epsilon_r = 2.56$ ,  $\tan\delta = 0.031$ . But the 3D printer used for additive layering of PLA filament automatically generates a mesh structure to account for thermal expansion. As a result the relative permittivity of the receptacle is close to air (simulated value of 1.1). Change in permittivity from 4.4 to 1.1 (without losses) results in a decrease of the realized gain from 4.1 dB to 3 dB. However, antipodal radiation pattern is conserved.

Appendix C.b) presents relevant information on the materials and 3D printers in context of fabrication. A discussion on change of material is also presented later in chapter 5 (section 5.2.) Next, tolerances in fabrications and measurements are discussed, which may then be used subsequently to explain any deviations in the simulated and measured performance.

- Quality of materials:

The performance of the device depends primarily on the quality of the build. The alumina sheets are ordered from Goodfellow™ with a 5% tolerance on the smallest dimension (12.5 mm). 99.7% pure alumina corresponds to the relative permittivity value of 9.9. The manufactured alumina sheets are shown in Fig. 4.11. The corresponding dimensions are given in Table 4.10.

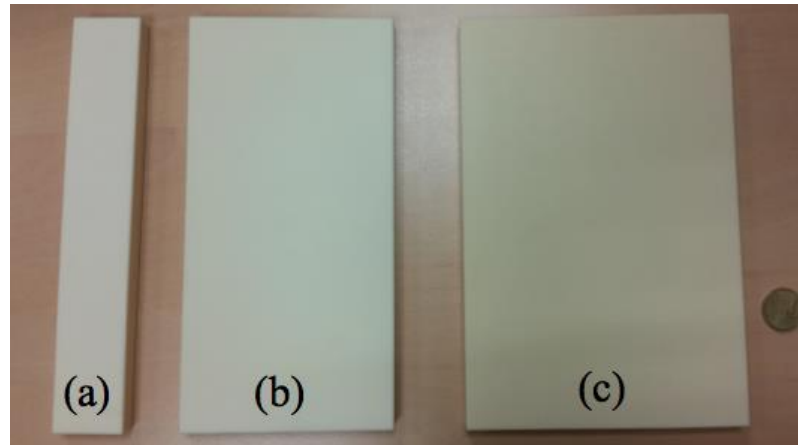


Fig. 4.11 Three layers of alumina sheets: (a) Bottom, (b) Middle, (c) Top.

Table 4.10 Alumina sheet dimensions

Layer	Dimension (mm)
(a)	187.5 by 125 by 12.5 ( $\pm 0.6$ )
(b)	187.5 by 93.75 by 12.5 ( $\pm 0.6$ )
(c)	187.5 by 31.25 by 12.5 ( $\pm 0.6$ )

As for the 3D printed receptacles, the photo-curable resin based design is built in a relatively superior quality. The photograph of the fabricated receptacle is shown in Fig. 4.12. The Objet's Eden260 VS polyjet printer is used for designing the FullCure superstrate. It takes longer time to complete the process but has 16-micron layer accuracy. The alumina sheets fit inside the receptacle without any extra machining effort. However, a little material has been manually filed off from the L-bends on the backside to facilitate the positioning of antenna vis-à-vis the superstrate. Also, measured electrical properties ( $\epsilon_r = 2.8$ ,  $\tan \delta = 0.02$ ) in X-band of sample of Fullcure are used in the simulations.

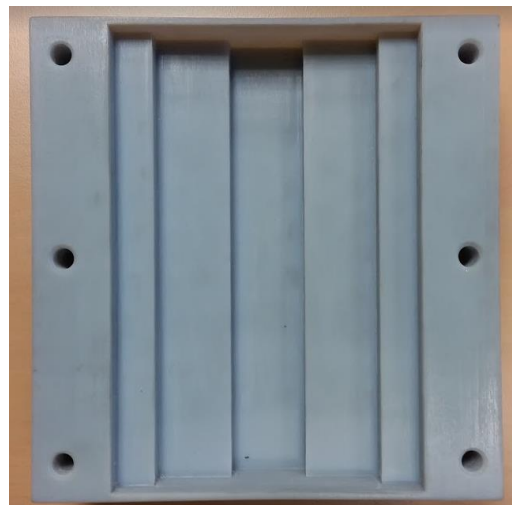


Fig. 4.12 Receptacle made from photo cured FullCure resin.

PLA based superstrate based is designed using filament based 3D printing process. The photograph of the fabricated receptacle is shown in Fig. 4.13. This requires passing the filament through a heated nozzle, which is then used to deposit the material in shape of the superstrate. While this process allows rapid prototyping, the build of the final product is not ideal. Firstly, the relative permittivity in the medium is close to air due to the auto-generated mesh structure by the 3D printer. A cross-section showing this mesh is shown in Fig. 4.14. Furthermore, the heat retained in the superstrate results in expansion in certain dimension. Therefore, material is manually filed away from prototype to allow fitting the alumina slabs and antennas in the superstrate. This degrades the condition of the final device. As the auto-generated mesh is comprised of air, the losses in this superstrate are ignored. The relative permittivity value is found out using retroactive simulation. This will be described in the last sub-section.

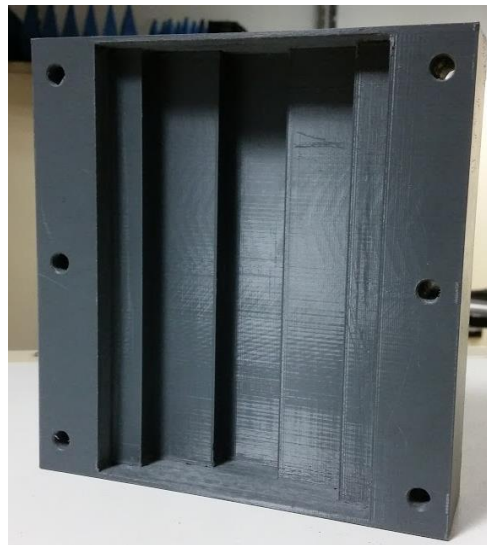


Fig. 4.13 Receptacle made from PLA filament.

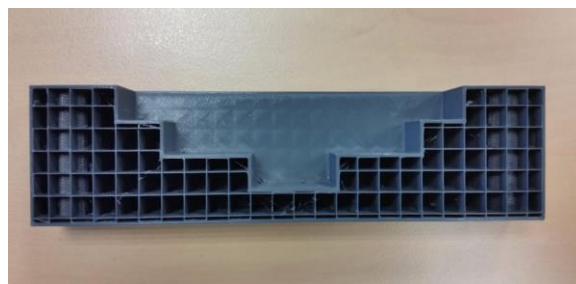


Fig. 4.14 Cross-section of PLA based superstrate showing mesh structure.

- Measurement conditions:

Apart from the fabrication tolerances, conditions of the measurement may be kept in mind while evaluating the results. The measurements are carried out in far field in the anechoic chamber at Telecom ParisTech. The room can be used from 700 MHz upwards, which is compatible with current requirements. Antenna Under Test (AUT), here dielectric

superstrate with the new antenna, is placed on computer controlled rotating platform. A second antenna (ETS Lindgren Model 3117) is used as the reference on a static mast. Observations are made in three planes of the Cartesian coordinate system ( $x y$ ,  $y z$  and  $x z$ ). It may be noted here that AUT is not exactly aligned with the reference antenna due to limitations of the available positioning system. A shift of 5-10 cm is incurred (depending on plane and direction of measurement). This introduces deviation in measured results compared to simulation in certain directions in all the three planes. Furthermore, superstrate is slightly tilted ( $2^{\circ}$ - $3^{\circ}$ ) during measurements in  $y z$  plane due to its heavy weight. Deviation in the results may also be expected due to the different operational frequency of the antenna in simulation and measurement, as discussed in 4.3.1. Finally, it also may be noted that a 15 mm Plexiglas sheet is used to fix the antenna superstrate assembly to the mast for measurement in  $x y$  and  $x z$  planes, whereas a ABS plastic based 3D printed supporting structure is used for the same purpose in  $y z$  plane. In the next sub-section, the measured performances of the new antenna with FullCure and PLA superstrates are discussed in detail.

#### **4.3.4 Performance of the new antenna with 3D printed superstrates**

In this sub-section, the measured performance of the two versions of the dielectric superstrate is presented. FullCure superstrate is discussed first.

##### *4.3.4.1 Performance of new antenna with FullCure superstrate*

The first superstrate is designed using Objet's FullCure range of photo curable resin material printed in Objet Eden260 VS printer at Airbus Group Innovations, Suresnes. As said in the previous sub-section, properties of this material have been borrowed from the results of a previous characterization effort in X-band:  $\epsilon_r = 2.8$ ,  $\tan \delta = 0.02$ . This material has also been used previously in [2], [93]. The magnitude of the reflection coefficient of the new antenna with FullCure superstrate is plotted in Fig. 4.15. The operating frequency of the antenna superstrate assembly is 1.10 GHz in simulation and is 1.14 GHz in measurement. This shift may be explained mainly by the differing operational frequencies of the source antenna itself in simulation and measurement. The simulated bandwidth ( $|S_{11}| < -10$  dB) of the antenna is 65 MHz (5.9% at 1.10 GHz) and measured bandwidth is 65 MHz (5.2% at 1.14 GHz). An antipodal radiation pattern with a peak realized gain 2.7 dB is achieved at 1.10 GHz in simulation, as shown in Fig. 4.16. The figure also identifies the  $x y$ ,  $y z$  and  $x z$  planes in which the radiation patterns are compared.

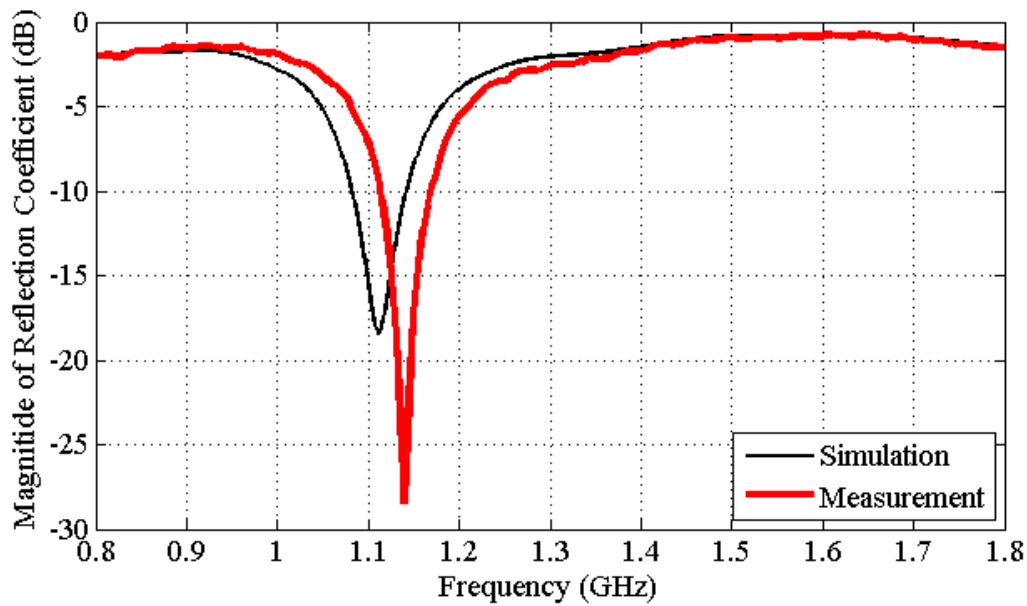


Fig. 4.15 Comparison of simulated and measured magnitudes of reflection coefficient for new antenna with FullCure superstrate.

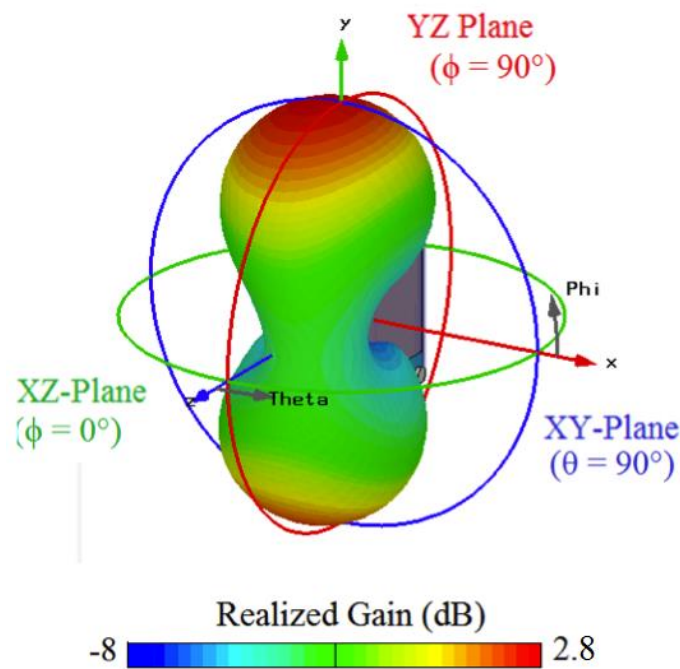


Fig. 4.16 Simulated realized gain (dB) of new antenna with FullCure superstrate at 1.10 GHz.

Next, the measured performance of the FullCure superstrate is presented from Fig. 4.17 to Fig. 4.25 at 1.11 GHz (lower bound of measured impedance bandwidth), 1.14 GHz (measured operating frequency) and 1.17 GHz (upper bound of measured impedance bandwidth). Co polar and cross-polar radiation patterns are plotted in  $x y$ ,  $y z$  and  $x z$  planes. Black lines in these plots correspond to simulated results and red lines correspond to measurements. Solid lines represent the co-polar patterns and dashed lines represent the

cross-polar patterns. As the operating bandwidths in simulation and measurement are not same, the measured performance at operating frequency is compared with simulated performance at 1.10 GHz (simulated operating frequency.) Only measured performance is presented at the 1.11 GHz and 1.17 GHz. The cross polarization levels in the plots are deemed acceptable if they are at least 10 dB smaller than the co polar level in the main lobe.

- At 1.11 GHz:

In Fig. 4.17-19, measured co-polar and cross-polar radiation patterns are plotted at lower frequency bound of measured impedance bandwidth i.e. 1.11 GHz. Solid red lines represent co-polar patterns and dashed red lines represent cross-polar patterns. In Fig. 4.17,  $x$   $y$  plane co polar pattern shows two distinct lobes along  $\phi = \pm 100^\circ$  with peak realized gain of 0.7 dB and a null in broadside direction (-8.3 dB at  $\phi = 0^\circ$ ). Cross-polar level in the lobe along  $\phi = -100^\circ$  is 8.2 dB smaller than co polar level.

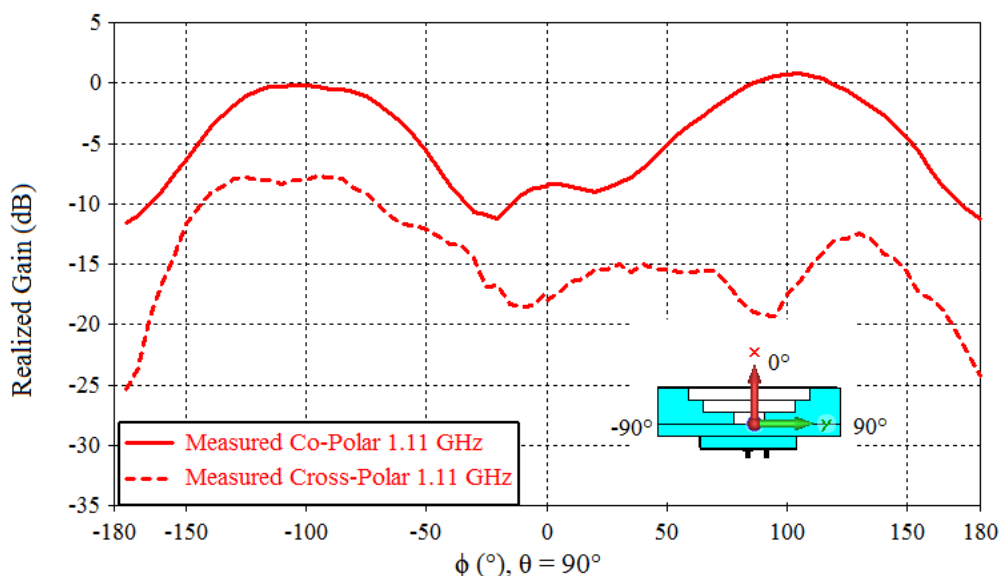


Fig. 4.17 Measured realized gain of FullCure superstrate at 1.11 GHz in  $x$   $y$  plane ( $\theta = 90^\circ$ ).

In Fig. 4.18,  $y$   $z$  plane co polar pattern shows two distinct lobes along  $\theta = \pm 90^\circ$  with peak realized gain of 2.8 dB and a null along  $z$ -axis (minima along  $\theta = 5^\circ, -175^\circ$ ). Cross-polar level in main lobes ( $\theta = \pm 90^\circ$ ) is at least 10.5 dB smaller than co-polar component. But it increases to -3.3 dB along positive  $z$ -axis ( $\theta = 0^\circ$ ).

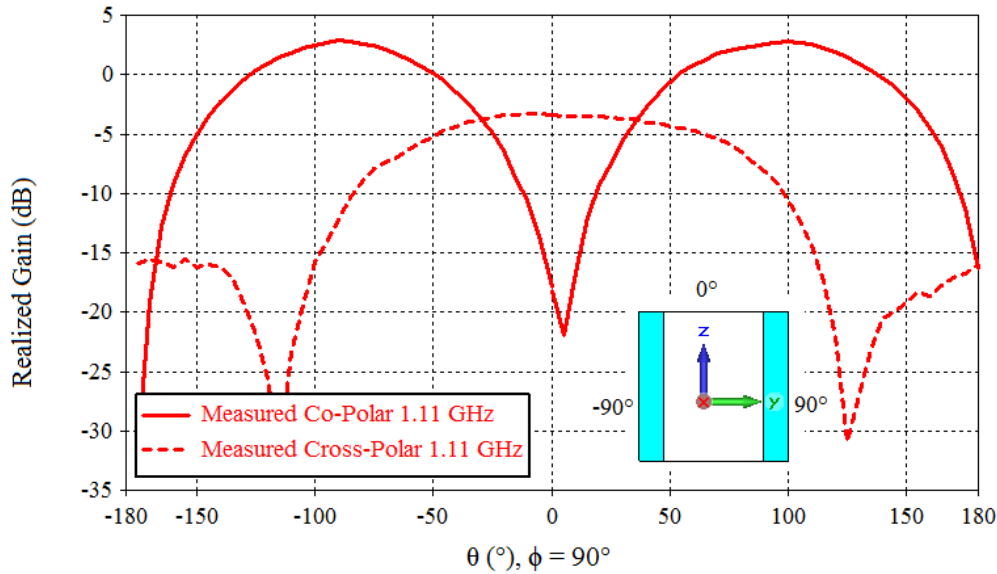


Fig. 4.18 Measured realized gain of FullCure superstrate at 1.11 GHz in  $y z$  plane ( $\phi = 90^\circ$ ).

In Fig. 4.19, co polar level in  $x z$  plane is -2.4 dB and cross-polar level is -15 dB in the plane. Results show that directivity of antenna is altered in accordance with coordinate transformation at lower bound of impedance bandwidth.

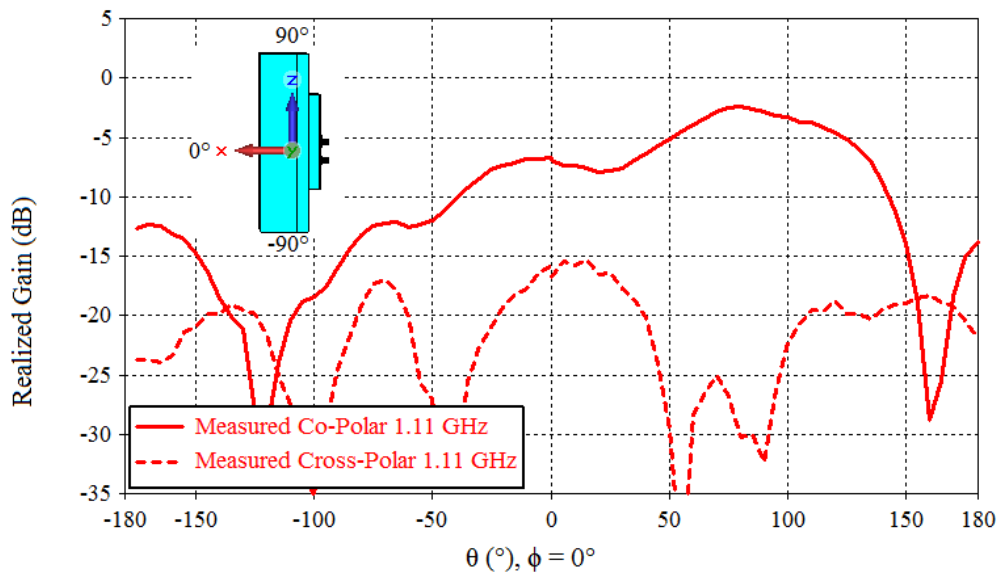


Fig. 4.19 Measured realized gain of FullCure superstrate at 1.11 GHz in  $x z$  plane ( $\phi = 0^\circ$ ).

- At operational frequency, 1.14 GHz:

In Fig. 4.20, the simulated co-polar component in  $x y$  plane ( $\theta = 90^\circ$ ) is represented by solid black line with a peak realized gain of 2.4 dB at  $\phi = \pm 100^\circ$ , where  $\phi = \pm 90^\circ$  corresponds to  $y$ -axis. A null is achieved in the broadside direction ( $\phi = 0^\circ$ ) with -18.6 dB. The measured co-polar component is represented by solid red line with a peak realized gain of 1.8 dB at  $\phi = 100^\circ$ . The second lobe is also observed, with peak realized gain of 0.4 dB at  $\phi$

=  $-85^\circ$ . The two patterns show a broad agreement as far as the reorientation is concerned. The smaller value of realized gain may be attributed to the non-alignment of AUT with the reference antenna during measurement. A tertiary lobe in the broadside direction is also observed with a value of  $-6.6$  dB along  $\phi = 0^\circ$ . The simulated cross-polar pattern (dashed black line) is at least  $12.7$  dB smaller than co-polar pattern in the direction of the two main lobes. But the cross polarization level is  $-4.7$  dB at  $\phi = -85^\circ$ , as seen in dashed red line.

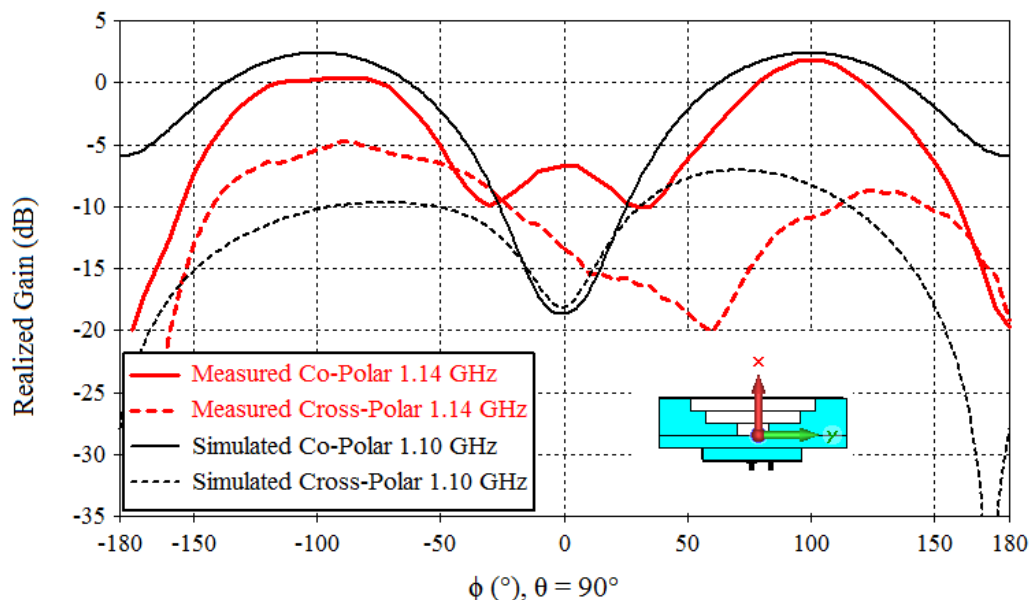


Fig. 4.20 Comparison of simulated (1.10 GHz) and measured (1.14 GHz) realized gains of FullCure superstrate in  $x y$  plane ( $\theta = 90^\circ$ ).

In Fig. 4.21, the simulated co-polar component in  $y z$  plane ( $\phi = 90^\circ$ ) presents a peak realized gain of  $\sim 2.3$  dB at  $\theta = -92^\circ, 95^\circ$ , where  $\theta = \pm 90^\circ$  corresponds to  $y$ -axis in the plane. A null is achieved along  $z$ -axis ( $\phi = 0^\circ, 180^\circ$ ) with  $-20.6$  dB at  $\phi = 2^\circ$ . The measured co-polar component has a peak realized gain of  $3.5$  dB at  $\theta = -90^\circ$  (along  $y$ -axis). The second lobe at  $\theta = 90^\circ$  has a realized gain value  $3.2$  dB. The shape of simulated (dashed black line) and measured (dashed red line) cross-polar patterns is nearly identical, and as in the previous case measured cross polarization level is  $-0.7$  dB along  $z$ -axis ( $\theta = 0^\circ$ ). The two patterns show close agreement, and the shifts may be explained by the slight tilted in antenna superstrate in measurement plane.

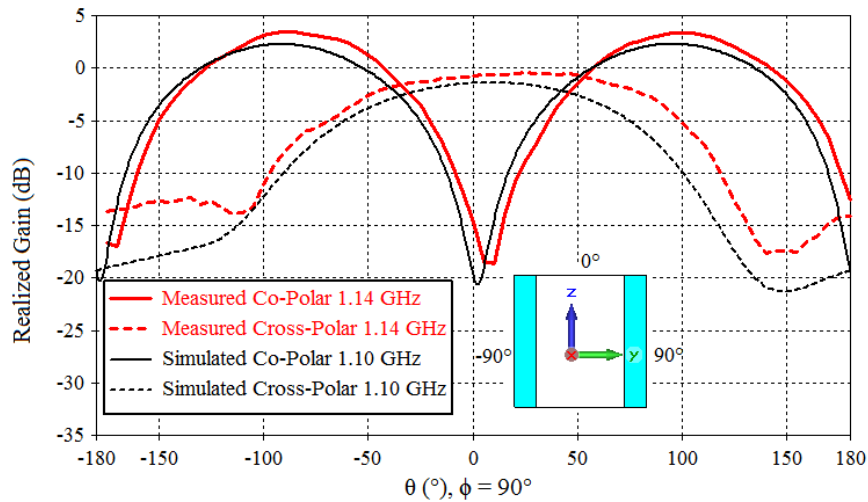


Fig. 4.21 Comparison of simulated (1.10 GHz) and measured (1.14 GHz) realized gains of FullCure superstrate in  $y z$  plane ( $\phi = 90^\circ$ ).

In Fig. 4.22, the simulated co-polar component in  $x z$  plane ( $\phi = 0^\circ$ ) is represented by solid black line with a peak realized gain of -1 dB at  $\theta = 101^\circ$ . The measured co-polar component is represented by solid red line with a peak realized gain of -0.7 dB at  $\theta = 85^\circ$ . The realized gain along  $x$ -axis ( $\theta = 0^\circ$ ) is almost same as in Fig. 4.20. The simulated and measured results are in close agreement with each other. The low gain in  $x z$  plane is expected as the superstrate is designed to reorient the radiation along  $y$ -axis. Maximum cross polarization level in the measurement is -12.3 dB at  $\phi = 0^\circ$ .

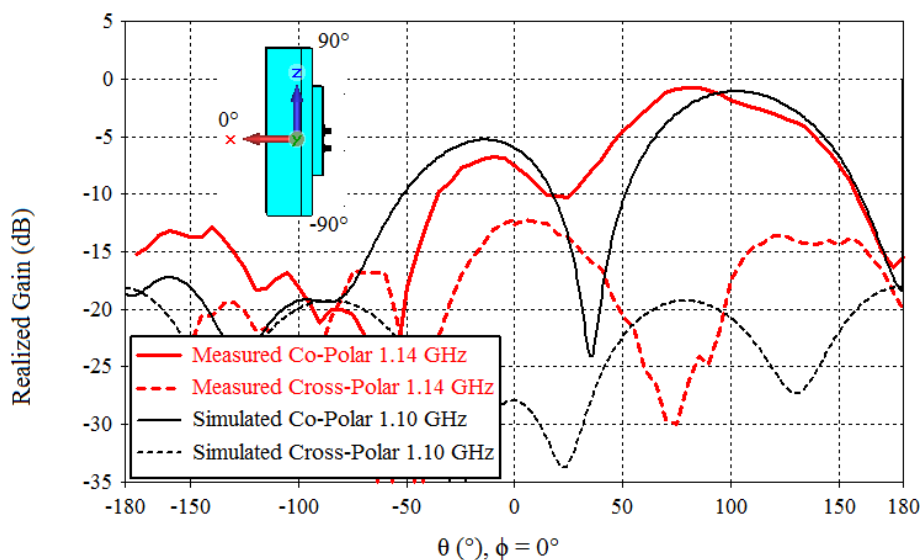


Fig. 4.22 Comparison of simulated (1.10 GHz) and measured (1.14 GHz) realized gains of FullCure superstrate in  $x z$  plane ( $\phi = 0^\circ$ ).

- At 1.17 GHz:

In Fig. 4.23-25, measured co-polar and cross-polar radiation patterns are plotted at the upper frequency bound of measured impedance bandwidth i.e. 1.17 GHz. Solid red lines

represent the co-polar patterns and dashed red lines represent cross-polar patterns. In Fig. 4.23, co polar pattern in  $x y$  plane shows two distinct lobes along  $\phi = -81^\circ, 95^\circ$  with peak realized gain of 0.7 dB. A tertiary lobe along null broadside direction is also observed (-5 dB at  $\phi = 0^\circ$ ). Cross-polar level in lobe along  $\phi = -85^\circ$  is 4 dB smaller than co polar pattern. In general, copolar level is high in the two lobes.

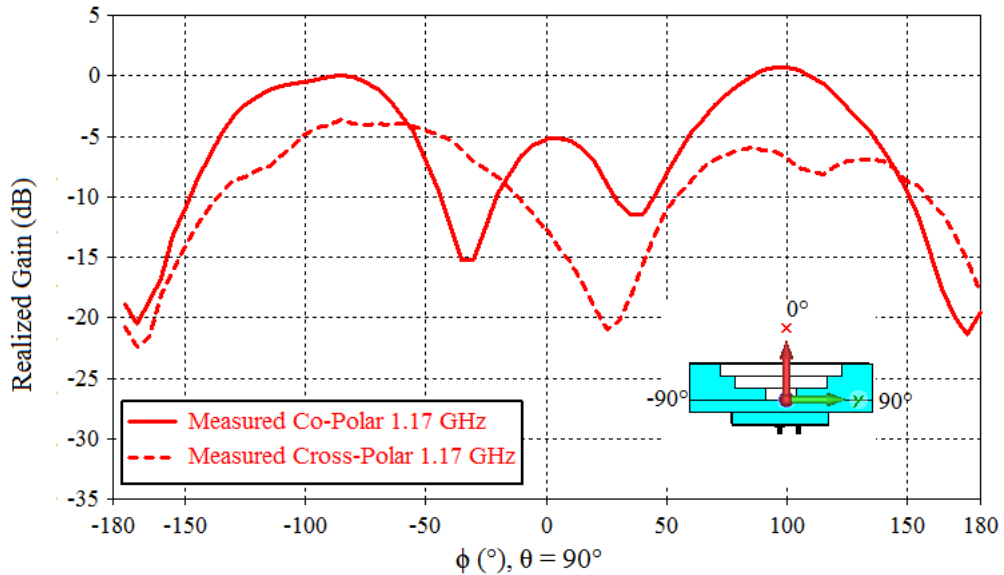


Fig. 4.23 Measured realized gain of FullCure superstrate at 1.17 GHz in  $x y$  plane ( $\theta = 90^\circ$ ).

In Fig. 4.24,  $y z$  plane co polar pattern shows two distinct lobes along  $\theta = \pm 95^\circ$  with peak realized gain of 2.1 dB and a null along  $z$ -axis (minima along  $\theta = 5^\circ, -170^\circ$ ). The cross-polar level in the main lobes ( $\theta = \pm 90^\circ$ ) is at least 6 dB smaller than the co-polar component.

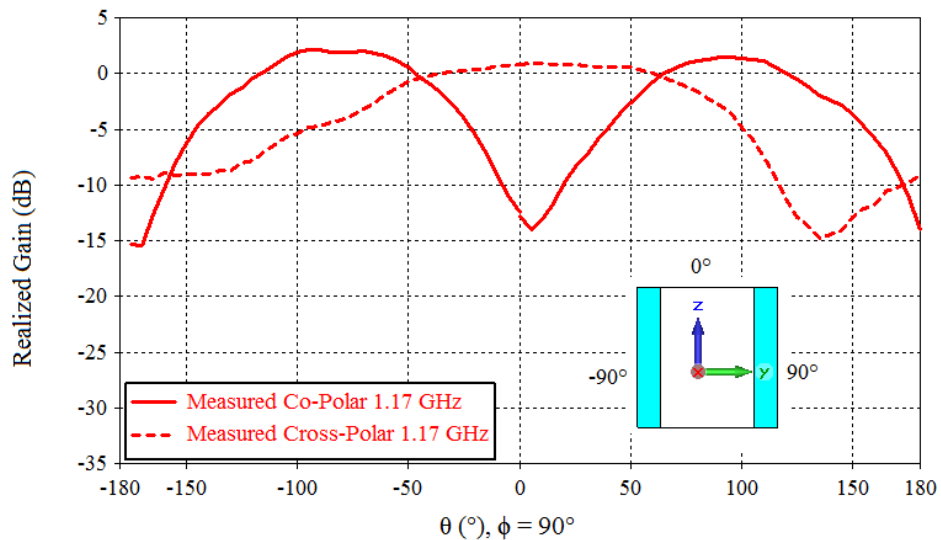


Fig. 4.24 Measured realized gain of FullCure superstrate at 1.17 GHz in  $y z$  plane ( $\phi = 90^\circ$ ).

In Fig. 4.25, co polar level in  $xz$  plane is  $-0.2$  dB and cross-polar level is  $-11$  dB in the entire plane. These results show that directivity of antenna is altered as per design at the upper bound of impedance bandwidth.

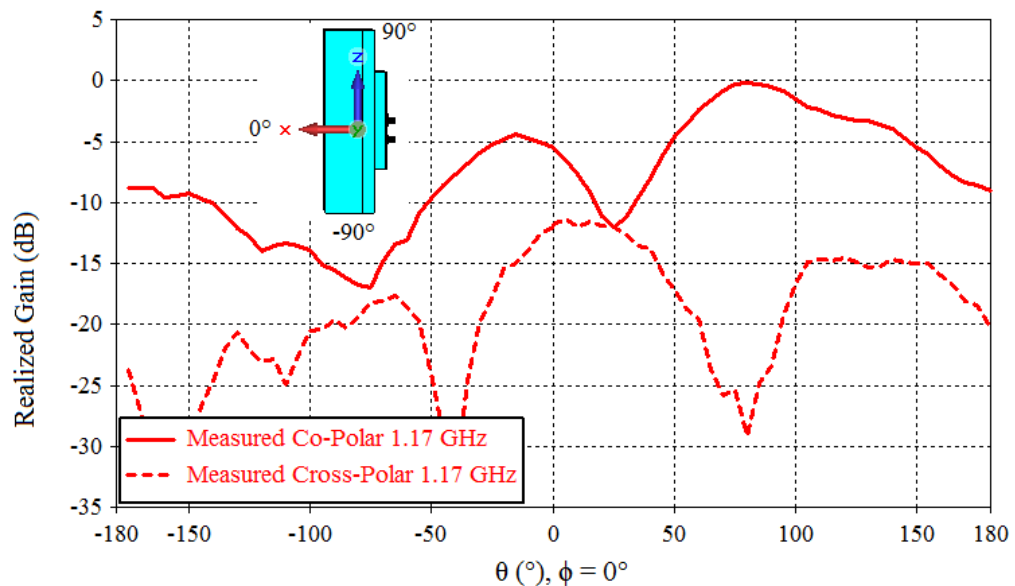


Fig. 4.25 Measured realized gain of FullCure superstrate at 1.17 GHz in  $xz$  plane ( $\phi = 0^\circ$ ).

In general, the antenna's directivity appears to be modified as per the coordinate transformation using the FullCure superstrate. The simulation and measurement are in broad agreement with each other at the corresponding operational frequencies. Peak realized gain is achieved in the azimuthal plane along  $y$ -axis. At the operating frequency, the maximum realized gain in measurement is  $3.5$  dB in  $yz$  plane. The co-polarization level is a problem in the design, but its origin has already been identified in chapter 3 during the design of dielectric superstrate with pixilated profile (3.3.3.2). The antenna superstrate assembly is capable of conserving the antipodal radiation behavior on the lower and upper bounds of the impedance bandwidth. As a general rule, the level of cross polarization in measurement increases from lower to higher frequencies in impedance bandwidth. The reorientation performance of the superstrate validates the proof-of-concept. In next sub-section, performance of PLA superstrate is discussed.

#### 4.3.4.2 Performance of new antenna with PLA Superstrate

The second superstrate is designed using a PLA filament. The prototype is made thanks to help received from Airbus Group Innovations, Suresnes. Electrical properties of this material are made available thanks to a previous characterization effort in X-band:  $\epsilon_r = 2.56$ ,  $\tan \delta = 0.03$ . But 3D printer used for this filament takes in account thermal expansion due to heat retention, and therefore auto-generates a mesh to prevent any deformation. Hence,

electrical properties inside effective medium do not correspond to those of the PLA filament but are close to air. As also said earlier in 4.3.3, losses are ignored in simulation. Magnitude of reflection coefficient is plotted in Fig. 4.26. Measured operating frequency of the antenna and PLA superstrate is 1.245 GHz. Using retroactive simulations, the relative permittivity of the printed structure is found approximately equal to 1.1. This is shown in Fig. 4.26, where the simulated curve (black) is fit to the measured curve (red). The simulated and measured bandwidths ( $|S_{11}| < -10$  dB) of the antenna superstrate assembly are nearly identical: 64 MHz in simulation (5.1% at 1.245 GHz) and 60 MHz in measurement (4.9%). An antipodal radiation pattern with a peak realized gain 3 dB is achieved at 1.245 GHz in simulation, as shown in Fig. 4.16. The figure also shows  $x y$ ,  $y z$  and  $x z$  planes in which the radiation patterns are compared.

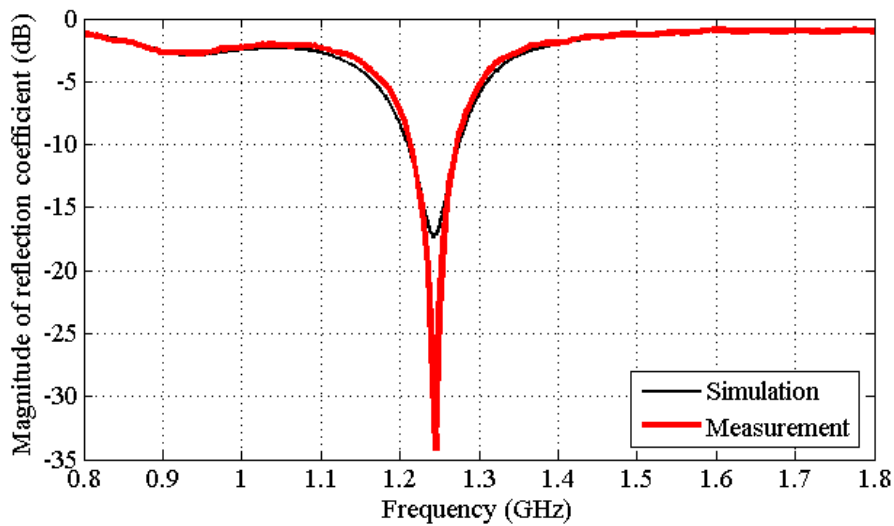


Fig. 4.26 Simulated and measured magnitudes of reflection coefficient for PLA superstrate.

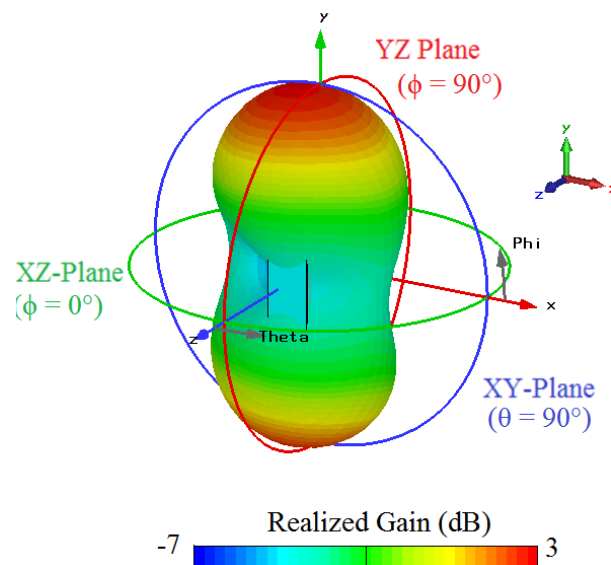


Fig. 4.27 Simulated realized gain (dB) of new antenna with PLA superstrate at 1.245 GHz.

Next, the measured performance of this PLA superstrate is presented in its operational bandwidth from Fig. 4.28 to Fig. 4.36. The cross polarization levels in the plots are deemed acceptable if they are at least 10 dB smaller than the co polar level in the main lobe.

- At 1.21 GHz:

In Fig. 4.28-30, the measured co-polar and cross-polar radiation patterns are plotted at lower frequency bound of measured impedance bandwidth i.e. 1.21 GHz. The performance in  $x y$  plane is plotted in Fig. 4.28; co polar patterns shows two distinct lobes along  $\phi = \pm 100^\circ$  in simulation with peak realized gain of 1.7 dB, and 2.4 dB at  $\phi = -95^\circ, 115^\circ$  in measurement. In both simulation and measurement, level of cross-polar component is at least -10 dB in the plane. While two lobes are not pronounced (with only 2 dB difference between broadside and azimuth), the maximum is in the azimuthal plane nevertheless. It is also noticed that the measured co-polar pattern in  $x y$  plane is not smooth, unlike the one obtained with FullCure superstrate (Fig. 4.20). It is tough to pinpoint to one single reason for this. The quality of the build is poor and has been machined to fit. In addition, the effect of mesh generated by the 3D printer has not been taken in to account in simulations. Overall, the simulated and measured results are in close agreement.

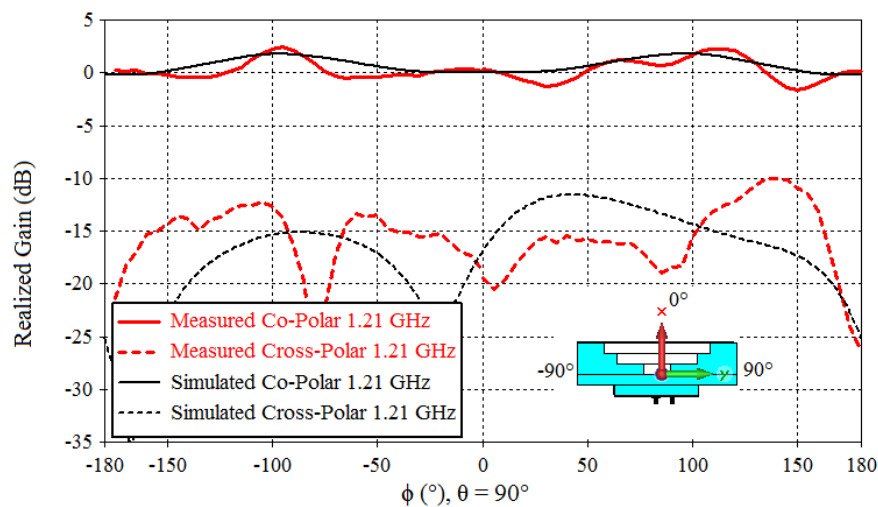


Fig. 4.28 Comparison of simulated and measured realized gain (dB) of PLA superstrate at 1.21 GHz in  $x y$  plane ( $\theta = 90^\circ$ ).

In Fig. 4.29,  $y z$  plane co polar pattern shows two distinct lobes along  $\theta = \pm 90^\circ$  with peak realized gain of 2.4 dB and a null along  $z$ -axis (minima along  $\theta = 0^\circ, -175^\circ$ ). The cross-polar level in the main lobes ( $\theta = \pm 90^\circ$ ) is at least 13.5 dB smaller than the co-polar component but, like in all other  $y z$  plane plot, presents an increased level along  $z$ -axis ( $\theta = 0^\circ$ ) to a value of -6.6 dB. A near complete agreement between simulation and measurement is observed in this plane.

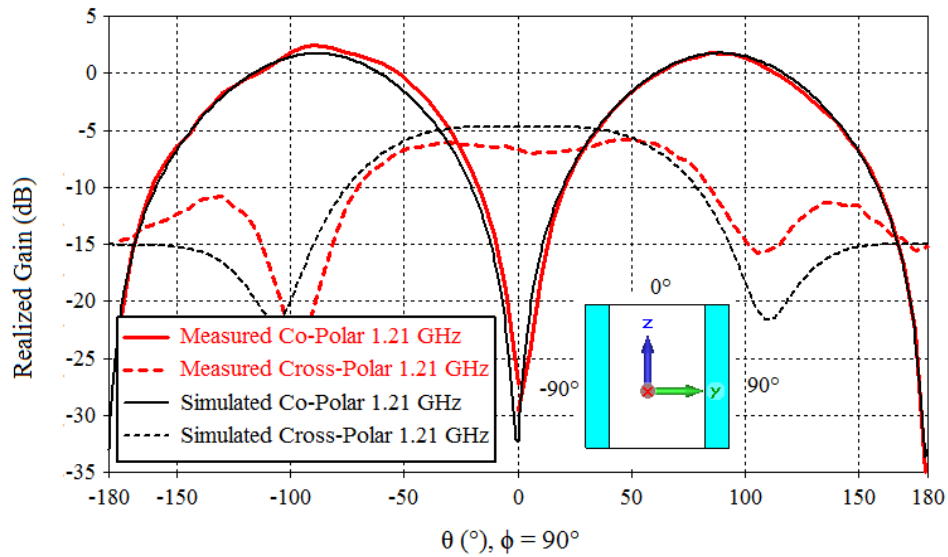


Fig. 4.29 Comparison of simulated and measured realized gain (dB) of PLA superstrate at 1.21 GHz in  $y z$  plane ( $\phi = 90^\circ$ ).

In Fig. 4.30, measured co polar level in  $x z$  plane is 1.8 dB and cross-polar level is -12 dB in the entire plane. While the amplitude of realized gain may differ, the simulated and measured patterns are in broad agreement with each other in this plane also.

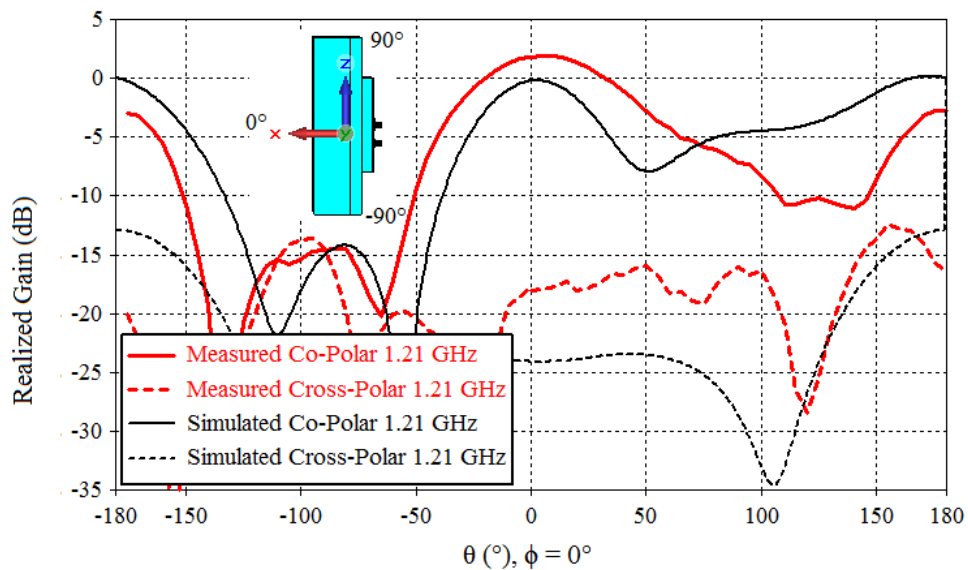


Fig. 4.30 Comparison of simulated and measured realized gain (dB) of PLA superstrate at 1.21 GHz in  $x z$  plane ( $\phi = 0^\circ$ ).

- At operational frequency, 1.245 GHz:

In Fig. 4.31, the simulated co-polar component in  $x y$  plane ( $\theta = 90^\circ$ ) has a peak realized gain of 2.8 dB at  $\phi = \pm 97^\circ$ , where  $\phi = \pm 90^\circ$  corresponds to  $y$ -axis in the plane. The measured co-polar component has a peak realized gain of 4.1 dB at  $\phi = -100^\circ$ . The second lobe is also observed, with peak realized gain of 3.7 dB at  $\phi = 115^\circ$ . A tertiary lobe in the broadside direction is also observed with a value of 0 dB along  $\phi = 0^\circ$ . The measured cross-

polar pattern is at least 14 dB smaller than co-polar pattern in the direction of the two main lobes.

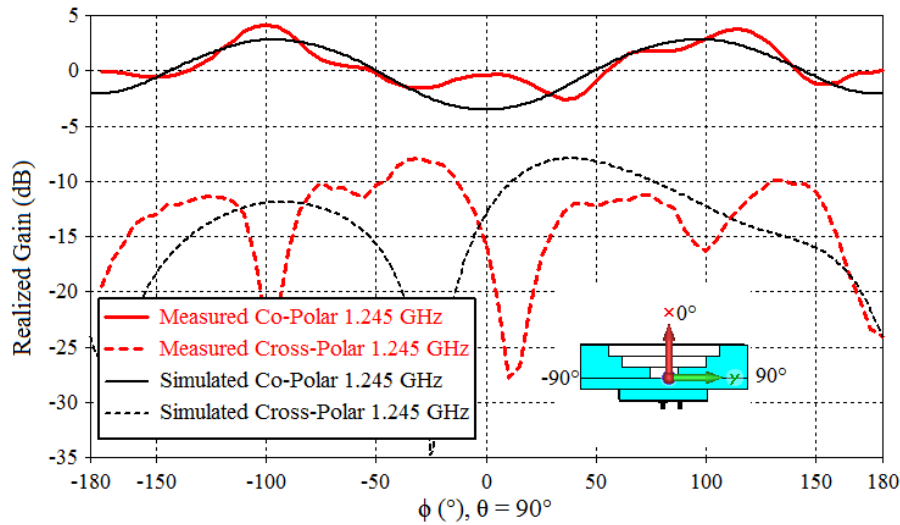


Fig. 4.31 Comparison of simulated and measured realized gain (dB) of PLA superstrate at 1.245 GHz in  $x y$  plane ( $\theta = 90^\circ$ ).

In Fig. 4.32, the simulated co-polar component in  $y z$  plane ( $\phi = 90^\circ$ ) has a peak realized gain of  $\sim 2.7$  dB at  $\theta = -86^\circ, 87^\circ$ , where  $\theta = \pm 90^\circ$  corresponds to  $y$ -axis in the plane. A null is achieved along  $z$ -axis ( $\phi = 0^\circ, 180^\circ$ ) with  $-28.6$  dB at  $\phi = 0^\circ$ . The measured co-polar component has a peak realized gain of 4.1 dB at  $\theta = -90^\circ$  (along  $y$ -axis). The second lobe at  $\theta = 90^\circ$  has a realized gain value 3.6 dB. These peak values also correspond to the realized gain obtained in  $x y$  plane along  $y$ -axis. The simulated and measured cross-polar patterns are nearly identical. In both the lobes along the  $y$ -axis, the cross-polar level is at least 11.5 dB smaller than the co-polar level. The simulated and measured patterns are in close agreement.

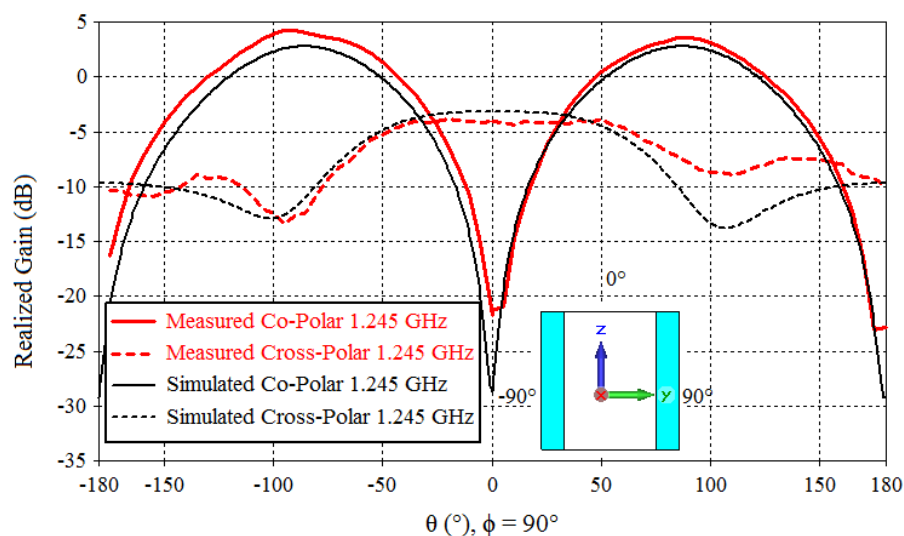


Fig. 4.32 Comparison of simulated and measured realized gain (dB) of PLA superstrate at 1.245 GHz in  $y z$  plane ( $\phi = 90^\circ$ ).

In Fig. 4.33, the simulated co-polar component in  $xz$  plane ( $\phi = 0^\circ$ ) is represented by solid black line with a peak realized gain of -1.9 dB at  $\theta = 6^\circ$ . The measured co-polar component is represented by solid red line with a peak realized gain of 1 dB at  $\theta = 15^\circ$ . The low gain in  $xz$  plane is expected as the superstrate is designed to reorient the radiation along  $y$ -axis. The maximum cross polarization level in the plot is -12.3 dB. The simulated and measured results are in broad agreement with each other.

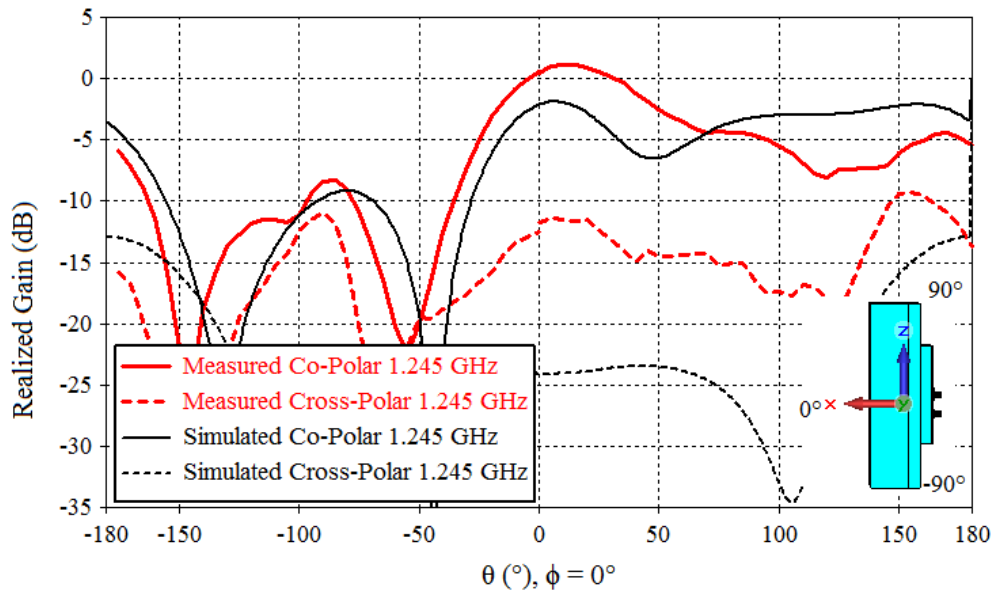


Fig. 4.33 Comparison of simulated and measured realized gain (dB) of PLA superstrate at 1.245 GHz in  $xz$  plane ( $\phi = 0^\circ$ ).

- At 1.27 GHz:

In Fig. 4.34-36, the measured co-polar and cross-polar radiation patterns are plotted at the upper frequency bound of measured impedance bandwidth i.e. 1.27 GHz. In Fig. 4.34, co polar patterns in  $xy$  plane shows two distinct lobes along  $\phi = \pm 96^\circ$  in simulation with peak realized gain of 2.6 dB, and 3.6 dB at  $\phi = -100^\circ, 110^\circ$  in measurement. In simulation, level of co-polar pattern in broadside direction ( $\phi = 0^\circ$ ) is at -8.6 dB; a tertiary lobe along null broadside direction is also observed (-2 dB at  $\phi = 0^\circ$ ). Nevertheless, the two lobes in azimuthal plane are pronounced. The cross-polar level in the two lobes is at least 14 dB smaller than the co polar level.

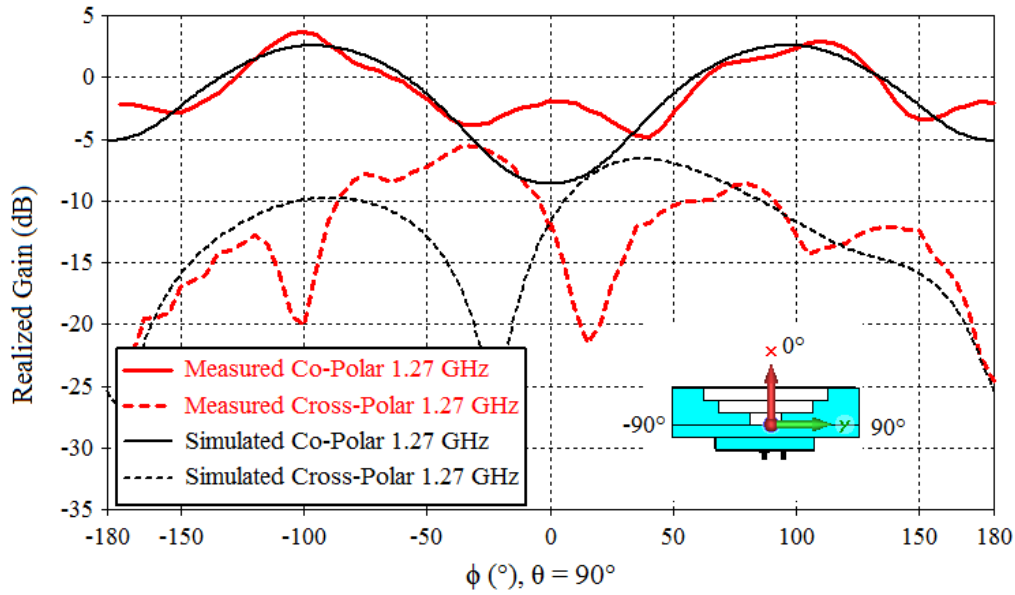


Fig. 4.34 Comparison of simulated and measured realized gain (dB) of PLA superstrate at 1.27 GHz in  $x y$  plane ( $\theta = 90^\circ$ ).

In Fig. 4.35, simulated and measured performance in  $y z$  plane is compared. Co polar pattern shows two distinct lobes along  $\theta = \pm 84^\circ$  with peak realized gain of 2.6 dB and a null along  $z$ -axis ( $\theta = 0^\circ, 180^\circ$ ). In measurement, the peak realized gain of 3.4 dB is obtained at  $\theta = -82^\circ$ . The cross-polar level in the main lobes ( $\theta = \pm 90^\circ$ ) is 9.5 dB smaller than the co-polar component.

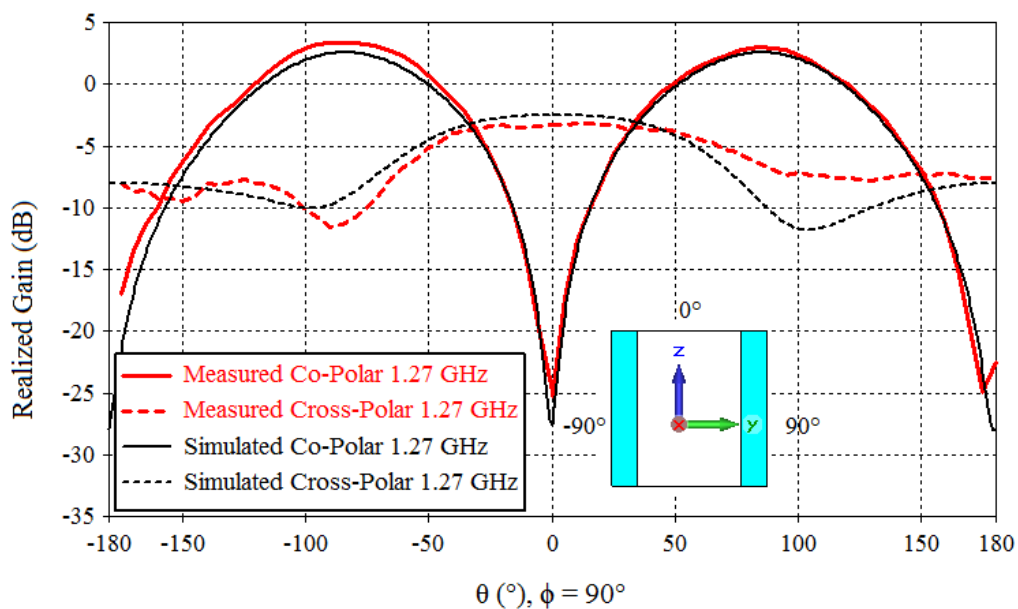


Fig. 4.35 Comparison of simulated and measured realized gain (dB) of PLA superstrate at 1.27 GHz in  $y z$  plane ( $\phi = 90^\circ$ ).

In Fig. 4.36, simulated co polar level in  $x z$  plane is -2.3 dB and measured co polar component is -1.7 dB. Highest cross-polar level is -8.3 dB in this plane. These results confirm

that the superstrate conserve the antipodal radiation pattern in upper bound of the impedance bandwidth.

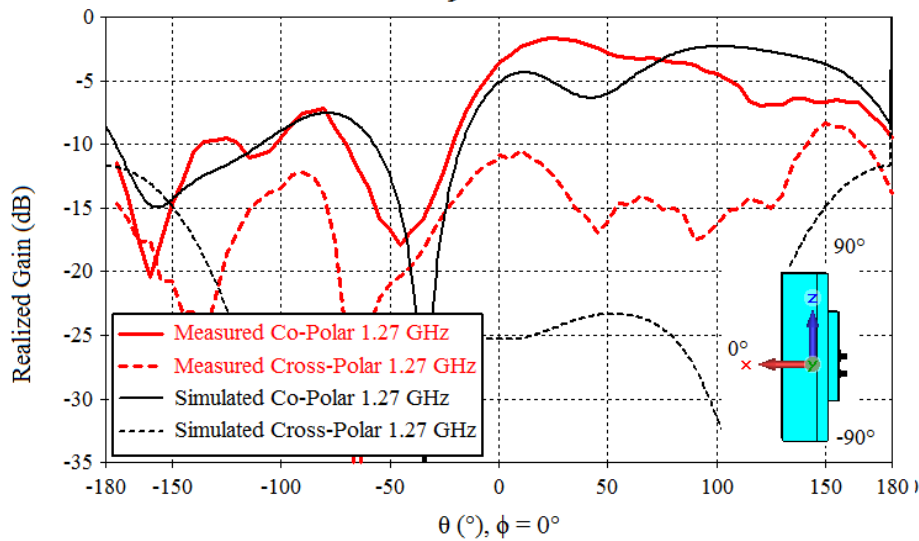


Fig. 4.36 Comparison of simulated and measured realized gain (dB) of PLA superstrate at 1.27 GHz in  $xz$  plane ( $\phi = 0^\circ$ ).

In a general conclusion on the measurement performance of the PLA superstrate, the antenna's directivity is modified as per the coordinate transformation. This is especially visible in the close agreement between simulated and measured performances achieved in  $yz$  plane. The  $xy$  plane also shows the reorientation towards the azimuthal plane; however the measured plots are not smooth, unlike the ones achieved in the FullCure superstrate. While it is difficult to pin-point a single reason, it is mainly attributed to significant deviation from simulated profile due to mesh structure with in the superstrate generated during 3D printing and the eventual post fabrication machining done to overcome the expansion due to heat retention in the material. Thus, these results also underline the importance of quality of the printing process. Like previously, the level of cross polarization increases from lower to higher frequencies in the impedance bandwidth. Nevertheless, it is concluded the superstrate is capable of reproducing the reorientation despite all the fabrication errors. The maximum realized gain is 4.1 dB along the  $y$ -axis, as witnessed in the co-polar plots of  $xy$  and  $yz$  planes at the operating frequency.

## 4.4 Discussion

In this chapter, the fabrication of the dielectric superstrate has been discussed. The contribution of this chapter is two fold. Firstly, the two material fabrication strategy is a very simple approach to interpret a spatial transformation with a stark permittivity gradient that is originally comprised of large number of permittivity values. The systematic simplification allows designing the superstrate with only two dielectric materials arranged in four separate

pieces (one 3D printed receptacle and 3 alumina sheets.) Secondly, two versions of the receptacles have been fabricated using two different processes of 3D printing: UV light cured FullCure resin based process and PLA filament based process. Both concepts are in broad agreement with simulated performance. Moreover, the discussion also highlights the advantages and problems associated with the two processes. The FullCure design offers better quality, but is costly and requires longer time to complete. The PLA based design is much more economical and faster to build, but the quality of fabrication is significantly inferior to the FullCure based solution.

In the next chapter, extrapolations of the design ideas discussed in chapter 3 and 4 have been presented. New design ideas pertaining to installation of the superstrates on large structures are also presented.



## 5. Extrapolations and New Designs

In the previous chapters, the design and implementation of a TO inspired dielectric superstrate has been presented for completely reorienting antenna radiation pattern in the azimuthal plane. The wave-propagation behavior inside this profile has been designed by coordinate transformation technique. The procedure described in chapter 3 incorporates certain design freedoms in form of compression,  $n$ -index shift, virtual space, etc. which all can be used to adapt the spatial transformations for other applications. In this chapter, new designs based on the original spatial transformation of chapter 3 are presented, which use these degrees of freedoms in the design to achieve unique behaviors. Also, the simplicity of solution presented in chapter 4 is investigated. A general design guideline towards interpretation of superstrates based on similar transformation is provided. Finally, a few results are presented to comment on possible future research tracks originating from the presented results.

### 5.1 Extrapolations using degrees of freedom in design

As stated above, a couple of degrees of freedoms are available in the design procedure described in chapter 3, which can be further used to extrapolate the previously presented solution towards new applications. The degrees of freedom and their application are explained below:

- *An interplay of compression and shift factors:*

In the previous chapters, a complete reorientation in azimuthal plane was achieved inside a compressed space using careful tuning of compression and  $n$ -index shift factors. The first case study presents a new solution based on same root spatial transformation, where a wide HPBW radiation pattern in one plane is achieved by tuning  $a$ ,  $b$  and  $m$ .

- *Choice of virtual space:*

The transformation used in the previous chapters transformed a Cartesian space into a virtual space comprised of two-quarter ellipses. The chosen virtual space was entirely dictated by the desired reorientation pattern, wherein an antipodal radiation pattern was desired. An alternate application will be presented in the second case study to reorient electromagnetic waves uniquely in quarter-space.

### 5.1.1 Case 1: Superstrate for semi-circular radiation pattern

The spatial coverage offered by a typical patch antenna is limited to a quarter space i.e. HPBW around  $90^\circ$ . Wide beams are of significant interests in a variety of applications, for example to improve link budget for wireless applications, obstacle detection in radars, etc. One such TO inspired wide beam dielectric solution has been recently proposed in [111], where the authors present a fan beam radiation pattern in Ku-band (12.4-18 GHz). Non-uniformly perforated F4B superstrates are used to fabricate the lenses, where the variation in permittivity is between 1.07 and 2.65. The aperture of the lens is  $10\lambda$  at the operating frequency of 15 GHz.

Indeed, enhancing the HPBW can greatly increase the applicability of patch-based solutions in aerospace industry. For example, GNSS (Global Navigation Satellite System) applications require conformal or low-profile antennas installed on top of airplane fuselage. Such antennas are required to provide wide-angle coverage to maintain communication links with satellites during the rolling motion of aircraft. In this section, a dielectric superstrate inspired from Transformation Optics is presented which allows modifying the radiation pattern of a patch antenna for increasing its HPBW. Fig. 5.1 is a representative figure showing the original and modified radiation patterns.

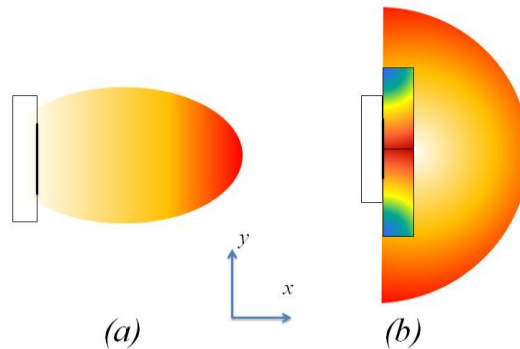


Fig. 5.1 Radiation patterns: (a) antenna alone, (b) antenna with dielectric superstrate to increase HPBW.

The degrees of freedom offered by compression and shift factors are used to achieve a completely new behavior inside previously defined transformation. When placed over the patch antenna, this superstrate increases the half power beam width (HPBW) of a classical patch antenna. In fact, wave propagation is introduced in the azimuthal plane of the device, which is typically a function of fish-eye lenses [54]. Interplay of spatial compression factors ( $a$  &  $b$ ) and refractive index shift factor ( $m$ ) in (3.20) is used to derive a dielectric profile for the required semispherical reoriented wave front.

### 5.1.1.1 Interplay of $a$ , $b$ and $m$

The size of the superstrate is fixed using the axial and lateral compression factors. The spatial compression factors are chosen:  $a = 3$ ,  $b = 1.5$ , which corresponds to a size of the  $0.67\lambda \times 0.16\lambda$  in terms of wavelength at design frequency,  $f = 1.25$  GHz. Next, the value of  $m$  in ( 3.20 ) is iterated in simulation. For  $m = 5.5$ , a semi-circular wave front is achieved. The permittivity variation inside an optimized profile is shown in Fig. 5.2. It may be noted here that the patch antenna is modeled by ideal current sheet backed with PEC sheet, as detailed earlier in chapter 3.

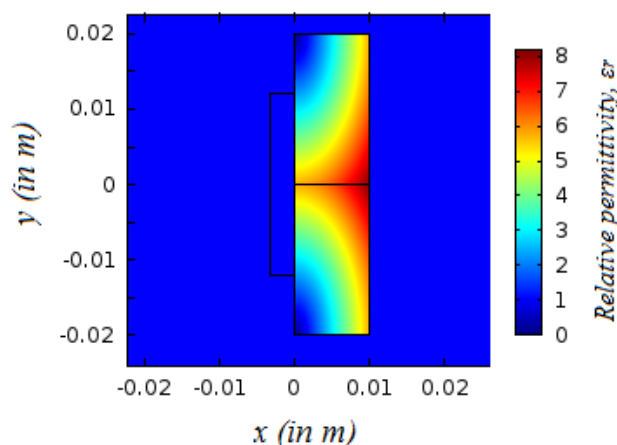


Fig. 5.2 Relative permittivity profile ( $\epsilon_r$ ) in the transformed profile for a semi-cylindrical wavefront.

The variation in permittivity inside the profile is  $0 < \epsilon_r < 8.14$ . The dispersive values in the profile ( $\epsilon_r < 1$ ) are spatially located in small region in the top and bottom left corners in the profile. The normalized electric field  $E_z$  is plotted in Fig. 5.3. The coordinate transformation with chosen parameters reorients the electric field along  $y$ -axis while also allowing propagation in the entire half plane along positive  $x$ -axis. The wave front is semi-circular in shape, which allows envisaging the superstrate to greatly increase the antenna HPBW.

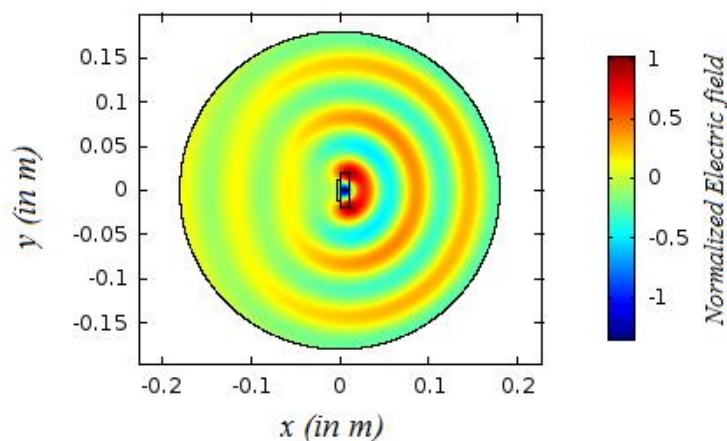


Fig. 5.3 Normalized electric field,  $E_z$  (V/m) at 1.25 GHz.

### 5.1.1.2 Dielectric superstrate for semi circular radiation pattern

Next, the continuous profile is discretized in to a profile with finite number of permittivity values. Like in 3.3.2.3, the profile is discretized in to 48 pixels, arranged in 3 layers with 16 pixels each; the dielectric permittivity of these blocks varies between 1 and 8. Dispersive permittivity values in the continuous profile are ignored due to their small spatial presence in the profile. The individual pixel dimension in terms of wavelength is approximately  $0.05\lambda$  by  $0.04\lambda$ . The discretized profile is then extruded along  $z$ -axis. The length is optimized for a semicircular radiation pattern. The cuboidal profile is shown in Fig. 5.4. The dimension of the cuboidal superstrate is 240 mm by 160 mm by 39 mm ( $\lambda$  by  $0.66\lambda$  by  $0.16\lambda$ ).

The square patch antenna previously used in chapter 3 is used again in these simulations. The characteristics of this antenna can be recalled: it is a coaxially fed square patch antenna designed to function at 1.25 GHz. It has a peak directivity of 6.9 dBi at the design frequency with the maximum in the broadside direction (along  $x$ -axis). The HPBW of the antenna is  $92^\circ$ , corresponding to the coverage of a quarter space. It is desired to improve this coverage using the dielectric superstrate. Also as in chapter 3, a dielectric layer is used as an interface between the antenna and the superstrate to provide impedance matching at the design frequency. The relative permittivity of this layer is 1.5. This layer is 12 mm thick, which leads to an overall thickness of the superstrate to  $\sim 0.21\lambda$  at 1.25 GHz.

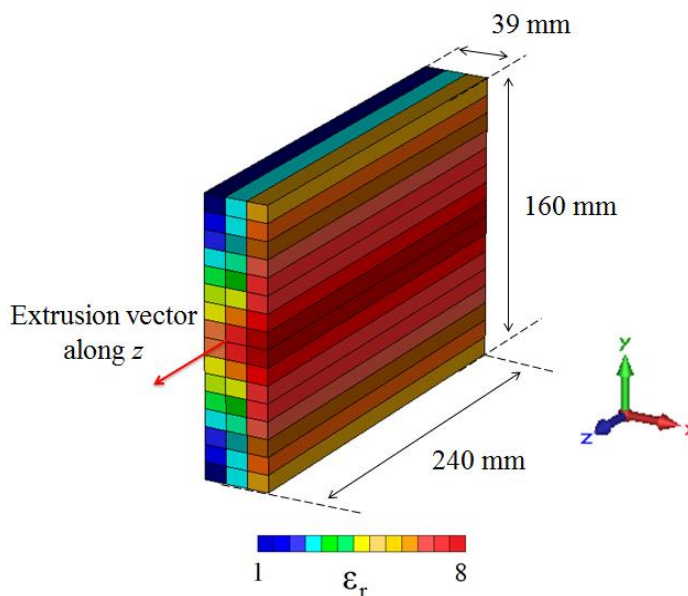


Fig. 5.4 3D superstrate designed from a discretized profile; variation in permittivity restricted between 1 and 8.

The magnitudes of reflection coefficient of antenna alone and antenna with TO-superstrate are compared in Fig. 5.5. It is seen that the antenna without and with the dielectric superstrate are matched at the design frequency.

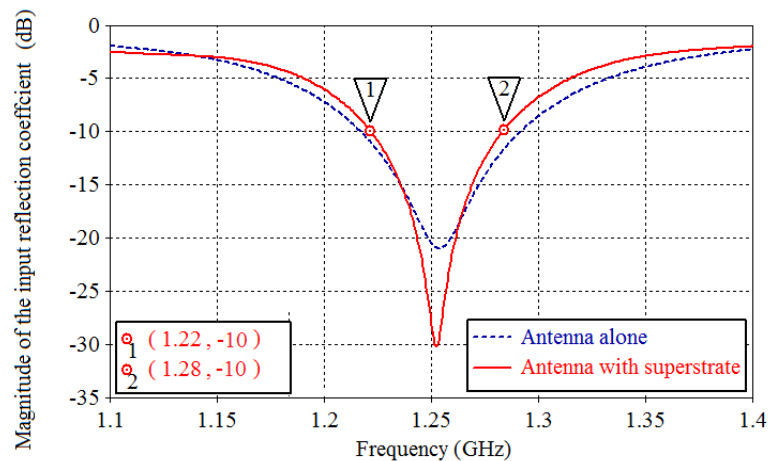


Fig. 5.5 Comparison of magnitudes of reflection coefficient of antenna alone and antenna with superstrate.

The bandwidth of the antenna with superstrate (4.8% at 1.25 GHz) is only slightly diminished in comparison to the original antenna (6.4% at 1.25 GHz). This again underlines the distinct advantage of the dielectric-only nature of the solution. In Fig. 5.6, 3D polar plots of directivity of antenna alone and antenna with superstrate are compared at 1.25 GHz. Fig. 5.6 (a) plots directivity for antenna alone; the maximum directivity is 6.9 dBi and the HPBW is  $92^\circ$ . The maximum directivity of the antenna superstrate assembly is 3.2 dBi in the broadside, as seen in Fig. 5.6 (b). However, values are limited to a maximum of 2 dBi in both the plots so as to clearly highlight the reorientation of field along  $y$ -axis due to superstrate. The contribution of superstrate is clearly visible in Fig. 5.6(b). Next, the co and cross polarizations of the antenna-superstrate are studied in three different planes at design frequency,  $f = 1.25$  GHz. In Fig. 5.7, directivity of the superstrate antenna is plotted in the  $x$ - $y$  plane.

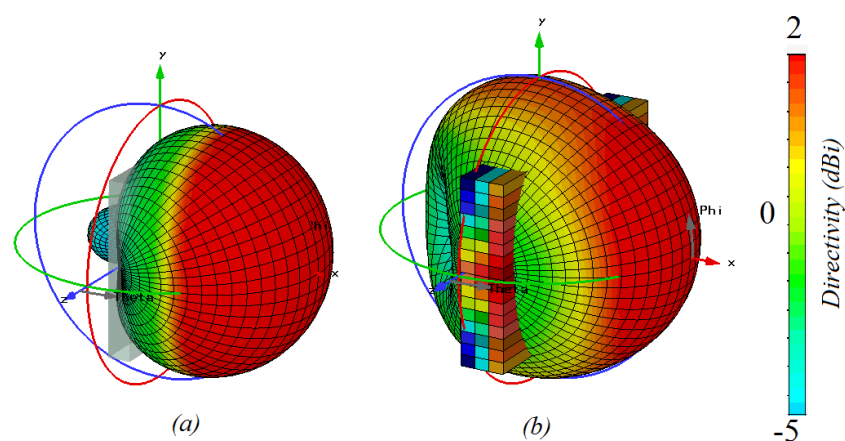


Fig. 5.6 Directivity (dBi): (a) Antenna alone (b) Antenna with superstrate. Maximum value in plots limited to 2 dBi for highlighting reorientation along  $y$ -axis.

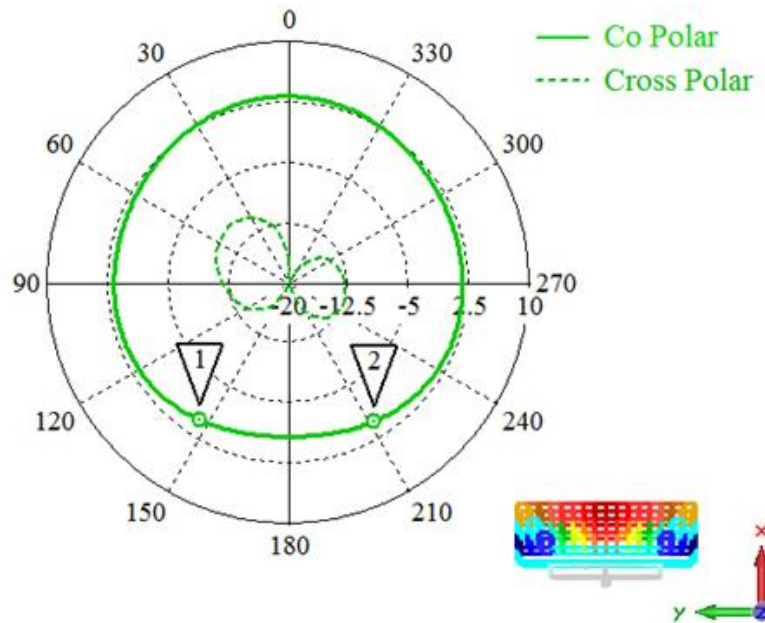


Fig. 5.7 Directivity (dBi) in  $x y$  plane at 1.25 GHz.

A huge increase in HPBW is obtained thanks to the superstrate ( $297^\circ$  between  $148^\circ$  and  $-149^\circ$  ( $209^\circ$ )). The difference between peak co and cross polarization levels in  $x y$  plane is 13 dB. In Fig. 5.8, directivity of the superstrate antenna is plotted in the  $x z$  plane.

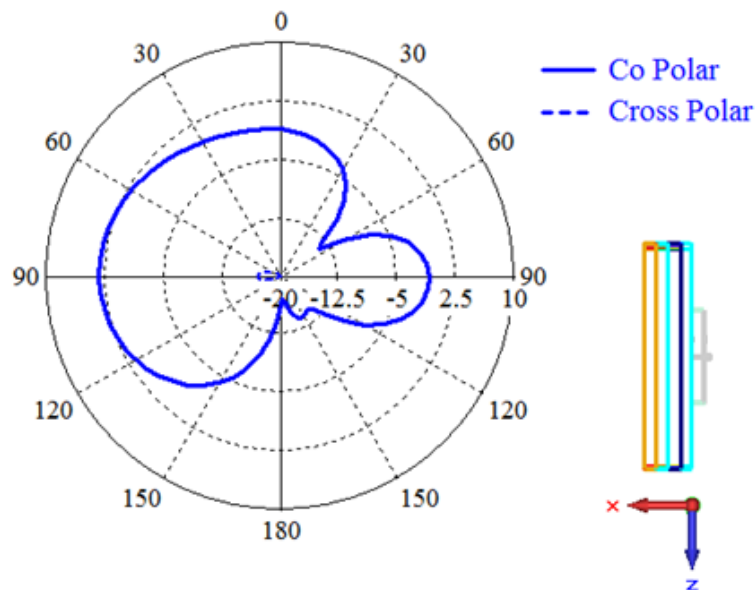


Fig. 5.8 Directivity (dBi) in  $x z$  plane at 1.25 GHz.

In  $x z$  plane, the HPBW is only slightly affected by superstrate's presence: the HPBW of the antenna alone is  $91^\circ$  and the one of the antenna with superstrate is  $94^\circ$ . This is an expected behavior due to the shape of the superstrate and polarization of antenna. The maximum directivity of the antenna superstrate assembly at 1.25 GHz is 3.2 dBi along  $x$ -axis.

The difference between peak co and cross polarization levels in  $xz$  plane is -20 dB. In Fig. 5.9, directivity of the superstrate antenna is plotted in the  $yz$  plane.

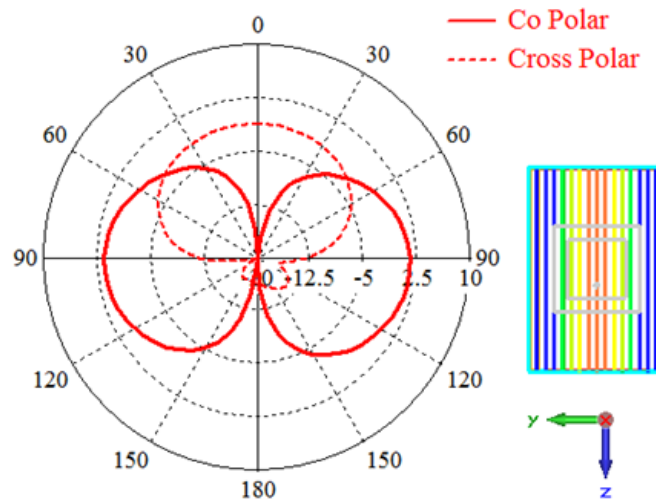


Fig. 5.9 Directivity (dBi) in  $yz$  plane at 1.25 GHz.

The patch antenna without the superstrate has a peak directivity of  $\sim -2.7$  dBi and a quasi-omnidirectional pattern in  $yz$  plane. In contrast, the radiation pattern of patch antenna with superstrate is antipodal in  $yz$  plane, with a peak directivity of 1.5 dBi along the positive and negative  $y$ -axis. This highlights the positive contribution of superstrate towards enhancing directivity along  $y$ -axis. It is noted that the cross-polar level is greater than the co polar in negative  $z$ -axis. But along  $y$ -axis, the co polarization level is 12.6 dB higher than cross-polar level.

A comparison of the antenna without and with superstrate is provided in Table 5.1, where HPBW in  $xy$  plane and peak directivities are compared at different frequencies inside the operational bandwidth.

Table 5.1 Directivity and HPBW comparison of patch antenna with and without superstrate.

Frequency (in GHz)	Antenna alone		Antenna + Superstrate	
	HPBW (x y plane)	Maximum directivity (dBi)	HPBW (x y plane)	Maximum directivity (dBi)
1.22	93°	6.8	234°	4.0
1.23	93°	6.8	275°	3.8
1.24	93°	6.9	288°	3.5
1.25	92°	6.9	297°	3.2
1.26	92°	6.9	302°	2.9
1.27	91°	6.9	306°	2.5
1.28	91°	6.9	308°	2.1

The antenna without superstrate has a uniform performance across the bandwidth, with a peak directivity of 6.9 dBi and HPBW of 92° at the design frequency. In the case of

antenna with superstrate, the peak directivity decreases, but the HPBW is hugely increased compared to antenna alone. It may be further noted here that the HPBW of the antenna superstrate assembly is nearly identical in the higher frequencies in the operational bandwidth ( $297^\circ$  at 1.25 GHz,  $308^\circ$  at 1.28 GHz). However, strong variation of HPBW is observed in the lower frequencies inside the operational bandwidth. HPBW increases from  $234^\circ$  at 1.22 GHz to  $297^\circ$  at 1.25 GHz.

A further insight to the directivity of antenna with superstrate is needed. In Fig. 5.10, directivities are plotted versus frequency. Frequencies inside operational bandwidth are considered. Directivity value along x-axis ( $\theta = 90^\circ, \phi = 0^\circ$ ) is plotted in black lines, whereas directivity value along y-axis ( $\theta = 90^\circ, \phi = 90^\circ$ ) is plotted in red lines. Dashed lines in the plot correspond to antenna alone; solid lines in the plot correspond to antenna with superstrate.

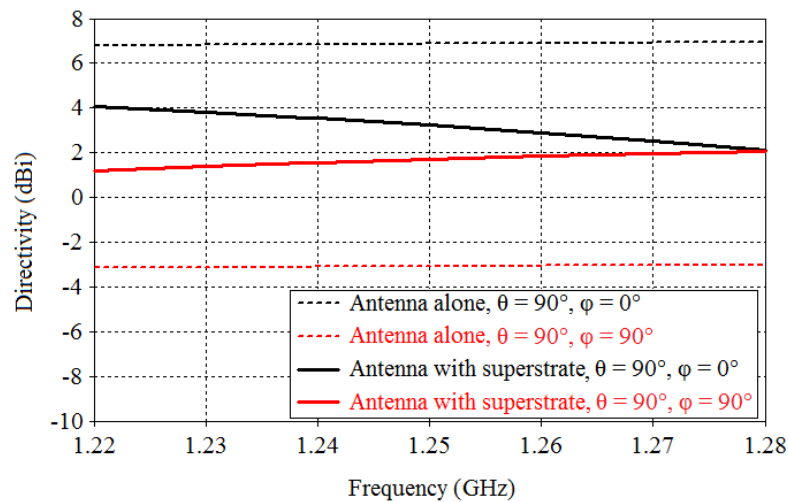


Fig. 5.10 Directivity values in operational bandwidth at x and y-axes for an antenna without and with superstrate (dBi).

Upon comparing dashed (antenna alone) with solid (antenna with superstrate) red lines in the plot, it is seen that directivity value increases along y-axis due to the use of this superstrate at all the frequencies in the operational bandwidth. The spatial transformation enacted using the spatially varying permittivity values opens up the broadside radiation pattern in the  $x y$  plane along y-axis. Consequently, HPBW also increases. Indeed, this increase comes at the sacrificial cost of maximum directivity in the operating bandwidth, as seen in the black dashed (antenna alone) and solid (antenna with superstrate) lines in the plot. The peak directivity for antenna without superstrate is about 6.9 dBi, but decreases when superstrate is used, such that directivity values along  $x$  and  $y$ -axes are equal (2 dBi) at 1.28 GHz. The results validate the proposed concept. The pixilated profile reproduces the behavior dictated by spatial transformation. The optimized device offers *at least*  $234^\circ$  wide HPBW in its operational bandwidth. Fabrication strategies such as one suggested in Chapter 4 can be considered for fabricating the concept.

## 5.1.2 Reconfigurable Materials

Reconfigurable materials can allow further extrapolation of the concept and can open up a new window in interpretation of the presented profiles. Active switchable metamaterials have been discussed in literature [107], [112]. A medium designed using active metamaterials may allow changing dynamically the  $n$ -index in the profile. Nematic crystals with voltage-controlled permittivity may also be considered for designing switchable profiles. As described previously in chapter 3 (in 3.2.3),  $p$  allows controlling the  $n$ -index and consequently the radiation patterns. As an example, a switching operation between antipodal and semi-spherical radiation patterns is discussed. The relative permittivity profile designed in 3.3.3.2 corresponding to the dielectric superstrate for antipodal radiation pattern is considered. It is assumed that the permittivity values within this profile can be controlled using voltage-controllable dielectric. A representative figure is shown in Fig. 5.11.

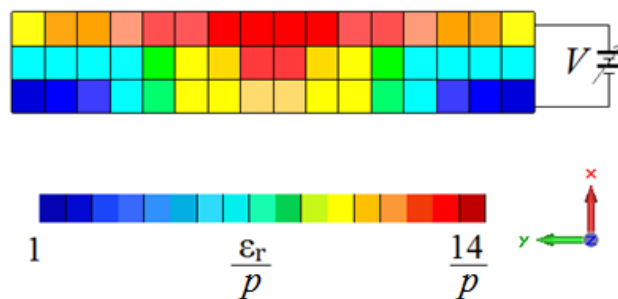


Fig. 5.11 Voltage controlled permittivity values in profile. Changing  $V$  represents a change in  $p$ .

Here, voltage  $V$  may be used to control permittivity of all pixels, such that a change in voltage  $V$  changes  $\epsilon_r$  value of each pixel. This change is enacted in simulation through a parameter  $p$ . Permittivity values of all pixels in the profile are divided by  $p$ . The 3D plots of directivity at 1.25 GHz are shown in Fig. 5.12 for two values of  $p$ .

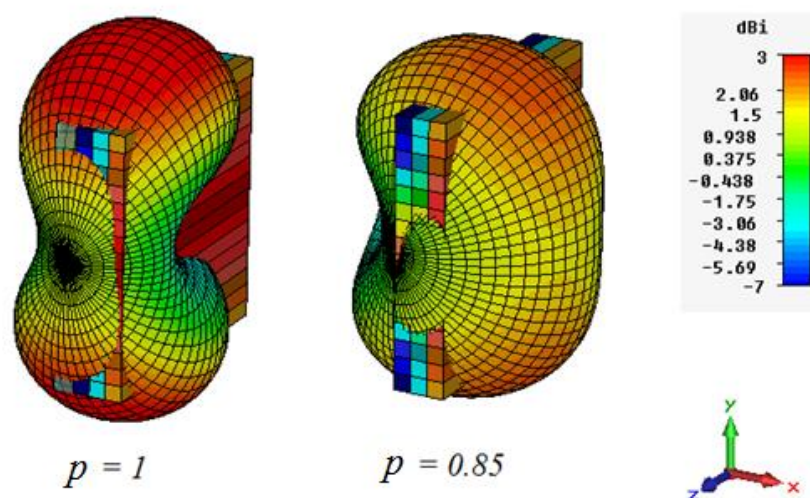


Fig. 5.12 Directivity plot of superstrate with controllable permittivity values.

For  $p = 1$ , the material profile is equivalent to the one presented in chapter 3, hence an antipodal radiation is achieved. For  $p = 0.85$ , the radiation pattern is quasi-spherical with two tilted beams. This shows that it should be possible to achieve the two radiation patterns from a single structure by simply switching between the two profiles. However, this requires designing corresponding active switchable profile, which is a significant challenge.

In the next sub-section, a TO concept is proposed to reorient the electromagnetic waves in uniquely one half space.

### 5.1.3 Case 2: Dielectric superstrate for single beam in azimuth

For many applications, an antenna with one-sided radiation pattern with a peak in azimuthal plane is required. Usually, unidirectional end-fire antennas arrays are used for such applications, which provide high gain in the azimuthal plane. However, two or more antenna elements are required. A TO inspired dielectric superstrate may be envisaged that provides unidirectional radiation in the azimuthal plane of a patch antenna. Such a radical modification in propagation direction is analogous to sharp waveguide bends like those presented in [48]. A non-TO based 3D-printed dielectric waveguide bend is presented in [85], which achieves the bending in spatially variant photonic crystal with constant permittivity. The polycarbonate based ABS blend ( $\epsilon_r = 2.45$ ) is used for printing this bend, which introduces a  $90^\circ$  change in direction of propagation of highly collimated beam of a horn antenna. While the performance of the device is great, the size of the fabricated waveguide is  $1.75\lambda$ . In comparison, the presented concept shall allow reorientation in a much thinner profile, however at the expense of level of collimation. This superstrate device is presented in detail in this section. Fig. 5.13 shows a representative image of radiation patterns of the original antenna and the desired reorientation.

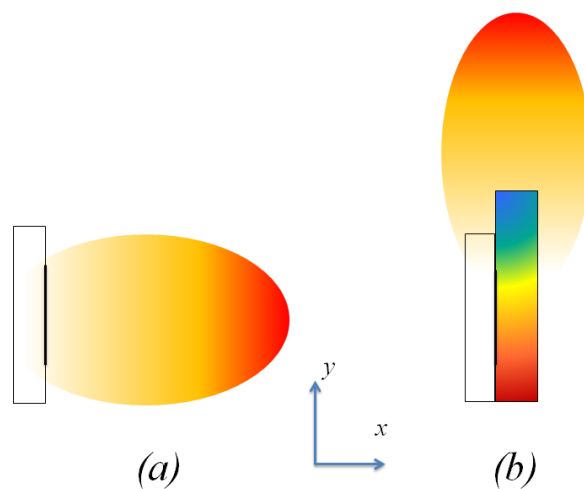


Fig. 5.13 Radiation patterns: (a) antenna alone, (b) antenna with dielectric superstrate for reorientation in single direction in azimuth.

### 5.1.3.1 Spatial transformation from Cartesian to quarter circle

The compression and n-index shift factors were used in the previous section as degree of freedom to achieve a new radiation behavior. In this section, the position of the source is changed with respect to the virtual space such that the radiation pattern is reoriented uniquely in half space. To design such a superstrate would require a spatial transformation between the Cartesian space and a single quarter ellipse. In Fig. 5.14, the representative image of the spatial transformation used to enact the end-fire superstrate is shown.

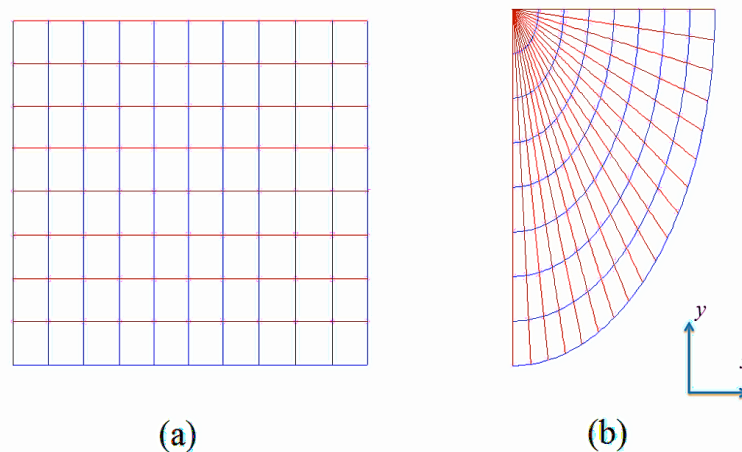


Fig. 5.14 (a) Physical square Cartesian space, (b) Virtual space for reorientation in azimuthal plane along y-axis

The simulations are carried out at the design frequency,  $f = 1.25$  GHz. The spatial transformation defined in chapter 3 is used to link a square shaped physical domain defined in Cartesian coordinate system with a virtual space comprised with a single quarter circle. The original size of the physical space is  $0.5\lambda$  by  $0.5\lambda$ , which is then further compressed and adjusted for an appropriate refractive index profile. The virtual space aims to guide electromagnetic waves travelling in positive  $x$ -axis along positive  $y$ -axis.

The superstrate is positioned over the patch antenna as shown in Fig. 5.15. The spatial compression factors are chosen as  $a = 4.16$ ,  $b = 0.8$  which implies an axial compression and a lateral expansion. This results in a device of size  $0.625\lambda \times 0.12\lambda$  at 1.25 GHz. Next,  $m$  in ( 3.20 ) is optimized using parametric simulations to reorient electromagnetic wave in azimuthal plane of the source. The permittivity variation inside the profile is shown in Fig. 5.15, where  $m = 14$ .

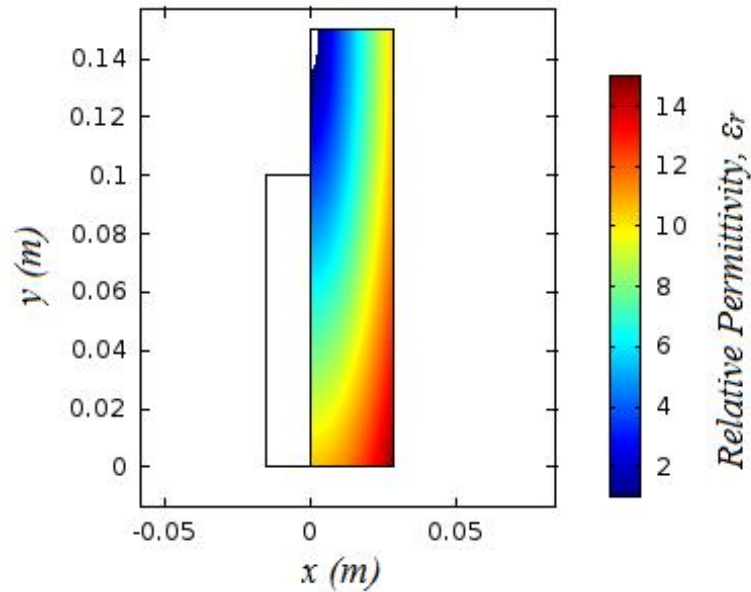


Fig. 5.15 Relative permittivity profile ( $\epsilon_r$ ) in the transformed profile for reorienting electromagnetic waves along positive y-axis.

The variation in permittivity inside the profile is  $0 < \epsilon_r < 14.9$ , dispersive values in the profile are seen in the white zone in the upper corner of the profile, highlighting their small spatial presence. They can be conveniently ignored during the profile discretization and be reassigned as  $\epsilon_r = 1$ . The normalized electric field  $E_z$  is plotted in Fig. 5.16.

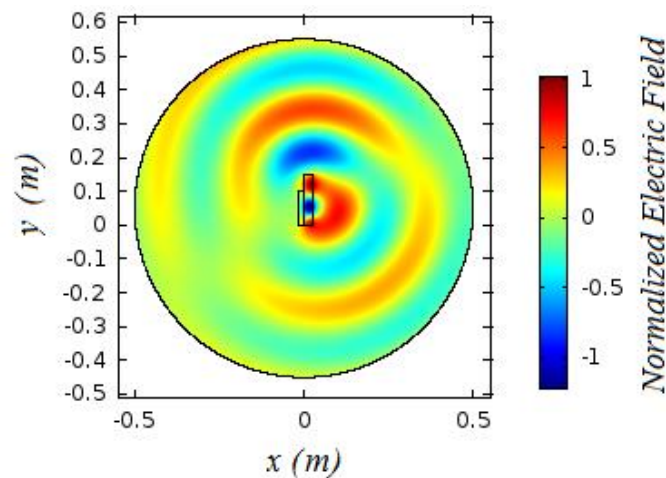


Fig. 5.16 Normalized electric field,  $E_z$  (V/m) at 1.25 GHz.

The transformed space largely reorients the electromagnetic waves along the y-axis. However as seen in the plot, a secondary lobe may be expected in negative y-axis. This is possibly due to the chosen asymmetrical placement of the source with respect to the transformed space, and may be corrected by parametric simulation over the position of the antenna. But this is not investigated further in this study. In the next sub-section, the discretized version of the above profile is studied.

### 5.1.3.2 Superstrate for reorienting electromagnetic waves in one direction

In this sub-section, full wave solutions calculated in CST Microwave Studio for the discretized version of the profile are discussed. The antenna used in chapter 3 is reused as the source; its characteristics have already been recalled in the last section. The continuous profile obtained in the previous section is discretized in 24 pixels (3 layers of 8 pixels each.) As in the previous cases, the discretized profile is extruded along  $z$ -axis. The length of extrusion along  $z$  is parametrically optimized for complete reorientation along  $y$ . The dimensions of the final superstrate are 187.5 mm x 150 mm x 28.8 mm ( $0.78\lambda$  by  $0.62\lambda$  by  $0.12\lambda$ ), as shown in Fig. 5.17.

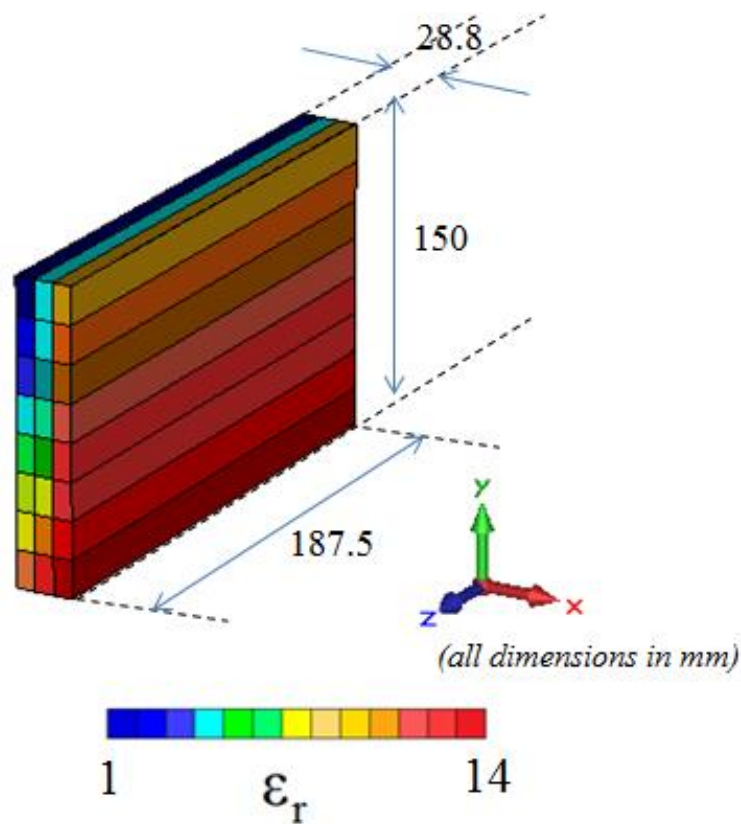


Fig. 5.17 3D superstrate designed from a discretized profile; variation in permittivity restricted between 1 and 14.

The relative permittivity in the profile varies between 1 and 14. As in the previous cases, an impedance matching layer is also used to match the superstrate to the antenna at the design frequency. The thickness of the superstrate is 12 mm, which means that the overall thickness of the superstrate is  $0.17\lambda$  at the design frequency. The dielectric constant of this layer is  $\epsilon_r = 2.2$ , which allows the superstrate to be matched at the design frequency ( $f = 1.25$  GHz). The magnitude of the reflection coefficient is plotted in Fig. 5.18.

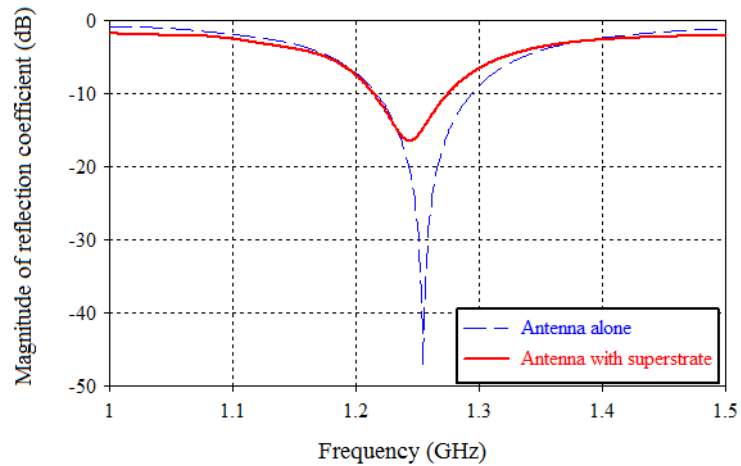


Fig. 5.18 Comparison of magnitudes of reflection coefficient of antenna alone and antenna with superstrate.

The bandwidth of the antenna superstrate assembly is 60 MHz (4.8% at 1.25 GHz). In Fig. 5.19, a 3D polar plot of directivity of the antenna superstrate assembly is plotted at the design frequency.

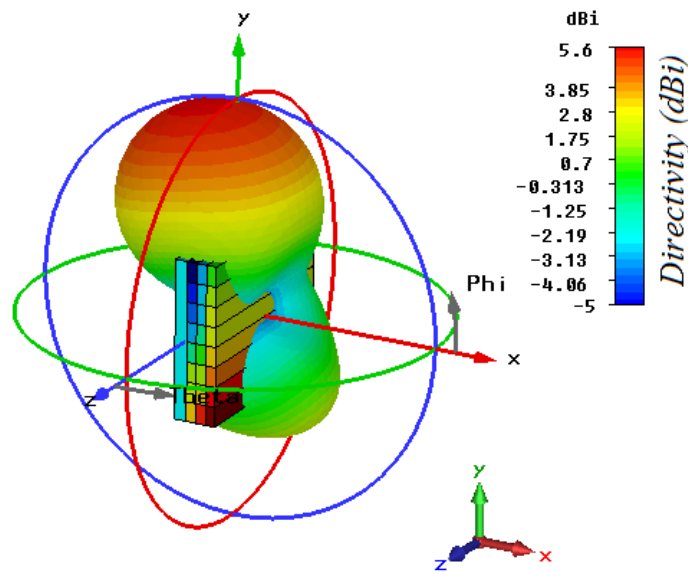


Fig. 5.19 Directivity (dBi) of the antenna superstrate assembly at 1.25 GHz.

As seen in the figure, the peak gain of this design is 5.6 dBi. For reference, maximum directivity of patch antenna without superstrate is 6.9 dBi. The difference in directivities of antenna without and with superstrate is expected because the spatial transformation defined earlier does not result in complete reorientation either. However, it may be remarked that the directivity in the present study is higher than the superstrates designed in chapter 3 (superstrate for antipodal radiation) and superstrate with semi-circular radiation pattern as discussed above. This is expected as the electromagnetic waves are concentrated uniquely in

one half plane using the transformed space; unlike in the other cases where propagation split in two different lobes or spread across half space. Next, the co and cross polarizations of the antenna-superstrate are studied in three different planes at the design frequency,  $f = 1.25$  GHz. In Fig. 5.20, the directivity in  $x$   $y$  plane is plotted.

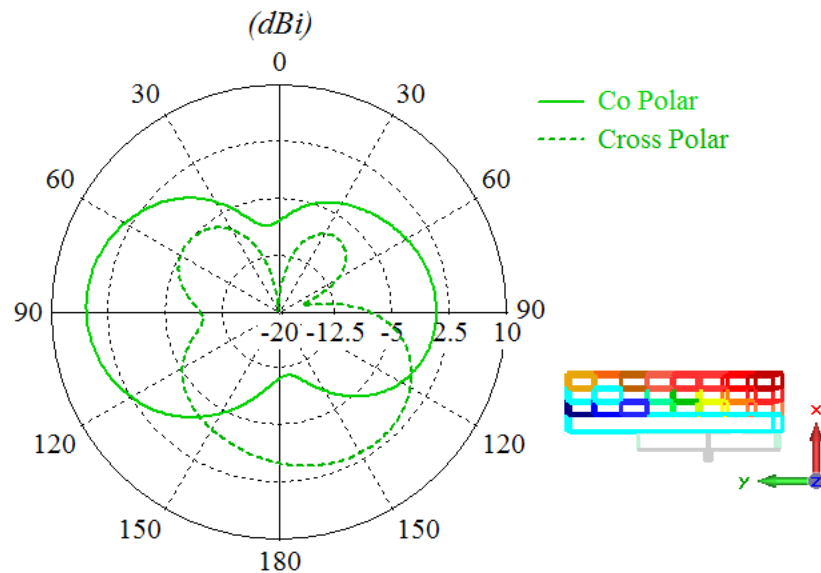


Fig. 5.20 Directivity (dBi) in  $x$ - $y$  plane at 1.25 GHz.

The superstrate increases the directivity along  $y$ -axis. Peak directivity in the co-polar component is 5.3 dBi along  $y$ -axis; directivity along negative  $y$ -axis is 0.8 dBi. The cross polarization level is greater than co-polar level along negative  $x$ -axis. However, in the main lobe, along positive  $y$ -axis the co polarization is 15 dB higher than cross polarization. In Fig. 5.21, the directivity in  $y$   $z$  plane is plotted.

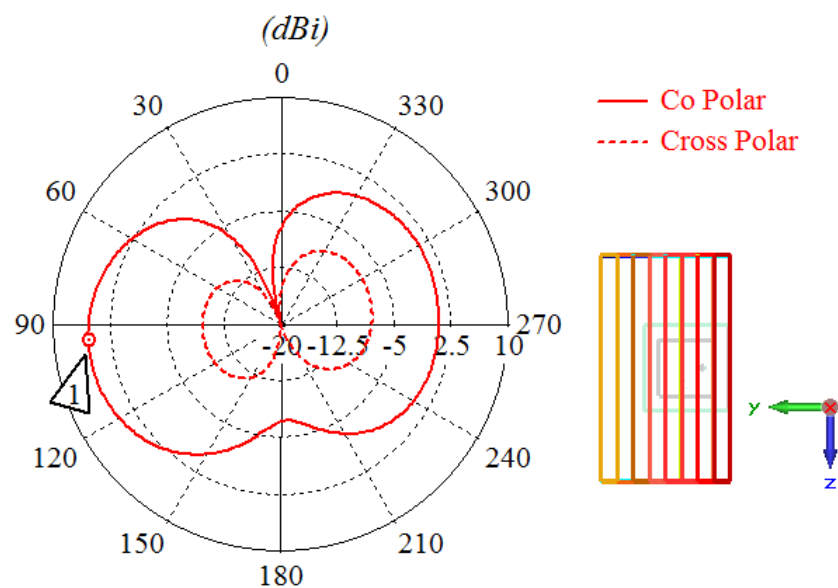


Fig. 5.21 Directivity (dBi) in  $y$ - $z$  plane at 1.25 GHz.

As also seen in the  $x y$  plane, superstrate increases the directivity along  $y$ -axis. Peak directivity in this plane is 5.3 dBi. Peak directivity in negative  $y$ -axis is 0.9 dBi. The cross polarization levels are low in comparison to the co-polar levels; co-polar along positive  $y$ -axis is 15 dBi higher than cross-polar level. In Fig. 5.22, the directivity in  $x z$  plane is plotted.

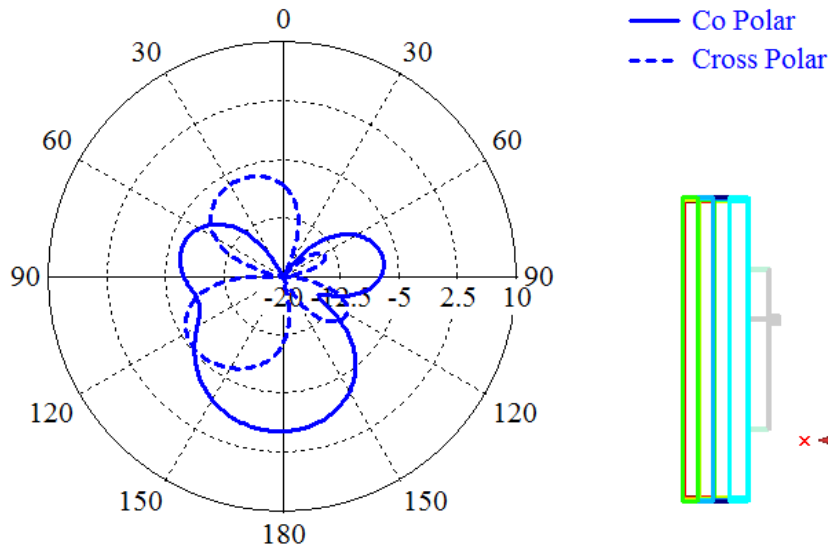


Fig. 5.22 Directivity (dBi) in  $x$ - $z$  plane at 1.25 GHz.

Peak directivity in the  $x z$  plane is -0.3 dBi. Along positive  $x$ -axis, the directivity is -7.3 dBi. It may be recalled that the peak directivity of antenna without superstrate along positive  $x$ -axis is 6.9 dBi. This implies that the superstrate reduced the directivity along positive  $x$ -axis by ~14 dB. The level of cross polarization is also comparable to co-polarization in this plane. However, this may be ignored as only the performance along positive  $y$ -axis is of interest.

For a better illustration of the superstrate's influence on the antenna's radiation pattern, the directivities of the antenna without and with superstrate are compared in a two dimensional plot in Fig. 5.23. The maximum directivity of the antenna is 6.9 dBi and antenna with superstrate is 5.6 dBi. However, for the purpose of illustration, the directivity values are restricted in the (-5, 5) dBi range. It is seen that the maxima shifts from  $(\theta = 0^\circ, \phi = 0^\circ)$  to  $(\theta = 90^\circ, \phi = 90^\circ)$  due to the presence of the superstrate. The secondary lobe is seen at  $(\theta = 120^\circ, \phi = -90^\circ)$ .

Thus, this study shows that the spatial transformation relations can be adapted to suit an application with asymmetrical placement of source. As stated in the beginning, the position of the antenna may be optimized further to reduce the lobe along negative  $y$ -axis. In the next section, a design guideline for practical implementation of these dielectric superstrates will be presented.

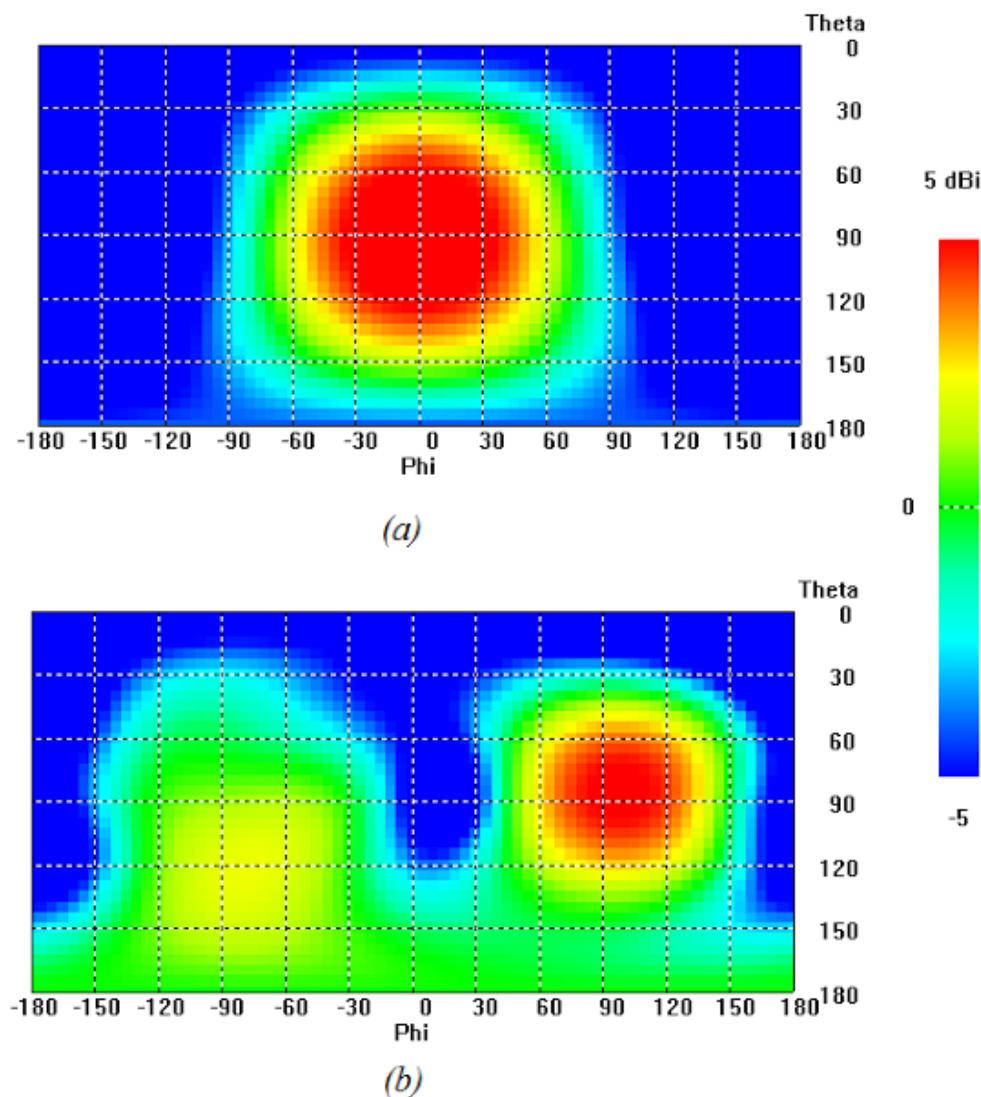


Fig. 5.23 Directivity plot (dBi) at 1.25 GHz (a) Antenna alone; (b) Antenna with superstrate.

## 5.2 Guideline for practical implementation using two materials

In Chapter 4, two-material fabrication of the dielectric superstrate was presented. The spatial transformation could be achieved in a rather simple arrangement of two dielectric materials to interpret low and high relative permittivity values in the profile. The extremely high permittivity values ( $\epsilon_r > 9$ ) in the discretized profile were replaced with highest achievable permittivity in fabrication i.e. alumina; and the rest were interpreted using by the low permittivity 3D printable dielectric material. The staircase structure was originated from the pixelated profile and led to an easy implementation using 3D printing techniques. The simplicity of the design is intriguing. In view of the more designs presented in this chapter, a general guideline for implementation of similar designs is desired. In this section, an insight is provided on practical implementation of the presented TO solutions.

Shifting the refractive index profile allows changing the output wave front, as seen earlier in the multiple examples in this chapter. It may be recalled from chapter 3,  $n$  – index shift factor  $m$  acts radially on the magnitude of the permittivity values in the profile (see 3.2.4) and consequently the refractive index. This implies that by controlling the distribution of high and low relative permittivity values in the transformed profile along the elliptical locus defined by ( 3.12 ), the resulting radiation pattern may be controlled. To verify this proposition, a superstrate is designed in CST Microwave Studio as shown in Fig. 5.24.

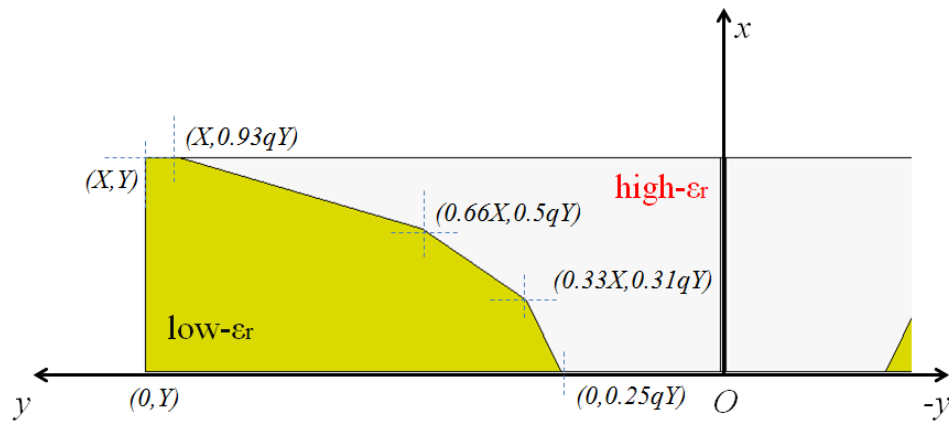


Fig. 5.24 Distribution of two materials along quasi-elliptical locus controlled by parameter ‘ $q$ ’.

Here, two low and high- $\epsilon_r$  materials are defined along a quasi-elliptical locus; low- $\epsilon_r$  (yellow) is 4.4 and high- $\epsilon_r$  (grey) is 9.9. Let us assume the superstrate has physical dimensions of  $X \times 2Y$  in the Cartesian space. The position of points lying on the elliptical locus is controlled by a parameter ‘ $q$ ’. By changing its value, the material distribution in the profile can be controlled, as shown in Fig. 5.25.

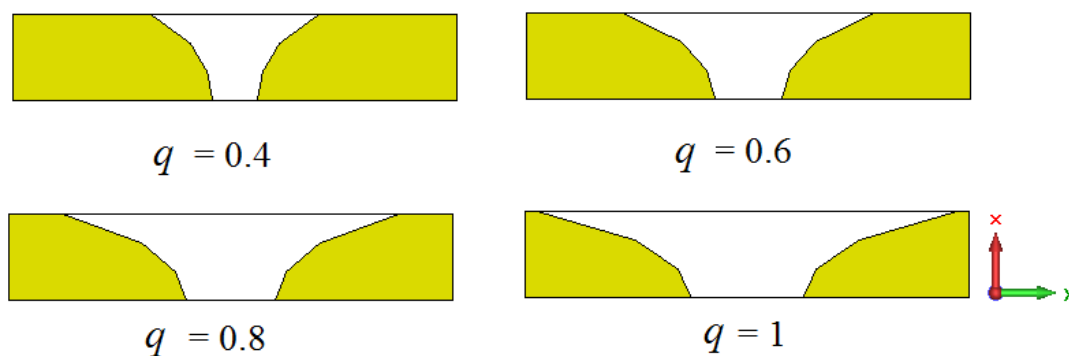


Fig. 5.25 Material distribution corresponding to different values of  $q$ .

As seen in the figure above,  $q$  acts on the material distribution within the profile as  $m$  acts on permittivity distribution in continuous profiles. To feed these superstrates, antenna used in chapter 3 is reused. As in the previous cases, a dielectric layer is used to match the patch antenna to the superstrate at 1.25 GHz. The relative permittivity of this 12.5 mm thick

dielectric layer is,  $\epsilon_r = 1.8$ . Parametric simulations are carried out for four different values of  $q$ . The magnitude of the reflection coefficient is plotted in Fig. 5.26.

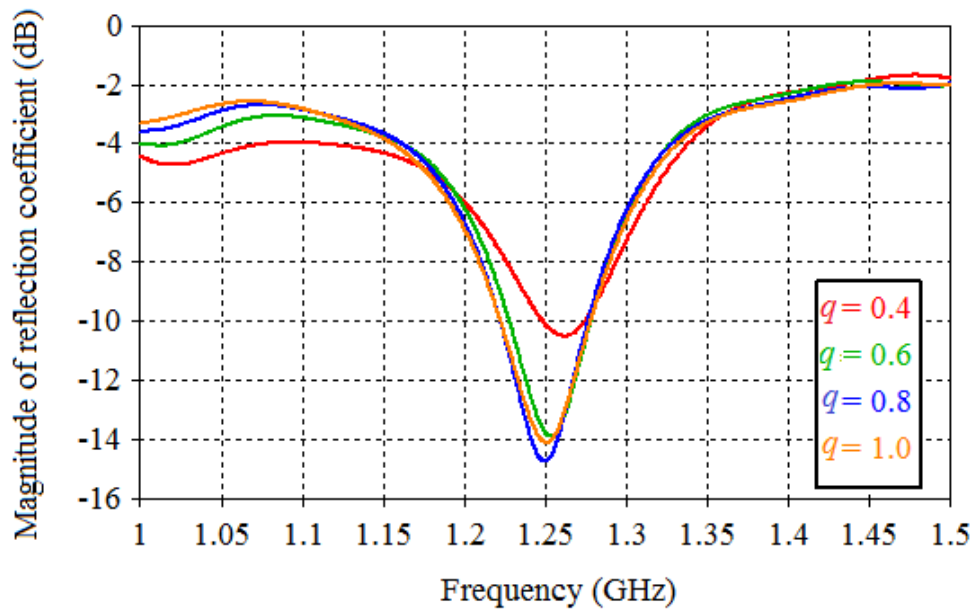


Fig. 5.26 Magnitude of reflection coefficient of the superstrates for different values of  $q$ .

The antenna superstrate assembly is matched at the design frequency of 1.25 GHz. Thus, antenna couples power to the superstrate in all iterations over ' $q$ '. Next, a comparison of the directivities in individual iterations is presented. As in all the designs presented in this thesis, the superstrate in this study also acts in  $x-y$  plane. In Fig. 5.27, the directivity in  $x-y$  plane ( $\theta = 90^\circ$ ) is plotted.

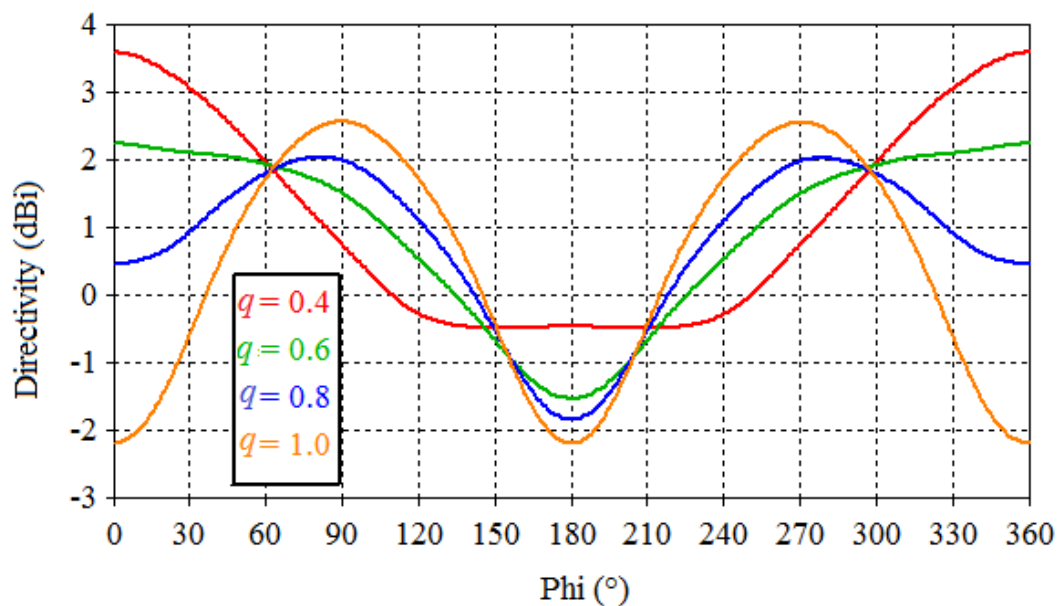


Fig. 5.27 Comparison of directivity in  $x-y$  plane ( $\theta = 90^\circ$ ) for different values of  $q$ .

For  $q = 0.4$  (red line), the superstrate has peak directivity in the broadside ( $\phi = 0^\circ$ ). The HPBW is in excess of  $180^\circ$ . Thus  $q = 0.4$  corresponds to implementation of the superstrate designed in 5.1.1. As  $q$  increases ( $q = 0.6$  (green),  $q = 0.8$  (blue)), the plot maximum shifts towards azimuth ( $\phi = \pm 90^\circ$ ). For  $q = 1$ , an antipodal radiation with plot maximum in azimuth is obtained. Generally, wider the distribution of high  $\epsilon_r$  material about x-axis, higher is the value of directivity along y-axis ( $\phi = \pm 90^\circ$ ).

Another important question that needs to be answered is what pair of permittivity values is required to achieve an optimum radiation pattern. The profile corresponding to  $q = 1$  is chosen to study this. Then, a parametric simulation is run on the high- $\epsilon_r$  value, which is governed by a factor ‘ $epsh$ ’ in the calculation. The low- $\epsilon_r$  value is kept constant at 4.4. Once again, the antenna superstrate assembly is matched at the design frequency for all iterations. In Fig. 5.28, the radiation pattern in  $x y$  plane is plotted.

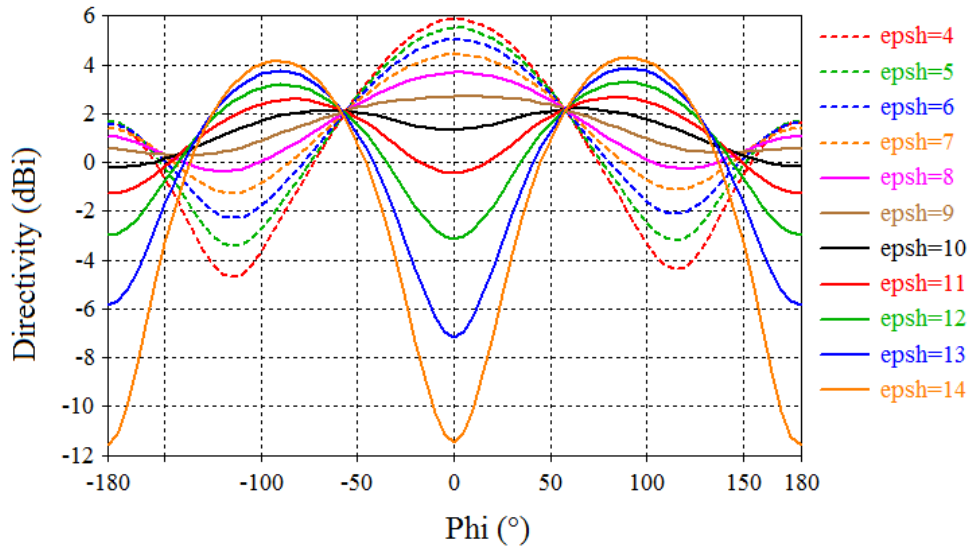


Fig. 5.28 Directivity in  $x y$  plane ( $\theta = 90^\circ$ ) for different values of  $epsh$ .

The values of  $epsh$  are iterated from 4 to 14. The higher bound is linked to the highest permittivity value in the pixelated profiles (chapter 3). For  $epsh = 4$  to 9, the peak directivity is in the broadside direction ( $\phi = 0^\circ$ ). As  $epsh$  increases, the peak directivity in broadside decreases and HPBW increases. For higher values of  $epsh$ , an antipodal directivity pattern is achieved in  $x-y$  plane with plot maximum lying in azimuthal plane ( $\phi = \pm 90^\circ$ ). As  $epsh$  increases from 4 to 14, the broadside directivity reduces.

This study can be used as general guideline for practical implementation of superstrates with different radiation patterns. Stacked slabs such as shown in Chapter 4 or blocks machined to obey the quasi-elliptical loci may be used for interpreting the spatial transformations. For  $q = 1$ , a complete reorientation in azimuthal plane is achieved.

The next section will present some simulation results on the performance of the TO superstrates in presence of ground planes.

### 5.3 Integration of antenna and superstrate into a structure, limitations

As evoked in the problem statement, the proposed superstrates can find use in a variety of applications, especially in aerospace applications. For example, these superstrates can be integrated on an aircraft at various positions (fuselage, wings, tail, etc.) to assure coverage in azimuthal plane. However, the effect of the surrounding structures has not been taken in account in the initial design. In this section, primary investigations on radiation performance of the superstrate in presence of the surrounding structures are presented.

#### 5.3.1 Antenna superstrate assembly in presence of PEC plane

In this section, simulation results to show effect of the electrically conducting ground plane on the superstrate's performance are presented. The superstrate with antipodal radiation pattern as described in chapter 3 is surrounded by circular ground plane. A representative image of the design is shown in Fig. 5.29.

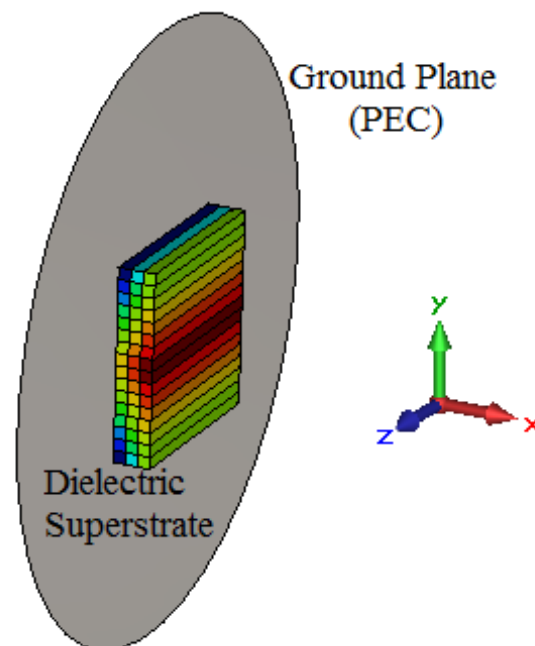


Fig. 5.29 Dielectric superstrate in presence of large ground plane.

In CST Microwave Studio, a PEC sheet is used to simulate the circular ground plane. The radius of the sheet is  $\sim 3\lambda$  at 1.25 GHz, but has been truncated in the image above for the purpose of illustration. The antenna and the impedance matching layer are behind the ground plane. In practice, this implies that antenna and dielectric layers are flush-mounted in the

large electrically conducting structure. The size of hole in the ground plane to accommodate antenna and dielectric matching layer is equal to the dimensions of dielectric layer. The realized gain at 1.25 GHz is shown in Fig. 5.31.

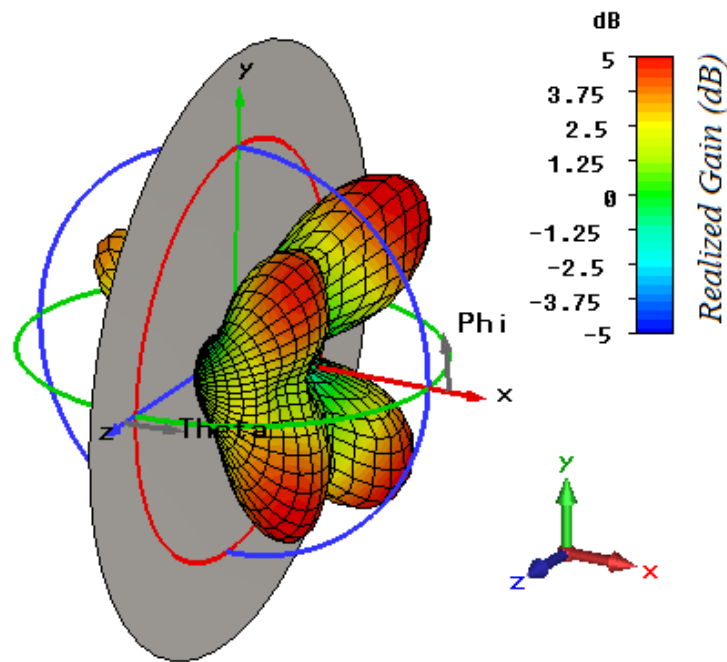


Fig. 5.30 3D polar plot of realized gain of dielectric superstrate in presence of a circular PEC plane at 1.25 GHz.

The surrounding ground plane changes the radiation pattern obtained earlier with the spatially transformed profile. The field reoriented along y-axis due to superstrate reflects from the PEC sheet and results in a multi lobe pattern. A radiation null appears in the radiation pattern along the azimuthal plane. As the PEC sheet acts as a reflector, peak realized gain in the plot is 5.6 dB, which is higher than the 3.5 dB gain of superstrate without surrounding ground plane. The desired reorientation in the azimuthal plane is lost due to the ground plane. This degraded performance of the superstrate in presence of surrounding ground plane is a problem and requires further investigation. In the next section, use of Perfect Magnetic Conductor (PMC) is discussed to solve this problem.

### 5.3.2 PMC based ground plane

In order to investigate the degraded performance of the dielectric superstrate in presence of ground plane, the problem is studied afresh in COMSOL Multiphysics. As may be recalled, the reorientation behavior has been originally designed in COMSOL as a two dimensional problem with reduced complexity. It is desired to study the effect of introduction of PEC sheet in this original problem. The reoriented field due to the superstrate without surrounding ground planes is shown in Fig. 5.31 (a). The superstrate reorients the

electromagnetic waves emanating from patch antenna along  $x$ -axis in the  $y$ -axis, where the electric field is polarized along  $z$ -axis. Next, PEC and PMC surfaces of finite size ( $\lambda$ ) along  $y$ -axis are used to simulate the presence of a flat ground planes of finite length, as shown in Fig. 5.31 (b) & (c). COMSOL is also adapted for this study as it allows defining PMC surfaces.

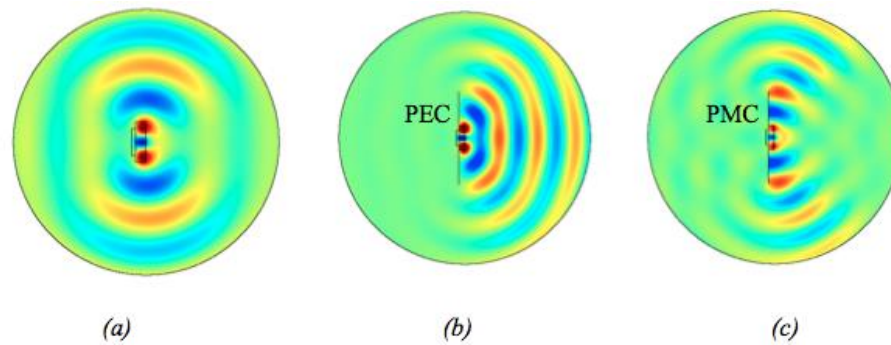


Fig. 5.31 Wave propagation with a surrounding ground plane (a) Without ground plane (b) With a PEC ground plane (c) With a PMC ground plane.

The tangential component of the electric field is zero on the surface of a perfect electrical conductor. Hence, there is no propagation along PEC reflector, leading to a blind spot in the azimuthal plane. The reflection from PEC surface leads to the reconstitution of pattern in the broadside, as shown in Fig. 5.31 (b). This highlights the nature of the problem in installation of superstrate. The behavior of superstrate may be further investigated by studying the performance in presence of reflectors of different sizes and curvature. However, this is beyond the context of the present discussion.

As per the design procedure set earlier in chapter 3, the electric field is polarized along  $z$ -axis, which excludes use of electrically conducting structures in the vicinity of the superstrate. A theoretical solution to this problem is to replace the PEC ground plane by a PMC plane. Unlike PEC, the image electric currents do not cancel each other out, hence the tangential electric field does not vanish on PMC. As a result, the wave propagates along the plane. This is shown in Fig. 5.31 (c). The field does not reconstitute in the broadside.

It is important to note that PMC is a theoretical surface and does not exist in nature. Artificial magnetic conductors (AMC) can be used to achieve the behavior in a limited frequency range. AMC are designed using patterned metallic surfaces and are usually fabricated using standard PCB manufacturing techniques [113]. In the next section, preliminary results on use of AMC to support wave propagation along azimuthal plane are presented.

### 5.3.3 Possibility of using AMC as a support structure

In this section, a simulation is proposed to verify the possibility of using AMC as surrounding structures. To reduce complexity in the study, a rectangular waveguide in TE mode is used as source instead of the dielectric superstrate. Both types of conductors are compared: PEC sheet and AMC, as shown in Fig. 5.32.

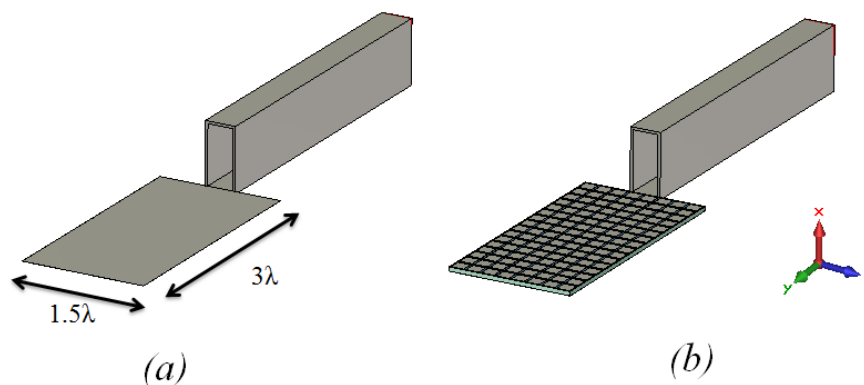


Fig. 5.32 Rectangular waveguide for parallel incidence of electric field on: (a) PEC, (b) AMC.

The size of both conductors is identical:  $3\lambda$  by  $1.5\lambda$  (approx.). The length of the conductors is similar to the radius of circular ground plane. The orientation of the waveguide shown in the figure allows an electric field parallel to the conductors. Furthermore, the waveguide illuminates conductors in grazing incidence, as would be the case when using the dielectric superstrate. The simulation is carried out at 10 GHz keeping in mind eventual lab tests because the dimensions of the AMC and waveguide in X-band are small and manageable in lab conditions. Consequently, the dimensions of waveguide in simulations correspond to a WR90 waveguide (22.86 mm by 10.16 mm), which operates in X-band (8.2-12.4 GHz).

#### 5.3.3.1 Design of AMC

AMC's are usually designed by printing metallic patches on dielectric substrate backed by metallic ground plane. In this study, a square shaped metallic patch is used.

One interesting property of magnetic conductors is that the incident electric field is reflected in-phase, whereas it is out-of-phase in case of electrical conductors. This property is used to design the AMC using a technique called reflection phase characterization [114]. A plane wave with normal incidence on the AMC unit cell is simulated. At the operating frequency of the unit cell, the phase of reflection coefficient is  $0^\circ$ . This technique enables to design the unit cell of AMC operating at 10 GHz. However as a grazing incidence condition is needed, the plane wave with different angle of incidence is required. This is possible in CST Microwave studio using Frequency Domain solver. In the present study, unit cell is characterized for a plane wave incident at  $80^\circ$  (with respect to the normal direction of the

AMC) where E-field is parallel to the surface. It may be noted here that this value is an approximation used in design to simulate grazing incidence. The representative image of the unit cell is shown in Fig. 5.33.

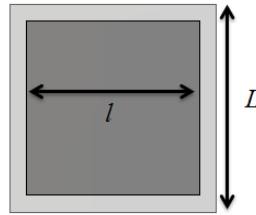


Fig. 5.33 AMC unit cell

A 1.58 mm thick PEC backed FR-4 layer is used as the substrate. The side of the PEC square patch is  $l = 5$  mm, side of unit cell  $L = 6$  mm. The phase of reflection coefficient is plotted in Fig. 5.34.

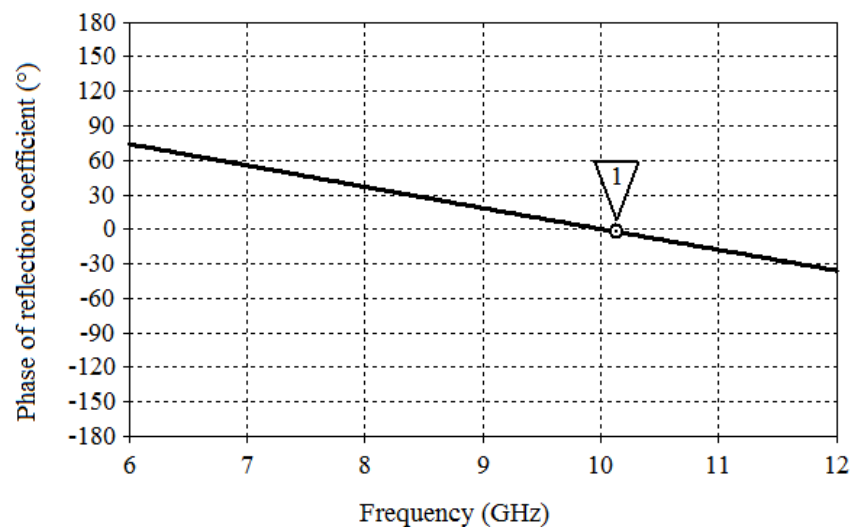


Fig. 5.34 Phase of reflection coefficient of the unit cell for a plane wave incident at  $80^\circ$ .

For the above unit cell, it is found that the phase of reflection coefficient is  $0^\circ$  at 10.02 GHz. This unit cell is used to design the AMC reflector shown in Fig. 5.32 (b).

### 5.3.3.2 Comparison of PEC and AMC reflectors

Full wave simulations are carried out to compare the performance of finite sized PEC and AMC reflectors upon illumination from rectangular waveguide. The expected propagation along the y-axis is achieved at 10.2 GHz. The shift from 10.02 GHz to 10.2 GHz may be due to the fact that AMC unit cell characterization assumed an infinite sized surface, whereas the size of AMC illuminated using waveguide is finite. In Fig. 5.35, the directivities for the two cases are compared using 3D polar plots. The values in the two plots are limited in the (-10, 10 dBi) range to facilitate visual comparison.

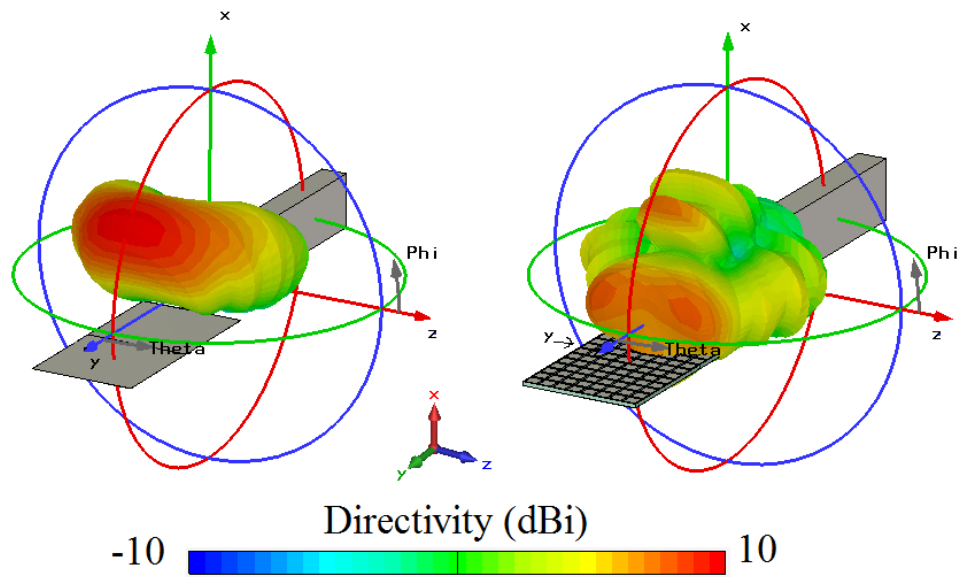


Fig. 5.35 Directivity (dBi) comparison for PEC and AMC reflectors.

As seen in the figure above, the field reflects at an angle from the PEC sheet. Consequently, there is no radiation along the surface of the PEC reflector (y-axis in the plot). On the other hand, use of AMC as reflector in the second scenario allows achieving radiation along the surface of AMC reflector (z-axis in the plot). The directivities in the two cases are also compared in the  $y z$  plane, as shown in Fig. 5.36. Directivity of PEC reflector is plotted in black dashed line, and that of AMC reflector in red solid line.

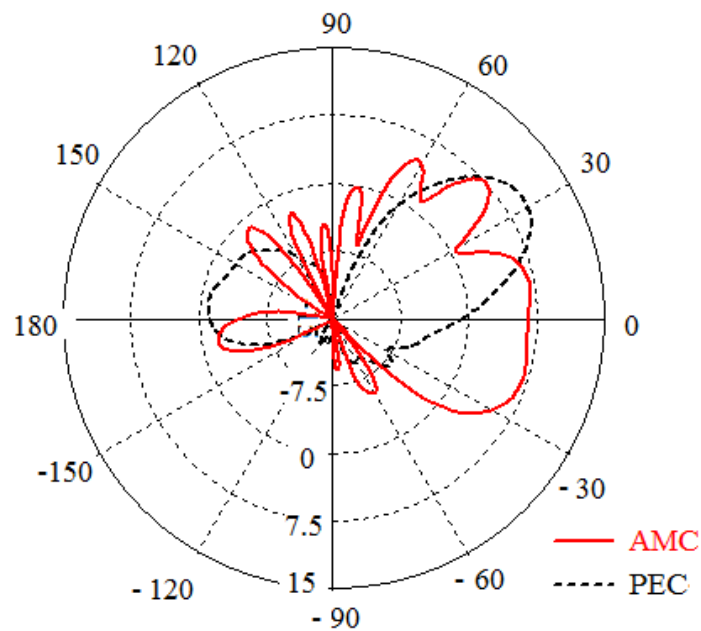


Fig. 5.36 Comparison of directivities (dBi) of PEC and AMC reflectors in  $x y$  plane.

For PEC reflector, the main lobe in the plot points at an angle of  $32^\circ$  and the directivity along the surface of PEC reflector is -0.3 dBi. On the other hand, directivity along the surface of AMC reflector is 6.9 dBi. Thus, an improvement of 7 dB is achieved along the surface using AMC reflector. These results are encouraging and show that further investigations in the use of printed surfaces around the dielectric superstrate may allow conserving the radiation pattern dictated by spatial transformation.

As said in the beginning of this section, these are the results of primary investigations in use of AMC's as surrounding structures. This research theme may be developed further to study different associated problems. For example, the AMC reflector can be used to modify or correct the faults in radiation patterns by locally changing the structure of the AMC reflector. This approach has been studied and published previously in [115]. A hybrid reflector containing both electric and magnetic conductors is used to correct the fault in the radiation pattern of an ultra-wide band dipole antenna and restore the gain in the broadside direction. This is not discussed any further as it is beyond the purview of this thesis.

## 5.4 Discussion

This chapter tried to explore various design possibilities arising out of the spatial transformation. It was shown that degrees of freedom incorporated during the analytical design could be used to achieve different wave propagation behaviors in low-profile dielectric superstrates. A design guideline regarding interpretation of spatial transformation using two materials was also presented. Some preliminary results on use of AMC surface around the dielectric superstrate were also presented. Next, a recapitulation of the research work of this thesis is presented in conclusion.



## 6. Conclusions and Perspectives

### 6.1 Conclusions

The research presented in this thesis has showed that TO method can be used to design simple devices using only a few standard dielectric materials, which allow drastically changing the radiation pattern of patch antennas. Thus, the typical radiation pattern of patch antennas, which has a maximum in the broadside, has been radically modified in presence of these dielectric superstrates. Furthermore, reduction in thickness of the superstrate (in terms of wavelength at the frequency of operation) vis-à-vis conventional TO superstrate solutions is an advantage, and allows envisaging their use in a variety of application areas. These solutions are expected to be of particular interest for high velocity vehicles like airplanes, where conformity of the antenna is a key design advantage for the aircraft's performance. The results presented in this thesis also attest the potential of 3D printing technology, which has allowed a simple fabrication for the unconventionally shaped superstrate.

The literature study presented in the chapter 2 allowed sketching a background to the problem and has helped identify possibilities and limitations of TO method. It has also highlighted recent advances in domain of TO, which has provided important design metrics and information e.g. bandwidth, solutions with high permittivity dielectric materials, etc. It was also seen through means of comparison that many TO solutions tend to be bulky which limits their use low profile applications.

Chapter 3 presented an analysis of the TO concept from mathematical construction of spaces to a full wave simulation results of a concept device. The design proposed by Clemente Arenas in his Ph.D. dissertation was achieved reorientation in azimuthal plane in a anisotropic material profile with permittivity varying between 1 and 15 and permeability between 0.3 and 3. Respecting the design methodology initially developed by Clemente Arenas, the spatial transformation relations were improved in this thesis to enable a dielectric only design. Furthermore, different spatial compression factors and refractive index shift factor were incorporated in the coordinate transformation relations, which were then used as degrees of freedom in the design. For example, axial ( $a$ ) and lateral ( $b$ ) compression factors values of 4.16 and 1.6 were used to design the dielectric superstrate for antipodal radiation pattern, such that the lateral footprint and thickness was reduced from  $\lambda$  by  $0.5\lambda$  to  $0.625\lambda$  by  $0.12\lambda$ . Role of intermediate dielectric layer to match antenna and superstrate was also studied

in detail. Finally, full wave simulations were carried on superstrate designed using finite number of isotropic dielectric materials. The permittivity in the transformed profile varied from 1 to 14. The results showed that it was possible to transform the broadside radiation pattern of the patch antenna with a realized gain of approximately 7 dB into an antipodal radiation pattern with two beams in azimuthal plane and a realized gain of approximately 3.5 dB.

Design, fabrication and validation by measurements of 3D printed dielectric superstrates were presented in chapter 4. The design approach was based on effective medium approximation and was guided primarily by choice of dielectric materials required to interpret the variation in permittivity. Considering large variation in permittivity of solution developed in chapter 3, two materials: alumina and a second material compatible with 3D printer, were used to design the solution. Two interpretations of the pixelated profile were discussed: the first presented a strict, pixel by pixel interpretation of the discrete profile developed in chapter 3, and a second lenient interpretation, using only two permittivity values were shown to obey the spatial transformation with antipodal radiation patterns with a null in broadside and maximum realized gain in the azimuthal plane. The simplification of the transformation in to profile with only two permittivity values was a crucial one, specially when compared to the preliminary solution presented by Clemente Arenas. The lenient version of the profile was chosen for fabrication of proof-of-concept. With the help extended by Airbus Group Innovations, two versions of 3D printed receptacles were fabricated. The first receptacle was designed using Objet's FullCure range of photo curable resins, whereas the second was designed using a PLA filament. Measured performance showed a broad agreement with the simulated results, such that the maximum realized gain was achieved in azimuthal plane and a decrease in the realized gain was observed in the broadside direction. While the realized gain of antenna alone at operating frequency is 5.7 dB, maximum realized gains in azimuthal planes of the FullCure and PLA superstrates were 2.4 and 3.3 dB. Regarding the complexity of fabrication, 3D printing technology has highly facilitated quick fabrications of complex shapes, and was beneficial in the context of this thesis for rapid prototyping of proof-of-concepts.

The extrapolations and complementary designs presented in chapter 5 provided further insight into various aspects of the design. First, the degrees of freedom identified in chapter 3 were used to adapt the spatial transformation towards new radiation patterns and consequently enabled the design of low profile dielectric superstrates for new applications. Different designs have allowed achieving interesting behaviors i.e. large HPBW in one plane (greater than  $234^\circ$  in the operational bandwidth), end-fire radiation in azimuthal plane of patch antenna (peak realized gain of 5.3 dB in the azimuthal plane). Moreover, this strong

change in the radiation patterns is achieved in electrically thin profiles (equal to or smaller than  $0.16\lambda$ .) Inspired from the two material fabrications as described in chapter 4, an investigation on influence of composition and proportion of materials in the design of dielectric superstrates was presented. It was shown that controlling the distribution of materials could allow synthesizing different radiation patterns. Finally, use of artificial magnetic conductors has been proposed to support the superstrate's integration in a large structure or in presence of a large ground plane.

## 6.2 Perspectives

There is a multitude of research activity that can be based on the presented research work. As suggested in section 5.3, the integration of the superstrates on large electrically conducting structures is an immediate concern and remains an unaddressed problem in the context of dielectric superstrates. However preliminary studies presented in chapter 5 using rectangular waveguides indicate that metamaterials based AMC surfaces may present an interesting solution to the problem. This opens up a very interesting area of research that requires studying patterned surfaces with isotropic and anisotropic impedances in vicinity of the dielectric superstrate. The challenge in this study is to control multiple design variables like grazing incidence, bandwidth of the device, etc. that requires dedicated research. Equally interesting is the possibility of implementing the spatial transformation in 2D optically transformed surfaces and may lead to novel physical phenomenon, for example wave splitter, conversion of a planar surface wave into a semicircular wave front, surface wave bends etc.

Secondly, fabrication processes also provide interesting challenges. Design concepts presented in chapter 5 can be optimized and fabricated using the 3D printing procedures. A strict interpretation of the discretized profile can be pursued to identify new challenges related to fabrication. Furthermore, access to high permittivity materials is a design constraint in implementation of these low profile superstrates. While alumina has been used in this research work for practically implementing the high permittivity region, other high permittivity materials may also be used e.g. titanate powders. An access to higher permittivity profile may consequently allow designing thinner profiles.

As far as new application areas for superstrates are concerned, these superstrates can be used with patch antenna array for expanding the coverage area towards the azimuthal plane. Similarly, a superstrate array solution may also be envisaged for active scanning applications in azimuthal plane. Equally interesting research track is to investigate a reconfigurable device designed using switchable metamaterials, which may allow dynamic

switching between the broadside radiation pattern of the patch antenna and an azimuthal coverage using the superstrate.

While integration of these superstrates in airplanes and other high velocity platforms to benefit from the low profile has already been suggested as the primary application, the low profile also provides an esthetic advantage over other solutions. This is an advantage for its application in consumer electronics. Apart from suggested applications in L-band, the superstrates may also be used for other applications in other frequency ranges. For example, TO concept with large HPBW can be used for providing wide-angle coverage in Wi-Fi or other consumer applications in 5 GHz band.

## List of Publications

1. C. Joshi, A.C. Lepage and X. Begaud, “Low profile superstrate using Transformation Optics for semicircular radiation pattern of antenna”, *Applied Physics A*, vol. 123, no. 2, 144, February 2017, doi: 10.1007/s00339-017-0787-7.
2. C. Joshi, A.C. Lepage and X. Begaud, “A Dielectric-only superstrate inspired from transformation optics for complete reorientation of electromagnetic waves in azimuthal plane”, *EPJ Applied Metamaterials*, vol. 3, 5, July 2016, doi: 10.1051/epjam/2016009.
3. C. Joshi, A. C. Lepage, J. Sarrazin and X. Begaud, “Enhanced Broadside Gain of an Ultrawideband Diamond Dipole Antenna Using a Hybrid Reflector,” in *IEEE Transactions on Antennas and Propagation*, vol. 64, no. 7, pp. 3269-3274, July 2016, doi: 10.1109/TAP.2016.2565695.

### Conferences:

1. C. Joshi, A.C.Lepage and X. Begaud, “Practical Realization of a Transformation Optics based Dielectric Superstrate for Patch Antenna using 3D Printing”, *META 2017*, Incheon, South Korea
2. C. Joshi, A.C.Lepage and X.Begaud, “Superstrat tout diélectrique pour le contrôle du rayonnement d’une antenne- prototypage et mesures”, *JNM-2017*, Saint Malo, France.
3. C. Joshi, A.C.Lepage and X. Begaud, “Low Profile Superstrate using Transformation Optics to modify Radiation Pattern of Antenna”, *META 2016*, July 2016, Malaga, Spain.
4. C. Joshi, M. Clemente Arenas, A. C. Lepage and X. Begaud, “Material Influence in a TO Superstrate for Antipodal Radiation”, *EuCAP’2016 10th European Conference on Antennas and Propagation*, April, 2016, Davos, Switzerland.
5. C. Joshi, M. Clemente Arenas, A. C. Lepage and X. Begaud, “Influence of Material Parameters in a Superstrate Made by Transformation Optics to Drastically Change the Radiation Pattern of an Antenna”, *1st International Workshop on Metamaterials-by-Design*, December, 2015, Paris, France.
6. C. Joshi, M. Clemente Arenas, A. C. Lepage and X. Begaud, “Analyse de l’influence des matériaux composant un dispositif à Transformation d’Espace pour le contrôle du rayonnement d’une antenne”, *Assemblée Générale GDR Ondes*, October 2015, Lyon, France.
7. C. Joshi, A. C. Lepage, J. Sarrazin and X. Begaud, “Size, Gain and Bandwidth trade-offs for Wideband Diamond Dipole with AMC reflector”, *2nd International Conference on Communication Systems*, October 2015, Pilani, India.

*Conclusions and Perspectives*

8. C. Joshi, J. Sarrazin, A. C. Lepage and X. Begaud, “Antenne planaire, large bande et directive avec un réflecteur hybride”, 19èmes Journées Nationales Microondes, June 2015, Bordeaux, France.
9. C. Joshi, J. Sarrazin, A. C. Lepage and X. Begaud , “Wideband Diamond Dipole Antenna with Broadside Radiation Characteristics”, EuCAP, April, 2015, Lisbon, Portugal.

## References

- [1] J. B. Pendry, D. Schurig, and D. R. Smith, “Controlling Electromagnetic Fields,” *Science (80-. )*, vol. 312, no. 5781, pp. 1780–1782, Jun. 2006.
- [2] M. D. Clemente-Arenas, “Application de la transformation d’espace à la conception d’antennes à diagrammes de rayonnement contrôlé,” Ph.D. Thesis, Télécom ParisTech, 2014.
- [3] V. G. Veselago, “The Electrodynamics of Substances With Simultaneously Negative Values of  $\epsilon$  and  $\mu$ ,” *Soviet Physics Uspekhi*, vol. 10, no. 4. pp. 509–514, 1968.
- [4] J. B. Pendry, “Negative refraction makes a perfect lens,” *Phys. Rev. Lett.*, vol. 85, no. 18, pp. 3966–3969, 2000.
- [5] D. F. Sievenpiper, M. Sickmiller, and E. Yablonovitch, “3D Wire Mesh Photonic Crystals,” *Phys. Rev. Lett.*, vol. 76, no. 14, pp. 2480–2483, 1996.
- [6] J. B. Pendry, A. J. Holden, W. J. Stewart, and I. Youngs, “Extremely Low Frequency Plasmons in Metallic Mesostructures,” *Phys. Rev. Lett.*, vol. 76, no. 25, pp. 4773–4776, Jun. 1996.
- [7] J. B. Pendry, A. J. Holden, D. J. Robbins, and W. J. Stewart, “Magnetism from Conductors , and Enhanced Non-Linear Phenomena,” vol. 47, pp. 1–21, 1999.
- [8] D. R. Smith, W. J. Padilla, D. C. Vier, S. C. Nemat-Nasser, and S. Schultz, “Composite Medium with Simultaneously Negative Permeability and Permittivity,” *Phys. Rev. Lett.*, vol. 84, no. 18, pp. 4184–4187, 2000.
- [9] R. A. Shelby, D. R. Smith, and S. Schultz, “Experimental verification of a negative index of refraction.,” *Science*, vol. 292, no. 5514, pp. 77–79, 2001.
- [10] D. Schurig, J. J. Mock, and D. R. Smith, “Electric-field-coupled resonators for negative permittivity metamaterials,” *Appl. Phys. Lett.*, vol. 88, no. 4, pp. 1–3, 2006.
- [11] M. Khorasaninejad, W. T. Chen, R. C. Devlin, J. Oh, A. Y. Zhu, and F. Capasso, “Metalenses at visible wavelengths: Diffraction-limited focusing and subwavelength resolution imaging,” *Science (80-. )*, vol. 352, no. 6290, pp. 1190–1194, 2016.
- [12] A. J. Ward and J. B. Pendry, “Refraction and geometry in Maxwell’s equations,” *J. Mod. Opt.*, vol. 43, no. 4, pp. 773–793, 1996.
- [13] J. B. Pendry, “Perfect cylindrical lenses.,” *Opt. Express*, vol. 11, no. 7, pp. 755–760, 2003.
- [14] U. Leonhardt, “Optical Conformal Mapping and Dielectric Invisibility Devices,” *Arxiv.Org*, p. Physics/0602092, 2006.
- [15] V. M. Shalaev, “Transforming Light,” *Science (80-. )*, vol. 322, no. 5900, pp. 384–

- 386, 2008.
- [16] A. M. Patel, “Controlling Electromagnetic Surface Waves with Scalar and Tensor Impedance Surfaces,” Ph.D. Thesis, The University of Michigan, 2013.
  - [17] A. M. Patel and A. Grbic, “Analytical modeling of a printed-circuit tensor impedance surface,” in *2012 IEEE/MTT-S International Microwave Symposium Digest*, 2012, pp. 1–3.
  - [18] A. M. Patel and A. Grbic, “A Printed Leaky-Wave Antenna Based on a Sinusoidally-Modulated Reactance Surface,” *IEEE Trans. Antennas Propag.*, vol. 59, no. 6, pp. 2087–2096, Jun. 2011.
  - [19] A. M. Patel and A. Grbic, “Modeling and Analysis of Printed-Circuit Tensor Impedance Surfaces,” *IEEE Trans. Antennas Propag.*, vol. 61, no. 1, pp. 211–220, Jan. 2013.
  - [20] A. M. Patel and A. Grbic, “Effective Surface Impedance of a Printed-Circuit Tensor Impedance Surface (PCTIS),” *IEEE Trans. Microw. Theory Tech.*, vol. 61, no. 4, pp. 1403–1413, Apr. 2013.
  - [21] R. G. Quarfoth and A. Patel, “Surface wave polarization converter,” in *2015 IEEE International Symposium on Antennas and Propagation & USNC/URSI National Radio Science Meeting*, 2015, pp. 659–660.
  - [22] R. G. Quarfoth, “Anisotropic artificial impedance surfaces,” Ph.D. Thesis, University of California, San Diego, 2014.
  - [23] E. Martini, M. Mencagli, D. Gonzalez-Ovejero, and S. Maci, “Flat Optics for Surface Waves,” *IEEE Trans. Antennas Propag.*, vol. 64, no. 1, pp. 155–166, Jan. 2016.
  - [24] M. Mencagli, E. Martini, D. Gonzalez-Ovejero, and S. Maci, “Metasurfing by transformation electromagnetics,” *IEEE Antennas Wirel. Propag. Lett.*, vol. 13, pp. 1767–1770, 2014.
  - [25] M. Mencagli, C. Della Giovampaola, and S. Maci, “A Closed-Form Representation of Isofrequency Dispersion Curve and Group Velocity for Surface Waves Supported by Anisotropic and Spatially Dispersive Metasurfaces,” *IEEE Trans. Antennas Propag.*, vol. 64, no. 6, pp. 2319–2327, 2016.
  - [26] D. A. Roberts, N. Kundtz, and D. R. Smith, “Optical lens compression via transformation optics,” *Opt. Express*, vol. 17, no. 19, pp. 16535–42, 2009.
  - [27] P. H. Tichit, S. N. Burokur, and A. de Lustrac, “Reducing physical appearance of electromagnetic sources,” *Opt. Express*, vol. 21, no. 4, pp. 5053–62, 2013.
  - [28] P. H. Tichit, S. N. Burokur, and A. De Lustrac, “Engineering of source appearance via transformation optics concept,” in *Antennas and Propagation (EuCAP), 2013 7th European Conference on*, 2013, pp. 1396–1400.

- [29] W. Yan, M. Yan, and M. Qiu, “Necessary and sufficient conditions for reflectionless transformation media in an isotropic and homogenous background,” <http://arxiv.org/abs/0806.3231>, 2008.
- [30] Y. Lai, J. Ng, H. Y. Chen, D. Han, J. Xiao, Z. Q. Zhang, and C. T. Chan, “Illusion optics: The optical transformation of an object into another object,” *Phys. Rev. Lett.*, vol. 102, no. 25, pp. 1–23, 2009.
- [31] Y. Li, F. Kong, and K. Li, “Transformation Optics Methodology for Changing the Appearance of an Object,” vol. 20, no. 2, pp. 321–324, 2016.
- [32] J. Yi, P. H. Tichit, S. N. Burokur, and A. De Lustrac, “Illusion optics: Optically transforming the nature and the location of electromagnetic emissions,” *J. Appl. Phys.*, vol. 117, no. 8, 2015.
- [33] P. H. Tichit, S. N. Burokur, J. Yi, and A. De Lustrac, “Transformation electromagnetics for antennas with an illusion on the radiation pattern,” *IEEE Antennas Wirel. Propag. Lett.*, vol. 13, pp. 1796–1799, 2014.
- [34] K. G. Balmain and A. Luttgen, “Planar Anisotropic Resonance-Cone Metamaterials,” in *Negative-Refractive Metamaterials: Fundamental Principles and Applications*, G. V. Eleftheriades and K. G. Balmain, Eds. Wiley, 2005.
- [35] Z. Wang, Z. Wang, J. Wang, B. Zhang, J. Huangfu, J. D. Joannopoulos, M. Soljagic, and L. Ran, “Gyrotropic response in the absence of a bias field,” *Proc. Natl. Acad. Sci.*, vol. 109, no. 33, pp. 13194–13197, Aug. 2012.
- [36] W. Cai, U. K. Chettiar, A. V. Kildishev, and V. M. Shalaev, “Optical cloaking with metamaterials,” *Nat. Photonics*, vol. 1, no. April, p. 224, 2007.
- [37] P. H. Tichit, S. N. Burokur, D. Germain, and A. De Lustrac, “Design and experimental demonstration of a high-directive emission with transformation optics,” *Phys. Rev. B - Condens. Matter Mater. Phys.*, vol. 83, no. 15, 2011.
- [38] H. Xu, B. Zhang, T. Yu, G. Barbastathis, and H. Sun, “Dielectric waveguide bending adapter with ideal transmission: practical design strategy of area-preserving affine transformation optics,” *J. Opt. Soc. Am. B*, vol. 29, no. 6, p. 1287, 2012.
- [39] W. Tang, C. Argyropoulos, E. Kallos, W. Song, and Y. Hao, “Discrete coordinate transformation for designing all-dielectric flat antennas,” *IEEE Trans. Antennas Propag.*, vol. 58, no. 12, pp. 3795–3804, 2010.
- [40] D. H. Werner and D.-H. Kwon, *Transformation Electromagnetics and Metamaterials: Fundamental Principles and Applications*. London: Springer-Verlag, 2014.
- [41] M. A. F. C. Junqueira, L. H. Gabrielli, and D. H. Spadoti, “Comparison of Anisotropy Reduction Strategies for Transformation Optics Designs,” *IEEE Photonics J.*, vol. 7, no. 1, pp. 1–10, Feb. 2015.

- [42] L. Xu and H. Y. Chen, “Conformal transformation optics,” *Nat. Photonics*, vol. 9, no. 1, pp. 15–23, 2014.
- [43] D. Schurig, J. J. Mock, B. J. Justice, S. A. Cummer, J. B. Pendry, A. F. Starr, and D. R. Smith, “Metamaterial electromagnetic cloak at microwave frequencies,” *Science*, vol. 314, no. 5801, pp. 977–980, 2006.
- [44] B. J. Justice, J. J. Mock, L. Guo, A. Degiron, D. Schurig, and D. R. Smith, “Spatial mapping of the internal and external electromagnetic fields of negative index metamaterials,” *Opt. Express*, vol. 14, no. 19, p. 8694, Sep. 2006.
- [45] M. Rahm, D. Schurig, D. A. Roberts, S. A. Cummer, D. R. Smith, and J. B. Pendry, “Design of electromagnetic cloaks and concentrators using form-invariant coordinate transformations of Maxwell’s equations,” *Photonics Nanostructures - Fundam. Appl.*, vol. 6, no. 1, pp. 87–95, 2008.
- [46] R. Liu, C. Ji, J. J. Mock, J. Y. Chin, T. J. Cui, and D. R. Smith, “Broadband Ground-Plane Cloak,” *Science (80-. )*, vol. 323, no. 5912, pp. 366–369, Jan. 2009.
- [47] A. Alu and N. Engheta, “Achieving transparency with plasmonic coatings,” *Phys. Rev. E - Stat. Nonlinear, Soft Matter Phys.*, vol. 72, no. 1, Feb. 2005.
- [48] D. A. Roberts, M. Rahm, J. B. Pendry, and D. R. Smith, “Transformation-optical design of sharp waveguide bends and corners,” *Appl. Phys. Lett.*, vol. 93, no. 25, pp. 1–4, 2008.
- [49] J. Luo, P. Xu, H. Chen, B. Hou, L. Gao, and Y. Lai, “Realizing almost perfect bending waveguides with anisotropic epsilon-near-zero metamaterials,” *Appl. Phys. Lett.*, vol. 100, no. 22, p. 221903, 2012.
- [50] H. Feng Ma, J. Hui Shi, W. Xiang Jiang, and T. Jun Cui, “Experimental realization of bending waveguide using anisotropic zero-index materials,” *Appl. Phys. Lett.*, vol. 101, no. 25, p. 253513, 2012.
- [51] P.-H. Tichit, S. N. Burokur, and A. de Lustrac, “Waveguide taper engineering using coordinate transformation technology,” *Opt. Express*, vol. 18, no. 2, p. 767, Jan. 2010.
- [52] Y.-L. Wu, Z. Zhuang, L. Deng, and Y.-A. Liu, “Three-dimensional multiway power dividers based on transformation optics,” *Sci. Rep.*, vol. 6, p. 24495, Apr. 2016.
- [53] D.-H. Kwon and D. H. Werner, “Flat focusing lens designs having minimized reflection based on coordinate transformation techniques,” *Opt. Express*, vol. 17, no. 10, pp. 7807–7817, 2009.
- [54] G. Du, C. Yu, and C. Liu, “Transformation Optical Design for 2D Flattened Maxwell Fish-eye Lens,” in *Antennas & Propagation (ISAP), 2013 Proceedings of the International Symposium on*, 2013, pp. 1–3.
- [55] F. Kong, B. I. Wu, J. A. Kong, J. Huangfu, S. Xi, and H. Chen, “Planar focusing

- antenna design by using coordinate transformation technology,” *Appl. Phys. Lett.*, vol. 91, no. 25, 2007.
- [56] L. Liang and S. V. Hum, “Realizing a Flat UWB 2-D Reflector Designed Using Transformation Optics,” *IEEE Trans. Antennas Propag.*, vol. 62, no. 5, pp. 2481–2487, May 2014.
- [57] P. H. Tichit, “Transformations d’espaces et applications électromagnétiques dans les domaines optiques et micro-ondes,” Ph.D. Thesis, Université de Paris 11, 2012.
- [58] P. H. Tichit, S. N. Burokur, C.-W. Qiu, and A. De Lustrac, “Experimental verification of isotropic radiation from a coherent dipole source via electric-field-driven LC resonator metamaterials,” *Phys. Rev. Lett.*, vol. 111, no. 13, pp. 1–5, 2013.
- [59] Q. Wu, Z. H. Jiang, O. Quevedo-Teruel, J. P. Turpin, W. Tang, Y. Hao, and D. H. Werner, “Transformation optics inspired multibeam lens antennas for broadband directive radiation,” *IEEE Trans. Antennas Propag.*, vol. 61, no. 12, pp. 5910–5922, 2013.
- [60] J. Yi, S. N. Burokur, and A. de Lustrac, “Conceptual design of a beam steering lens through transformation electromagnetics,” *Opt. Express*, vol. 23, no. 10, p. 12942, 2015.
- [61] J. Yi, S. N. Burokur, and A. De Lustrac, “Experimental validation of a transformation optics based lens for beam steering,” *Appl. Phys. Lett.*, vol. 107, no. 15, pp. 10–16, 2015.
- [62] J. B. Pendry and D. R. Smith, “The quest for the superlens,” *Sci. Am.*, vol. 295, pp. 60–67, 2006.
- [63] W. Cai, D. A. Genov, and V. M. Shalaev, “A Superlens Based on Metal-Dielectric Composites,” *Phys. Rev. B - Condens. Matter Mater. Phys.*, vol. 72, no. 19, Jun. 2005.
- [64] M. Tsang and D. Psaltis, “Magnifying perfect lens and superlens design by coordinate transformation,” *Phys. Rev. B - Condens. Matter Mater. Phys.*, vol. 77, no. 3, 2008.
- [65] M. Yan, W. Yan, and M. Qiu, “Cylindrical superlens by a coordinate transformation,” *Phys. Rev. B - Condens. Matter Mater. Phys.*, vol. 78, no. 12, 2008.
- [66] Y. Lai, J. Ng, H. Y. Chen, D. Z. Han, J. Xiao, Z. Q. Zhang, and C. T. Chan, “Optical illusion effects created by using metamaterials,” in *2009 International Conference on Electromagnetics in Advanced Applications*, 2009, pp. 841–843.
- [67] W. X. Jiang, H. F. Ma, Q. Cheng, and T. J. Cui, “Illusion media: Generating virtual objects using realizable metamaterials,” *Appl. Phys. Lett.*, vol. 96, no. 12, pp. 1–9, 2010.
- [68] Y. Lai, J. Ng, H. Y. Chen, Z. Q. Zhang, and C. T. Chan, “Illusion optics,” *Front. Phys. China*, vol. 5, no. 3, pp. 308–318, 2010.

- [69] D.-H. Kwon and D. H. Werner, "Polarization splitter and polarization rotator designs based on transformation optics," *Opt. Express*, vol. 16, no. 23, p. 18731, Nov. 2008.
- [70] T. Zhai, Y. Zhou, J. Zhou, and D. Liu, "Polarization controller based on embedded optical transformation," *Opt. Express*, vol. 17, no. 20, pp. 17206–13, 2009.
- [71] J. Andkjær and O. Sigmund, "Topology optimized low-contrast all-dielectric optical cloak," *Appl. Phys. Lett.*, vol. 98, no. 2, p. 21112, 2011.
- [72] J. Li and J. B. Pendry, "Hiding under the carpet: A new strategy for cloaking," *Phys. Rev. Lett.*, vol. 101, no. 20, pp. 1–11, 2008.
- [73] J. Valentine, J. Li, T. Zentgraf, G. Bartal, and X. Zhang, "Dielectric Optical Cloak," *Nat. Mater.*, vol. 8, no. 7, pp. 568–571, Apr. 2009.
- [74] T. Ergin, N. Stenger, P. Brenner, J. B. Pendry, and M. Wegener, "Three-Dimensional Invisibility Cloak at Optical Wavelengths," *Science (80-. )*, vol. 328, no. 5976, pp. 337–339, Apr. 2010.
- [75] H. F. Ma and T. J. Cui, "Three-dimensional broadband ground-plane cloak made of metamaterials," *Nat. Commun.*, vol. 1, no. 3, pp. 1–6, Jun. 2010.
- [76] S. G. Park, K. Lee, D. Han, J. Ahn, and K. H. Jeong, "Subwavelength silicon through-hole arrays as an all-dielectric broadband terahertz gradient index metamaterial," *Appl. Phys. Lett.*, vol. 105, no. 9, 2014.
- [77] W. X. Jiang, C. W. Qiu, T. C. Han, Q. Cheng, H. F. Ma, S. Zhang, and T. J. Cui, "Broadband All-Dielectric Magnifying Lens for Far-Field High-Resolution Imaging," *Adv. Mater.*, vol. 25, no. 48, pp. 6963–6968, Dec. 2013.
- [78] J. Hunt, N. Kundtz, N. Landy, V. Nguyen, T. Perram, A. Starr, and D. R. Smith, "Broadband wide angle lens implemented with dielectric metamaterials," *Sensors*, vol. 11, no. 8, pp. 7982–7991, 2011.
- [79] R. Yang, W. Tang, and Y. Hao, "A broadband zone plate lens from transformation optics," *Opt. Express*, vol. 19, no. 13, p. 12348, Jun. 2011.
- [80] W. X. Jiang, S. Ge, T. C. Han, S. Zhang, M. Q. Mehmood, C.-W. Qiu, and T. J. Cui, "Shaping 3D Path of Electromagnetic Waves Using Gradient-Refractive-Index Metamaterials," *Adv. Sci.*, vol. 3, no. 8, p. 1600022, Aug. 2016.
- [81] D. Shin, J. Kim, D.-S. Yoo, and K. Kim, "Design of 3D isotropic metamaterial device using smart transformation optics," *Opt. Express*, vol. 23, no. 17, p. 21892, 2015.
- [82] M. Yin, X. Yong Tian, L. Ling Wu, and D. Chen Li, "All-dielectric three-dimensional broadband Eaton lens with large refractive index range," *Appl. Phys. Lett.*, vol. 104, no. 9, pp. 1–5, 2014.
- [83] F. Zhou, W. Cao, B. Dong, T. Reissman, W. Zhang, and C. Sun, "Additive Manufacturing of a 3D Terahertz Gradient-Refractive Index Lens," *Adv. Opt. Mater.*,

- vol. 4, no. 7, pp. 1034–1040, Jul. 2016.
- [84] J. Yi, G.-P. Piau, A. de Lustrac, and S. N. Burokur, “Electromagnetic field tapering using all-dielectric gradient index materials,” *Sci. Rep.*, vol. 6, p. 30661, 2016.
- [85] R. C. Rumpf, J. J. Pazos, J. L. Digaum, and S. M. Kuebler, “Spatially variant periodic structures in electromagnetics,” *Philos. Trans. A. Math. Phys. Eng. Sci.*, vol. 373, no. 2049, p. 20140359-, 2015.
- [86] R. C. Rumpf, J. Pazos, C. R. Garcia, L. Ochoa, and R. Wicker, “3D Printed lattices with spatially variant self-collimation,” *Prog. Electromagn. Res.*, vol. 139, pp. 1–14, 2013.
- [87] Rui Yang, Wenxuan Tang, and Yang Hao, “Wideband Beam-Steerable Flat Reflectors via Transformation Optics,” *IEEE Antennas Wirel. Propag. Lett.*, vol. 10, pp. 1290–1294, 2011.
- [88] M. C. Arenas, A. C. Lepage, X. Begaud, P. H. Tichit, and A. de Lustrac, “All standard materials flat reflector made by transformation electromagnetics,” *Int. J. Microw. Wirel. Technol.*, vol. 6, no. 2, pp. 201–206, Apr. 2014.
- [89] O. Quevedo-Teruel, W. Tang, R. C. Mitchell-Thomas, A. Dyke, H. Dyke, L. Zhang, S. Haq, and Y. Hao, “Transformation optics for antennas: why limit the bandwidth with metamaterials?,” *Sci. Rep.*, vol. 3, p. 1903, May 2013.
- [90] S. Zhang, Y. Vardaxoglou, W. Whittow, and R. Mittra, “3D-printed flat lens for microwave applications,” *2015 Loughbrgh. Antennas Propag. Conf.*, pp. 1–3, 2015.
- [91] C. Mateo-Segura, A. Dyke, H. Dyke, S. Haq, and Y. Hao, “Flat luneburg lens via transformation optics for directive antenna applications,” *IEEE Trans. Antennas Propag.*, vol. 62, no. 4, pp. 1945–1953, 2014.
- [92] Y. Li and Q. Zhu, “Luneburg lens with extended flat focal surface for electronic scan applications,” *Opt. Express*, vol. 24, no. 7, p. 7201, 2016.
- [93] J. Yi, “Transformation optics : Application for antennas and microwave devices,” Ph.D. Thesis, Université Paris Saclay, 2015.
- [94] J. YI, S. N. Burokur, G.-P. Piau, and A. de Lustrac, “Coherent beam control with an all-dielectric transformation optics based lens,” *Sci. Rep.*, vol. 6, no. November 2015, p. 18819, 2016.
- [95] J. Yi, S. N. Burokur, G.-P. Piau, and A. de Lustrac, “Restoring in-phase emissions from non-planar radiating elements using a transformation optics based lens,” *Appl. Phys. Lett.*, vol. 107, no. 2, p. 24101, Jul. 2015.
- [96] J. B. Pendry, Y. Luo, and R. Zhao, “Transforming the optical landscape,” *Science (80-. )*, vol. 348, no. 6234, pp. 521–524, 2015.
- [97] H. Y. Chen, C. T. Chan, and P. Sheng, “Transformation optics and metamaterials,”

- Nat. Mater.*, vol. 9, no. 5, pp. 387–396, 2010.
- [98] H. Chen, J. B. Pendry, and D. R. Smith, “Special issue on transformation optics,” *J. Opt.*, vol. 18, no. 4, p. 40201, Apr. 2016.
- [99] C. García-Meca and C. Barceló, “Nontensorial Transformation Optics,” *Phys. Rev. Appl.*, vol. 5, no. 6, p. 64008, Jun. 2016.
- [100] D. E. Brocker, J. P. Turpin, and D. H. Werner, “Gradient index lens optimization using Transformation Optics,” in *2014 IEEE Antennas and Propagation Society International Symposium (APSURSI)*, 2014, pp. 755–756.
- [101] B. B. Tierney and A. Grbic, “Optimization as an alternative to transformation optics,” in *2016 10th European Conference on Antennas and Propagation (EuCAP)*, 2016, pp. 1–2.
- [102] O. Ozgun and M. Kuzuoglu, “Remesh-free Shape Optimization by Transformation Optics,” *IEEE Trans. Antennas Propag.*, pp. 1–1, 2016.
- [103] A. Vakil, “Transformation optics using Graphene: one atom thick optical devices based on graphene,” Ph.D. Thesis, University of Pennsylvania, 2012.
- [104] A. Vakil and N. Engheta, “One-Atom-Thick IR Metamaterials and Transformation Optics Using Graphene,” *Arxiv*, vol. arXiv:1101, no. 6035, pp. 1–21, Jan. 2011.
- [105] A. Vakil and N. Engheta, “Transformation Optics Using Graphene,” *Science (80-. )*, vol. 332, no. 6035, pp. 1291–1294, 2011.
- [106] T. J. Cui, M. Q. Qi, X. Wan, J. Zhao, and Q. Cheng, “Coding Metamaterials, Digital Metamaterials and Programming Metamaterials,” *Light Sci. Appl.*, no. August, p. 19, 2014.
- [107] A. D. Boardman, V. V. Grimalsky, Y. S. Kivshar, S. V. Koshevaya, M. Lapine, N. M. Litchinitser, V. N. Malnev, M. Noginov, Y. G. Rapoport, and V. M. Shalaev, “Active and tunable metamaterials,” *Laser Photon. Rev.*, vol. 5, no. 2, pp. 287–307, Mar. 2011.
- [108] T. Driscoll, H. T. Kim, B. G. Chae, B. J. Kim, Y. W. Lee, N. M. Jokerst, S. Palit, D. R. Smith, M. Di Ventra, and D. N. Basov, “Memory Metamaterials,” *Science (80-. )*, vol. 325, no. 5947, pp. 1518–1521, 2009.
- [109] Y. Yang, A. Q. Liu, L. K. Chin, X. M. Zhang, D. P. Tsai, C. L. Lin, C. Lu, G. P. Wang, and N. I. Zheludev, “Optofluidic waveguide as a transformation optics device for lightwave bending and manipulation,” *Nat. Commun.*, vol. 3, p. 7, 2012.
- [110] M. Clemente Arenas, A. C. Lepage, and X. Begaud, “Antipodal radiation pattern of a patch antenna combined with superstrate using transformation electromagnetics,” *Appl. Phys. A*, vol. 117, no. 2, pp. 699–703, Nov. 2014.
- [111] R. Yang, X. Kong, H. Wang, H. Su, Z. Lei, J. Wang, A. Zhang, and L. Chen, “Transformation-optical Fan-beam Synthesis,” *Sci. Rep.*, vol. 6, p. 20530, Feb. 2016.

- [112] J. P. Turpin and D. H. Werner, "Switchable near-zero-index magnetic metamaterial for dynamic beam-scanning lens," in *IEEE Antennas and Propagation Society, AP-S International Symposium (Digest)*, 2012.
- [113] D. F. Sievenpiper, "High-Impedance Electromagnetic Surfaces," Ph.D. Thesis, University of California, Los Angeles, 1999.
- [114] F. Yang and Y. Rahmat-Samii, "Reflection Phase Characterizations of the EBG Ground Plane for Low Profile Wire Antenna Applications," *IEEE Trans. Antennas Propag.*, vol. 51, no. 10 I, pp. 2691–2703, 2003.
- [115] C. Joshi, A. C. Lepage, J. Sarrazin, and X. Begaud, "Enhanced Broadside Gain of an Ultrawideband Diamond Dipole Antenna Using a Hybrid Reflector," *IEEE Trans. Antennas Propag.*, vol. 64, no. 7, pp. 3269–3274, Jul. 2016.



# Appendices

## Appendix A. Software

The electromagnetic simulation in this thesis is carried on two commercial software suites: COMSOL Multiphysics™ and CST Microwave Studio™.

### a) COMSOL Multiphysics

COMSOL is a software suite for studying the coupled problems in physics and engineering. It is cross-platform software that can be run on Windows, MacOS or Linux. It can calculate solutions for 1D, 2D or 3D problems using finite element analysis. Various design modules pertaining to electrical, thermal, mechanical, etc. can be integrated in a single design problem. The software is widely used in the physics and larger engineering community. The results presented in this thesis have been calculated on COMSOL Multiphysics 4.3a. Different design modules in COMSOL may be used for simulating TO problems e.g. RF, Wave Optics, and Ray Optics. In the current thesis, RF module has been used.

Regarding its application towards studying Transformation Optics problems, the wave propagation behavior inside a transformed space can be modeled with relative ease in COMSOL design environment. This is due to following features:

- In TO method, electromagnetic properties (e.g. permittivity, permeability, field strength, etc.) vary as per a coordinate transformation between a physical and virtual space. This coordinate transformation can be defined as a design variable in COMSOL. Consequently, these variables can be used to calculate permittivity/permeability values in the spatially transformed profile.
- TO solutions are inherently anisotropic. Material anisotropy can also be completely defined using ‘Wave Equation’ in the RF Module of COMSOL. Multiple wave equations can also be added, each corresponding to a different spatially transformed region. Different definitions are possible: isotropic, diagonal, symmetric or anisotropic permittivity/permeability.
- Ideal current sheets can be used in COMSOL, which allow modeling metallic patches in patch antennas. This permits latter’s easy modeling without worrying about other design considerations like input impedance matching.

- Unique polarization of electric field can be assigned to a current sheet in a 2D problem. In the present thesis, a  $z$ -polarized electric field has been used. This facilitates the simulation of a reduced two dimensional problem.

All these design features make COMSOL a great design tool for studying the problem in reduced complexity. However, CST Microwave Studio is preferred for full-wave simulations. This is discussed next.

## **b) CST Microwave Studio**

CST Microwave Studio is a powerful electromagnetic software suite which is widely used in the RF and Antenna design community. In this thesis, the transient solver of CST Microwave Studio has been used to present the results of TO designs. Frequency domain solver has been used for characterization of unit cell of an artificial magnetic conductor for an obliquely incident plane wave.

The software is a great design enabler. 3D modeler of CST Microwave studio gives the user access to a wide variety of standard design shapes (cuboid, cylinder, sphere, etc.) Additionally, complex shapes like curved geometries can also be designed easily using analytical faces. This facilitates the design and study of complex geometries. The software also allows exporting the three-dimensional design information in different CAD file-formats, which facilitates the 3D printing of the designs. For example, TO receptacles designed in this thesis have been exported in .STL format.

CST offers a comprehensive library of standard commercially available materials. These materials can be assigned to different objects in the material definition. The materials have pre-defined properties like permittivity, permeability, electric and magnetic dispersion, etc. This is of great use when designing a prototype with commercial materials to closely simulate the performance of device. In context of this thesis, the results of simulation of prototype presented in chapter 4 used CST's material definition of Alumina. Apart from standard dielectric materials, CST also allows defining new materials with desired properties. In this research, this has been amply used during the definition of pixilated profile. Furthermore, the standard software also allows defining an anisotropic material, but only diagonal elements of permittivity and permeability tensor. However, 'Create Full Tensor Material' macro is available in the package for a full anisotropic definition, which allows defining the off-diagonal elements in the tensor. But unlike COMSOL, it is not possible to design a continuous gradient material.

The transient solver is fast and accurate. This is also corroborated through the close agreement of simulated and measured performances of the devices fabricated in this thesis. Increasing the mesh density in features of small dimensions can enhance the simulation

accuracy. This can be done in the ‘Local Mesh Properties’ option for the objects in the design. While local meshing may significantly increase the simulation time, selecting ‘Use subgridding’ under the ‘Specials’ tab in ‘Global Mesh Properties’ may considerably reduce this computation time. In the context of this thesis, the number of mesh cells in the calculation tends to increase due to use of at least 3 local mesh cells in the small dimensions (individual pixels in material profile of dielectric superstrate, multilayer substrate of new antenna in chapter 4, etc). Thus, subgridding has been used extensively to reduce the computation time.

The software is great for antenna design. A variety of results like S-parameters, Directivity, Realized Gain, etc. can be displayed using a variety of 1D, 2D and 3D plots.

## Appendix B. Cylindrical Superstrate

In Chapter 3, a cuboidal dielectric superstrate has been proposed for reorientation of electromagnetic waves in azimuthal plane. The two dimensional pixilated profile is extruded along  $z$ -axis for conserving the spatial transformation (Fig. 3.23). Alternatively, a cylindrical superstrate may also be designed by revolving the superstrate about  $x$ -axis, as shown in Fig. B.1. Cylindrical superstrates for antipodal radiation have previously been discussed in the thesis of Clemente Arenas, but the profile contained both permittivity and permeability values. Here, the simulated performance of a cylindrical dielectric superstrate is discussed.

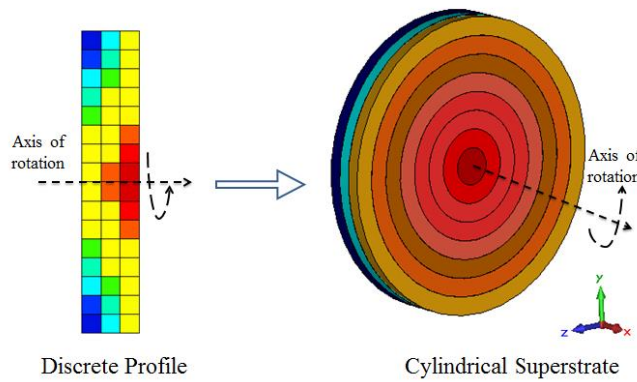


Fig. B.1 A three-dimensional cylindrical superstrate designed from the two dimensional pixilated profile.

The discretized 2D profile is rotated along  $x$ -axis such that the spatial transformation is conserved along the radial plane. It may be noted here that the diameter of the cylindrical profile here is 170 mm. At this diameter, the area of aperture of the cylindrical superstrate is equal to that of cuboidal superstrate. The advantage of the cylindrical profile is that a antipodal radiation may be achieved in any direction in the azimuthal plane due to the radial symmetry. This operation is shown below by using this superstrate along with a dual-orthogonal polarized antenna with two input ports. The design of the antenna is same as described in chapter 3, but has an extra input port in the orthogonal plane. A cylindrical dielectric layer of relative permittivity,  $\epsilon_r = 1.8$  is used to match the cylindrical superstrate to the patch antenna. Following input configurations for the two port antenna are studied:

Port 1	Port 2
ON	OFF
ON, $0^\circ$	ON, $0^\circ$ (in phase)
OFF	ON
ON, $0^\circ$	OFF, $180^\circ$ (out of phase)

Here, the phase shift at input is considered at the operating frequency of 1.25 GHz. The magnitude of reflection coefficient for above input configurations is plotted in Fig. B.2.

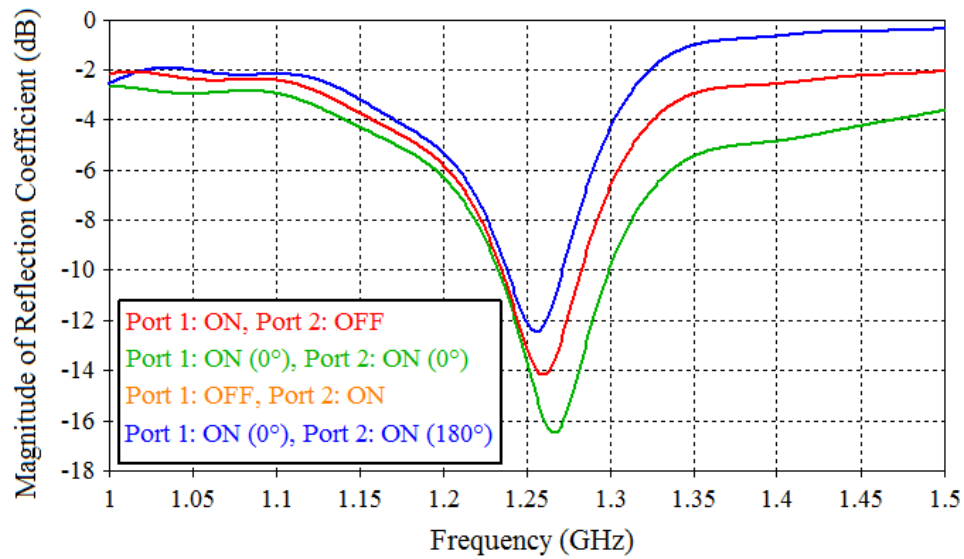


Fig. B.2 Magnitude of reflection coefficient of different of input excitations of antenna-cylindrical superstrate assembly.

It is seen that the antenna superstrate assembly is matched for any excitation at or in the neighboring frequencies of 1.25 GHz ( $|S_{11}| < -10$  dB). In the figure, traces for individual excitations of both ports are identical. In Fig. B.3, the realized gain patterns of the antenna superstrate assembly are compared at 1.25 GHz for each of these excitations. It is seen that by controlling the phase at the input ports of the patch antenna, this solution may allow achieving a complete visibility in the azimuthal plane.

The radiation performance of the cylindrical performance of the superstrate is similar to that of the cuboidal superstrate presented in chapter 3. The peak realized gain is 3.3 dB in the  $y z$  plane (azimuth). A broadside null is achieved along  $x$ -axis. The level of cross polarization is high in the azimuthal plane in certain directions, as also seen in the simulated and measured radiation performances of cuboidal superstrates described in chapters 3-5.

This superstrate presents the advantage of quasi-omnidirectional visibility using electronic switching. Like the cuboidal superstrate, its fabrication may be envisaged using the two material fabrication strategy discussed in chapter 4. Next, a discussion on materials and fabrication processes is provided below.

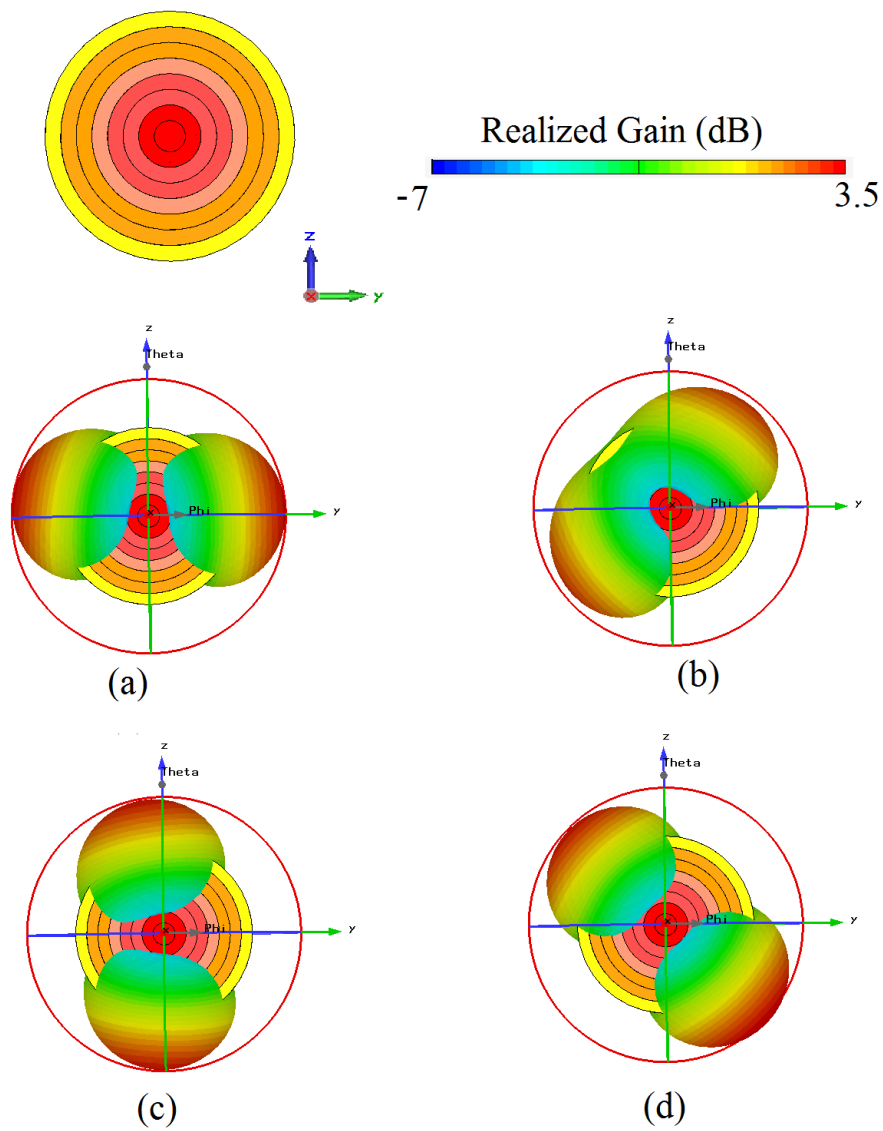


Fig. B.3 3D polar plots of realized Gain of antenna-cylindrical superstrate as seen in y z plane (top-view): (a) Port-1ON, Port 2-OFF, (b) Port-1ON ( $0^\circ$ ), Port 2-ON ( $0^\circ$ ), (c) Port-1OFF, Port 2-ON, (d) Port-1ON ( $0^\circ$ ), Port 2-ON ( $180^\circ$ .)

## Appendix C. Materials

The fabricated prototypes presented in this thesis are comprised of high permittivity alumina slabs and 3D printed receptacles. Here, supplementary information on their properties and fabrication is provided.

### a) Alumina

Unlike other high permittivity materials which are hard to buy off-the-shelf, Alumina is present in about 15% of the minerals found in the earth's crust. It is abundantly available and can be easily bought from the vendors. The combination of high thermal conductivity, low thermal expansion and high compressive strength leads to good thermal shock resistance. It is also inert to most common chemicals. Alumina also shows good electrical insulation, good wear resistance and high hardness, and is therefore suitable for many industrial applications. Due to these properties, it is equally difficult to machine the Alumina in lab. Diamond tools are needed to machine Alumina in the required shape. The dielectric constant of Alumina varies from 9 to 10, depending upon its purity. Alumina sheets used to fabricate the prototypes are 99.7% pure and ordered from Goodfellow™. The information on properties of Goodfellow's alumina products are available on its website, and are recapitulated in the tables below.

#### Chemical Resistance

Acids - concentrated	Good
Acids - dilute	Good
Alkalis	Good
Halogens	Good
Metals	Good

#### Electrical Properties

Dielectric constant	9.0-10.1
Dielectric strength ( kV mm <sup>-1</sup> )	10-35
Volume resistivity @25C ( Ohmcm )	>10 <sup>14</sup>

#### Mechanical Properties

Compressive strength ( MPa )	2200-2600
Hardness - Knoop ( kgf mm <sup>-2</sup> )	2100
Hardness - Vickers ( kgf mm <sup>-2</sup> )	1500-1650
Shear strength ( MPa )	330
Tensile modulus ( GPa )	300-400

#### Physical Properties

Apparent porosity ( % )	0
Density ( g cm <sup>-3</sup> )	3.9
Water absorption - saturation ( % )	0

#### Thermal Properties

Coefficient of thermal expansion @20-1000C ( x10 <sup>-6</sup> K <sup>-1</sup> )	8.0
--	-----

Melting point ( C )	2100
Specific heat @25C ( J K <sup>-1</sup> kg <sup>-1</sup> )	850-900
Thermal conductivity @20C ( W m <sup>-1</sup> K <sup>-1</sup> )	26-35
Upper continuous use temperature ( C )	1700

## b) Additive Manufacturing: Printers & compatible materials

Additive manufacturing, popularly called 3D printing, is a disruptive technology that challenges the norms of the conventional fabrication processes. This technology allows fabricating complex three dimensional shapes by successively designing layers. The information on the shape of the object is stored in a digital file format compatible with a 3D printer (e.g. OBJ, STL, CWPRJ, etc.)

The advantage of 3D printing is most certainly in two aspects. Firstly, a very high degree of precision may be achieved by controlling the deposition rates. The precision in terms of designing sharp bends and corners cannot be achieved by conventional procedures like milling due to cylindrical bids; as a result the corners are always rounded. In such scenario, 3D printing is an ideal choice as the corners can be grown layer by layer. Secondly, the rapid prototyping allows saving a lot of time over conventional fabrication techniques.

In context of the solutions fabricated in this thesis, receptacle's definition is exported in STL format directly from the 3D modeler in CST Microwave Studio. Two versions of 3D printed receptacle are developed in this thesis using two different processes. Relevant information on the printers and materials is provided below.

### i. FullCure Superstrate

The FullCure based receptacle is developed at the Airbus Group Innovations, Suresnes using the 3D printing solutions package by Stratasys™. The Objet Eden260 VS is Stratasys' mid-range 3D printer in the Design Series. The printer is shown in Fig. C.1.



Fig. C.1 Objet Eden260 VS by Stratasys™.

This printer is used for fabricating single material designs (as the receptacle presented in this thesis.) It uses Polyjet printing technology, which is similar to the Inkjet printers in its operation. Instead of ink, tiny drops of liquid plastic material are deposited using jets. These drops are then cured instantly using ultraviolet light, resulting in their solidification. Models up to 255 mm by 252 mm by 200 mm can be fabricated in this printer with up to 16-micron layer accuracy. For complex shapes like holes, the 3D printer automatically jets a second support material, which can be later washed using water. In the following table, the specifications of the printer are provided. More information on this printer and other printers from Stratasys may be consulted on their website.

Model Materials	Rigid Opaque: VeroWhitePlus™*, VeroBlackPlus™**, VeroGray™*, VeroBlue™* Rubber-like**: TangoPlus™, TangoBlackPlus™, TangoBlack™, TangoGray™ Transparent: VeroClear™* and RGD720** Simulated Polypropylene**: Rigur™ and Durus™ High Temperature** Bio-compatible** *Works with SUP705 or SUP707 **Works with SUP705
Support Material	SUP705 (WaterJet removable) and SUP707 (soluble)
Maximum Build Size (XYZ)	255 mm by 252 mm by 200 mm
System Size and Weight	870 mm by 1200 mm by 735 mm; 254 kg
Resolution	X-axis: 600 dpi; Y-axis: 600 dpi; Z-axis: 1600 dpi
Accuracy	20-85 microns for features below 50 mm; up to 200 microns for full model size
Minimum Layer Thickness	Horizontal build layers as fine as 16 microns
Build Modes	High-speed: 30-micron resolution High-quality: 16-micron resolution
Software	Objet Studio™ intuitive 3D printing software

Workstation Compatibility	Windows 7/ Windows 8
Network Connectivity	LAN - TCP/IP
Operating Conditions Temperature	18-25°C (64-77°F); relative humidity 30-70% (non-condensing)
Power Requirements	100-200 VAC, 50/60Hz, 14A; 200-240 VAC, 50-60Hz, 7A
Regulatory Compliance	CE, FCC/RoHS

The material used at Airbus Group Innovations, Suresnes facility has been previously characterized in X-band for its electrical properties. At 10 GHz,  $\epsilon_r = 2.8$  and  $\tan\delta = 0.02$ .

### *ii. PLA Superstrate*

The PLA receptacle presented in this thesis is fabricated using Fused Filament Fabrication (FFF) technique. CraftBot 3D printer by CraftUnique™ is used along to fuse a Poly Lactic Acid (PLA) Filament. The solid filament, commercially available in form spindles by weight, is fused by passing it through a heated nozzle. This fused material is then deposited on a heated platform in the desired shape. A problem encountered during the fabrication of voluminous solid objects is that the fused material often retains the heat in certain regions of the object, while cools in others. This non-uniform dissipation results in stresses in the design and consequently the shape of objects may be deformed. The printer takes this in account and auto-generates a mesh like structure. A representative image of the printer is shown in Fig. C.2.

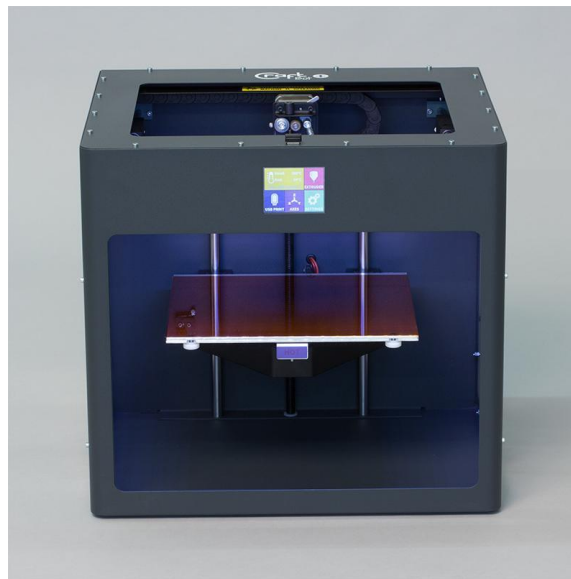


Fig. C.2 CraftBot 3D printer by CraftUnique™

The printer's characteristics are listed in the table below. More details can be found on CraftUnique's website.

Maximum Build Size (XYZ)	250 mm by 250 mm by 200 mm
Layer resolution	100 micron (ultra) 200 micron (high) 300 micron (medium)
Position precision	X, Y: 4 micron Z: 2 micron
Filament diameter	1.75 mm
Nozzle diameter	0.4 mm
Ambient temperature	15-32 °C
Storage temperature	0-32 °C
Operating nozzle temperature	180-260 °C
Temperature of build platform	50°-110°

The PLA filament is commercially available from Arianoplast™, a french enterprise. It can be found under the trade name of Ingeo 4043D, and is widely used for 3D printing. Generally speaking, this material is resistant to moisture retention during cooling. Its electrical properties have been measured for Airbus Group Innovations as a previous characterization in X-band. At 10 GHz,  $\epsilon_r = 2.56$  and  $\tan\delta = 0.03$ . It may be noted here that commercial 3D printer filaments of a certain kind of material (e.g. PLA) are sold in different colors, as shown in Fig. C.3. The addition of color may induce changes in the electrical properties of the filament. Thus a red PLA filament is not identical to a white PLA filament. This is an additional source of error during the design and must be factored in during simulations.



Fig. C.3 3D printer compatible PLA filaments of different colors (Arianoplast™.)

### *iii. Premix TP20280*

As also explained in the thesis, effective medium approximation is used to design the gradient in the relative permittivity for 3D printed TO solutions. The range of permittivity achievable inside is often limited by the relative permittivity of 3D printer's material. Relative

## *Appendices*

permittivity of most commercially available 3D printer filaments is limited to a value of 3. Recently, Premix™ has presented new range of 3D printer filaments specifically for antenna and RF applications, whose relative permittivity value goes as high as 4.4. One such material is PrePerm-TP20280. It is an ABS based grade and is compatible with commercial printers capable of reaching a nozzle temperature of 260 °C. The advantage of this product is the low losses ( $\tan\delta = 0.004$ ), which makes it suitable for many RF applications. The advertised use of this filament is in prototyping of dielectric lenses for antennas. This filament may eventually be used in context of the designs presented in this thesis for prototyping different superstrate.



# Contrôle du diagramme de rayonnement d'une antenne en technologie imprimée à l'aide d'un superstrat diélectrique inspiré de la transformation d'espace

**RESUME :** La Transformation d'Espace appelée aussi Transformation Optique (TO) est un outil de conception électromagnétique puissant qui a permis la conception de nouveaux dispositifs tels que la célèbre "cape d'invisibilité". Cette thèse s'inscrit dans la continuité directe de celle de M.D. Clemente Arenas (Application de la transformation d'espace à la conception d'antennes à diagramme de rayonnement contrôlé, 2014) et porte sur l'utilisation de la TO pour modifier drastiquement le rayonnement d'une antenne patch. Ces fortes modifications du rayonnement sont habituellement obtenues avec l'aide d'un superstrat encombrant et constitué de matériaux ayant une perméabilité et permittivité exotiques (métamatériaux). L'objectif est donc ici de réduire cet encombrement et de simplifier la réalisation en utilisant des matériaux diélectriques standards. Ainsi, grâce au superstrat développé, une antenne patch ayant un gain réalisé de 7 dB devient une antenne présentant deux lobes dans le plan azimutal de gain réalisé de 3.5 dB. Le superstrat, d'épaisseur  $0.12\lambda$ , est conçu à l'aide de deux matériaux uniquement : Alumine ( $\epsilon_r = 9.9$ ) et Fullcure ( $\epsilon_r = 2.8$ ), alors que le profil initial comporte une permittivité variant entre 1 et 15 et une perméabilité entre 0.3 et 3. Divers degrés de libertés dans la conception permettent d'adapter notre solution pour concevoir d'autres superstrats avec des fonctionnalités différentes: diagramme ayant une ouverture de plus de  $180^\circ$  dans un plan, diagramme end-fire, etc. Les applications visées sont notamment celles de l'aéronautique pour lesquelles il existe aujourd'hui sur les avions plusieurs dizaines d'antennes pour assurer toutes les liaisons nécessaires aux communications, à l'identification, au positionnement, etc. La géométrie du porteur conduit alors à utiliser plusieurs antennes protubérantes pour remplir cette mission. Cependant pour un avion, ces excroissances contribuent à dégrader l'aérodynamisme de l'appareil ce qui se traduit par une consommation plus importante. Le but est donc de proposer des solutions antennaires à rayonnement non-conventionnel et non protubérante compatible avec une intégration sur dérive ou fuselage. Le concept est validé à l'aide d'une maquette réalisée avec une imprimante 3D et avec le soutien d'Airbus Group Innovations.

**Mots clés :** Transformation d'espace, superstrat diélectrique, antenne patch, impression 3D.

## Controlling radiation pattern of patch antenna using Transformation Optics based dielectric superstrate

**ABSTRACT :** Transformation Optics (TO) is a powerful electromagnetic design tool that enables the design of new devices such as the famous "invisibility cloak". This thesis is in direct continuation of that of M.D. Clemente Arenas (Application de la transformation d'espace à la conception d'antennes à diagramme de rayonnement contrôlé, 2014) and focuses on the use of the TO to drastically change radiation of a patch antenna. These sharp changes in radiation pattern are usually obtained using bulky superstrates made of metamaterials having exotic permeability and permittivity values. The objective of this thesis is to reduce the thickness of the superstrate and simplify the fabrication by enabling the use of standard dielectric materials. Thus, a patch antenna with realized gain of 7 dB is transformed, with the help of proposed superstrate, into an antenna having two lobes in the azimuth plane with realized gain of 3.5 dB. The  $0.12\lambda$  thick superstrate is designed using two standard dielectric materials only: Alumina ( $\epsilon_r = 9.9$ ) and FullCure ( $\epsilon_r = 2.8$ ), whereas the previous solution had variation in permittivity between 1 and 15 and in permeability between 0.3 and 3. Various degrees of freedom in the design allow adapting this solution to develop new superstrates for other applications: radiation pattern with HPBW greater than  $180^\circ$  in one plane, end-fire radiation pattern, etc. Target applications include those of aeronautics. Today, dozens of antennas on an aircraft are required to ensure the necessary communications links, identification, positioning and other purposes. The structure of the aircraft necessitates use multiple antennas to fulfill this mission, which are fixed and protrude on fuselage or wings. However, for an aircraft, these protuberances contribute to the aerodynamic drag, which results in higher fuel consumption. Therefore, the objective is to propose conformal antenna solutions with unconventional radiation pattern, which can be eventually integrated on fuselage or rudder. The concept is validated using a model made with a 3D printer and with the support of Airbus Group Innovations.

**Keywords :** Transformation Optics, dielectric superstrate, patch antenna, 3D printing.

